UNIVERSITI TEKNOLOGI MARA

PHOTOCATALYTIC ESTERIFICATION OF WASTE COOKING OIL USING TiO_2/EFBA AND ZNO/EFBA UNDER UV-VISIBLE LIGHT IRRADIATION

SITI FADHILAH BINTI IBRAHIM

PhD

June 2026

UNIVERSITI TEKNOLOGI MARA

PHOTOCATALYTIC ESTERIFICATION OF WASTE COOKING OIL USING TiO_2/EFBA AND ZNO/EFBA UNDER UV-VISIBLE LIGHT IRRADIATION

SITI FADHILAH BINTI IBRAHIM

Thesis submitted in fulfilment
of the requirements for the degree of
Doctor of Philosophy
(Science)

Faculty of Applied Science

June 2026

CONFIRMATION BY PANEL OF EXAMINERS

I certify that a Panel of Examiners has met on 21st January 2026 to conduct the final examination of Siti Fadhilah binti Ibrahim on her Doctor of Philosophy thesis entitled "Photocatalytic Esterification of Waste Cooking Oil using TiO_2/EFBA and ZnO/EFBA under UV-Visible Light Irradiation" in accordance with Universiti Teknologi MARA Act 1976 (Akta 173). The Panel of Examiners recommends that the student be awarded the relevant degree. The Panel of Examiners was as follows:

Che Puteh Osman, PhD
Associate Professor
Faculty of Applied Sciences
Universiti Teknologi MARA
(Chairman)

Hamizah Mohd Zaki, PhD
Associate Professor
Faculty of Applied Sciences
Universiti Teknologi MARA
(Internal Examiner)

Gaanty Pragas A/L Maniam, PhD
Professor
Faculty of Industrial Sciences and Technology
Universiti Malaysia Pahang Al-Sultan Abdullah
(External Examiner)

PROFESSOR DR HJH ZURAEDA IBRAHIM
Dean
Institute of Postgraduates Studies
Universiti Teknologi MARA

Date: 5 June 2026

AUTHOR'S DECLARATION

I declare that the work in this thesis was carried out in accordance with the regulations of Universiti Teknologi MARA. It is original and is the results of my own work, unless otherwise indicated or acknowledged as referenced work. This thesis has not been submitted to any other academic institution or non-academic institution for any degree or qualification.

I, hereby, acknowledge that I have been supplied with the Academic Rules and Regulations for Post Graduate, Universiti Teknologi MARA, regulating the conduct of my study and research.

Name of Student	:	Siti Fadhilah Binti Ibrahim
Student ID. No.	:	2022347267
Programme	:	Doctor of Philosophy (Science) - AS950
Faculty	:	Applied Sciences
Thesis Title	:	Photocatalytic Esterification of Waste Cooking Oil using TiO_2/EFBA and ZnO/EFBA under UV-Visible Light Irradiation
Signature of Student	:	
Date	:	June 2026

ABSTRACT

The increasing global energy demand and environmental concerns have intensified the search for sustainable fuel alternatives. Biodiesel derived from waste cooking oil (WCO) is a promising option because it is renewable, non-edible, and helps reduce waste. However, the high free fatty acid (FFA) content in WCO limits conventional base-catalysed transesterification and requires an effective pretreatment process. This study aimed to develop and optimize a photocatalytic esterification process for high-FFA WCO using semiconductor photocatalysts based on titanium dioxide (TiO_2) and zinc oxide (ZnO). To enhance catalytic performance, TiO_2 and ZnO were immobilized on empty fruit bunch ash (EFBA), an agricultural waste rich in mineral oxides that can function as both a support and co-catalyst. The photocatalysts were synthesized via the wet impregnation technique, and the effects of TiO_2/ZnO-to-EFBA mass ratio and calcination temperature were investigated. Comprehensive characterization techniques, including XRD, FESEM–EDX, HRTEM, UV–Vis DRS, PL, FTIR, BET surface area analysis, CO_2 -TPD, TGA, and XRF, were employed to evaluate the physicochemical properties of the catalysts. XRD analysis revealed the presence of EFBA-derived crystalline phases which act as mediators for electron–hole transfer and help suppress charge recombination. BET analysis indicated increased surface areas for both TiO_2/EFBA (T11) and ZnO/EFBA (Z11), facilitating improved adsorption of FFA and methanol on catalytic active sites. In addition, PL quenching suggested enhanced suppression of electron–hole recombination after EFBA incorporation. Photocatalytic activity was evaluated under UV, visible, and xenon light irradiation. UV-A irradiation (365 nm) provided the most effective activation of the photocatalysts. Using a one-variable-at-a-time (OVAT) optimization approach, the T11 catalyst with a 1:1 mass ratio achieved 78% FFA conversion within 2 h, whereas Z11 with the same ratio achieved 85% conversion within 4 h. These results indicate that T11 provides faster reaction kinetics, while Z11 offers higher conversion and improved operational stability. Radical scavenger experiments confirmed that hydroxyl radicals (•OH), superoxide radicals ($\bullet O_2^-$), electrons (e^-), and holes (h^+) are the key reactive species involved in the photocatalytic esterification mechanism. Both catalysts maintained good catalytic performance over five reuse cycles, demonstrating excellent stability and reusability. Following photocatalytic esterification, the treated WCO was further converted into biodiesel via alkaline transesterification. Gas chromatography–mass spectrometry (GC–MS) analysis confirmed a fatty acid methyl ester (FAME) content of 89.2%, and the produced biodiesel satisfied the quality requirements specified in ASTM D6751 and EN 14214 standards. Overall, this study demonstrates a low-energy and waste-integrated approach for biodiesel production, highlighting the potential of EFBA-supported photocatalysts for sustainable fuel generation from high-FFA waste feedstocks.

ACKNOWLEDGEMENT

Alhamdulillah, all praise to Allah SWT for His endless guidance, protection, and blessings throughout my research journey, which has now come to completion.

First and foremost, I would like to express my deepest gratitude to my supervisor, Dr. Norshahidatul Akmar Mohd Shohaimi, for her kindness, patience, and unwavering guidance throughout my PhD journey. I am also sincerely grateful to my co-supervisors, Dr. Zul Adlan Mohd Hir, Dr. Mohd Sufri Mastuli, and Prof. Dato' Dr. Taufiq Yap Yun Hin, for their invaluable knowledge, advice, and encouragement, which have been essential to the success of this research.

To my beloved family, especially my father and siblings, thank you for your love, support, and prayers. To my late mother, your memory continues to inspire me every day, and I carry your strength in my heart throughout this journey.

I would also like to extend my gratitude to Universiti Teknologi MARA (UiTM) Jengka, Pahang, and the Chemistry Laboratory, Faculty of Applied Sciences (FSG), for providing the facilities and support needed for this research. My sincere thanks go to all the laboratory officers and assistants who assisted me during my experiments. To my friends, thank you for standing by me through long hours in the lab, sharing both the joyful and challenging moments along the way.

Finally, I want to acknowledge myself for perseverance and determination. Even when the journey felt overwhelming, I chose to keep moving forward. This experience has taught me that with Allah's guidance, resilience, and faith, any obstacle can be overcome, and the path of knowledge is truly ours to shape.

TABLE OF CONTENTS

		Page
CONFIRMATION BY PANEL OF EXAMINERS		**ii**
AUTHOR'S DECLARATION		**iii**
ABSTRACT		**iv**
ACKNOWLEDGEMENT		**v**
TABLE OF CONTENTS		**vi**
LIST OF TABLES		**x**
LIST OF FIGURES		**xii**
LIST OF SYMBOLS		**xvii**
LIST OF ABBREVIATIONS		**xviii**
CHAPTER 1 INTRODUCTION		**1**
1.1	Research Background	1
1.2	Problem Statement	5
1.3	Research Objectives	6
1.4	Scope of Study	6
1.5	Significance of Study	7
CHAPTER 2 LITERATURE REVIEW		**9**
2.1	Biodiesel Overview	9
2.2	Waste Cooking Oil as Feedstock	13
2.3	Photocatalysis	16
	2.3.1 Factor Affecting Photocatalytic Performance	17
	2.3.2 Semiconductor Photocatalyst Materials	17
2.4	Photocatalytic Esterification	19
2.5	Transesterification	23
2.6	Photocatalyst	25
	2.6.1 Titanium Dioxide-Based Photocatalyst	27
	2.6.2 Zinc Oxide-Based Photocatalyst	30

2.7 Modification Strategies for Semiconductor Photocatalyst 32
2.7.1 Empty Fruit Bunch Ash (EFBA) 33
2.7.2 EFBA-supported TiO_2/ZnO Photocatalyst 36
2.8 One-Variable-at-a-Time (OVAT) Parameters for Photocatalytic Esterification 37
2.8.1 Effect of Alcohol to Oil Molar Ratio 37
2.8.2 Effect of Catalyst Loading 38
2.8.3 Effect of Reaction Time 38
2.9 Effect of EFBA doping on Optimal Operational Parameters 38
2.10 Light Source 39
2.10.1 Ultraviolet (UV) Light 39
2.10.2 Visible Light 40
2.10.3 Xenon Light 40
2.11 Research Gap and Study Relevance 40

CHAPTER 3 METHODOLOGY 42
3.1 Introduction 42
3.2 Apparatus 43
3.3 Chemicals 44
3.4 Pre-treatment of WCO 44
3.4.1 Saponification Test 45
3.4.2 Acid Value Test 45
3.4.3 Moisture Content Test 47
3.5 Preparation Photocatalyst 47
3.6 Characterization of Photocatalyst 48
3.6.1 Powder X-Ray Diffraction (XRD) 48
3.6.2 Field Emission Scanning Electron Microscopy (FESEM) 49
3.6.3 Energy-Dispersive X-ray (EDX) 50
3.6.4 High-Resolution Transmission Electron Microscopy (HRTEM) 50
3.6.5 Ultraviolet-Visible Diffuse Reflectance Spectroscopy (UV-Vis-DRS) 50
3.6.6 Photoluminescence Spectroscopy (PL) 52
3.6.7 Fourier Transform Infrared spectroscopy (FTIR) 52

3.6.8 Brunauer-Emmet-Teller (BET) 52
3.6.9 Temperature Programmed Desorption of Carbon Dioxide (CO_2-TPD) 53
3.6.10 Thermogravimetric Analysis (TGA) 54
3.6.11 X-ray Fluorescence (XRF) 54
3.7 Photocatalytic Esterification of WCO 54
3.8 Reusability Test of Esterified WCO 56
3.9 Scavenger Analysis 56
3.10 Transesterification of Esterified WCO 57
3.11 Gas Chromatography-Mass Spectrometry (GC-MS) analysis 57
3.12 Fuel Test Analysis of WCO-Biodiesel 59
3.12.1 Density of Fuel 59
3.12.2 Heat of Combustion 59
3.12.3 Kinematic Viscosity 60
3.12.4 Cloud Point 60
3.12.5 Sulphur Content 61
3.12.6 Flash Point 61
3.12.7 Pour Point 62

CHAPTER 4 RESULTS AND DISCUSSION 63
4.1 Analytical Results of WCO Pre-treatment and Composition 63
4.2 Characterization Analysis of Photocatalyst 64
4.2.1 X-Ray Diffraction (XRD) Analysis 64
4.2.2 Field Emission Scanning Electron Microscopy–Energy Dispersive X-ray spectroscopy (FESEM–EDX) and Mapping Analysis 69
4.2.3 High-Resolution Transmission Electron Microscopy (HRTEM) and Selected Area Electron Diffraction (SAED) Analysis 75
4.2.4 Ultraviolet–Visible Diffuse Reflectance Spectroscopy (UV–Vis–DRS) and Photoluminescence (PL) Analysis 79
4.2.5 Fourier-Transform Infrared Spectroscopy (FTIR) Analysis 87
4.2.6 Brunauer–Emmett–Teller (BET) Surface Area and Porosity Analysis 90

4.2.7 Carbon Dioxide Temperature–Programmed Desorption (CO_2-TPD) Analysis of Basic Surface Functionality 94
4.2.8 Thermogravimetric Analysis (TGA) 97
4.2.9 X-ray Fluorescence (XRF) Analysis 100
4.3 Optimization on the Photocatalytic Esterification Reaction 103
4.3.1 Photocatalytic Performance of TiO_2 and TiO_2/EFBA 103
4.3.2 Photocatalytic Performance of ZnO and ZnO/EFBA 114
4.3.3 Effect of Reactive Species Scavenger on Photocatalytic Activity 126
4.3.4 Reusability Test 129
4.3.5 Proposed Photocatalytic Reaction Mechanism 132
4.4 Fatty Acid Methyl Ester (FAME) Composition and Yield Analysis 134
4.5 Evaluation of Fuel Properties 135

CHAPTER 5 CONCLUSIONS AND RECOMMENDATIONS 137
5.1 Conclusions 137
5.2 Recommendations 138

REFERENCES 140

APPENDICES 163

AUTHOR'S PROFILE 174

LIST OF TABLES

Tables	Title	Page
Table 2.1	Biodiesel Production Share (%) and Major Feedstocks by Country (European Biodiesel Board, 2023)	10
Table 2.2	Molecular Structure and Molecular Weight of Selected FAMEs (Belousov et al., 2021; Khethiwe et al., 2020)	11
Table 2.3	Physicochemical Properties of WCO Biodiesel as Reported by Three Studies, Benchmarked Against ASTM D6751 and EN 14214 Standards	15
Table 2.4	Summary of Selected Studies on Photo-Trans-Esterification for Biodiesel Production	19
Table 2.5	Summary of Homogeneous Catalyst Use for Biodiesel Production from Various Feedstocks	23
Table 2.6	Summary of Heterogeneous Catalysts in Biodiesel Production	26
Table 2.7	Summary of Common Semiconductor Photocatalysts Used in Biodiesel Production	27
Table 2.8	Major Inorganic Oxide Constituents of EFBA Contributing to Photocatalytic Activity	35
Table 3.1	Sample Codes and Compositions of EFBA-Doped TiO_2 and ZnO Catalysts Prepared at Varying Metal-to-EFBA Mass Ratios	48
Table 3.2	Summaries the OVAT and Post OVAT Experimental Parameters	56
Table 4.1	Physicochemical Properties and Fatty Acid Composition of WCO Prior to Pre-Treatment	64
Table 4.2	Crystalline Phase Identification and Corresponding Chemical Formulas for XRD-Labeled Peaks Observed in EFBA, TiO_2, and TiO_2/EFBA Composites	65
Table 4.3	Crystallite Sizes of EFBA, TiO_2, and TiO_2/EFBA Composite Catalysts Determined via XRD Analysis	67

Table 4.4	Identified Crystalline Phases and Corresponding Chemical Formulas Based on XRD Analysis of EFBA, ZnO, and Z11	68
Table 4.5	The Elemental Composition of the EFBA, TiO_2 and T11 Composites	71
Table 4.6	The Elemental Composition of the EFBA, ZnO and Z11 Composites	74
Table 4.7	Bandgap Energy of TiO_2 and TiO_2/EFBA Composites Using Tauc Plot Method	80
Table 4.8	BET Surface Area, Total Pore Volume, and BJH Desorption Average Pore Width of EFBA, TiO_2, and TiO_2/EFBA Composites	91
Table 4.9	BET Surface Area, Total Pore Volume, and BJH Desorption Average Pore Width of EFBA, ZnO, and ZnO/EFBA Catalysts	94
Table 4.10	CO_2 Adsorption Capacity of EFBA, TiO_2, and T11 at Different Desorption Temperatures	95
Table 4.11	CO_2 Adsorption Capacity of EFBA, ZnO, and Z11 at Different Desorption Temperatures	97
Table 4.12	TGA Analysis for EFBA, TiO_2 and T11	98
Table 4.13	TGA Analysis for EFBA, ZnO and Z11	100
Table 4.14	XRF Analysis of the Optimized T11 Catalyst in its Fresh State and After the 5th Recycling Cycle	101
Table 4.15	The XRF Analysis of ZnO and Z11 Catalyst in its Fresh State and After the 5th Recycling Cycle	102
Table 4.16	Composition of FAME in WCO-Derived Biodiesel Based on GC-MS Analysis	135
Table 4.17	Comparison of WCO-Biodiesel Properties from This Study with Conventional Diesel and Relevant Fuel Standards (ASTM D6751, EN 14214)	136

LIST OF FIGURES

Figures	Title	Page
Figure 1.1	The Global Energy Consumption Projections by Fuel Type, 2030 – 2050 (Energy Agency, 2024)	2
Figure 2.1	Molecular Structure of Triglycerides	10
Figure 2.2	Global Biodiesel Production by Region (2018–2024), Showing Contributions from the EU, USA, Brazil, Indonesia, Argentina, and Others (Oils & Fats International, 2024)	12
Figure 2.3	Schematic Representation of the Photocatalytic Mechanism in a Semiconductor Such as TiO_2 under UV Irradiation	20
Figure 2.4	Alkali-Catalyzed Transesterification (Farouk et al., 2024)	24
Figure 2.5	Effect of a Catalyst on Activation Energy During a Chemical Reaction	25
Figure 2.6	Crystal Structure of TiO_2 Phase of Rutile, Brookite and Anatase	29
Figure 2.7	Crystal Structures of the Three Polymorphs of ZnO	31
Figure 3.1	Flowchart Illustrating the Biodiesel Production Workflow, Including Pretreatment via Photocatalytic Esterification and Subsequent Alkaline Transesterification	43
Figure 3.2	Visual Comparison of the Test Sample Before (Yellowish) and After (Orange-Red) the Acid Value Titration	46
Figure 3.3	Illustration Diagram of Photo-Esterification in Photo-Reactor Box	55
Figure 4.1	XRD Patterns of EFBA, TiO_2, and TiO_2/EFBA Composites. Key Crystalline Phases are Annotated with Labels. Full Phase Assignments are Listed in Table 4.2	65
Figure 4.2	XRD Diffractograms of EFBA, ZnO, and ZnO/EFBA Composite (Z11). Complete Phase Assignments are Detailed in Table 4.4	68

Figure 4.3	FESEM Analysis of a) EFBA at 3 k× Magnification, b) TiO_2 at 50 k× Magnification, c) T11 at 5 k× Magnification and d) T11 at 50 k× Magnification	70
Figure 4.4	Elemental Mapping of T11 Composites at 25 k× Magnification, 20 kV Accelerating Voltage, and a Scale of 5 µm	72
Figure 4.5	FESEM Analysis of a) EFBA at 3 k× Magnification, b) ZnO at 50 k× Magnification, c) Z11 at 5 k× Magnification and d) Z11 at 50 k× Magnification	73
Figure 4.6	Elemental Mapping of Z11 Composites at 25 k× Magnification, 20 kV Accelerating Voltage, and a Scale of 5 µm	74
Figure 4.7	HRTEM Analysis of a-c) EFBA, d-f) TiO_2 and g-i) T11	75
Figure 4.8	a) SAED of TiO_2 and b) SAED of T11	77
Figure 4.9	HRTEM Images of a-c) EFBA, d-f) ZnO and g-i) Z11 at Different Magnification	78
Figure 4.10	SAED Patterns of (a) ZnO and (b) Z11	79
Figure 4.11	Reflectance of TiO_2 and TiO_2/EFBA Composites (a) and Tauc Plot Derived from Kubelka–Munk Function of TiO_2 and TiO_2/EFBA Composites (b)	80
Figure 4.12	PL Analysis of a) TiO_2 at 275 nm Excitation, b) T11 at 275 nm Excitation, c) T11 at 375 nm Excitation and d) T11 at 450 nm Excitation	82
Figure 4.13	Deconvulated PL Spectra of T11 at 375 nm Excitation	83
Figure 4.14	UV-Vis Diffuse Reflectance Spectra of ZnO and Z11 (a), and Tauc Plot Derived from Kubelka–Munk Function of ZnO and Z11 Composites (b)	84
Figure 4.15	PL Analysis of a) ZnO at 275 nm Excitation, b) ZnO at 375 nm Excitation, c) Z11 at 275 nm Excitation, d) Z11 at 375 nm Excitation and e) Z11 at 450 nm	85
Figure 4.16	Deconvulated PL Spectra of Z11 at 375 nm Excitation	86
Figure 4.17	FTIR Analysis of EFBA, TiO_2 and TiO_2/EFBA Composites	87
Figure 4.18	FTIR Analysis of a) ZnO and b) Z11	89
Figure 4.19	Nitrogen Adsorption-Desorption Isotherms of EFBA, TiO_2, and TiO_2/EFBA Composites Catalysts	91

Figure 4.20	Nitrogen Adsorption-Desorption Isotherms of ZnO and Z11 Catalysts	93
Figure 4.21	CO_2-TPD Profiles of EFBA, TiO_2, and T11	95
Figure 4.22	CO_2-TPD Profiles of EFBA, ZnO, and Z11	97
Figure 4.23	The TGA Analysis for EFBA, TiO_2 and T11	98
Figure 4.24	The TGA Analysis for EFBA, ZnO and Z11	100
Figure 4.25	Effect of Reaction Time on a) FFA Content and b) Conversion for TiO_2 and TiO_2/EFBA 1:1 (T11) under UV-A Irradiation (λ = 365 nm) with 20:1 Methanol-to-WCO Molar Ratio and 4 wt% Catalyst Loading	104
Figure 4.26	Effect of Methanol-to-WCO Molar Ratio on a) FFA Content and b) FFA Conversion for TiO_2 and T11 under UV-A Irradiation (λ = 365 nm), with 2 h Reaction Time and 4 wt% Catalyst Loading	106
Figure 4.27	Effect of Catalyst Loading on a) FFA Content Reduction and b) FFA Conversion, Catalyzed by TiO_2 and TiO_2/EFBA 1:1 (T11) under 20:1 Methanol-to-Oil Molar Ratio and 2 h Reaction Time	108
Figure 4.28	Effect of Different Light Sources on FFA Content Reduction and Conversion During Photo-Esterification Catalyzed by TiO_2/EFBA 1:1 (T11) under Optimized Conditions: 2 h Reaction Time, 20:1 Methanol-to-WCO Molar Ratio, and 4 wt% Catalyst	110
Figure 4.29	Effect of TiO_2/EFBA Mass Ratio on FFA Content Reduction and Conversion Under 2 h Reaction Time, 20:1 Methanol-to-WCO Molar Ratio, and 4 wt% Catalyst Loading	112
Figure 4.30	Effect of T11 Thermal Treatment Temperature on FFA Content Reduction and Conversion under 2 h Reaction Time, 20:1 Methanol-to-WCO Molar Ratio, and 4 wt% Catalyst Loading	113
Figure 4.31	Effect of Reaction Time on a) FFA Content Reduction and b) FFA Conversion, Catalyzed by ZnO and ZnO/EFBA 1:1 (Z11), under Fixed Conditions: 20:1 Methanol-to-WCO Molar Ratio and 4 wt% Catalyst Loading	115

Figure 4.32 Effect of Methanol-to-WCO Molar Ratio on a) FFA Content Reduction and b) FFA Conversion, Catalyzed by ZnO (5 h Reaction Time, 4 wt% Catalyst Loading) and ZnO/EFBA 1:1 (Z11) (4 h Reaction Time, 4 wt% Catalyst Loading). 117
Figure 4.33 Effect of Catalyst Loading on a) FFA Content Reduction and b) FFA Conversion, Catalyzed by ZnO (5 h Reaction Time, 24:1 Methanol-to-WCO Molar Ratio) and ZnO/EFBA (Z11) (4 h Reaction Time, 16:1 Methanol-to-WCO Molar Ratio), under 4 wt% Catalyst Loading. 119
Figure 4.34 Effect of Various Light Sources on FFA Content Reduction and FFA Conversion During Photo-Esterification Catalyzed by Z11. Reactions were Conducted under 4 wt% Catalyst Loading, 4 h Reaction Time, and a 16:1 Methanol-to-WCO Molar Ratio 120
Figure 4.35 Influence of Thermal Treatment Temperature on (a) FFA Content Reduction and Conversion using ZnO at 2 wt% Catalyst Loading, 5 h Reaction Time, and 24:1 Methanol-to-WCO Molar Ratio, and (b) Z11 under 4 wt% Catalyst Loading, 4 h Reaction Time, and 16:1 Methanol-to-WCO Molar Ratio 122
Figure 4.36 Effect of ZnO to EFBA Mass Ratio on FFA Content Reduction and FFA Conversion Efficiency under Photo-Esterification Conditions. Reactions Were Carried Out at 4 wt% Catalyst Loading, 4 h Reaction Time, and a 16:1 Methanol-to-WCO Molar Ratio 124
Figure 4.37 Visual Comparison of Esterified Waste Cooking Oil (WCO) Following Photo-Esterification using (a) ZnO and (b) Z11 Catalysts 126
Figure 4.38 FFA Content Reduction and Conversion over Scavenger Agent Catalyze by T11 with Optimized Reaction Condition of 2 h Reaction Time and 20:1 Methanol to WCO Molar Ratio and 4 wt% Catalyst Loading 127
Figure 4.39 FFA Content Reduction and Conversion over Scavenger Agent Catalyze by Z11 with Optimized Reaction Condition of 4 h

	Reaction Time and 16:1 Methanol to WCO Molar Ratio and 4 wt% Catalyst Loading	128
Figure 4.40	FFA Content Reduction and Conversion Over Reusability Test Catalyze by T11 with Optimized Reaction Condition of 4 h Reaction Time and 20:1 Methanol to WCO Molar Ratio and 4 wt% Catalyst Loading	129
Figure 4.41	Reusability Test on (a) FFA Content Reduction and Conversion Using ZnO at 2 wt% Catalyst Loading, 5 h Reaction Time, and 24:1 Methanol-to-WCO Molar Ratio, and (b) Z11 under 4 wt% Catalyst Loading, 4 h Reaction Time, and 16:1 Methanol-to-WCO Molar Ratio	131
Figure 4.42	Schematic Illustration of the Photocatalytic Esterification Mechanism over Z11 under UV-A Irradiation	132

LIST OF SYMBOLS

Symbols

FFA	Free Fatty Acid Content
AV	Acid Value
SV	Saponification Value
c	Ester Content (FAME)
Y	Mass of Pure Biodiesel
α	Absorption Coefficient (UV-Vis DRS)
h	Planck's Constant
v	Frequency of Incident Light
λ	Wavelength
E_g	Bandgap Energy
(αhv)n	Tauc Function for Bandgap Estimation (n =1/2 for Indirect, 2 for Direct)
D	Crystallite Size (Scherrer Equation)
θ (theta)	Bragg Angle in XRD Analysis

LIST OF ABBREVIATIONS

Abbreviations

ASTM	American Society for Testing and Materials
BET	Brunauer-Emmett-Teller (Surface Area)
BJH	Barrett-Joyner-Halenda (Pore Size Distribution Method)
CB	Conduction band
DRS	Diffuse Reflectance Spectroscopy
EDTA	Ethylenediaminetetraacetic Acid (Hole Scavenger)
ROS	Reactive Oxygen Species
EFBA	Empty Fruit Bunch Ash
FA	Fatty Acid
FAME	Fatty Acid Methyl Ester
PL	Photoluminescence

CHAPTER 1
INTRODUCTION

1.1 Research Background

Energy exists in various forms, including thermal, chemical, electrical, and mechanical energy. Despite advances in alternative energy technologies, the global energy landscape remains heavily reliant on fossil fuels, such as petroleum, coal, and natural gas. These resources currently supply more than 90% of the total energy demand across key sectors, including transportation, agriculture, and residential consumption (Energy Agency, 2024).

This persistent reliance, driven by rapid population growth and economic expansion, poses significant challenges to long-term energy security and environmental sustainability. According to the U.S. Energy Information Administration (EIA), (2023), global liquid fuel production was projected to reach 102.61 million barrels per day by 2024, indicating that continued growth may worsen these challenges.

Figure 1.1 presents the global energy fuel production projections from 2030 to 2050 under three different scenarios. The Stated Policies Scenario (STEPS) shows that energy demand continues to rise, indicating that fossil fuels are expected to remain a dominant component of the global energy mix if current policies remain unchanged. This trend suggests that, without stronger policy interventions and deployment of renewable technologies, dependence on conventional fuels will likely persist in the coming decades.

Additionally, fossil fuel combustion contributes substantially to greenhouse gas emissions, accounting for major a share of anthropogenic CO_2 release and exacerbating climate change and public health risk (Boehm & Schumer, 2023). Furthermore, fuel price volatility exposes economies to instability and highlights the urgency of transitioning toward renewable and sustainable energy systems.

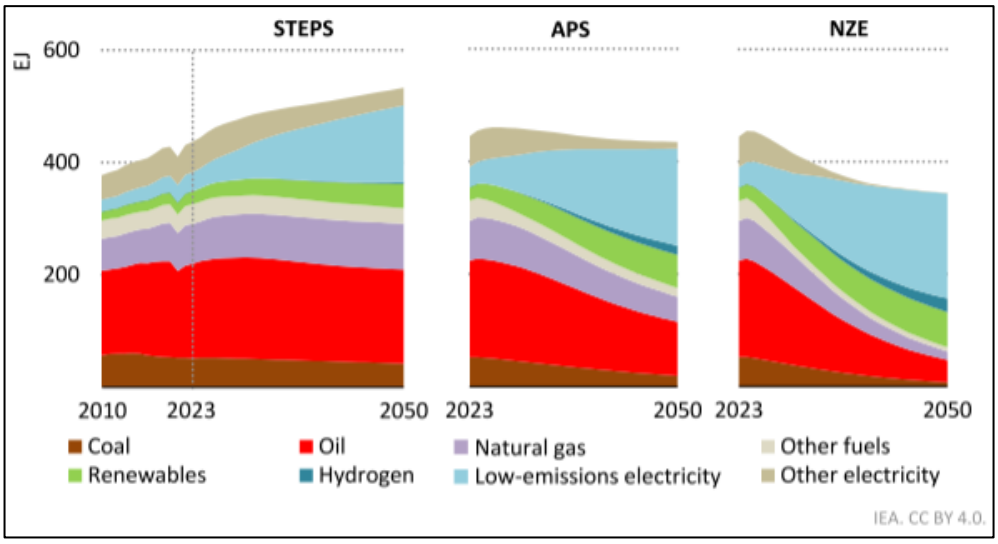


Figure 1.1 The Global Energy Consumption Projections by Fuel Type, 2030 – 2050 (Energy Agency, 2024)

In response to these challenges, global interest in renewable energy sources, including solar energy, wind energy, hydropower, and biofuels, has increased significantly. These alternatives offer cleaner, more sustainable pathways to reduce environmental pollution and dependence on fossil fuels (Ngobeh et al., 2023). Among these, biodiesel has gained considerable attention due to its compatibility with existing engines and infrastructure. Biodiesel, composed of fatty acid methyl esters (FAME), is biodegradable and non-toxic. It can be used either in pure form or blended with petroleum diesel without requiring engine modifications (Awogbemi et al., 2020). Its relatively high cetane number (typically 50-56) improves combustion efficiency and contributes to reduced emissions of CO_2, SO_2, particulate matter (PM), and polycyclic aromatic hydrocarbons (PAHs) (Aljaafari et al., 2022). Additionally, biodiesel is produced in accordance with international standards, including EN 14214, ASTM D6751 and Malaysia's MS 2008:2008 specifications. Biodiesel's performance, safety, and compliance make it a practical and environmentally responsible alternative to conventional fossil diesel.

Malaysia holds a strategic advantage in biodiesel production as the world's second-largest producer of palm oil. The biodiesel industry has expanded substantially since the implementation of the National Biofuel Policy in 2006, which introduced the B5 mandate (5% palm biodiesel and 95% petroleum diesel), later increased to B10 by 2014 (Mahayuddin et al., 2022). Nevertheless, concerns regarding land use limitations,

fluctuations in palm oil production, feedstock cost escalation, and market instability raise questions about the long-term sustainability of palm-based biodiesel (Hanafiah et al., 2022). These challenges highlight the need to explore alternative non-edible feedstocks. Potential second-generation feedstocks include Jatropha curcas, rubber seed oil, palm fatty acid distillate, animal fats, grease trap waste, microalgae residues, and waste cooking oil (WCO). Among these, WCO is particularly attractive due to its low cost, abundant availability, and dual environmental benefits: reducing waste disposal while minimizing food-fuel competition (Ferrusca et al., 2023).

WCO exhibits physical properties suitable for biodiesel production, with a density of 860−900 kg/m³ and a kinematic viscosity of 4–6 mm²/s at 40 °C (Niyas & Shaija, 2023). These values are comparable to those of edible feedstock oils, confirming its potential as a viable alternative. Despite its advantages, WCO typically contains high levels of free fatty acids (FFAs) and moisture, which hinder direct transesterification. FFAs above 1 wt% lead to saponification when reacting with alkaline catalysts such as NaOH and KOH, thereby reducing biodiesel yield (Maniam et al., 2023; Suzihaque et al., 2022). Pretreatment using conventional homogeneous acid catalysts such as HCl and H_2SO_4 is commonly employed for FFA reduction. However, issues such as difficult separation, reduced efficiency, and toxic waste generation remain significant drawbacks (Ferrusca et al., 2023). Extensive studies have investigated various heterogeneous catalysts for high-FFA feedstocks, including SBA-15 silica (Verma et al., 2020), biomass-derived catalysts (Juera-Ong et al., 2022; Okechukwu et al., 2022), and kaolinite-based materials (Khalid et al., 2024). These heterogeneous catalysts improve reaction selectivity, enhance reusability, and minimize waste generation. However, such thermal catalytic systems require high energy input and long reaction times due to mass transfer limitations and slower reaction kinetics. This complicates achieving high conversion efficiency and reduces biodiesel quality.

Heterogeneous semiconductor photocatalysts, such as TiO_2, ZnO, g-C_3N_4, and CdS, have been extensively studied for the photocatalytic conversion of FFA into FAME (Naveed et al., 2023). These catalysts can initiate redox reactions under light irradiation, typically in the ultraviolet (UV) to visible range, allowing low-energy activation under ambient conditions. This makes photocatalysis a promising alternative to conventional thermal catalysis. Moreover, photocatalytic systems can be reused multiple times, thereby reducing waste generation and improving sustainability. Among

these materials, TiO_2 and ZnO are chemically stable and non-toxic photocatalysts. However, when used individually, they exhibit limitations due to their wide bandgap energies (~3.0–3.2 eV), which restrict light absorption to the UV region. Since UV light represents less than 5% of the solar spectrum, this results in poor visible-light activity. To address this limitation, various strategies such as heterojunction formation (e.g., Z-scheme, S-scheme, and p-n junction systems) and coupling with other semiconductors have been developed to narrow the bandgap, enhance charge separation efficiency, and broaden light absorption. The synergistic interaction between coupled components can effectively suppress electron-hole recombination, thereby significantly enhancing catalytic activity and long-term stability (Kadem et al., 2023).

The residues derived from oil palm empty fruit bunches (EFB), including fibers, shells, and mesocarp, represent promising low-cost supporting materials. In Malaysia, the palm oil industry generates approximately 94.7 million tonnes of this lignocellulosic biomass annually (MIDA, 2025). Among these residues, empty fruit bunch ash (EFBA) has emerged as a potential support for enhancing photocatalyst performance. EFBA contains significant amounts of inorganic oxides, such as K_2O, CaO, MgO, and SiO_2, which can modify the physicochemical properties of semiconductor materials. These inorganic constituents can improve surface basicity, facilitate electron transport, and enhance charge separation, thereby boosting photocatalytic activity. Furthermore, EFBA-derived materials are highly economical, with an estimated cost of approximately RM 30 - 50 per tonne (Ahmad et al., 2024). However, the relatively poor mechanical strength and irregular morphology of EFBA may reduce the durability and structural stability (Ozoani et al., 2024). Among the synthesis methods, wet impregnation is particularly effective due to its simplicity, uniform nanoparticles distribution, and scalability for practical applications (da Cunha et al., 2021).

In conclusion, this study presents an innovative approach for biodiesel production by integrating EFBA, a by-product of the palm oil industry, with TiO_2 and ZnO photocatalysts to enhance photocatalytic esterification efficiency under both UV and visible light irradiation. This strategy enables the effective utilization of low-quality feedstocks such as WCO while promoting a waste-to-resource approach. The findings highlight the potential of EFBA-supported photocatalysts, addressing an important gap in existing biodiesel production strategies. By advancing catalyst design and utilizing renewable feedstocks, this study contributes to addressing current energy and

environmental challenges, while supporting the development of cleaner and scalable biodiesel production technologies aligned with Malaysia's sustainability goals.

1.2 Problem Statement

Petroleum-based fossil fuels are limited resources and are expected to decline due to increasing global energy demand. In addition, strong dependence on fossil fuels has led to unstable fuel prices and environmental pollution, creating the need for alternative sustainable energy sources. Although biodiesel has been extensively investigated because it is renewable and biodegradable, its large-scale production faces several challenges. The high cost of edible feedstock oils increases production expenses and creates competition with the food supply. As a result, biodiesel is often more expensive than petroleum-based diesel, which limits widespread commercial use. Waste cooking oil (WCO) has been considered a promising feedstock for biodiesel production due to its low cost, non–edible nature, and wide availability. However, WCO contains high levels of free fatty acids (FFAs), which cause saponification during base-catalyzed transesterification. This leads to catalyst deactivation and reduced biodiesel yield. Although acid–catalyzed pretreatment can reduce the FFA content, it requires high energy input, long reaction times, and involves corrosive chemicals. Therefore, an alternative pretreatment method such as photo-esterification under milder conditions is needed to improve the efficiency and sustainability of biodiesel production from WCO.

Photo-esterification has emerged as a green alternative for biodiesel pretreatment, offering high conversion efficiency, lower energy consumption, and shorter reaction times. Semiconductor photocatalysts such as TiO_2 and ZnO are widely studied due to their thermal stability and catalytic activity under ambient conditions. However, their wide bandgap energies (~3.0–3.2 eV), rapid electron-hole recombination, and limited visible-light absorption restrict their photocatalytic performance. Coupling these semiconductors with suitable inorganic materials can improve charge separation, reduce electron–hole recombination, and enhance visible-light responsiveness. Conventional synthetic supporting materials such as SiO_2, Al_2O_3, and activated carbon have been widely used to enhance photocatalyst performance due to their high surface area and stability. However, these materials are often expensive, energy–intensive to produce, which limits their large–scale sustainability. Empty fruit

bunch ash (EFBA), a palm oil biomass waste rich in CaO, K_2O, MgO, and SiO_2, has the potential to improve surface basicity, light absorption, and charge transport properties. In addition, EFBA may reduce particle agglomeration and facilitate catalyst recovery. However, EFBA exhibits poor structural stability, which may weaken the mechanical strength of the photocatalyst. Therefore, further investigation is required to develop a stable and efficient EFBA–modified photocatalyst with enhanced structural stability and photocatalytic performance for effective pretreatment of high-FFA WCO.

1.3 Research Objectives

1. To synthesize EFBA-supported TiO_2 and ZnO photocatalysts and correlate with their physicochemical properties.
2. To establish the optimal reaction conditions for photocatalytic esterification of WCO using a one-variable-at-a-time (OVAT) screening approach.
3. To determine the functional basis for the high catalytic activity and to assess the factors governing its durability across multiple reaction cycles.
4. To validate transesterification of esterified WCO and assess biodiesel quality through FAME composition analysis and compliance with ASTM D6751 and EN 14214 standards.

1.4 Scope of Study

This study evaluates EFBA–supported TiO_2 and ZnO photocatalysts for the photoesterification of WCO. Kinetic modeling and pilot-scale validation were not included, as the focus was on mechanistic elucidation and material performance under controlled conditions. Photocatalysts were synthesized via the wet impregnation method and characterized using XRD, FESEM-EDX, HRTEM-SAED, UV–Vis DRS, PL, BET, FTIR, CO_2-TPD, TGA, and XRF. These analyses assessed structural integrity, surface functionality, optical behavior, and elemental composition, focusing on EFBA integration into the catalyst.

Reaction optimization was conducted using an OVAT approach, evaluating reaction time, methanol-to-oil molar ratio, catalyst loading, light source, thermal treatment, and semiconductor-to-EFBA mass ratio. OVAT enabled clear isolation of individual parameter effects and facilitated clear mapping of cause-effect relationships

within a novel catalyst system. Scavenger experiments identified key reactive oxygen species (ROS), including hydroxyl and superoxide radicals, and clarified their role in the esterification. Catalyst stability and recyclability were assessed through repeated reaction cycles and XRF analysis to detect elemental leaching.

Finally, the esterified WCO underwent transesterification using an optimized method from previous studies. The resulting biodiesel was analyzed by gas chromatography–mass spectrometry (GC–MS) and evaluated against international standards, including ASTM D6751, to confirm compliance with biodiesel quality requirements. Overall, the study provided a detailed understanding of EFBA-supported semiconductor photocatalysts as a sustainable pretreatment strategy for biodiesel production from high-FFA WCO.

1.5 Significance of Study

This study supports both global and national energy transitions toward sustainable energy by proposing a cleaner, low-energy approach to biodiesel production. In Malaysia, initiatives such as the National Energy Transition Roadmap (NETR) (Ministry of Economy, 2023) and the Twelfth Malaysia Plan (12MP) (Yaakob, 2021) emphasize the use of renewable energy, circular economy practices, and industrial decarbonization. By utilizing WCO as a feedstock, this research aligns with national goals to reduce dependence on fossil fuels while minimizing environmental impact. Additionally, it helps mitigate waste disposal issues and avoids the food-fuel conflict associated with edible oils.

The EFBA-supported TiO_2 and ZnO semiconductor photocatalysts developed in this study exhibit low toxicity, good thermal stability, and reusability. Their application in photo-esterification enables effective FFA reduction under UV-visible irradiation while operating under mild and energy-efficient reaction conditions. Optimization of key reaction parameters, including catalyst dosage, methanol-to-oil ratio, and reaction time, provides valuable insights into reaction efficiency and reproducibility. These photocatalysts support green chemistry principles and low-carbon fuel development.

Furthermore, the integration of EFBA into functional photocatalyst systems promotes waste valorization in line with the national Circular Economy Blueprint. Such composite photocatalysts enhance heterojunction formation, improve charge separation

efficiency, and increase catalyst reusability, which are critical for long-term industrial implementation. Overall, this study provides foundational knowledge for the development of scalable and sustainable biodiesel pretreatment strategies using waste-derived photocatalysts. These findings support Malaysia's clean energy objectives and contribute to broader climate change mitigation efforts.

CHAPTER 2
LITERATURE REVIEW

2.1 Biodiesel Overview

Biodiesel has evolved from early experiments with vegetable oils by Rudolf Diesel in the 1890s (Jacob-Lopes et al., 2025). However, direct use of vegetable oils in diesel engines leads to several operational problems, including poor fuel atomization, incomplete combustion, carbon deposition in engine components, and injector clogging. These issues mainly arise from the high viscosity, low volatility, and relatively low cetane number of raw vegetable oils compared with petroleum diesel (Saanyol et al., 2022). Consequently, chemical modification of feedstock oils is required to improve fuel properties and ensure compatibility with conventional diesel engines.

Several conversion techniques have been developed to transform vegetable oils into suitable diesel substitutes, including transesterification, pyrolysis, and emulsification. Among these methods, transesterification is the most widely applied due to its relatively mild operating conditions, high conversion efficiency, and ability to produce biodiesel with physicochemical properties similar to petroleum diesel. In this process, triglycerides in the vegetable oil react with short-chain alcohols in the presence of a catalyst to form biodiesel or called fatty acid methyl esters (FAME) and glycerol as a by-product (Yusuf et al., 2024).

The development of transesterification technology in 1937 significantly improved the feasibility of biodiesel production by enabling the efficient conversion of triglycerides into FAME (Mathew et al., 2021). Biodiesel is often considered a carbon-neutral fuel because the carbon dioxide released during combustion can be partially offset by carbon uptake during feedstock growth (Hu et al., 2025; Xu et al., 2022). However, the sustainability of biodiesel largely depends on feedstock selection and production methods. Table 2.1 presents the production of biodiesel using different types of feedstocks across various countries. Based on the table, Asian countries such as Indonesia, Malaysia, and Thailand predominantly utilize palm oil for biodiesel production. This preference is mainly attributed to the abundant availability of palm oil in these countries, making it a more cost-effective and reliable feedstock.

Table 2.1
Biodiesel Production Share (%) and Major Feedstocks by Country (European Biodiesel Board, 2023)

Country	Production share (%)	Major feedstocks
European Union	31.3	Rapeseed oil/ waste cooking oil
United States	19.2	Soybean oil/ diverse other oil
Indonesia	18.9	Palm oil
Brazil	11.7	Soybean oil
China	4.2	Waste cooking oil
Argentina	3.1	Soybean oil
Thailand	2.6	Palm oil
Malaysia	2.4	Palm oil
Columbia	1.3	Palm oil
Canada	0.7	Waste cooking oil
India	0.3	Palm oil

A wide range of feedstocks has been investigated for biodiesel production, including edible vegetable oils (e.g., palm, soybean, and canola), animal fats (e.g., tallow and lard), and non-edible or waste-derived oils such as Jatropha curcas, grease trap waste, palm fatty acid distillate, and waste cooking oil (WCO) (Weldeslase et al., 2023). Among these, vegetable oils are the most widely studied due to their abundance, consistent composition, and high triglyceride content. Triglycerides consist of three fatty acid chains esterified to a glycerol backbone and represent the primary constituents of vegetables oils (Jafarihaghighi et al., 2020) as shown in Figure 2.1. The long-chain fatty acids classified as saturated fatty acids (e.g., myristic, palmitic, and stearic acids) or unsaturated fatty acids (e.g., oleic, linoleic, and linolenic acids). During transesterification, these fatty acids are converted into mono-alkyl esters that form the biodiesel product.

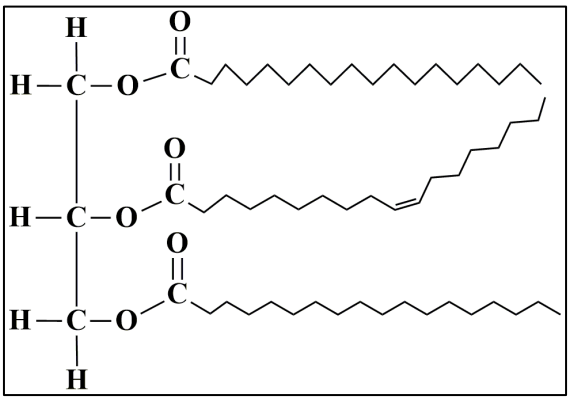


Figure 2.1 Molecular Structure of Triglycerides

The composition of FAME significantly influences the combustion characteristics and physicochemical properties of biodiesel. According to Table 2.2, FAME with shorter carbon chains exhibits lower viscosity due to their lower molecular weight and lower cetane numbers. They also have higher volatility, which improves fuel atomization during combustion. In contrast, long-chain saturated FAME typically possess higher cetane numbers, improved oxidation stability, and higher melting points (Boichenko et al., 2025). This indicates a trade-off in biodiesel: saturated FAME support better ignition, while unsaturated FAME enhance cold flow properties. Therefore, an ideal biodiesel composition usually contains a balanced mixture of saturated and unsaturated fatty acids. Biodiesel also exhibits a relatively high flash point of approximately 150 °C, making it safer to store and transport compared with conventional diesel fuels (Suzihaque et al., 2022). In addition, several studies have reported that biodiesel possesses higher lubricity and a lower sulfur content than petroleum diesel, which contributes to reduced particulates emissions and improved engine performance. These physicochemical properties highlight the importance of feedstock selection in determining biodiesel quality and production feasibility.

Table 2.2
Molecular Structure and Molecular Weight of Selected FAMEs (Belousov et al., 2021; Khethiwe et al., 2020)

Methyl ester (X:Y)	Structure	Molecular weight (g/mol)
Methyl octanoate (C8:0)	$CH_3(CH_2)_6COOCH_3$	158.2
Methyl decanoate (C10:0)	$CH_3(CH_2)_8COOCH_3$	186.3
Methyl laurate (C12:0)	$CH_3(CH_2)_{10}COOCH_3$	214.3
Methyl myristate (C14:0)	$CH_3(CH_2)_{12}COOCH_3$	242.4
Methyl palmitate (C16:0)	$CH_3(CH_2)_{14}COOCH_3$	270.5
Methyl stearate (C18:0)	$CH_3(CH_2)_{16}COOCH_3$	298.5
Methyl oleate (C18:1)	$CH_3(CH_2)_7CH{=}CH(CH_2)_7COOCH_3$	296.5
Methyl linoleate (C18:2)	$CH_3(CH_2)_4CH{=}CHCH_2CH{=}CH(CH_2)_7COOCH_3$	294.5
Methyl linolenate (C18:3)	$CH_3CH_2CH{=}CHCH_2CH{=}CHCH_2CH{=}CH(CH_2)_7COOCH_3$	292.5
Methyl arachidate (C20:0)	$CH_3(CH_2)_{18}COOCH_3$	326.6
Methyl behenate (C22:0)	$CH_3(CH_2)_{20}COOCH_3$	354.6
Methyl erucate (C22:1)	$CH_3(CH_2)_7CH{=}CH(CH_2)_{11}COOCH_3$	352.6
Methyl ricinoleate (C18:1, OH)	$CH_3(CH_2)_5CH(OH)CH_2CH{=}CH(CH_2)_7COOCH_3$	312.5

Note: X:Y denotes the number of carbon atoms (X) and double bonds (Y) in the fatty acid chain.

Biodiesel production is strongly influenced by the presence of free fatty acids (FFAs) in feedstock oils. FFAs are fatty acids that are not esterified with glycerol molecules. When alkaline catalysts such as NaOH or KOH are used in transesterification reactions, FFAs react with the base catalyst through the carboxylic acid group (–COOH) to form soap via saponification reactions. This undesirable side reaction reduces catalyst activity, complicates product separation, and ultimately decreases biodiesel yield. Therefore, feedstocks containing high FFA levels (typically greater than 1 wt%) generally require a pretreatment step such as esterification prior to alkaline transesterification (Hayyan et al., 2022). These challenges highlight the importance of developing advanced catalytic systems. Such systems must efficiently process high-FFA feedstocks to maintain high biodiesel yield and quality.

Globally, biodiesel production has increased steadily due to growing concerns regarding energy security and environmental sustainability. Figure 2.2 illustrates global biodiesel production trends from 2018 to 2024, reflecting the increasing demand for renewable fuels. By 2025, global biodiesel production is projected to reach approximately 41.4 billion liters, with Malaysia contributing about 1.58 billion liters annually (USDA Foreign Agricultural Service, 2024).

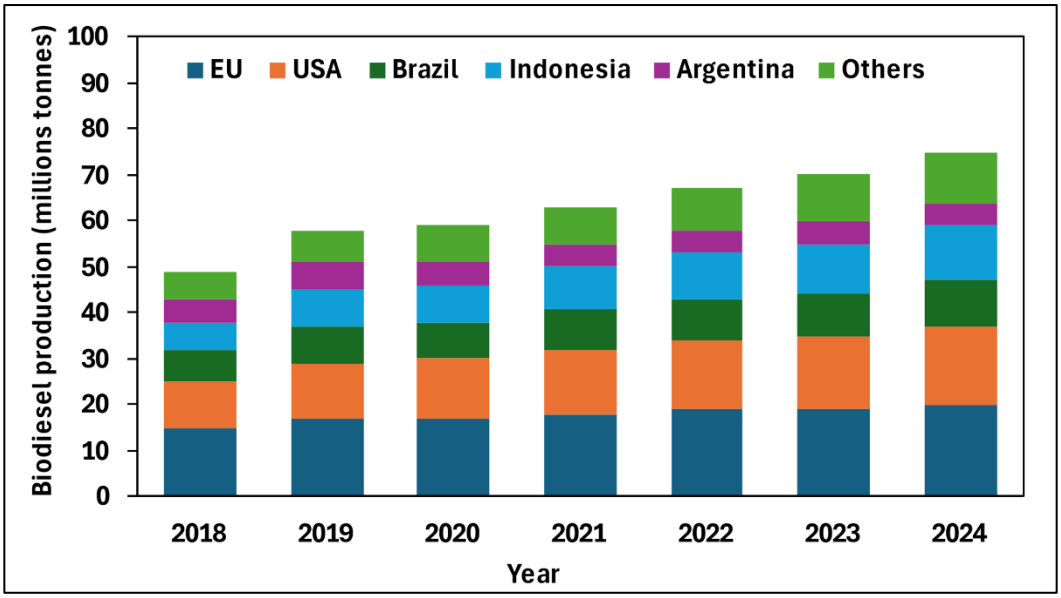


Figure 2.2 Global Biodiesel Production by Region (2018–2024), Showing Contributions from the EU, USA, Brazil, Indonesia, Argentina, and Others (Oils & Fats International, 2024)

However, the extensive use of edible oils for biodiesel production has raised several sustainability concerns, including deforestation, biodiversity loss, and competition between food and fuel resources. These concerns have shifted research attention toward non-edible and waste-derived feedstocks, particularly waste cooking oil (WCO), which offers a more sustainable and cost-effective alternative (Senusi et al., 2024). WCO utilization not only reduces biodiesel production costs but also addresses waste management issues. Therefore, the development of efficient catalytic systems capable of processing low-cost, high-FFA feedstocks such as WCO has become a critical research focus for improving the sustainability and economic feasibility of biodiesel production.

2.2 Waste Cooking Oil as Feedstock

Waste cooking oil (WCO) refers to edible oils or fats that have been repeatedly used for cooking or frying at high temperatures, typically between 150–200 °C. Prolonged heating during frying accelerates triglyceride hydrolysis, oxidation, and polymerization reactions, which generate FFAs, peroxides, and other polar compounds that degrade oil quality. As a result, the oil becomes unsuitable for further food preparation and may pose potential health risks if reused excessively. Moreover, the elevated levels of FFAs (approximately 0–15%), water, food residues, and degraded organic compounds significantly alter the physicochemical properties of the oil, leading to increased viscosity, darker color, and higher acid value (Outili et al., 2023; Randhawa & Mukherjee, 2023).

Conventional pretreatment techniques include acid-catalyzed esterification, adsorption, and chemical neutralization commonly used to convert FFA into FAME. However, several studies have reported that homogeneous acid catalysts require high alcohol-to-oil ratios, prolonged reaction times, and involve corrosive chemicals, making the process energy intensive and less favorable for industrial applications. Adsorption processes employ materials such as activated carbon, zeolite, silica gel, or clay to capture oxidation products and remove FFAs. However, high-quality adsorbents are relatively expensive and may not be suitable for large-scale applications. In addition, adsorbents can become saturated and require regeneration, while the disposal of spent adsorbents containing impurities raises environmental concerns. In recent years,

semiconductor-based photocatalysts have emerged as a promising alternative approach for the pretreatment high-FFA feedstocks (Barange et al., 2023). Photocatalytic processes can effectively promote the esterification of FFAs under mild reaction conditions while minimizing the use of corrosive chemicals. This approach has gained increasing attention for improving the efficiency and sustainability of biodiesel production from waste-derived feedstocks.

Despite these limitations, WCO has attracted considerable attention as a potential alternative feedstock for biodiesel production. WCO primarily consists of triglycerides, monoglycerides, and diglycerides, which serve as the main precursors for biodiesel synthesis. It commonly contains fatty acids such as oleic, linoleic, and linolenic acids, where the presence of unsaturated fatty acids contributes to improved cold flow properties of the resulting biodiesel. In addition, previous studies have reported that biodiesel produced from WCO shows comparable engine performance to biodiesel derived from fresh vegetable oils, indicating no significant adverse effects on engine operation or emissions (Medjahed et al., 2025).

The utilization of WCO also provides important economic and environmental benefits. The global generation of WCO is estimated to exceed several million tonnes annually, representing a significant potential resource for biodiesel production. Converting this waste into biodiesel can contribute to reducing global energy demand and dependence on fossil fuels. Furthermore, feedstock costs account for up to 70% of the total biodiesel production cost (Idris et al., 2024). Therefore, the use of low-cost feedstocks such as WCO can significantly reduce the overall production expenses. In Malaysia, the market price of WCO is considerably lower than that of refined palm oil, further highlighting its economic attractiveness for biodiesel production.

Improper disposal of WCO also causes serious environmental problems. It is estimated that more than 60% of WCO generated annually is discarded improperly. When disposed of into sewer systems, WCO can solidify and accumulate within pipelines, leading to blockages that disrupt wastewater flow to treatment facilities. In aquatic environments, improper disposal may result in the formation of surface films, increased organic loading in water bodies, reduced dissolved oxygen levels, and disruption of aquatic ecosystems (Kumar et al., 2025). In addition, the energy and economic costs associated with improper WCO disposal have been estimated to be approximately 3 kWh kg^{-1} and significant financial losses, respectively. Therefore, the

utilization of WCO for biodiesel production offers an effective strategy to mitigate waste disposal issues while simultaneously generating renewable energy (Zhang et al., 2025).

Table 2.3 summarizes several studies on biodiesel production from WCO. The properties of biodiesel derived from WCO generally comply with international fuel standards such as ASTM D6751 and EN 14214. Previous studies have reported that WCO-derived biodiesel exhibits relatively high cetane numbers (up to 89.06) and high flash points (>150 °C), indicating favorable combustion characteristics and safe fuel handling (Salim et al., 2022). Moreover, the moisture content and density value fall within acceptable range, ensuring stability and making fuel compatible with injection system. In addition, the kinematic viscosity also meets both ASTM and EN standards, which is crucial for proper fuel atomization and efficient combustion.

Table 2.3
Physicochemical Properties of WCO Biodiesel as Reported by Three Studies, Benchmarked Against ASTM D6751 and EN 14214 Standards

Property	Standard		(Hisham & Jamil, 2020)	(Park et al., 2019)	(Qamar et al., 2020)
	ASTM D 6751	EN 14214			
Moisture (%)	≥0.050	-	0.03	-	-
Density (g/cm^3)	0.82 – 0.90	0.86 – 0.90	0.88	0.85	-
Kinematic viscosity at 40 °C (mm^2/s)	1.9 – 6.0	3.5 – 5.0	-	3.90	3.94
Flash point (°C)	≥130	> 120	160.00	-	157
Acid value (mg KOH/g)	≤ 0.8	< 0.5	0.62	0.47	0.29
Cetane number	≥ 50	≥51	89.06	-	52.51
% FFA (mg KOH/g)	≤2.5	-	0.30	0.24	0.15

However, WCO-based biodiesel may produce slightly higher NO_x emissions due to its higher cetane number and oxygen content compared with petroleum diesel. On the other hand, significant reductions in carbon monoxide (CO) emissions have been observed due to more complete fuel oxidation during combustion. Overall, WCO represents a highly promising as it can achieve physicochemical properties that can comply with international standard, yet chemically challenging feedstock for biodiesel production. Its efficient conversion into biodiesel requires advanced pretreatment strategies capable of reducing the high FFA content while maintaining sustainable and cost-effective processing conditions.

2.3 Photocatalysis

Photocatalysis is a light-driven catalytic process in which semiconductor materials absorb photons and promote chemical reactions at their surface. According to the International Union of Pure and Applied Chemistry Gold Book, photocatalysis is defined as the change in the rate of a chemical reaction or its initiation under ultraviolet, visible, or infrared irradiation in the presence of a photocatalyst that absorbs light and participates in the chemical transformation of the reactants. Unlike conventional catalytic processes that rely primarily on thermal activation, photocatalysis utilizes light energy to generate reactive charge carriers within semiconductor materials, enabling chemical transformations under milder conditions. Consequently, photocatalysis has gained considerable attention as a sustainable approach for environmental remediation, renewable energy production, and green chemical synthesis (Lojpur, 2025).

The development of heterogeneous photocatalysis can be traced to early photochemical studies by Sergei Plotnikow (1910) and Lev Landau (1912–1913), who reported materials capable of initiating chemical transformations under light irradiation (Sordello et al., 2022). However, modern semiconductor photocatalysis was established following the pioneering work of Akira Fujishima and Kenichi Honda, who demonstrated photoelectrochemical water splitting using titanium dioxide under ultraviolet irradiation in 1972 (Kamat & Sivula, 2022). This discovery highlighted the potential of semiconductor materials to convert solar energy into chemical energy and laid the foundation for extensive research into photocatalytic materials and mechanisms.

In heterogeneous photocatalysis, the photocatalyst is typically present as a solid phase while the reactants exist in liquid or gaseous phases. The reactions occur at the catalyst surface, where the adsorption of reactant molecules is followed by photo-induced redox reactions. When light with energy equal to or greater than the band gap of the semiconductor is absorbed, electrons are excited from the valence band to the conduction band, leaving behind positively charged holes in the valence band. This process generates electron-hole pairs that can migrate to the catalyst surface and participate in oxidation-reduction reactions with adsorbed species. Conduction band electrons typically reduce electron acceptors such as dissolved oxygen, while valence band holes oxidize donor species such as water or hydroxyl ions to produce reactive

intermediates. These reactive species contribute to various photocatalytic processes including pollutant degradation, hydrogen evolution, and organic transformation reactions (Paiu et al., 2025).

2.3.1 Factor Affecting Photocatalytic Performance

The efficiency of photocatalysis is strongly influenced by several physicochemical factors. One important factor is the crystal facet orientation of the photocatalyst surface. Different crystal facets possess distinct atomic arrangements and surface energies, which can significantly affect the adsorption behavior of reactants, charge carrier mobility, and catalytic activity. For example, in TiO_2, the (001) facet exhibits higher surface reactivity due to its higher surface energy, whereas the (101) facet is thermodynamically more stable but generally less reactive (Zhang et al., 2024). Such facet-dependent catalytic behavior highlights the importance of surface engineering strategies in enhancing photocatalytic performance.

Another critical factor affecting photocatalytic efficiency is the generation and recombination of photogenerated charge carriers. Ideally, the photogenerated electrons and holes migrate to the catalyst surface and participate in redox reactions before recombination occurs. However, rapid electron-hole recombination remains one of the major limitations in photocatalytic systems, significantly reducing the number of active charge carriers available for chemical reactions (Tuama et al., 2024). Light intensity also plays an important role in determining photocatalytic kinetics. Increasing irradiation intensity can enhance the generation of electron-hole pairs and accelerate reaction rates; however, excessive irradiation may promote charge carrier recombination due to the simultaneous generation of large numbers of electrons and holes (Cho et al., 2025). Consequently, optimizing irradiation conditions is crucial to achieving efficient photocatalytic performance.

2.3.2 Semiconductor Photocatalyst Materials

Various semiconductor materials have been investigated as photocatalysts, including titanium dioxide, zinc oxide, cadmium sulfide, graphitic carbon nitride, and bismuth vanadate. Among these materials, titanium dioxide and zinc oxide remains the

most widely studied due to its chemical stability, low toxicity, and strong oxidative capability. However, its relatively large band gap limits its activation primarily to ultraviolet light, which constitutes only a small fraction of the solar spectrum. In contrast, visible-light-responsive materials such as graphitic carbon nitride and cadmium sulfide have attracted increasing attention due to their ability to utilize a broader portion of the solar spectrum (Zhang et al., 2023). Nevertheless, these materials often suffer from issues such as photocorrosion, limited stability, and rapid charge recombination, which restrict their practical applications. To enhance the efficiency of photocatalytic reactions, researchers have explored various catalyst modification strategies, including doping, heterojunction formation, and surface engineering, which improve light absorption, charge separation, and reaction kinetics.

Recently, photocatalysis has also emerged as a promising approach in biodiesel production, particularly in the pretreatment of feedstocks containing high levels of FFA. Conventional biodiesel synthesis often requires high temperatures and strong acid or base catalysts, which may lead to soap formation and catalyst deactivation. In contrast, photocatalytic esterification provides an alternative pathway that can operate under relatively mild conditions, reduced energy consumption, and the possibility of utilizing renewable solar energy. In such systems, photocatalysts facilitate the conversion of FFA into FAME through photo-induced redox reactions under light irradiation. Several studies have demonstrated the feasibility of photo-assisted esterification processes using various semiconductor catalysts under ambient conditions (Crisóstomo et al., 2025).

Despite these advancements, the application of photocatalysis in biodiesel synthesis remains relatively limited compared to other photocatalytic applications such as environmental remediation and hydrogen production. Challenges such as catalyst stability, low quantum efficiency, and insufficient visible-light utilization continue to hinder large-scale implementation. Therefore, the development of advanced photocatalysts with improved light absorption, enhanced charge separation, and greater catalytic stability remains an important research focus.

Table 2.4 summarizes previous studies on photocatalytic esterification processes, highlighting recent progress in biodiesel production under ambient conditions. Based on the studies listed in the table, photocatalytic esterification has successfully produced high-quality biodiesel with conversion yields exceeding 90%.

This indicates the strong potential of photocatalytic processes as an efficient and sustainable approach for biodiesel production under mild reaction conditions.

Table 2.4
Summary of Selected Studies on Photo-Trans-Esterification for Biodiesel Production

Feedstock	Photocatalyst	Light sources	Optimized conditions	Key findings	Reference
Castor oil	Sulfonic acid functionalized porphyrin (SAFPBM)	Visible light (5W/9W/12W LED)	6:1 methanol-to-oil ratio, 15 mg catalyst, 18 h ambient temperature	94% biodiesel yield, 7 recycle of catalyst	(Bhansali et al., 2021)
Kemiri Sunan (Reutialis trisperma oil)	CuO/TiO_2	UV irradiation	30:1 methanol-to-oil ratio, 4% catalyst, 4 h reaction time, 5 % (w/w) catalyst	59% FFA conversion	(Redjeki et al., 2021)
Frying sunflower oil	Sulphonic acid functionalized pyridinium ionic liquid (PcFASPyIL)	2 × 5W LED	12:1 molar ratio, 20 mg catalyst, 24 h reaction time	90% biodiesel yield, 7 time recycle of catalyst	(Patil et al., 2024)
Canola oil	TiO_2	UVA/sunlight	55:1 methanol-to-oil molar ratio, 20% catalyst, 4 h reaction time, 65°C reaction temperature	73% biodiesel yield with methanol and 38% with ethanol	(Welter et al., 2022)
Used frying oil (palm oil)	Porphyrin photocatalyst intertwined with ionic liquid and sulfonic acid (PPCILS)	5W LED	10:1 ethanol-to-oil molar ratio, 20 mg catalyst, 15 h reaction time	90.23% biodiesel yield	(Chandroday et al., 2024)
Jatropha curcas oil	Si/MgO heterojunction	Visible light (38,490 lx, Lux Meter Model: AF803) and solar radiation intensities	12:1 methanol-to-oil molar ratio, 2 wt% catalyst, 3.5 h reaction time	96% biodiesel yield	(Islam et al., 2023)

2.4 Photocatalytic Esterification

Photocatalytic esterification is particularly used for the pretreatment of high-FFA feedstock oils. This solar-driven process has attracted widespread attention due to its high efficiency, environmental friendliness, energy-saving characteristics, and simple operation. The photocatalytic mechanism generally follows the Langmuir-Hinshelwood reaction model, where the reactants are adsorbed on the catalyst surface before undergoing reaction (Ramos-Justicia et al., 2026). The reaction begins with photon absorption by the catalyst, followed by the generation and migration of electron-hole pairs that participate in oxidation-reduction processes. Surface redox reactions lead

to the formation of reactive oxygen species (ROS), such as hydroxyl radicals (•OH) and superoxide radicals ($•O_2^-$). These radicals activate both alcohol and FFA molecules, enabling their conversion into esters.

Furthermore, methanol and FFA can also be converted into radical species during the reaction. Methanol (CH_3OH) is adsorbed on the surface of the photocatalyst and reacts with photogenerated holes to form methanol free radicals ($CH_3O•$). Meanwhile, FFA (R–COOH) reacts with photogenerated electrons to form FFA free radicals (R–COO•) (Figure 2.3). The generation of these radicals occurs simultaneously with the formation of electron-hole pairs under light irradiation. Ester bond formation occurs when the activated methoxy species reacts with activated FFA on the catalyst surface. The products formed are FAME and water as a by-product. The final step involves the release of FAME molecules from the catalyst surface and their separation into the liquid phase (Crisóstomo et al., 2025).

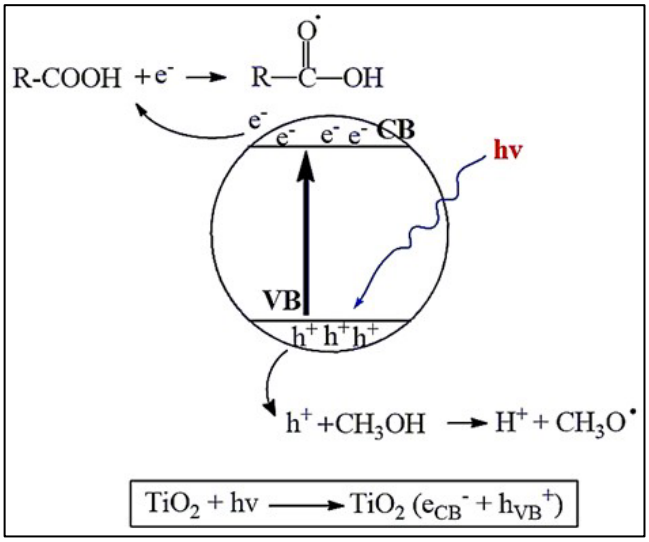


Figure 2.3 Schematic Representation of the Photocatalytic Mechanism in a Semiconductor Such as TiO_2 under UV Irradiation

The reaction mechanism follows the Langmuir-Hinshelwood-Hougen-Watson (LHHW) model, comprising photon absorption, charge separation, surface radical formation, and product desorption (Gadore & Mishra, 2025; Huang et al., 2022; Moafi et al., 2023). The proposed mechanistic sequence for EFBA-supported semiconductor activation is outlined below.

Photon Absorption and Charge Separation

When TiO_2/EFBA or ZnO/EFBA is irradiated with light of energy equal to or greater than its bandgap, electrons are excited from the valence band (VB) to the conduction band (CB), creating electron–hole pairs:

$$TiO_2/EFBA \text{ @ } ZnO/EFBA + h\nu \rightarrow e^-_{CB} + h^+_{VB} \quad (2.1)$$

These charge carriers migrate to the surface, where they participate in subsequent redox reactions.

Surface Adsorption and Radical Generation

Methanol and FFA molecules are adsorbed onto the photocatalyst surface. Holes (h^+) oxidize methanol via homolytic cleavage of the O–H bond, forming methoxy radicals ($CH_3O\bullet$) and protons (H^+).

$$CH_3O \bullet\bullet\bullet H + h^+ \rightarrow CH_3O\bullet + H^+ \quad (2.2)$$

Simultaneously, electrons (e^-) reduce FFA molecules (R–COOH) to form carboxyl radicals (R–COOH•):

$$R\text{-}COOH + e^- \rightarrow R\text{-}COOH\bullet \quad (2.3)$$

These radicals interact to form a tetrahedral intermediate that subsequently rearranges and undergoes dehydration, yielding FAME:

$$CH_3O\bullet + R\text{-}COOH\bullet + \rightarrow R\text{-}COOCH_3 + H_2O \quad (2.4)$$

The $CH_3O\bullet$ and R–COOH• radicals form a transient tetrahedral intermediate, which rearranges and condenses to produce FAME and water.

Product Desorption and Cycle Regeneration

FAME and water molecules desorb from the catalyst surface into the liquid phase, completing the cycle. Stirring facilitates mass transfer, enhancing adsorption-desorption dynamics.

In addition to methoxy and carboxyl radicals, ROS such as hydroxyl radicals (•OH) and superoxide radicals ($\bullet O_2^-$) also participate. •OH radicals, are produced by the oxidation of surface hydroxyl groups or water by holes, while $\bullet O_2^-$ arises from the reduction of molecular oxygen by electrons. These species improve reaction kinetics and help suppress charge recombination, maintaining photocatalyst activity.

Radical Scavenger Studies

To elucidate the dominant reactive species, radical scavenger experiments are commonly employed. Specific scavengers such as isopropanol (•OH), benzoquinone ($O_2\bullet^-$), and EDTA (h^+) selectively quench targeted species. A decline in FFA conversion efficiency upon scavenger addition confirms the involvement of the corresponding species in the esterification pathway. The observed inhibition patterns indicate the mechanistic participation of reactive oxygen species in the reaction process. These results validate the roles of hydroxyl radicals, superoxide radicals, and photogenerated holes and electrons in the EFBA-integrated esterification pathway. This mechanistic framework, supported by scavenger experiments and spectroscopic analyses, explains the enhanced catalytic performance for semiconductor photocatalyst.

In addition, vigorous stirring is an important factor that accelerates the transfer rate of adsorption and desorption of reactants at the catalyst surface and liquid interface. Theoretically, photocatalytic processes require the oxidation of water to form hydroxyl radicals and oxygen to generate superoxide radicals. However, in photo-esterification reactions, the presence of oxygen and water can negatively affect the reaction process. Water may promote hydrolysis of the formed esters, thereby reducing biodiesel yield. Therefore, recent studies have focused on immobilizing semiconductor materials onto suitable supports that can act as electron donors or acceptors, which helps to enhance redox reactions and maintain efficient charge separation (Parvulescu et al., 2020).

2.5 Transesterification

Transesterification (or alcoholysis) is the second step following photo-esterification. This process involves replacing the alcohol in an ester with another alcohol. It is essential for converting the triglycerides in WCO into biodiesel. Typically, short-chain alcohols such as methanol or ethanol are used in the presence of a base catalyst. Transesterification is favored for its high conversion efficiency and relatively short reaction time (Asfaw et al., 2025). Methanol is commonly employed due to its low cost, high reactivity, and compatibility with WCO.

Table 2.5 presents previous studies employing homogeneous catalysts for biodiesel production, where conversion efficiencies exceeding 90% have been widely reported. This indicates that homogeneous catalysis is highly effective in promoting the transesterification reaction.

Table 2.5
Summary of Homogeneous Catalyst Use for Biodiesel Production from Various Feedstocks

Feedstock	Catalyst type	Acid value (mg KOH/g)	Reaction condition	Key finding	Reference
Waste cooking oil	NaOH	0.702	60 °C, 3 h, 6:1 methanol-to-oil ratio, 0.4 wt% catalyst	94.94% biodiesel yield	(Hamed et al., 2021)
Sunflower oil	KOH	0.5	60 – 65 °C, 3 h, 6:1 methanol-to-oil ratio, 0.5 - 1 wt% catalyst	99% biodiesel yield	(Fattah et al., 2020)
Waste cooking oil	Sulfuric acid (H_2SO_4)- pretreatment	5.42	65 °C, 2 h, 6:1 methanol-to-oil ratio, 3 wt% catalyst	98.5% FFA conversion	(Razzak et al., 2025)
Waste frying oil	Hydrochloric acid (HCl)- acid pretreatment	6.18	75 °C, 3 h, 9:1 methanol-to-oil ratio, 4 wt% catalyst	97.8% FFA conversion	
Waste vegetable oil	Phosphoric acid (H_3PO_4)- acid pretreatment	4.97	70 °C, 2.5 h, 8:1 methanol-to-oil ratio, 2 wt% catalyst	96.2% FFA conversion	

Base-catalyzed transesterification is particularly preferred in industrial applications due to its fast reaction rate and high conversion efficiency, even when using relatively low-quality feedstocks. Common catalysts include NaOH, KOH, alkaline metal alkoxides, and carbonates. However, the presence of water in the feedstock can lead to hydrolysis, soap formation, and a reduction in biodiesel yield. This limitation highlights the importance of pretreatment processes, such as photo-esterification, to reduce free fatty acid content and maximize the overall biodiesel conversion efficiency.

Being a reversible reaction, transesterification follows Le Chatelier's principle (Abdelrahman & Abo El-Khair, 2025). To shift the equilibrium toward FAME production, an excess of alcohol is typically used. However, excessive alcohol complicates glycerol separation, so the optimal alcohol-to-oil ratio must be determined empirically for each system.

The reaction proceeds via a nucleophilic substitution mechanism (Figure 2.4):

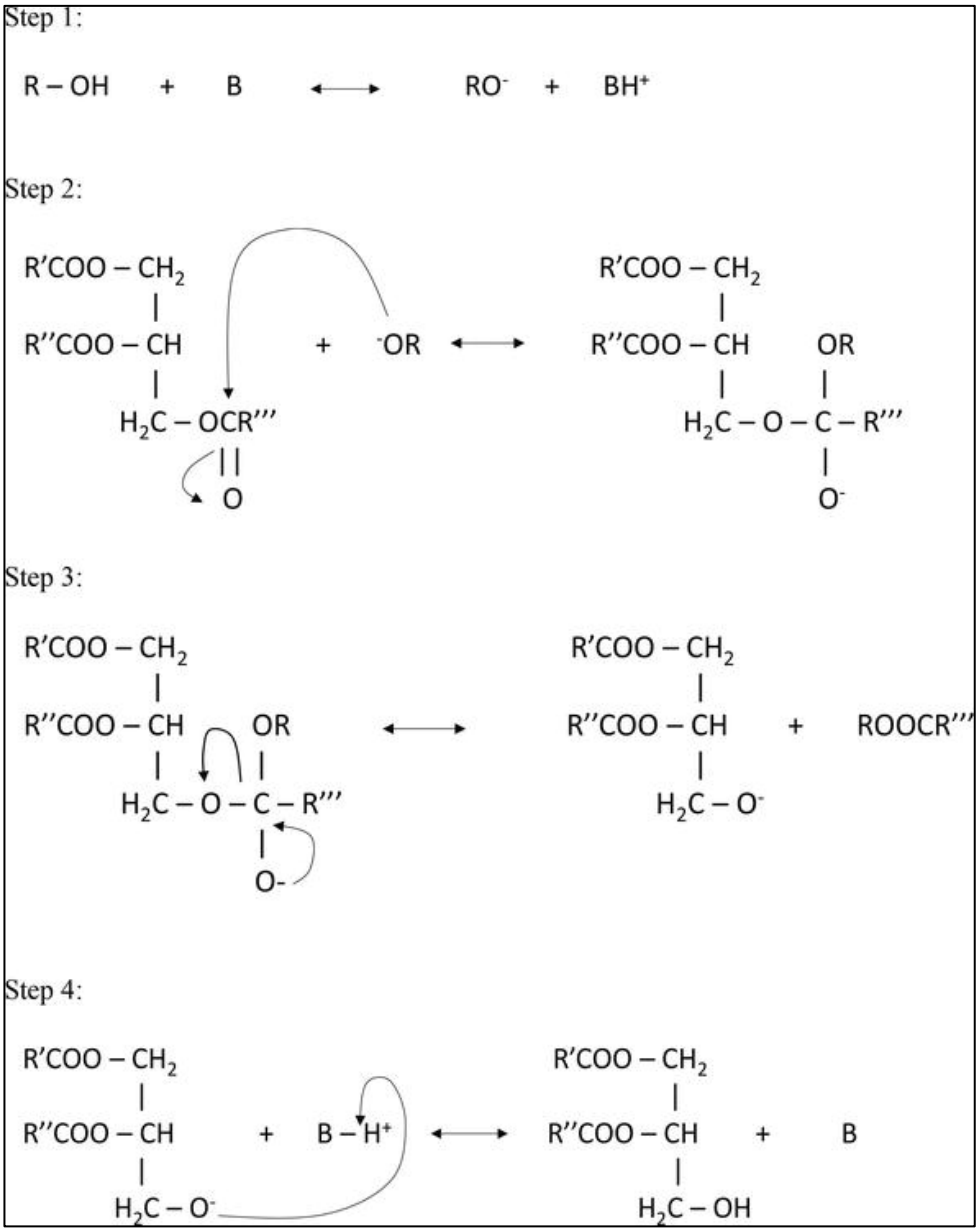


Figure 2.4 Alkali-Catalyzed Transesterification (Farouk et al., 2024)

1. Activation of alcohol: A base catalyst (e.g., NaOH or KOH) deprotonates methanol or ethanol, generating a nucleophilic alkoxide ion.
2. Nucleophilic targeting: The alkoxide ion targets the electrophilic carbonyl carbon of the triglyceride, forming a tetrahedral intermediate.
3. Intermediate rearrangement: The unstable intermediate undergoes rearrangement, resulting in bond cleavage that releases one molecule of FAME and forms a diglyceride.
4. Catalyst regeneration: The catalyst is regenerated through deprotonation, and the released proton binds to the glyceride species.
5. Sequential conversion: Steps 2–4 repeat for remaining ester bonds. Outcome: One triglyceride molecule ultimately yields three FAME molecules and one glycerol.

2.6 Photocatalyst

Catalysis plays a pivotal role in biodiesel production, enabling the conversion of triglycerides and FFA into FAME. Catalysts enhance these transformations by lowering the activation energy and introducing alternative reaction routes, thereby improving both reaction rate and efficiency. As illustrated in Figure 2.5, the presence of a catalyst significantly reduces the energy threshold required to initiate the reaction. Beyond increasing reaction speed, catalysts exhibit selectivity favouring the formation of desired products while minimizing side reactions (Niu et al., 2025).

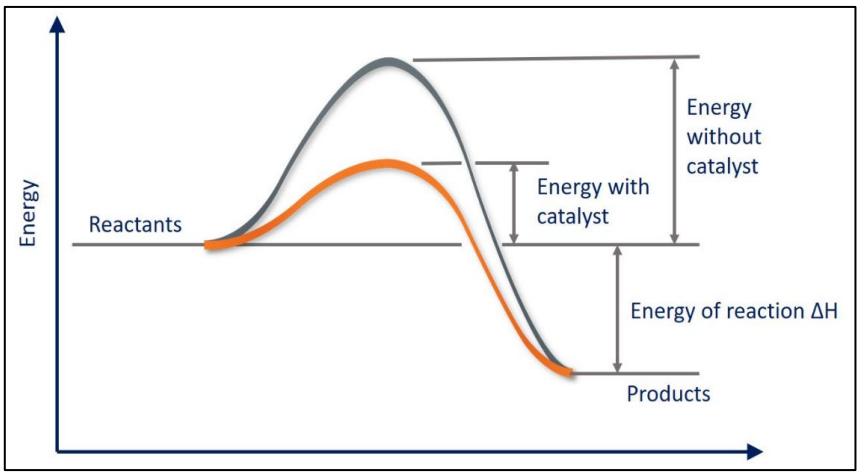


Figure 2.5 Effect of a Catalyst on Activation Energy During a Chemical Reaction

Catalytic systems used in biodiesel production are broadly classified into two categories: homogeneous and heterogeneous. Homogeneous catalysts share the same phase as the reactants, often enhancing molecular-level interactions. Heterogeneous catalysts, in contrast, remain in a separate phase, usually solid, which facilitates post-reaction recovery and supports continuous operation (Rizwanul-Fattah et al., 2020). Table 2.6 presents previous studies employing heterogeneous catalysts for biodiesel production. Based on the studies summarized in the table, most heterogeneous catalytic processes require relatively high reaction temperatures to effectively drive the transesterification reaction. This suggests that additional energy input is often necessary to overcome mass transfer limitations and improve catalytic activity.

Table 2.6
Summary of Heterogeneous Catalysts in Biodiesel Production

Catalyst type	Catalyst	Feedstock	Reaction conditions	Yield (%)	Reference
Solid base catalyst	Calcined Carob Pod Powder (CCPP)	Waste cooking oil	600 W microwave power, 9.87:1 methanol-to-oil ratio, 1 wt% catalyst,	98.2	(Oladipo et al., 2024)
Solid acid catalyst (Acidic metal oxide)	ZrO_2	Palm fatty acid distillate	120 °C, 3 h, 10:1 methanol- to-oil ratio, 5 wt% catalyst	92	(Bekhradinassab et al., 2025)
Monosaccharides-based-solid acid	Sulfonated glucose	Sewage sludge lipid	130 °C, 4 h, 25:1 methanol- to-lipid ratio, 1 ratio of catalyst to lipid	93.7	(Wang et al., 2025)
Bifunctional catalyst (mixed metal oxide)	SrO@WO_3@MCM-41	Corn oil	80 °C, 5 h, 6:1 methanol- to-oil ratio, 10 mg catalyst	96	(Tariq et al., 2025)
Bifunctional catalyst (mixed metal oxide)	SrO@WO_3@MCM-41	Waste cooking oil	100 °C, 6 h, 6:1 methanol- to-oil ratio, 20 mg catalyst	93	(Tariq et al., 2025)
Supported catalyst (Magnetic acid catalyst)	MoO_3/ $MnFe_2O_4$	Waste cooking oil	164.5 °C, 2.5 h, 32:1 methanol- to-oil ratio, 6.5 wt% catalyst	96.7	(dos Santos et al., 2025)
Photocatalyst (semiconductor photocatalyst)	SnS_2/ Fly ash nanocomposites	Oleic acid	64.85 °C, 50 min, 8:1 methanol- to-oil ratio, 3 wt% catalyst	99.89	(Gadore et al., 2025)

Although homogenous catalyst more preferable due to fast reaction time, high efficiency, however, this catalyst is hard to separate and produce waste. The heterogenous catalyst offer advantage of easy separation, catalyst recyclability and reduced chemical waste, making them attractive for sustainability (Medeiros Vicentini-Polette et al., 2021). Among heterogenous catalyst, semiconductor-based photocatalyst have gained attention due to their ability to utilize light energy to activate feedstock under mild condition. This offer both environmental and energy-saving benefits.

Semiconductor photocatalysts are chemically and biologically inert, relatively easy to synthesize, and cost-effective, as they can be activated by solar radiation. Table 2.7 presents a summary of common semiconductor photocatalysts used for the conversion of free fatty acids (FFA). Based on the studies listed in the table, the catalysts employed are predominantly semiconductor-based materials capable of facilitating electron transfer during the photocatalytic reaction. In addition, most reactions were conducted under mild operating conditions while achieving FFA conversion rates exceeding 90%. This suggests that semiconductor photocatalysts have strong potential for efficient biodiesel production through photocatalytic esterification under environmentally friendly and energy-saving conditions.

Table 2.7
Summary of Common Semiconductor Photocatalysts Used in Biodiesel Production

Photo - catalyst	Feedstock	Light source	Reaction condition	FFA (%)	Reference
La^{3+}/ZnO-TiO_2 (Lanthanum ion (La^{3+}) – dopant)	Waste cooking oil	UV light (254 nm, 30 W)	12:1 methanol-to-oil ratio, 3 h UV irradiation, 4 wt% catalyst, ~35 °C reaction temperature	96.14	(Guo et al., 2021)
8.5% Cr-TiO_2 (Chromium (Cra^{3+}) dopant)	Waste cooking oil	UV-C lamp (4 × 15 W, λ = 254 nm)	12:1 methanol-to-oil ratio, 3 h UV irradiation, 4 wt% catalyst, ~30 °C reaction temperature	89.5%	(Abbasi & Ahmadi, 2023)
5% CuO/TiO_2 (CuO (dopant)	Kemiri Sunan Oil	UV light	30:1 methanol-to-oil ratio, 4 h UV irradiation, 4 wt% catalyst, ~30 °C reaction temperature	59%	(Redjeki et al., 2021)
TiO_2/EFBA	Waste Cooking Oil	UV light (365 nm)	20:1 methanol-to-WCO ratio, 2 h UV irradiation, 4 wt% catalyst, 35 °C reaction temperature	78%	System studied in this work

2.6.1 Titanium Dioxide-Based Photocatalyst

Titanium dioxide (TiO_2) was first identified by the British mineralogist William Gregor in 1791. TiO_2 is formed when titanium reacts with oxygen, producing a stable inorganic oxide compound. The significance of TiO_2 in photocatalysis was later demonstrated by Akira Fujishima and Kenichi Honda, who pioneered the photoelectrochemical splitting of water using TiO_2 electrodes under ultraviolet irradiation in 1972. Their study showed that when TiO_2 is illuminated with light

possessing energy equal to or greater than its band gap, electron-hole pairs are generated, enabling redox reactions at the catalyst surface (Song et al., 2024).

TiO_2 has become one of the most widely studied semiconductor photocatalysts due to its favourable physicochemical properties, including high chemical stability, strong oxidative potential, excellent photocatalytic activity, low toxicity, and relatively low production cost. In addition, TiO_2 exhibits a high refractive index, strong dielectric properties, and high transparency in the visible and near-infrared regions, making it suitable for various photocatalytic applications (Shi et al., 2020).

TiO_2 functions as a semiconductor photocatalyst due to its band gap energy ranging from approximately 3.0–3.2 eV. This band gap allows TiO_2 to absorb ultraviolet (UV) light, which promotes electrons from the valence band (VB) to the conduction band (CB), leaving positively charged holes in the VB. These charge carriers can migrate to the catalyst surface and participate in oxidation-reduction reactions. The electronic structure of TiO_2 is mainly composed of oxygen 2p orbitals forming the valence band and titanium 3d orbitals forming the conduction band. The difference in orbital composition between the VB and CB facilitates charge separation and contributes to the relatively lower recombination rate of photogenerated electron-hole pairs compared with many other semiconductor materials (Nagakawa et al., 2020).

TiO_2 exists in three polymorphic phases: anatase, rutile, and brookite (Figure 2.6). Among these, anatase and rutile are the most commonly used in photocatalytic applications due to their favourable structural and electronic properties. Anatase possesses a tetragonal crystal structure with a density of approximately 3.89 g cm^{-3} and is metastable at ambient conditions, typically transforming into rutile at elevated temperatures around 600–700 °C. Anatase generally exhibits superior photocatalytic performance due to its higher surface area and lower recombination rate of photogenerated charge carriers. Rutile, on the other hand, is the thermodynamically stable phase with a density of approximately 4.25 g cm^{-3} and also exhibits a tetragonal crystal structure. It possesses a slightly smaller band gap (~3.0 eV), which can enhance light absorption and electrical conductivity. Brookite has an orthorhombic crystal structure and is less commonly applied due to the difficulty in synthesizing it in pure form (Song et al., 2020).

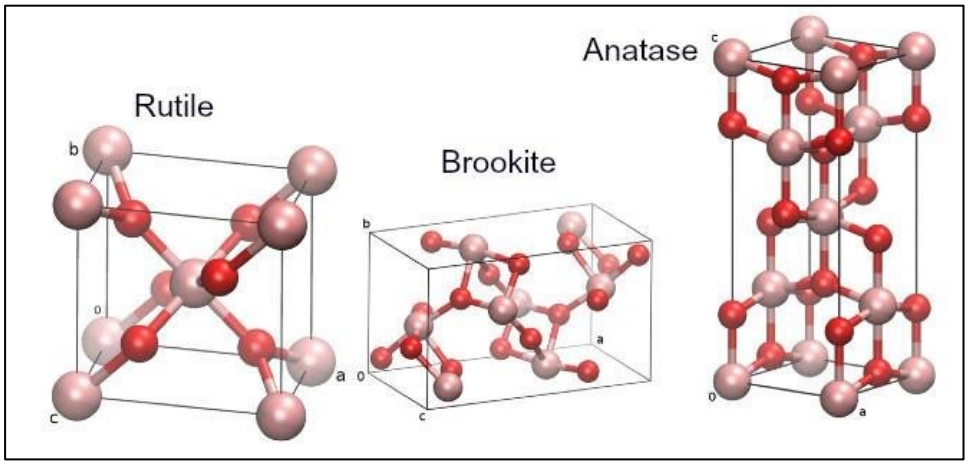


Figure 2.6 Crystal Structure of TiO_2 Phase of Rutile, Brookite and Anatase

Although anatase is often considered the most active phase for photocatalysis, studies have shown that combining anatase and rutile phases can further improve photocatalytic performance through the formation of heterojunction structures. One widely used commercial photocatalyst is Degussa P25, which consists of approximately 70–80% anatase and 20–30% rutile. The interface between these two phases forms an anatase-rutile heterojunction that promotes efficient charge separation (Wang et al., 2020). In this configuration, photogenerated electrons tend to transfer from the rutile phase to the anatase phase, where they become trapped, thereby suppressing electron-hole recombination and enhancing photocatalytic activity.

Despite these advantages, TiO_2 can only absorb UV light due to its relatively wide band gap. Since UV radiation accounts for only about 5% of the solar spectrum, the utilization efficiency of solar energy is limited. In addition, UV light sources often require high energy input and may pose safety concerns during prolonged exposure. Furthermore, the rapid recombination of photogenerated charge carriers reduces its quantum efficiency and overall catalytic performance. TiO_2 nanoparticles also possess high surface energy, which can lead to particle agglomeration through van der Waals interactions. Such agglomeration decreases the available active surface area, reduces light absorption efficiency, and increases the likelihood of charge recombination (Li et al., 2020). Consequently, significant research efforts have focused on modifying TiO_2 to enhance its visible-light activity and improve its photocatalytic efficiency under solar irradiation.

To overcome these limitations, various modification strategies have been developed, including elemental doping with metals or non-metals, coupling with other semiconductor materials, and immobilization on suitable support materials. However, elemental doping may introduce discrete energy levels within the band structure, which can act as recombination centers for photogenerated electrons and holes, thereby reducing photocatalytic efficiency (Khlyustova et al., 2020). Moreover, coupling with other metal or non-metal semiconductors may lead to complex synthesis procedures and poor interfacial compatibility, which can limit effective charge transfer between the coupled materials (Qi et al., 2024). In contrast, surface modification or immobilization on suitable support materials has emerged as a promising approach. In such systems, the support can function not only as a structural support but also as a co-catalyst that stabilizes the active catalyst and directly participates in the photocatalytic reaction. Furthermore, the support can facilitate electron transfer and improve charge separation, thereby enhancing overall photocatalytic performance (Khan & Shah, 2023). In addition, supported photocatalysts often exhibit higher surface area, improved dispersion of active sites, and stronger interactions between the catalyst and reactant molecules, which are beneficial for photocatalytic reactions such as photo-esterification (Tratrat et al., 2023).

2.6.2 Zinc Oxide-Based Photocatalyst

Zinc Oxide (ZnO) has emerged as a promising alternative photocatalyst due to its comparable band-gap energy and favourable optoelectronic properties (Wary et al., 2023). ZnO possesses a wide band gap of approximately ~3.0 eV, classifying it as an n-type semiconductor that is primarily responsive to UV light (Wu et al., 2025). Moreover, ZnO exhibits a relatively high exciton binding energy (~60 meV), which can promote lasing action and enables excitons to remain stable even above room temperature, an important characteristic for UV optical devices (Tashiro et al., 2023). In addition, ZnO has a high density (5606 kg m^{-3}) and a high melting point (2248 K; 1975 °C), both of which contribute to its excellent thermal and chemical stability (Mahesh et al., 2024).

ZnO exists in three polymorphs: hexagonal wurtzite, cubic zinc blende, and cubic rock salt (Figure 2.7). Among these structures, the wurtzite phase is

thermodynamically stable at ambient pressure and temperature. This phase exhibits tetrahedral coordination and polar surfaces, which induce spontaneous polarization along the c-axis. In the wurtzite lattice, each oxygen atom is tetrahedrally coordinated with four Zn^{2+} ions, forming a crystal structure with lattice parameters of a = 0.3296 nm and c = 0.52065 nm. This structural arrangement generates an internal electric field that facilitates effective separation of photogenerated electron-hole pairs, thereby enhancing charge carrier mobility (Sen et al., 2023). In contrast, the zinc blende structure is metastable and generally requires epitaxial growth on lattice-matched substrates, while the rock salt phase, characterized by octahedral coordination, is only stable under high-pressure conditions (~10 GPa) and is therefore unsuitable for photocatalytic applications under ambient conditions (Lahur et al., 2024). Consequently, the wurtzite structure is the most favourable phase for photocatalysis due to its structural stability and internal polarization properties that support efficient photocatalytic reactions.

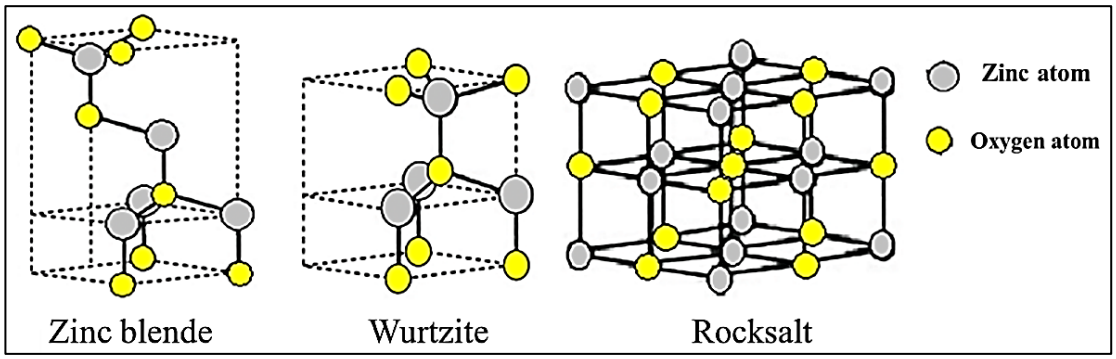


Figure 2.7 Crystal Structures of the Three Polymorphs of ZnO

The photocatalytic performance of ZnO, however, is limited by several factors, including photocorrosion and rapid charge carrier recombination. These limitations are largely associated with intrinsic crystal defects such as oxygen vacancies and zinc interstitials, which can impair charge mobility and reduce photocatalytic efficiency (Dimitropoulos et al., 2024). Additionally, photogenerated holes may oxidize lattice Zn^{2+} ions, leading to structural degradation and reduced long-term catalytic stability. Nevertheless, ZnO exhibits high breakdown strength and high electron saturation velocity, allowing the material to withstand strong electric fields while facilitating rapid charge transport. These characteristics contribute to the chemical stability and electronic robustness of ZnO, making it a promising photocatalyst (Salu et al., 2026).

Furthermore, ZnO remains an attractive candidate for photocatalytic biodiesel production due to its low cost, tuneable morphology, and compatibility with green modification strategies. However, ZnO nanoparticles are prone to agglomeration because of their high surface energy, similar to TiO_2, which can reduce surface area and photocatalytic activity (Pathak et al., 2025). To overcome this limitation, supporting materials are often employed to improve catalyst dispersion and stability.

2.7 Modification Strategies for Semiconductor Photocatalyst

The modification of semiconductor photocatalysts has been widely investigated to overcome the inherent limitations of single component photocatalysts. Several modification strategies have been proposed, including doping, heterojunction coupling, and surface modification. Doping involves introducing foreign atoms into the semiconductor lattice to modify its electronic structure. For example, nitrogen-doped TiO_2 can create localized energy states through orbital hybridization, enabling improved visible-light absorption. However, excessive doping may introduce structural defects and lattice distortion, which can weaken mechanical stability and reduce charge mobility and conductivity (Shah et al., 2025).

Another widely explored approach is heterojunction coupling between two semiconductors to improve charge separation efficiency. For instance, coupling indium sulfide with tungsten trioxide can extend light absorption into the visible region while effectively suppressing electron-hole recombination (Qiu et al., 2021). Nevertheless, the fabrication of heterojunction systems often requires precise band alignment between the two semiconductors. Poor interfacial contact or improper coupling may lead to particle agglomeration and reduced photocatalytic performance.

Among the available approaches, surface modification has emerged as a promising strategy for improving photocatalyst stability and dispersion. In this approach, photocatalysts are immobilized onto suitable support materials to prevent nanoparticle agglomeration and enhance catalyst stability. Surface modification can also introduce new surface energy states that facilitate charge transfer and improve photocatalytic activity. In addition, strong interactions between the photocatalyst and the support can enhance mechanical stability and catalyst durability (Ning et al., 2025).

Recently, waste-derived materials have gained considerable attention as sustainable support materials for photocatalysts. Examples include activated carbon (Meirelles et al., 2025), biochar (Cui et al., 2020), cellulose (Balakrishnan et al., 2025). These materials offer several advantages such as low cost, renewability, and high surface area, which contribute to improved catalyst dispersion and adsorption properties (Son et al., 2021). In particular, agricultural biomass waste such as rice husk, bagasse, and coffee husk has been widely explored due to its abundance and environmental sustainability.

More recently, biomass-derived ash materials have been investigated as potential photocatalyst supports due to their complex inorganic composition. Various types of ash, including municipal waste incineration ash, coal fly ash, rice husk ash, rice hull ash, bamboo ash, volcanic ash, and magnetic fly ash, have been explored for catalyst support applications. However, there are limitations have been reported for these materials. For example, municipal waste incineration ash and coal fly ash may contain hazardous heavy metals and toxic impurities, which could pose environmental risks and negatively affect catalytic stability (Katre et al., 2024).

In contrast, empty fruit bunch ash (EFBA), derived from oil palm biomass waste, has emerged as a promising alternative support material. EFBA typically contains high levels of silica, potassium, magnesium, and calcium oxides. These inorganic components can provide abundant active sites and enhance the interaction between the photocatalyst and the support surface. Consequently, the incorporation of EFBA as a support material can improve photocatalyst dispersion, enhance catalytic stability, and promote higher photocatalytic efficiency in photo-esterification processes.

2.7.1 Empty Fruit Bunch Ash (EFBA)

As previously mentioned, Malaysia is the second-largest producer of palm oil globally and generates approximately 19.7 million metric tonnes of palm oil industry waste in 2025/2026. During palm oil processing, fresh fruit bunches undergo sterilisation and stripping, producing substantial quantities of empty fruit bunch (EFB). Subsequent thermal treatment or incineration of solid residues at temperatures up to 600 °C produces several by-products, including mesocarp fibre (MF), palm kernel shell (PKS), and an ash residue known as empty fruit bunch ash (EFBA). It is estimated that

EFBA accounts for nearly 9 million tonnes of waste annually and is largely discarded, contributing to environmental pollution and greenhouse gas emissions (USDA/MPOB, 2026). Improper disposal can also increase waste management costs and disrupt drainage systems, highlighting the need for sustainable valorisation strategies (Hisham & Jamil, 2020).

Despite these environmental concerns, EFBA has recently attracted attention as a potential support material in catalytic systems. The utilisation of EFBA as a support can improve the surface area and dispersion of semiconductor photocatalysts. Valorisation of this ash therefore represents an effective strategy to convert agro-industrial waste into a value-added material while supporting sustainable resource management (Nextgreen Global Bhd, 2024; Wulandari et al., 2023). Chemically, EFBA contains complex inorganic oxides, particularly SiO_2, Al_2O_3, and K_2O, which contribute to surface reactivity and structural stability. In addition, minor components such as Fe_2O_3 and Mn_3O_4 may function as electron traps, suppressing charge carrier recombination during photocatalysis. Alkali oxides such as K_2O, Na_2O, and CaO further enhance surface basicity and hydrophilicity, which can facilitate hydroxyl radical formation during photocatalytic reactions. Consequently, EFBA may function not only as a structural support but also as an electronic modifier within photocatalytic systems (Ebitei et al., 2026).

Table 2.8 summarises the oxide composition reported for several biomass-derived ashes with similar inorganic characteristics. These materials share comparable mineral compositions dominated by silica, alumina, and alkaline oxides, suggesting their potential applicability as catalyst supports. Among reported studies, for instance, a SnS_2/biomass-ash photocatalyst achieved a biodiesel yield of 99.89 % under visible-light irradiation, highlighting the feasibility of ash-derived materials as catalyst supports. Similarly, Elanthikkal et al. (2023) reported that ZnO doped with date palm ash generated oxygen vacancies and reduced the bandgap from 4.28 eV to 4.09 eV, thereby improving visible-light absorption. These findings suggest that the dual functionality of biomass ash, acting both as a structural matrix and electronic modifier, can enhance photocatalytic activity (Mohamed et al., 2023).

Table 2.8
Major Inorganic Oxide Constituents of EFBA Contributing to Photocatalytic Activity

Biomass ash type	Oxides composition wt%									Reference
	SiO_2	K_2O	CaO	MgO	Fe_2O_3	Al_2O_3	Na_2O	P_2O_5	SO_3	
Empty fruit bunch ash	33.85	32.58	7.28	5.01	5.44	1.61	0.40	4.23	2.03	(Putra et al., 2023)
Palm oil fuel ash	39.1-76.4	1.7-13.5	3.2-14.0	1.5-5.9	1.1-8.6	0.9-11.4	-	-	0.1-9.2	(Oyehan et al., 2022)
Date palm biomass ash	48.99	3.17	39.54	-	3.30	1.71	-	-	2.41	(Elanthikkal et al., 2023)
Eucalyptus ash	1.76	4.64	43.80	8.36	2.43	5.06	0.28	3.32	-	(Silva et al., 2022)
Rice husk ash	92.21	4.08	0.73	0.39	0.19	0.03	0.08	1.48	0.32	(Santis et al., 2025)
Arundo donax L. ash	54.96	7.13	8.04	0.66	11.56	10.88	0.40	0.78	2.53	(Easwaran et al., 2022)
Mix biomass (wheat:corn:forestry = 5:2:3)	54.96	7.13	8.04	0.66	11.56	10.88	0.40	0.78	2.53	(Xu et al., 2023)

Nevertheless, several challenges remain when utilising EFBA as a catalyst support. High-temperature calcination (>500 °C), which is often required during catalyst preparation, may collapse the porous structure of EFBA and consequently reduce its surface area. Such structural degradation can negatively affect catalyst dispersion and activity. To mitigate these limitations, various post-treatment strategies have been proposed, including acid washing, mild calcination, and chemical activation. These treatments can restore porosity, increase surface hydroxyl groups, and enhance the anchoring of active photocatalyst nanoparticles on the ash surface (Ko et al., 2025).

To effectively integrate EFBA into photocatalytic systems, appropriate synthesis techniques are required to control catalyst dispersion and structural properties. Commonly employed preparation methods include sol-gel, hydrothermal, precipitation, and wet impregnation techniques (Mohamadpour & Amani, 2024). Among these approaches, wet impregnation is widely regarded as a practical and scalable method for biomass-supported catalysts. This technique utilises capillary forces within the porous support to distribute metal precursors uniformly, enabling precise control of metal loading and dispersion across the support surface (Kanchanakul et al., 2023; Ma et al., 2025). Moreover, this method is simple, cost effective, and adaptable for industrial-scale production.

2.7.2 EFBA-supported TiO_2/ZnO Photocatalyst

EFBA is typically rich in complex inorganic oxides that form a stable mineral matrix capable of anchoring semiconductor nanoparticles such as TiO_2 and ZnO. This mineral framework can enhance catalyst dispersion and structural stability. For instance, Tu et al. (2022) reported that TiO_2 supported on ash retained a dominant anatase phase. The formation of Si-O-Ti bonds stabilised Ti species on the support and suppressed grain growth during calcination. Moreover, this integration prevents undesirable phase transformation, thereby maintaining the active semiconductor phase and improving thermal stability. Moreover, Sharma et al. (2025) observed that Cu-doped fly ash-TiO_2 composites exhibited less than 5 % weight loss at 500 °C, indicating enhanced thermal stability. In another study, Sintipditsakul et al. (2025) reported that SiO_3 incorporation produced a rougher surface morphology, which improved ion diffusion and promoted interfacial charge transfer between the support and the semiconductor phase.

EFBA can influence the optical and electronic properties of semiconductor photocatalysts. The relatively high optical transparency of ash-derived matrices may reduce light scattering, thereby improving photon penetration and light utilisation. Gakuru et al. (2024) demonstrated that silicon and aluminium species originating from ash could partially substitute Ti^{4+} ions within the TiO_2 lattice, resulting in mild lattice contraction and improved crystallinity (Gartner et al., 2024; Gautam et al., 2020). This substitution promotes deeper photon penetration into the photocatalyst, thereby enhancing light-harvesting efficiency.

In addition, Wary et al. (2023) reported that alkali and alkaline earth metals present in biomass ash, particularly K^+ and Ca^{2+}, can substitute Zn^{2+} within the ZnO lattice. This substitution generates charge imbalance and oxygen vacancies, which act as shallow donor states that enhance visible-light absorption and promote charge mobility. Consistently, Dogar et al. (2020) found that ash-derived CaO, K_2O, and Fe_2O_3 reduced the bandgap of ZnO from 3.28 eV to 3.07 eV through the formation of mid-gap states, thereby improving charge separation efficiency. In addition, Zailan et al. (2020) reported that EFBA incorporation increased the specific surface area of ZnO from 5.80 $m^2\ g^{-1}$ to 14 $m^2\ g^{-1}$, thereby enhancing catalytic accessibility and reactant adsorption.

Surface modification enhances the photocatalytic activity and improves the efficiency of charge separation while increasing the availability of active sites for the reaction. This can be observed in the study by Hussein et al. (2022), where a ZnO-Ni-Co oxide composite derived from biomass ash achieved 93% degradation efficiency of methylene blue. These results highlight the feasibility of biomass ash-supported semiconductor systems for photocatalytic applications, including environmental remediation and renewable fuel production. Overall, incorporating EFBA into TiO_2 and ZnO photocatalytic systems provides several advantages, including structural stabilization, improved light absorption, enhanced surface properties, and more efficient charge transport.

2.8 One-Variable-at-a-Time (OVAT) Parameters for Photocatalytic Esterification

Photocatalytic esterification is a complex surface-driven process whose efficiency depends on a combination of physical and chemical parameters. Key factors such as alcohol-to-oil molar ratio, catalyst loading, and reaction time significantly influence FFA conversion rates, biodiesel yield, and reaction sustainability. These parameters affect light absorption, charge carrier dynamics, surface redox efficiency, and mass transfer limitations within the photocatalytic system. The OVAT method is employed in this study to isolate and evaluate individual parameters while holding others constant.

2.8.1 Effect of Alcohol to Oil Molar Ratio

The alcohol-to-oil molar ratio is a key parameter that drives methyl ester formation and enhances catalyst-reactant interactions (Masango et al., 2024). In photocatalytic systems, methanol can act as a proton donor during photon-induced excitation, thereby promoting charge separation. However, excessive methanol may dilute reactant concentrations, reduce surface contact, scatter incident light, and facilitate charge carrier recombination, ultimately reducing catalytic efficiency (Özyiğit et al., 2024). Identifying an optimal molar ratio is therefore essential to maximize yield without compromising light utilization. Siang Ng et al. (2020) achieved an 82% FFA

conversion using visible-light-active TiO_2 at a 15:1 methanol-to-oil ratio. This finding indicates that the optimal molar ratio varies depending on the type of catalyst and the illumination source.

2.8.2 Effect of Catalyst Loading

Catalyst loading affects the number of active sites and available surface area for light-driven redox reactions. At low concentrations, insufficient photocatalyst limits photon capture and reactant adsorption, reducing conversion efficiency (Guliani et al., 2022). Increasing dosage generally enhances performance, up to an optimal threshold. Excessive loading causes light scattering and agglomeration, which hinder quantum efficiency and reactant diffusion, especially in dense suspensions (Welter et al., 2022). For example, Liu et al. (2021) reported that FFA conversion with TiO_2 improved up to 4 wt% under UV light but plateaued beyond this point due to light attenuation. These drawbacks lead to decreased quantum efficiency and hinder reactant diffusion, particularly in dense suspensions.

2.8.3 Effect of Reaction Time

Reaction time governs the duration of charge carrier participation before recombination or deactivation. Initially, reaction rates are rapid due to high FFA concentration and active site availability. As equilibrium approaches, redox activity diminishes and conversion plateaus. While extended reaction times may seem beneficial, they can trigger reverse hydrolysis, thermal degradation, or catalyst fouling (Oladipo et al., 2024). Thus, optimal duration is essential for energy-efficient conversion and sustained activity

2.9 Effect of EFBA doping on Optimal Operational Parameters

EFBA doping can modify the structural and electronic properties of TiO_2 and ZnO photocatalysts. Therefore, careful evaluation is required to fully understand the synergistic effects of EFBA on both catalytic and photophysical performance. As reported by Shohaimi et al., (2024), excessive EFBA incorporation may introduce undesirable defects and excessive surface coverage, which can reduce photocatalytic

activity by limiting light absorption and blocking active sites. On the other hand, insufficient EFBA loading may lead to the agglomeration of nanoparticles, as the absence of an adequate supporting matrix reduces particle dispersion and stability. Therefore, optimizing the EFBA-to-photocatalyst mass ratio is crucial to achieving an optimal synergistic interaction between the semiconductor nanoparticles and the EFBA ash matrix.

2.10 Light Source

Light carries energy and behave as wave-particles duality. It provides energy to valence band and excited to the conduction band of semiconductor. Light is one of the important factors for the evaluation percentage FFA conversion (Markushyna & Savateev, 2022). According to the Grotthuss-Draper law, only absorbed photons can induce chemical transformations, while the Bunsen-Roscoe law links reaction rate to light intensity and exposure duration (Ma et al., 2025). Therefore, these laws provide theoretical foundation that photocatalyst need to test under controlled light sources such as UV lamp, LED lamp and Xenon lamp and with different wavelengths and light intensities/duration.

2.10.1 Ultraviolet (UV) Light

UV light means light beyond violet and discovered by a German electro chemist, Johann Wilhelm Ritter in 1801. From the electromagnetic spectrum, UV light lies between X-rays and visible region. UV light contains high energy and proportional to the frequency of light, $E = hv$. Where E is light energy, h is Plank's constant and v is frequency of the light. The wavelength of UV is spans from 100 to 400 nm and is subdivided into UV-A (315–400 nm), UV-B (280–315 nm), and UV – C (100–280 nm) (Papagiannaki et al., 2020). UV-A offers deeper penetration and lower energy consumption, as it placed at longer wavelength making it suitable for wide-bandgap semiconductors such as TiO_2 (~3.2 eV) and ZnO (~3.0 eV). UV – B and UV – C possess higher photon energy due to their shorter wavelengths. Therefore, they suffer from limited material penetration, elevated operational costs, and potential photocatalyst degradation (Makota et al., 2025).

2.10.2 Visible Light

Visible light, spanning 380–780 nm and comprising ~43% of the solar spectrum. Its widely explored for low-energy photocatalysis due to its compatibility with solar-driven systems (Andrade et al., 2023).

2.10.3 Xenon Light

Xenon arc lamps emit a full-spectrum output (200–2500 nm), closely replicating solar radiation. Their high color rendering index (CRI ~100) and stable temperature (~6200 K, 5927 °C) make them ideal for laboratory-scale solar simulation (Hmoudah et al., 2025). However, xenon lamps are energy-intensive and generate substantial heat, requiring complex cooling setups that elevate operational costs (Varón et al., 2023). Despite these limitations, xenon irradiation supports simultaneous activation of deep bandgap and surface trap states, an advantage for EFBA-supported TiO_2 and ZnO systems.

2.11 Research Gap and Study Relevance

Despite extensive research on TiO_2 and ZnO photocatalysts, several challenges persist. Their wide bandgaps restrict light absorption primarily to the UV region, thereby limiting photocatalytic activity under solar irradiation. In addition, the optimization of operational parameters for supported photocatalytic systems remains insufficiently explored. Few studies have systematically examined how EFBA support characteristics, such as porosity, basicity, and surface functionality, influence catalyst dosage, illumination response, and reaction duration. Furthermore, aspects related to scalability, catalyst regeneration, and long-term stability remain underexplored, with limited attention given to structural degradation and the valorization of EFBA waste as a catalyst support.

This study addresses these gaps by developing EFBA-supported TiO_2 and ZnO catalysts for the photocatalytic esterification of WCO. This work aims to (i) enhance charge separation efficiency, (ii) optimize key reaction parameters using the OVAT methodology, and (iii) validate mechanistic pathways through radical scavenger analysis. This approach supports circular economy principles by valorizing waste into

functional catalysts and establishes a sustainable pathway for high-FFA biodiesel production under low-energy conditions.

CHAPTER 3
METHODOLOGY

3.1 Introduction

This chapter details the experimental procedures, materials, and analytical methods employed to achieve the research objectives outlined in Chapter 1. The study was implemented in multiple stages, beginning with the synthesis of TiO_2/EFBA and ZnO/EFBA photocatalysts via wet impregnation. These composites were evaluated for their efficiency in the photocatalytic esterification of waste cooking (WCO) with high free fatty acid (FFA) content under light irradiation.

To assess catalyst performance, a one-variable-at-a-time (OVAT) approach was used to optimize reaction parameters including methanol-to-oil molar ratio, catalyst loading, irradiation time, calcination temperature, and mass ratios. The reaction's efficiency was quantified using titrimetric acid value tests before and after esterification. Catalyst stability and reusability were evaluated across multiple cycles, while mechanistic insights were obtained via scavenger trapping experiments targeting photogenerated species hydroxyl radical (•OH), superoxide radical ($\bullet O_2^-$), photogenerated hole (h^+), and photogenerated electron (e^-).

Subsequently, the esterified WCO underwent transesterification to convert triglycerides into fatty acid methyl ester (FAME). Biodiesel properties were characterized using gas chromatography mass spectra (GC–MS) analysis. Also, it was tested using ASTM D6751 standards.

An overview of the experimental workflow, including catalyst synthesis, characterization, reaction-based screening, and performance evaluation, is presented in Figure 3.1.

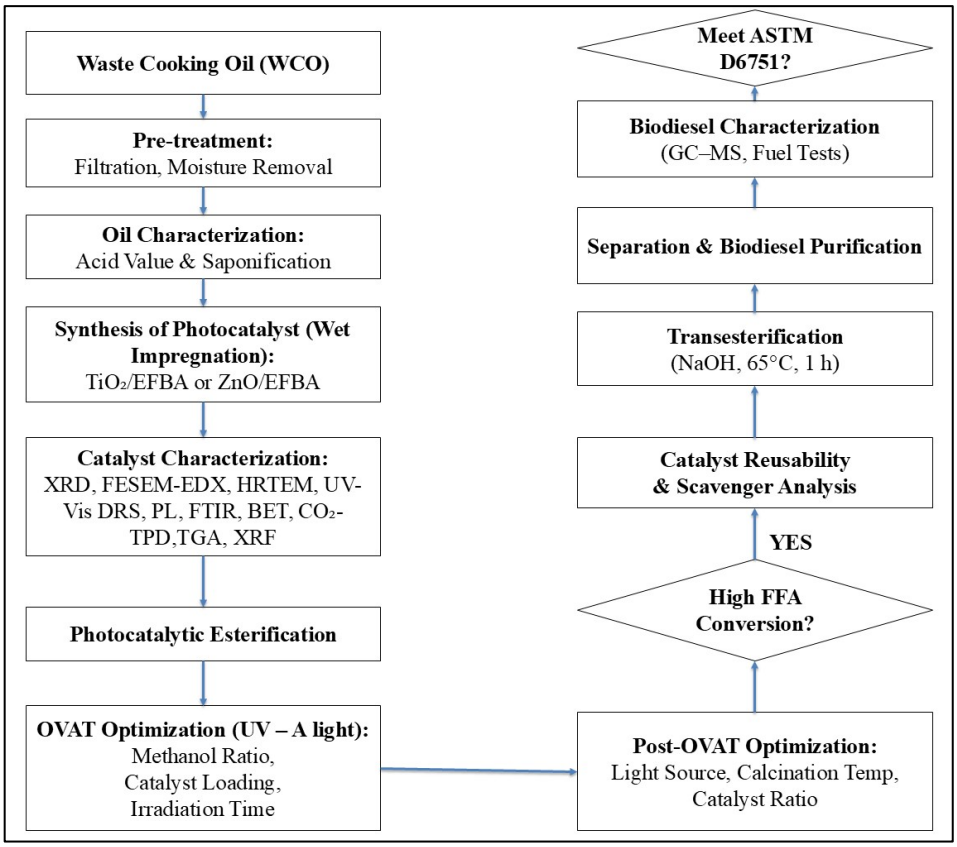


Figure 3.1 Flowchart Illustrating the Biodiesel Production Workflow, Including Pretreatment via Photocatalytic Esterification and Subsequent Alkaline Transesterification

3.2 Apparatus

The apparatus utilized in this study were categorized based on the experimental stages.

Stage 1 (photo-esterification); the basic apparatus included a closed wooden box reactor. The basic apparatus included 250 mL Duran glass bottles with caps, a magnetic stirrer, a thermometer, and a hotplate stirrer. Illumination was provided by an ultraviolet (UV) lamp (6 W, 254/365 nm), an LED lamp (12 W), and a xenon lamp (260 nm wavelength). The reaction temperature was maintained at 35 °C.

Stage 2 (trans-esterification): The transesterification stage employed standard apparatus based conventional reflux method. This included a two-neck round-bottom flask with a water-cooled reflux condenser to condense methanol vapor, and an oil bath to maintain a consistent temperature of 65 °C. For the washing step, equipment such as

a 500 mL separating funnel, filter funnel, dropper, and spatula was used to purify the product.

Additional equipment comprised sample bottles, a 50 mL burette, beakers (25, 50, and 100 mL), 250 mL conical flasks, and measuring cylinders (5, 10, and 50 mL), which support the titrimetric analysis and biodiesel handling. A drying oven was used to eliminate moisture prior to testing, while an air furnace was employed to calcine the prepared catalyst.

3.3 Chemicals

Titanium dioxide (TiO_2) with Degussa P25 (15% anatase and 85% rutile) and zinc oxide (ZnO) powders were procured from BT Science Sdn. Bhd., Selangor, Malaysia. Analytical grade reagent, including n-hexane, methanol, phenolphthalein (≥99% purity), and hydrochloric acid (HCl, ≥32% purity), were supplied by QReC (Asia) Sdn. Bhd. Methyl heptadecanoate, sodium hydroxide (NaOH), and potassium hydroxide (KOH) were obtained from Sigma-Aldrich (M) Sdn. Bhd. Scavenger agents used in mechanistic studies, ethylenediaminetetraacetic acid (EDTA), p-benzoquinone (p-BQ), isopropanol (IPA), and silver nitrate ($AgNO_3$), were acquired from BT Science Sdn. Bhd. All chemicals were used as received without further purification. Empty fruit bunch ash (EFBA), used as photocatalyst support material, was sourced from FTJ Bio Power Sdn. Bhd., while the feedstock waste cooking oil (WCO) was collected from a local restaurant in Bandar Jengka Pusat, Pahang.

3.4 Pre-treatment of WCO

Pre-treatment of WCO was conducted to ensure its suitability for photocatalytic esterification. The process included filtration, moisture removal, and physicochemical characterization via saponification and acid value tests. WCO was filtered to remove suspended solids and contaminants. The filtered WCO was heated to eliminate residual water, and moisture content was quantified as per AOCS Aa 3-38. Saponification and acid value tests were performed to determine molecular weight and FFA content, critical for calculating the methanol-to-oil molar ratio and evaluating FFA conversion efficiency.

3.4.1 Saponification Test

The saponification value (SV) indicates the milligrams of potassium hydroxide (KOH) required to saponify 1 g of oil and indirectly estimates triglyceride molecular weight. High FFA content can induce soap formation during transesterification, adversely affecting biodiesel yield and product separation.

Following ASTM D5558 (Chukwu et al., 2025), 2.000 ± 0.001 g of WCO was dissolved in 25 mL of 0.5 M isopropanol-KOH in a 100 mL conical flask. After complete dissolution, 5–7 drops of phenolphthalein were added. The sample was titrated with 0.5 M aqueous HCl until a pink-to-colourless endpoint was reached. A blank test was run in parallel without WCO.

The saponification value (SV) (mgKOH g^{-1}) of the sample was calculated using equations 3.1.

$$SV = \big((\mathrm{B} - \mathrm{S}) \times M \times 56.11\big)/W \tag{3.1}$$

Where, B is the volume of 0.5 M HCl solution required for titration of the blank (mL), S is the volume of 0.5 M HCl solution required for titration of sample (mL), M is the molarity of isopropanol-KOH, 56.11 is the molecular weight of KOH and W is the weight of the sample (g).

Using the saponification value, the molecular weight of the triglycerides (MW) was calculated as follows:

$$MW = (56.11 \times 3 \times 1000)/(SV) \tag{3.2}$$

3.4.2 Acid Value Test

The acid value (AV) quantifies the amount of KOH (mg) needed to neutralize FFAs in 1 g of oil. It aids in selecting suitable catalytic systems and operating conditions.

Based on AOCS Cd 3d-63 (AOCS-CD-3d - 63, 2009), 0.200 g of WCO was titrated with 0.1 M isopropanol-KOH after dissolution in 10 mL of toluene:isopropanol

(1:1) and addition of phenolphthalein. The endpoint was marked by a stable red coloration (Figure 3.2).

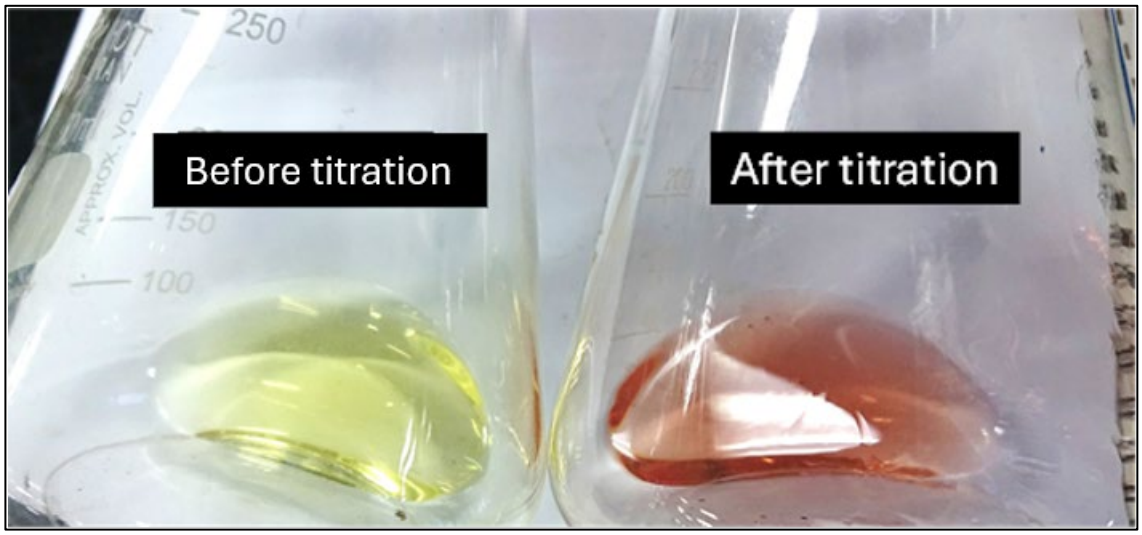


Figure 3.2 Visual Comparison of the Test Sample Before (Yellowish) and After (Orange-Red) the Acid Value Titration

The acid value (AV) was calculated using equation 3.3:

$$AV = (V \times M \times 56.11)/m \tag{3.3}$$

Where, AV is the acid value of the sample (mg KOH/g), V is the volume of isopropanol-KOH solution consumed to reach the endpoint (mL), M is the molarity of the KOH standard solution (0.1 M), 56.11 is the molecular weight of KOH (g/mol), m is the weight of the test sample (g).

The free fatty acid conversion (FFAs conversion %) was calculated to assess the photo-esterification reaction efficiency between FFAs and methanol. This conversion rate was determined based on the change in acid value before and after esterification, as per equation 3.4:

$$FFA\ conversion\ \% = (A_a - A_b)/A_a \times 100 \tag{3.4}$$

where Aa is the acid value of the WCO before esterification and Ab is the acid value of the WCO after esterification.

3.4.3 Moisture Content Test

To prevent catalyst deactivation, microbial growth, and incomplete transesterification, moisture content in WCO was reduced and measured.

Following AOCS Aa 3-38, filtered WCO was dried at 105 °C for 5 hours until a constant weight was achieved (triplicate trials). Initial and final weights were recorded to calculate moisture loss.

$$\text{Moisture content} = ((W_2 - W_3)/(W_2 - W_1)) \times 100 \quad (3.5)$$

Where:

W_1 = weight of the empty beaker

W_2 = weight of the beaker with sample before drying

W_3 = weight of the beaker with sample after drying

The difference between the initial and final weights of the WCO was used to determine the percentage of moisture content, ensuring compliance with the required standards.

3.5 Preparation Photocatalyst

Composites were synthesized via the wet impregnation method, following procedures adapted and supported by literature methods (Irshad et al., 2024; Yanti et al., 2023). EFBA was first washed thoroughly to remove residual contaminants, then filtered and oven-dried at 105 °C for 12 h. The dried ash was sieved using a 100-mesh screen to ensure uniform particle size and improved porosity and compatibility with metal oxide anchoring.

For TiO_2/EFBA composite synthesis: 1 g of EFBA was dispersed in 50 mL of distilled water in a 250 mL beaker and stirred at 350 rpm for 1 h at room temperature. Simultaneously, 1 g of TiO_2 (Degussa P25) was dissolved in 50 mL of distilled water under identical conditions. After 1 h, both suspensions were mixed and stirred for an additional 1 h at 350 rpm. The resulting slurry was filtered, washed with distilled water, and dried at 105 °C for 8 h. This procedure was repeated using TiO_2 to EFBA mass

ratios of 1:1, 1:2, 1:3, 2:1, and 3:1 to assess the effect of catalyst loading. Dried composites were calcined at 100 °C, 300 °C, and 500 °C for 3 h in a tubular furnace with a controlled heating rate of 5 °C/min.

ZnO/EFBA composites were prepared using the same protocol, substituting TiO_2 with ZnO. This systematic variation of mass ratios and calcination temperatures enabled evaluation of morphological changes and photocatalytic activity under different synthesis conditions, addressing optimization objectives outlined in Section 1.3.

To streamline discussion in subsequent chapters, each catalyst formulation was assigned a unique sample code, as summarized in Table 3.1. Codes T11–T31 correspond to TiO_2 : EFBA, while Z11–Z31 represent ZnO :EFBA.

Table 3.1
Sample Codes and Compositions of EFBA-Doped TiO_2 and ZnO Catalysts Prepared at Varying Metal-to-EFBA Mass Ratios

Sample Code	Metal oxide	Mass Ratio (Metal:EFBA)	Full Composition
T11	TiO_2	1:1	TiO_2/EFBA (1:1)
T12	TiO_2	1:2	TiO_2/EFBA (1:2)
T13	TiO_2	1:3	TiO_2/EFBA (1:3)
T21	TiO_2	2:1	TiO_2/EFBA (2:1)
T31	TiO_2	3:1	TiO_2/EFBA (3:1)
Z11	ZnO	1:1	ZnO/EFBA (1:1)
Z12	ZnO	1:2	ZnO/EFBA (1:2)
Z13	ZnO	1:3	ZnO/EFBA (1:3)
Z21	ZnO	2:1	ZnO/EFBA (2:1)
Z31	ZnO	3:1	ZnO/EFBA (3:1)

3.6 Characterization of Photocatalyst

The physicochemical characteristics of TiO_2/EFBA and ZnO/EFBA photocatalysts were evaluated to assess their structural integrity, morphological properties, elemental composition, and optical performance relevant to photo-esterification.

3.6.1 Powder X-Ray Diffraction (XRD)

A powder X-ray diffractometer (LabX XRD-6000, PANalytical, Shimadzu) was utilized to analyse the structural properties of the synthesized catalyst. XRD analysis

provided critical information on the crystallinity, phase composition, and crystal orientation of the material. Before analysis, the sample was finely ground to a powder like-talcum. The powdered sample was then evenly mounted on a quartz disc with a flat surface. The analysis employed Cu-Kα radiation (λ = 0.154 nm) at operating conditions of 30 kV and 15 mA. Scans were conducted over a 2θ range of 20°–80° with a scanning rate of 2° min^{-1}. The angle θ represents the angle between the incident X-ray beam and the diffracted beam. The resulting diffractograms were compared against reference patterns in the Joint Committee on Powder Diffraction Standards (JCPDS) database to identify the phases present based on their diffraction lines and intensities. Additionally, the average crystalline size of the photocatalysts was calculated using the Debye-Scherrer equation:

$$D = (k\lambda/\beta cos\theta) \tag{3.6}$$

Where, D represent mean crystalline size (nm), k is shape factor or Scherrer constant (0.9), λ is the x-ray wavelength (0.154 nm), β is the full width at half maximum (FWHM) of the diffraction peak and θ is Bragg's angle.

3.6.2 Field Emission Scanning Electron Microscopy (FESEM)

FESEM was employed to examine the surface morphology and structural features of the photocatalyst. The analysis was conducted using a JEOL JSM-7600F microscope operating at an accelerating voltage of 20 kV. The sample was prepared by grinding it into a fine powder to facilitate imaging. A double-sided carbon tape was affixed to the surface of a stub holder, and the powdered sample was mounted on conductive carbon tape. The sample was sputter-coated with a thin layer of gold for 3 minutes using a sputter coater. High-resolution images were obtained from signals generated by electron-sample interactions. The images were captured at various magnifications (3000, 5000, 50 000, and 100 000) to analyse the different structural features of the photocatalyst.

3.6.3 Energy-Dispersive X-ray (EDX)

EDX was performed alongside FESEM analysis to determine the elemental composition of the sample and confirm its purity. The analysis was conducted using an Oxford Instrument, X-MaxN.

3.6.4 High-Resolution Transmission Electron Microscopy (HRTEM)

HRTEM provides detailed visualization of features such as atomic arrangements and lattice spacing. The analysis was conducted using a JEOL JEM 2100-F microscope, operated at an accelerating voltage ranging from 80 kV to 200 kV. Sample preparation involved grinding the material to achieve a thickness of less than 100 nm, ensuring electron transparency. Ion milling was used to refine the sample further, protecting it from damage while preserving its microstructure. The prepared sample was then placed onto a thin TEM grid made of copper or gold, coated with a conductive carbon layer. The sample was dried in a vacuum oven to remove moisture before analysis. During the HRTEM examination, the setup was maintained under high vacuum to minimize electron scattering by air molecules. The sample was accurately positioned within the electron beam to achieve optimal high-resolution imaging.

3.6.5 Ultraviolet-Visible Diffuse Reflectance Spectroscopy (UV-Vis-DRS)

The UV-Vis-DRS measurement technique was employed to evaluate the optical properties and photoactivity of the synthesized photocatalysts. In this study, the Cary 5000 spectrophotometer, equipped with a PbSmart detector and covering a wavelength range of 175–3300 nm, was used. The instrument was operated with Cary WinUV software, which facilitated the integration of spectral data and diffuse reflectance measurements using an integrating sphere. Advanced optical detectors in the Cary 5000 ensured high-resolution and accurate measurements. For analysis, the sample was ground into a fine powder, placed in the sample holder, and inserted into the spectrometer. The wavelength range was set from 175 nm to 3300 nm, and transmittance data were recorded across this range. Using the transmittance data, the bandgap energy of the material was determined through the Tauc plot method.

The optical band gap energy (E_g) of the photocatalysts was estimated using the Tauc plot method, which relates the absorption coefficient (α) to the photon energy (hv) according to the following equation:

$$(ahv)^x = A\,(hv - E_g) \tag{3.7}$$

Where α is the absorption coefficient (cm^{-1}), h is Plank's constant (6.626×10^{-34} J.s), v is the frequency of incident light, hv is the photon energy (eV), A is the proportionality constant, $E_g$is the optical bandgap energy (eV), and x is a parameter depending on the electronic transition type ($x = 1/2$ is for direct allowed transition and $x = 2$ is for indirect allowed transition). The photon energy was calculated from the wavelength (λ, in nm) using:

$$E = hc/\lambda \;=\; 1240/\lambda \tag{3.8}$$

Where, c is speed of light (3.00×10^8 m s), and the result is expressed in electron volts (eV).

For powdered samples analysed via diffuse reflectance spectroscopy (DRS), the absorption coefficient was estimated using a modified Kubelka–Munk function:

$$F(R) = \;(1 - R)^2/2R \tag{3.9}$$

Where R is the reflectance (in decimal form). The function $F(R)$ is proportional to a and is commonly substituted into the Tauc equation for solid-state materials:

$$[F(R) \times hv]^x = \;A'\,(hv - E_g) \tag{3.10}$$

A plot of $[F(R) \times hv]^x$ versus hv was constructed, and the band gap energy (E_g) was determined by extrapolating the linear portion of the curve to the x-axis. The

x-intercept, where $[F(R) \times hv]^x = 0$, correspond to the bandgap energy of the photocatalyst.

3.6.6 Photoluminescence Spectroscopy (PL)

PL spectroscopy is a vital technique for characterizing semiconductors and nanomaterials, offering insights into their electronic and optical properties by analysing the light emitted after excitation. For this study, a Perkin-Elmer LS-55 Fluorescence Spectrometer was used, covering a wavelength range of 200 nm to 900 nm. Approximately 1 g of the sample was placed in the spectrometer's measurement chamber. The excitation source was activated to illuminate the sample at predetermined wavelengths. The emitted light was collected and passed through a monochromator, which separated the wavelengths before reaching the detector. The intensity of the emitted light at various wavelengths was recorded to generate the PL spectrum.

3.6.7 Fourier Transform Infrared spectroscopy (FTIR)

FTIR spectroscopy was employed to analyse the molecular structure, and functional groups present in the samples. In this study, FTIR analysis was performed using the FT-IR Spectrum 100 instrument (Perkin Elmer) equipped with an Attenuated Total Reflectance (ATR) accessory. The ATR technique requires minimal sample preparation. A small amount of the sample was directly placed onto the ATR crystal using a spatula. Data was collected over a wavelength range of 4000 to 400 cm^{-1}. The absorption peaks observed in the spectra correspond to specific molecular vibrations, providing both qualitative and quantitative insights into the sample composition

3.6.8 Brunauer-Emmet-Teller (BET)

The BET method was used to characterize the surface area and porosity of the materials. In this study, BET surface area measurements were performed using the Micromeritics ASAP 2010 analyser. High-purity nitrogen gas was utilized during the adsorption process, and the temperature was maintained at 77 K. Before adsorption, the sample was dried to remove moisture and contaminants. Approximately 0.5 g of the

catalyst was degassed for 12 hours at 150 °C to ensure the removal of any residual gases or impurities. The dried sample was then placed into the sample holder of the BET analyser. Nitrogen gas was introduced into the sample tube to facilitate the adsorption-desorption isotherm at liquid nitrogen temperature (-196 °C ~77 K). The pore diameter distribution was determined using the Barrett–Joyner–Halenda (BJH) technique from the desorption loop, while the surface area was calculated using the BET equation.

3.6.9 Temperature Programmed Desorption of Carbon Dioxide (CO_2-TPD)

The CO_2-TPD technique was employed to investigate the surface properties of the photocatalyst. In this study, a Thermo Finnigan TPDRO 1100 Series instrument was used to analyse the basicity distribution of the samples. Before analysis, the samples were prepared by drying to remove moisture and impurities. Approximately 0.05 g ± 0.01 g of the sample was placed into a quartz reactor tube, secured with quartz wool, and positioned within the TPD reactor chamber.

The sample underwent a pre-treatment process in which nitrogen gas (N_2) was passed through the sample at a flow rate of 20 mL·min^{-1} while the temperature was ramped from 50 °C to 150 °C and maintained for 1 hour. This step effectively eliminated moisture, unwanted substances, and residual gases from the sample and the reactor chamber. After cooling the sample to room temperature, high-purity CO_2 gas (99.999%) was introduced into the chamber for 30 minutes to allow adsorption onto the sample surface. Following the adsorption phase, the sample was purged with helium (He) as the carrier gas at a flow rate of 20 mL·min^{-1}. The temperature was then gradually increased from 50 °C to 950 °C, inducing CO_2 desorption from the sample. The desorbed CO_2 was monitored using a Thermal Conductivity Detector (TCD), which recorded the desorption signal as a function of temperature.

The desorption profile, represented as a plot of TCD signal versus temperature, provided quantitative information on the surface properties. The area under the desorption peaks was integrated to determine the amount of CO_2 adsorbed on the material, revealing the density of active sites and the strength of interactions between CO_2 and the sample surface.

3.6.10 Thermogravimetric Analysis (TGA)

The TGA is a thermal analysis technique used to measure changes in the mass of a sample as it is heated or cooled under controlled conditions. This method was employed to assess the thermal stability, composition, and decomposition behaviour of materials. In this study, the thermal stability and decomposition characteristics of the catalyst were analysed using a TGA-Pyris 2012 equipped with a GSA7-Perkin Elmer analyser. The sample preparation involved drying to eliminate moisture and volatile impurities, followed by weighing 10–50 mg of the catalyst. The prepared sample was placed in a platinum crucible and loaded into the TGA instrument.

The analysis was conducted by heating the sample from 50 °C to 950 °C at a constant rate of 10 °C·min^{-1} under an inert environment to prevent oxidation during the measurement. The TGA analyser, equipped with a highly sensitive balance, recorded the weight changes throughout the heating process. The resulting data, plotted as weight loss versus temperature, provided insights into the decomposition temperatures, mass loss, and thermal stability of the materials.

3.6.11 X-ray Fluorescence (XRF)

Wavelength Dispersive X-ray Fluorescence (WD-XRF) analysis is used to determine the elemental composition of materials. In this study, WD-XRF analysis was conducted using a Rigaku ZSX Primus II system, operating at a voltage of 50 kV and a current of 600 mA. Approximately 1 g of the prepared powder photocatalyst sample was placed in the path of the X-ray beam generated by an X-ray tube. The beam interacted with the sample, ejecting inner-shell electrons, and inducing the emission of characteristic fluorescent X-rays. These emitted X-rays were collected by a detector, which sorted them based on their energies. The data was processed to generate an XRF spectrum, displaying peaks corresponding to the different elements present in the sample.

3.7 Photocatalytic Esterification of WCO

Photocatalytic esterification was employed to evaluate the performance of TiO_2/EFBA and ZnO/EFBA catalysts in reducing the free fatty acid (FFA) content of

waste cooking oil (WCO), following the method described by (Dellisanti et al., 2024; Deng et al., 2021). The photo-esterification experiments were conducted in a closed-box reactor equipped with a 6 W UV lamp (λ = 365 nm) as the light source (Figure 3.3) A control experiment without light irradiation was also performed for comparison.

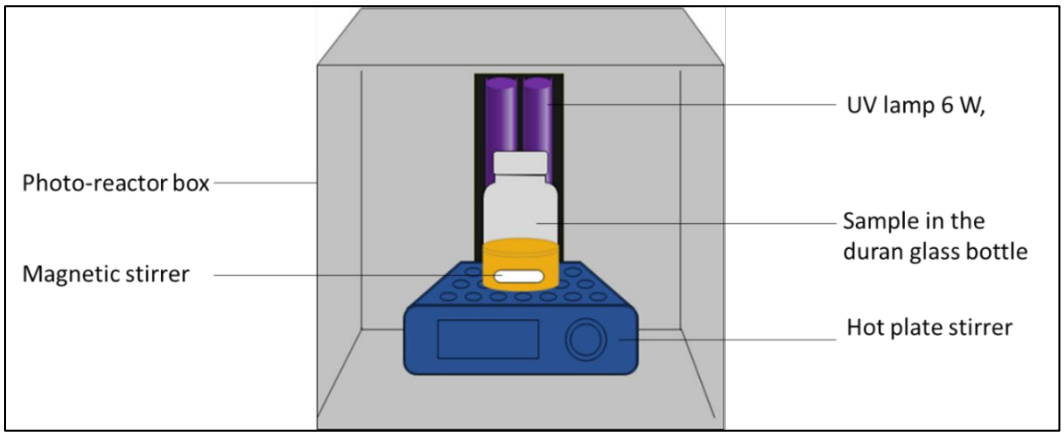


Figure 3.3 Illustration Diagram of Photo-Esterification in Photo-Reactor Box

The reaction mixture consisted of 10 g of WCO and methanol, with the addition of the photocatalyst. The mixture was continuously stirred at 350 rpm to ensure uniform light exposure and catalyst dispersion. After the photo-esterification process, the reaction mixture was centrifuged at 4500 rpm for 15 minutes to separate the components. The lower layer, containing unreacted triglycerides and insoluble catalysts, was further processed via transesterification, while the upper layer, containing unreacted methanol and water produced during the reaction, was separated. Catalysts were recovered by filtration and subsequently dried to remove excess methanol. The resulting esterified WCO was then subjected to transesterification.

The acid value was determined using a titration method (performed in triplicates) to calculate the FFA content and FFA conversion, based on (equation 3.4).

The One-Variable-At-a-Time (OVAT) approach was used to evaluate the effect of individual parameters on FFA reduction. A post-OVAT screening was then performed to refine catalyst synthesis and operational conditions. Table 3.2 summarizes the OVAT and post-OVAT experimental parameters:

Table 3.2
Summaries the OVAT and Post OVAT Experimental Parameters

Parameter Type	Parameter	Level tested
OVAT	methanol-to-WCO molar ratio	12:1, 16:1, 20:1, and 24:1
	catalyst loading (wt%)	1, 2, 3, 4, 5
	UV–A irradiation time (h)	1, 2, 3, 4, and 5
Post-OVAT	Light source	UV 254 nm, UV 365 nm, visible light (LED 12 W), and xenon lamp
	Calcination temperature (°C)	100, 300, 500
	Mass ratio of TiO_2/ZnO to EFBA (g)	1:1, 1:2, 1:3, 2:1, 3:1.

3.8 Reusability Test of Esterified WCO

The reusability test was conducted to evaluate the stability and effectiveness of the photocatalyst over multiple cycles of photo-esterification. In the first cycle, the biodiesel product was separated from the photocatalyst via centrifugation at 4500 rpm for 15 minutes. The biodiesel product was collected, dried in an oven, and analysed to determine its FFA percentage using the acid value test method. The spent photocatalyst was recovered and cleaned to remove residual organic materials adhering to its surface.

This cleaning process involved washing the photocatalyst with hexane using the following steps, 10 mL hexane was added to a centrifuge tube containing the spent photocatalyst. Then, the mixture was shaken briefly and centrifuged at 3000 rpm for 5 minutes. The washing process was repeated several times, replacing the hexane solution after each wash, until the catalyst surface was free from residual oil and organic impurities. After the final wash, the recovered photocatalyst was dried in an oven at 70 °C for 15 minutes. The cleaned photocatalyst was then reused in subsequent photo-esterification reactions under identical reaction conditions to maintain consistent reaction conditions across all reuse cycles. This cyclic process was repeated to investigate the long-term stability and effectiveness of the photocatalyst in the photo-esterification reaction.

3.9 Scavenger Analysis

The scavenger test is to identify the reactive species involved in the reaction. In this study, 2 mL of 0.1 M scavenger solution was added to the reaction mixture to selectively trap reactive species produced during the photocatalytic process. Four types

of scavengers were utilized: isopropanol (IPA) to capture hydroxyl radicals (•OH), benzoquinone (p-BQ) to trap superoxide radicals ($\bullet O_2^-$), ethylenediaminetetraacetic acid (EDTA) to sequester photogenerated holes (h^+), and silver nitrate ($NaNO_3$) to capture photogenerated electrons (e^-).

3.10 Transesterification of Esterified WCO

In this study, the esterified WCO, with a high FFA conversion, was then subjected to transesterification using fixed parameters derived from (Hsiao et al., 2021). The transesterification process was carried out using 5 g esterified WCO, 1 wt% NaOH as a catalyst, a reaction temperature of 65 °C, a reaction time of 1 h, and a methanol-to-oil molar ratio of 12:1 while stirring at 350 rpm. The reaction was performed using a conventional reflux method in a 100 mL two-neck round-bottom flask equipped with a water-cooled condenser. The reaction temperature was monitored and controlled using a thermometer inserted into one of the flask's necks.

After the reaction was completed, the mixture was allowed to settle in a separating funnel for 1 h and complete separation could take up to 24 h. The biodiesel (upper layer) was separated from the glycerol and unreacted materials (lower layer). The biodiesel was washed with warm water (>80 °C) to remove residual catalyst and impurities. The washing process was repeated until the wash water appeared clear, indicating the removal of unreacted materials. Washed biodiesel was oven-dried at 60 °C for 30 minutes to eliminate excess methanol. Anhydrous sodium sulphate (Na_2SO_4) was added to the biodiesel to remove any residual water. Finally, the biodiesel was weighed, and its mass was recorded for yield calculation. The final biodiesel product was analysed using GC-MS to confirm its composition and quality.

3.11 Gas Chromatography-Mass Spectrometry (GC-MS) analysis

GC-MS analysis was employed to identify and quantify the chemical composition of WCO biodiesel during the biodiesel production process. For this study, an Agilent Technologies GC system (7890B) equipped with a mass spectrometer (MSD 5977A) was utilized. A non-polar capillary GC column (Zebron ZB-FAME phase) was used, with the following specifications: length (L) of 60 m, inner diameter (ID) of 0.25 mm, and film thickness (FT) of 0.20 μm. The sample preparation involved dissolving

0.125 g of WCO biodiesel in 10 mL of GC-grade n-hexane (purity > 99%) and adding 2.5 mL of a 10 mg/mL internal standard solution (methyl heptadecanoate). Methyl heptadecanoate was selected due to its structural similarity to long-chain FAMEs, ensuring accurate integration and normalization across chromatographic peaks.

A 1 µL aliquot of the prepared sample was injected into the GC injection port in splitless mode. Helium was used as the carrier gas at a flow rate of 0.9 mL/min. The GC oven was programmed in three stages: initial temperature of 40 °C, held for 1 min, gradual increase to 80 °C, held for 2 min and further increase to 250 °C, held for 2 minutes, with a temperature ramp rate of 5 °C/min, respectively. The injector temperature was set to 80 °C, and the interface temperature was maintained at 260 °C. The identification of components was confirmed by comparing their mass spectra with the National Institute of Standards and Technology (NIST) database. The resulting chromatographic peaks corresponded to the FAMEs present in the biodiesel. The peak areas were integrated to determine the concentration of each ester. The percentage compositions of FAMEs were calculated based on the peak area relative to the total area under the curve, using the international standard EN 14103 and equations (3.11) to (3.13), adapted from Lokman Nolhakim et al. (2021) as detailed below:

The ester content of FAMEs was determined using equation (3.11):

$$Ester\ content, c = ((A_T - A_{IS})/A_{IS}) \times ((C_{IS} \times V_{IS})/m \times 100 \qquad (3.11)$$

Where A_T is total area of methyl ester from GC-MS analysis, A_{IS} is the area of internal standard from GC-MS analysis, C_{IS} is the concentration of internal standard (10 mg/mL), V_{IS} is the volume of internal standard (2.5 mL) and m is the mass of sample that mixed with internal standard (125 mg).

The mass of pure biodiesel was calculated using equation (3.12):

$$Y\ (g) = (c/100) \times d \qquad (3.12)$$

Where Y is the mass of pure biodiesel (g), c is the ester content calculated using equation (3.11) and d is mass of biodiesel after transesterification, washing and purification.

The FAME yield of biodiesel was determined using equation (3.13)

$$\text{FAME yield (\%)} = (\text{Y}/\text{mass feedstock oil}) \times 100 \quad (3.13)$$

Where Y is calculated using equation (3.12) and mass of feedstock oil is initial mass of esterified WCO used in transesterification (5 g).

3.12 Fuel Test Analysis of WCO-Biodiesel

3.12.1 Density of Fuel

The density of WCO biodiesel was measured at 30 °C in accordance with the ASTM D4052-11 standard, which specifies an acceptable density range of 870–900 kg/m³ for biodiesel. The analysis was conducted using a U-shaped oscillating tube density meter. In this method, the biodiesel sample was introduced into the oscillating tube of the density meter, where the tube's oscillation frequency was measured. The frequency was directly correlated to the density of the sample, allowing the instrument to calculate the density with high precision. This technique is suitable for samples with a total vapor pressure below 100 kPa and viscosities not exceeding 15,000 mm²/s at the test temperature.

3.12.2 Heat of Combustion

In this study, the heat combustion properties of WCO biodiesel were evaluated in accordance with ASTM D240-02, utilizing a bomb calorimeter to determine the energy content of the fuel. The bomb calorimeter operates by combusting the sample in an oxygen-rich environment, equipped with a temperature sensor to monitor temperature variations during the combustion process. The biodiesel sample was placed inside the combustion bomb, and oxygen was introduced to ensure complete

combustion. The bomb was then immersed in a water bath maintained at a controlled temperature. The sample was ignited electrically, initiating combustion, which subsequently increased the temperature of the surrounding water. Temperature changes were recorded before, during, and after combustion. The heat release was calculated based on these temperature variations and compared against a standard reference material, benzoic acid.

3.12.3 Kinematic Viscosity

Kinematic viscosity (v) is defined as the ratio of dynamic viscosity (η) to the density (ρ) of a liquid. In this study, the kinematic viscosity of WCO biodiesel was determined in accordance with ASTM D445-06 to evaluate the fuel's flow properties and behaviour under engine operating conditions. A capillary viscometer, calibrated for the desired kinematic viscosity range, was utilized for the analysis. The viscometer was equipped with a thermostatic bath to maintain a constant temperature of 50 °C, a timer to measure the flow time of the liquid, and a thermometer to monitor the sample temperature. The viscometer was immersed in the thermostatic bath and allowed sufficient time to reach thermal equilibrium at 50 °C. The biodiesel sample was then carefully introduced into the viscometer, ensuring no air bubbles were trapped inside. The flow time (t) was determined by allowing the sample to flow through the capillary under gravity and recording the time it took for a specific volume of liquid to pass between two marked points on the viscometer using a stopwatch. The kinematic viscosity (v) was calculated using the following equation:

$$v = K \times t \tag{3.14}$$

Where v is the kinematic viscosity, K is the capillary constant specific to the viscometer, and t is the average flow time in seconds.

3.12.4 Cloud Point

The cloud point test is essential for assessing the lowest temperature at which wax crystals begin to form in biodiesel, potentially leading to fuel flow issues. In this

study, the cloud point of WCO biodiesel was determined following the ASTM D2500-05 standard, which evaluates biodiesel performance under low-temperature conditions. This is particularly important for assessing fuel usability in cold climates, as biodiesel tends to gel at lower temperatures. The test was conducted using a cooling bath, a test jar, and a thermometer. Prior to testing, the biodiesel sample was filtered to remove impurities, ensuring accurate results. The sample was then heated above its expected cloud point before being gradually cooled at a controlled rate of 1 °C per minute. Periodic visual inspections were carried out at 3 °C intervals to detect the initial formation of cloudiness. The temperature at which the first visible signs of cloud formation appeared at the bottom of the test jar was recorded as the cloud point.

3.12.5 Sulphur Content

The sulphur content in WCO biodiesel was determined using the ASTM D5185-05 standard, which employs Inductively Coupled Plasma Optical Emission Spectroscopy (ICP-OES) for the precise detection and quantification of sulphur in liquid biodiesel samples. For the analysis, 1 g of WCO biodiesel was subjected to acid digestion using a mixture of nitric acid and hydrochloric acid in a digestion vessel to convert sulphur into a soluble form. Upon completion of digestion, the solution was diluted to 50 mL using deionized water. A calibration standard of known sulphur concentrations was prepared and analysed using ICP-OES to establish a calibration curve. The biodiesel sample was then injected into the ICP-OES system, where the intensity of emitted light at a wavelength of 181.975 nm, corresponding to sulphur's characteristic emission line under ICP-OES detection, was measured.

3.12.6 Flash Point

The flash point of the biodiesel product was determined in accordance with ASTM D93-08 using the Pensky-Martens Closed Cup (PMCC) Tester. This method is widely employed to assess the flammability and safe handling of biodiesel, ensuring compliance with safety standards for storage and transportation. The flash point of biodiesel typically ranges from 60 °C to 190 °C, and in this study, an automated PMCC tester equipped with electronic flash point detection was utilized. During the test, the

biodiesel sample was heated at a controlled rate while being continuously stirred at 90–120 rpm. When the temperature reached 24 °C below the anticipated flash point, an ignition source was introduced. Heating and testing proceeded in increments of 2 °C until a visible flash was observed. The flash point was recorded as the lowest temperature at which the vapor-air mixture above the sample momentarily ignited.

3.12.7 Pour Point

The pour point test was conducted to determine the lowest temperature at which biodiesel remains fluid and capable of flowing, a critical parameter for its performance in cold weather conditions. This study utilized ASTM D97-08 as the standard testing method for WCO biodiesel. Typically, the pour point of biodiesel ranges between -15 °C and 10 °C. The test was performed using a test jar, a cooling bath, and a calibrated thermometer. The clean WCO biodiesel sample was first heated to 105 °C to ensure the complete melting of any waxes or solidified components. After heating, the sample was cooled at a controlled rate of 3 °C per hour. At 3 °C intervals, the test jar was tilted to observe any movement in the sample. This process continued until no fluid movement was detected when the jar was held horizontally for 5 seconds. The temperature at which the sample ceased to flow was recorded as the pour point.

CHAPTER 4
RESULTS AND DISCUSSION

4.1 Analytical Results of WCO Pre-treatment and Composition

Chapter 4 presents the experimental findings on the photocatalytic esterification of high free fatty acid (FFA) waste cooking oil (WCO) using TiO_2/EFBA and ZnO/EFBA catalysts. The chapter begins with comprehensive physicochemical characterization of the synthesized catalysts, followed by systematic optimization of key reaction parameters using a one-variable-at-a-time (OVAT) approach. Mechanistic insights are elucidated through targeted scavenger studies to identify reactive oxygen species (ROS) involved in the esterification process. Photocatalytic performance is assessed primarily based on FFA conversion efficiency, with optimization focused on reaction time, methanol-to-WCO molar ratio, and catalyst dosage. Reusability and structural stability are evaluated across multiple cycles, offering critical insights into the system's effectiveness and long-term viability.

The physicochemical characteristics and fatty acid profile of the WCO used in this study are summarized in Table 4.1. These properties were determined through the ASTM D5558 and AOCS-3d-63 method. The acid value was 24.8 mg KOH g^{-1}, corresponding to an FFA content of 12.4 wt%. The saponification value was 184 mg KOH g^{-1}, resulting in an estimated molecular weight of 915 g mol^{-1}, which was used to calculate the required methanol-to-oil molar ratio.

GC–MS analysis identified oleic acid (C18:1, 27.36%), palmitic acid (C16:0, 21.38%), and stearic acid (C18:0, 2.70%) as the dominant components, consistent with typical vegetable-oil-based WCOs. The relatively low percentage of each fatty acid suggests that GC–MS detected minor fatty acids and that some signals may have been lost due to noise or compounds not included in the analysis. Additionally, since WCO is a complex mixture of various molecules, the intensities of major peaks may be reduced during GC–MS analysis. Nevertheless, the observed composition indicates that this WCO is suitable for biodiesel production, offering favorable oxidative stability and cold-flow properties.

Table 4.1
Physicochemical Properties and Fatty Acid Composition of WCO Prior to Pre-Treatment

Parameter	Unit	Value
Acid value	mg KOH g^{-1}	24.8
Free Fatty Acid (FFA)	wt%	12.4
Saponification value	mg KOH g^{-1}	184
Moisture content	wt%	1.49
Molecular weight	g mol^{-1}	915
Major fatty acids identified		
Oleic acid	C18:1	27.36%
Palmitic acid	C16:0	21.38%
Myristic acid	C14:0	0.54%
Palmitoleic acid	C16:1	0.14%
Others (saturated/ unsaturated traces)	-	~50.58% (e.g., methyl ester, isomers)

4.2 Characterization Analysis of Photocatalyst

4.2.1 X-Ray Diffraction (XRD) Analysis

X-ray diffraction (XRD) analysis was carried out to examine the crystal structure and phase composition of pure TiO_2, ZnO, empty fruit bunch ash (EFBA), and their composite photocatalysts, TiO_2/EFBA and ZnO/EFBA. The diffraction patterns, presented in Figure 4.1 and Figure 4.2, were interpreted using reference data from the International Centre for Diffraction Data (ICDD).

4.2.1.1 EFBA, TiO_2 and TiO_2/EFBA Composite Analysis

XRD pattern of EFBA exhibited broad but distinguishable peaks at $2\theta = 28.80°$ and 40.96°, corresponding to quartz (SiO_2) (211) and (210). The presence of quartz indicates that silica is major mineral component in EFBA. Additional reflections were observed for ferrosilicon (FeSi), calcium silicon ($CaSi_2$), aluminum oxide (Al_2O_3), and magnetite (Fe_3O_4), consistent with the mineral complexity typical of biomass-derived ash. The occurrence of these mineral phases suggests the introduction of additional active sites that can facilitate electron-transfer processes during photocatalysis. These features contribute to surface heterogeneity and light-scattering properties, which may enhance the overall photocatalytic performance (Ash et al., 2023; Maj et al., 2025).

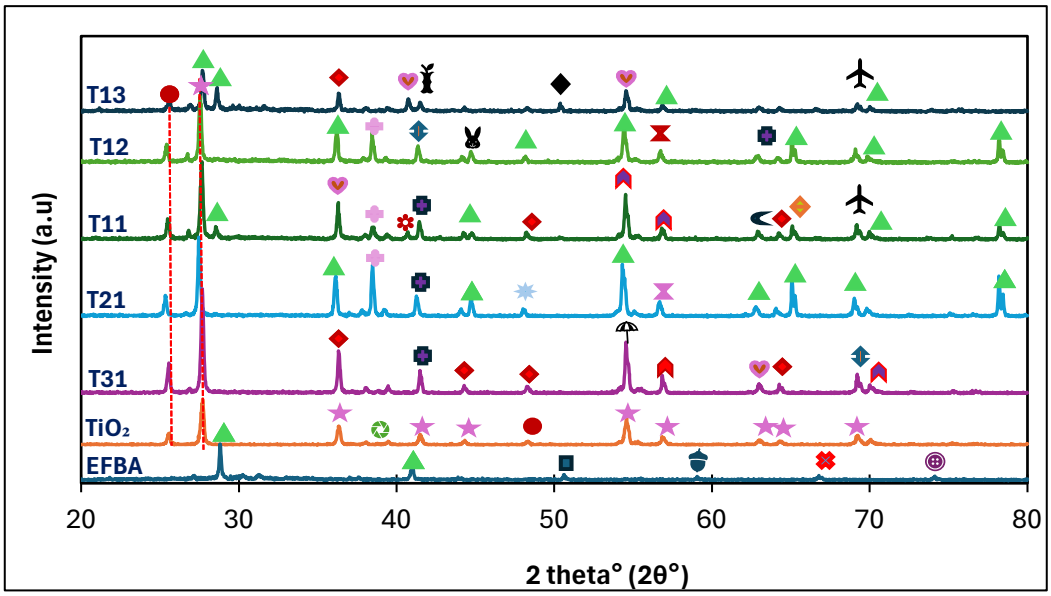


Figure 4.1 XRD Patterns of EFBA, TiO_2, and TiO_2/EFBA Composites. Key Crystalline Phases are Annotated with Labels. Full Phase Assignments are Listed in Table 4.2

Table 4.2
Crystalline Phase Identification and Corresponding Chemical Formulas for XRD-Labeled Peaks Observed in EFBA, TiO_2, and TiO_2/EFBA Composites

Label	Phase Name	Chemical Formula
●	Anatase	TiO_2
★	Rutile	TiO_2
✪	Brookite	TiO_2
▲	Quartz	SiO_2
▲	Enstatite	$Mg_2Si_2O_6$
◆	Hercynite	Al_2FeO_4
✿	Titanium	Ti
◆	Kennedyite	$FeMgO_5Ti_2$
✈	Armacolite	$FeMgO_5Ti_2$
⧗	Magnetite	Fe_3O_4
✸	Pyrrhotite	Fe_7S_8
⬢	Iron Oxide	FeO
⬍	Titanium Iron Oxide	$TiFe_2O_3$
■	Ferrosilicon (Iron Silicide)	FeSi
◖	Iron Phosphate Oxide	Fe_2O_5P
◓	Calcium Silicone	$CaSi_2$
◎	Iron Oxide	Fe_3O_5
🐰	Iron Sulfide	FeS
☂	Iron Silicate	$FeSiO_4$
♥	Wollastonite	$CaSiO_3$
⚷	Potassium Oxide	KO_2
◆	Potassium Phosphide	K_3P_{11}
✿	Aluminum	Al
✖	Aluminum Oxide	Al_2O_3

Pure TiO_2 exhibited a multiphasic system comprising anatase (JCPDS 01-083; 25.55°, 48.26°), rutile (JCPDS 01-088; 27.72°, 36.38°, 41.47°, 44.27°, 54.56°, 70.02°), and a minor brookite phase (37.98°). The dominant anatase peaks confirm that anatase remains the primary crystalline phase. Moreover, the coexistence of anatase and rutile suggests the formation of phase junctions, which can facilitate charge-carrier separation (Eddy et al., 2023). Following EFBA incorporation, the anatase and rutile peaks remain clearly visible, indicating that the crystal structure of TiO_2 was preserved during composite formation. This suggests that EFBA acts primarily as a support matrix rather than altering the TiO_2 lattice.

Several additional diffraction peaks were observed in the TiO_2/EFBA composites, corresponding to phases such as wollastonite ($CaSiO_3$), enstatite ($Mg_2Si_2O_6$), titanium iron oxide ($TiFe_2O_3$), armalcolite ($FeMgO_5Ti_2$), hercynite (Al_2FeO_4), and iron phosphate oxide (Fe_2O_5P). The appearance of these new phases is likely due to the integration of EFBA. This suggests that the formation of mixed oxide phases could create interfacial heterojunctions, promoting electron transfer between different semiconductor domains and thereby enhancing photocatalytic efficiency (Pinedo-Escobar et al., 2021).

Moreover, the appearance of $FeTi_2O_5$ and $TiFe_2O_3$ reflections suggests possible interactions between iron species from EFBA and the TiO_2 lattice. This indicates that localized electronic states are introduced within the band structure, which can facilitate redox cycling between Fe^{3+} and Fe^{2+} species. Consequently, EFBA may act as an electron mediator, promoting oxygen activation and the generation of reactive oxygen species (ROS) (Tanaka et al., 2020; Tang et al., 2025).

Across the investigated TiO_2-to-EFBA mass ratios (T31–T13), the overall phase composition remained largely unchanged, likely because EFBA acts as a support material and does not alter the TiO_2 lattice sites (Podelinska et al., 2025).

To quantify these changes, crystallite size estimation was performed using the Scherrer equation:

$$D = k\lambda/\beta cos\theta \quad (4.1)$$

Where D is the average crystallite size, $K = 0.9$ is the Scherrer constant, λ is the X-ray wavelength (Cu Kα = 1.5406 Å), β is the full width at half maximum (FWHM) of the peak in radians, and θ is the Bragg angle.

As shown in Table 4.3, pure TiO_2 exhibited a crystallite size of 37.65 nm, while EFBA showed a larger size of 43.84 nm. This suggests that EFBA contains mineral oxides that are less ordered and form larger crystallites, whereas TiO_2 is finer and more uniform. After incorporation of EFBA, the crystallite size of the composites increased to approximately 50–56 nm. This growth indicates that EFBA may act as a nucleation site, promoting crystal growth during thermal treatment. Although larger crystallite sizes can reduce the available surface area, the presence of active sites in the semiconductor catalyst may enhance the adsorption of reactant molecules (Bian et al., 2024).

Table 4.3
Crystallite Sizes of EFBA, TiO_2, and TiO_2/EFBA Composite Catalysts Determined via XRD Analysis

Catalyst	Crystallite size, D (nm)
EFBA	43.84
TiO_2	37.65
T31	53.95
T21	55.75
T11	50.89
T12	53.03
T13	50.20

4.2.1.2 ZnO and ZnO/EFBA Composite Analysis

Detailed structural characterization was performed for pure ZnO and the ZnO/EFBA composite with a 1:1 mass ratio (Z11). This composition was selected based on the optimal catalytic performance observed for the 1:1 TiO_2/EFBA system, which yielded the highest conversion. Therefore, ZnO/EFBA (Z11) was chosen for characterization to provide a consistent basis for comparison.

Pure ZnO (Figure 4.2), exhibited sharp, well-defined XRD peaks corresponding to the wurtzite hexagonal phase (JCPDS 01-075-0576), particularly in the 2θ range of 31.84°–78.45°, with dominant reflections at (100), (002), and (101) planes. Minor peaks at 38.25°, 45.14°, and 65.29° were attributed to nonstoichiometric ZnO_x or

orthorhombic O_2, likely arising from oxygen vacancies. These defect sites introduce localized energy levels within the band gap, enabling sub-bandgap excitation and enhancing photon absorption and catalytic performance (Orudzhev et al., 2023; Zhang & Li, 2022).

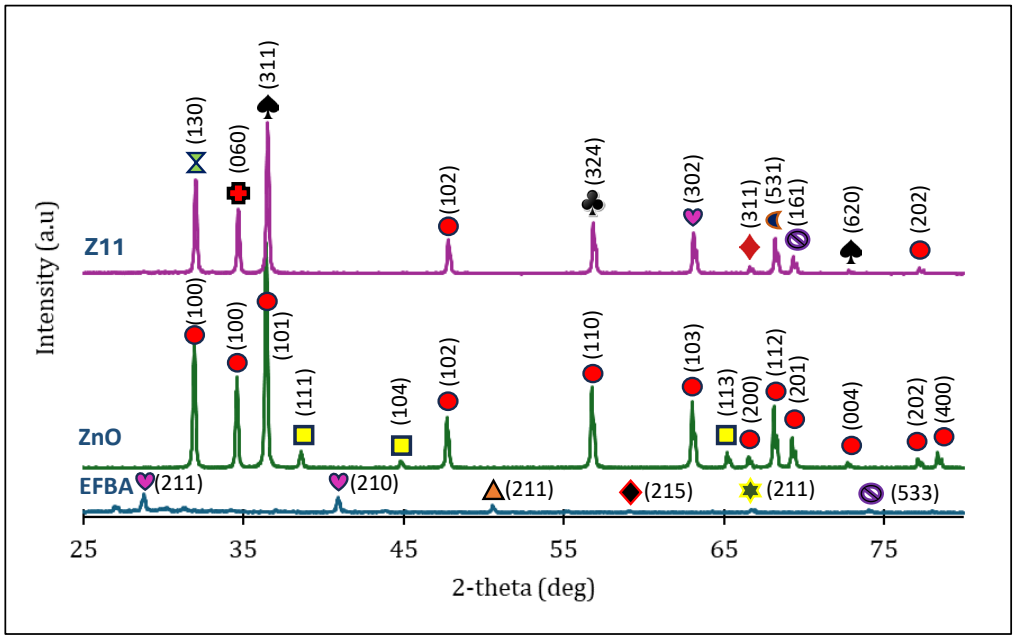


Figure 4.2 XRD Diffractograms of EFBA, ZnO, and ZnO/EFBA Composite (Z11). Complete Phase Assignments are Detailed in Table 4.4

Table 4.4
Identified Crystalline Phases and Corresponding Chemical Formulas Based on XRD Analysis of EFBA, ZnO, and Z11

Label	Phase Name	Chemical Formula
♥	Silicone Dioxide/Quartz	SiO_2
▲	Ferrosilicon	FeSi
♦	Calcium Disilicide	$CaSi_2$
✸	Aluminum Oxide	Al_2O_3
⊘	Iron Oxide/Magnetite	Fe_3O_4
●	Zinc Oxide	ZnO
■	Oxygen	O_2
⧗	Magnesium Iron Silicate/Forsterite	$FeMgO_4Si$
✚	Calcium Phosphate Silicate	$Ca_5O_{12}P_2Si$
♠	Iron Aluminum Oxide/Hercynite	Al_2FeO
♣	Potassium Iron Oxide	$FeKO_2$
◆	Calcium Iron Oxide	$Ca_2Fe_{22}O_{33}$
☾	Zinc Iron Aluminum Oxide	Al_2FeOZn

In the Z11 composite, the primary ZnO structure was largely retained; however, peak broadening and reduced intensity were observed, indicating mild lattice distortion due to EFBA incorporation. Additional diffraction peaks at approximately 32.03°,

34.68°, and 36.51° correspond to the formation of secondary mineral phases, including magnesium iron silicate ($FeMgO_4Si$), calcium phosphate silicate ($Ca_5O_{12}P_2Si$), and hercynite (Al_2FeO). Furthermore, the presence of $FeKO_2$, $Ca_2Fe_{22}O_{33}$, and Al_2FeZn reflections confirms the formation of a complex network of mixed metal oxides originating from the EFBA matrix. These mineral phases may play an important role in modifying the electronic environment of the composite catalyst.

Similar to T11, the presence of Fe-containing phases such as $FeKO_2$ and Al_2FeZn may act as electron reservoirs, facilitating interfacial band bending. These mechanisms can suppress rapid electron–hole recombination and prolong charge carrier lifetimes (Dharanya & Dharmalingam, 2022). Additionally, residual peaks corresponding to quartz (SiO_2) and magnetite (Fe_3O_4), observed at approximately 63.10° and 69.34°, confirm the incorporation of EFBA mineral components within the composite catalyst.

The crystallite sizes of EFBA, ZnO, and the Z11 composite were estimated using the Scherrer equation, yielding values of 43.84 nm, 60.63 nm, and 57.42 nm, respectively. The larger crystallite size observed for ZnO indicates the presence of relatively bigger crystalline domains compared with EFBA, suggesting greater structural ordering within its lattice. This can facilitate charge carrier mobility and reduce localization effects that promote recombination. The slight reduction in crystallite size after EFBA incorporation suggests that interfacial interactions may enhance photocatalytic performance by promoting heterojunction formation (Amakali et al., 2020).

4.2.2 Field Emission Scanning Electron Microscopy–Energy Dispersive X-ray spectroscopy (FESEM–EDX) and Mapping Analysis

4.2.2.1 EFBA and TiO_2-Based Composites Analysis

As shown in Figure 4.3a, EFBA exhibits irregular, porous, and agglomerated spherical particles with interconnected voids (~200–500 nm). This photocatalyst plays a dual-function role in photocatalysis. The porous structure allows deep infiltration of reactant molecules, increasing the accessibility of surface-anchored TiO_2 active sites. Furthermore, the irregular matrix promotes internal light scattering, enabling a more

uniform photon distribution throughout the composite. Consequently, EFBA's porous morphology supports both efficient reactant diffusion and sustained photoactivation, contributing to prolonged charge separation and enhanced catalytic turnover (Khalil et al., 2024).

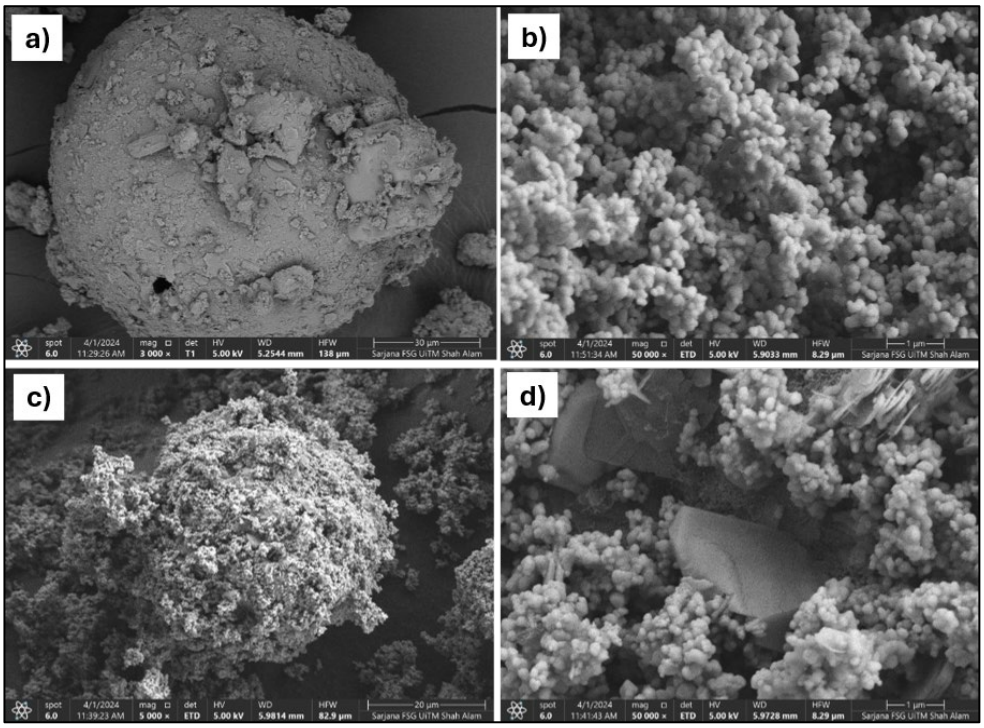


Figure 4.3 FESEM Analysis of a) EFBA at 3 k× Magnification, b) TiO_2 at 50 k× Magnification, c) T11 at 5 k× Magnification and d) T11 at 50 k× Magnification

In contrast, the pure TiO_2 sample (Figure 4.3b) shows a dense and tightly packed grain structure composed of nanoscale spherical particles (~25–45 nm). This morphology indicates strong van der Waals interactions, which can easily lead to particle aggregation and agglomeration, thereby reducing particle dispersion. Such aggregation may limit the accessibility of active sites and hinder light penetration into the catalyst structure (Mu et al., 2025; Tang et al., 2020).

Upon composites formation (Figure 4.3c–d), TiO_2 nanoparticles become more uniformly distributed across the EFBA matrix. The porous ash structure stabilizes the TiO_2 grains and reduces particle clustering. This improves the availability of active sites and enhances light penetration within the composite, thereby promoting improved photocatalytic activity (Panda et al., 2024).

EDX analysis shown in Table 4.5 onfirms successful incorporation of TiO_2 into the EFBA matrix. Ti content decreased from 53.85% in pure TiO_2 to 17.87% in T11, due to dilution by ash content. Oxygen remained dominant (41.04%), indicating preservation of a stable oxide framework. Additional elements such as K, Si, Ca, P, S, and Mg reflect the intrinsic mineral composition EFBA. These ash-derived elements likely exist in oxide forms (e.g., $K–O^-$, PO_4^{3-}, MgO, CaO, SO_4^{2-}). Such species can introduce Lewis's base sites by promotes adsorptive interactions and catalytic activation at the interface. Elements like K and Ca may participate in secondary oxide formation (e.g., $K_2Ti_6O_{13}$), potentially broadening light absorption (Maj et al., 2025).

Table 4.5
The Elemental Composition of the EFBA, TiO_2 and T11 Composites

Catalyst	Elemental composition (%)									
	Ti	O	K	Si	C	Cl	Ca	P	Mg	S
EFBA	-	41.04	24.74	9.34	11.02	3.38	5.90	1.45	1.42	1.70
TiO_2	53.85	46.15	-	-	-	-	-	-	-	-
T11	17.87	41.04	15.49	10.05	4.89	3.89	3.68	1.87	1.12	0.10

Elemental mapping (Figure 4.4) shows homogeneous distribution of Ti, O, Si, Ca, and K, confirming a well-integrated composite structure. These findings support strong interfacial contact between TiO_2 and ash components, consistent with XRD results.

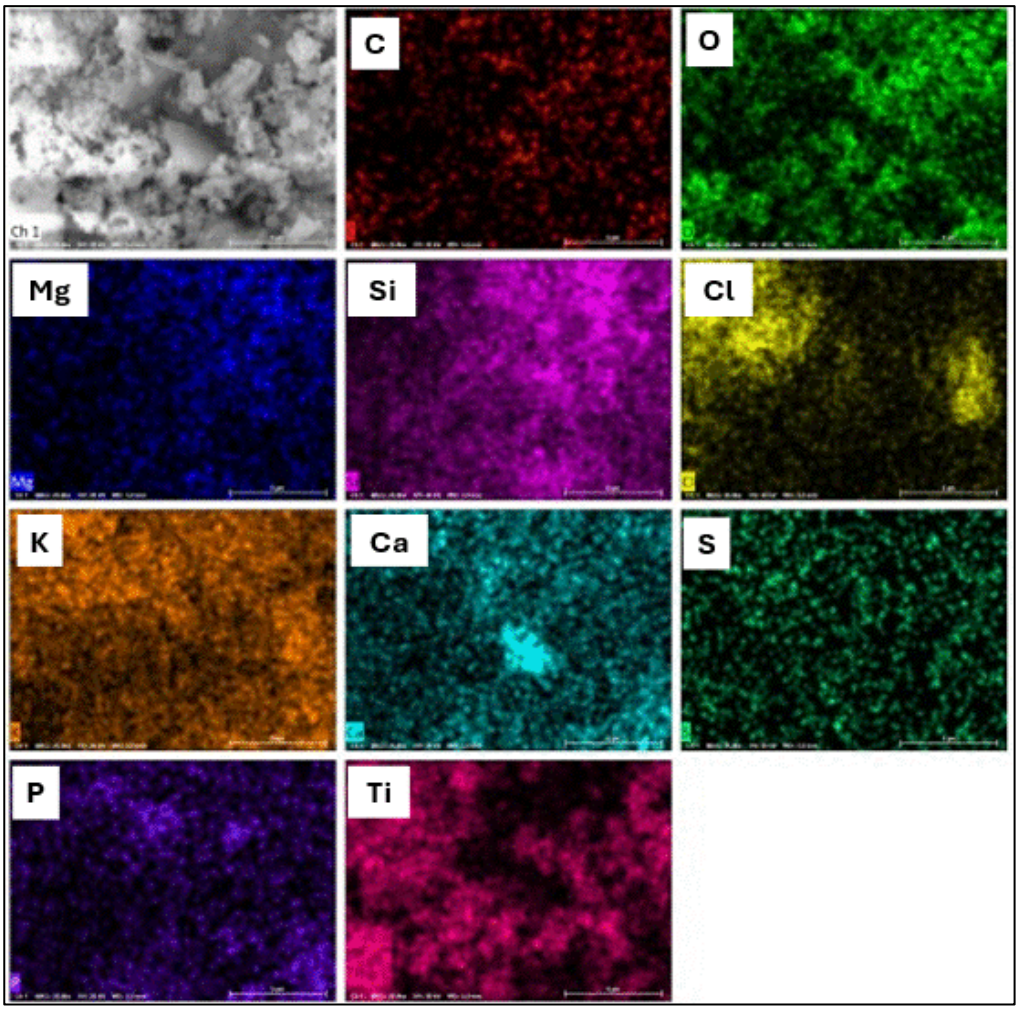


Figure 4.4 Elemental Mapping of T11 Composites at 25 k× Magnification, 20 kV Accelerating Voltage, and a Scale of 5 µm

4.2.2.2 ZnO and ZnO/EFBA Composite Analysis

Pure ZnO (Figure 4.5b) exhibits smooth, tightly packed nanograins with limited porosity. This compact morphology reflects high crystallinity and can facilitate efficient electron transport. However, the particle may easily agglomerate and likely reduce effective surface area and increase the probability of electron–hole recombination (Ou et al., 2024).

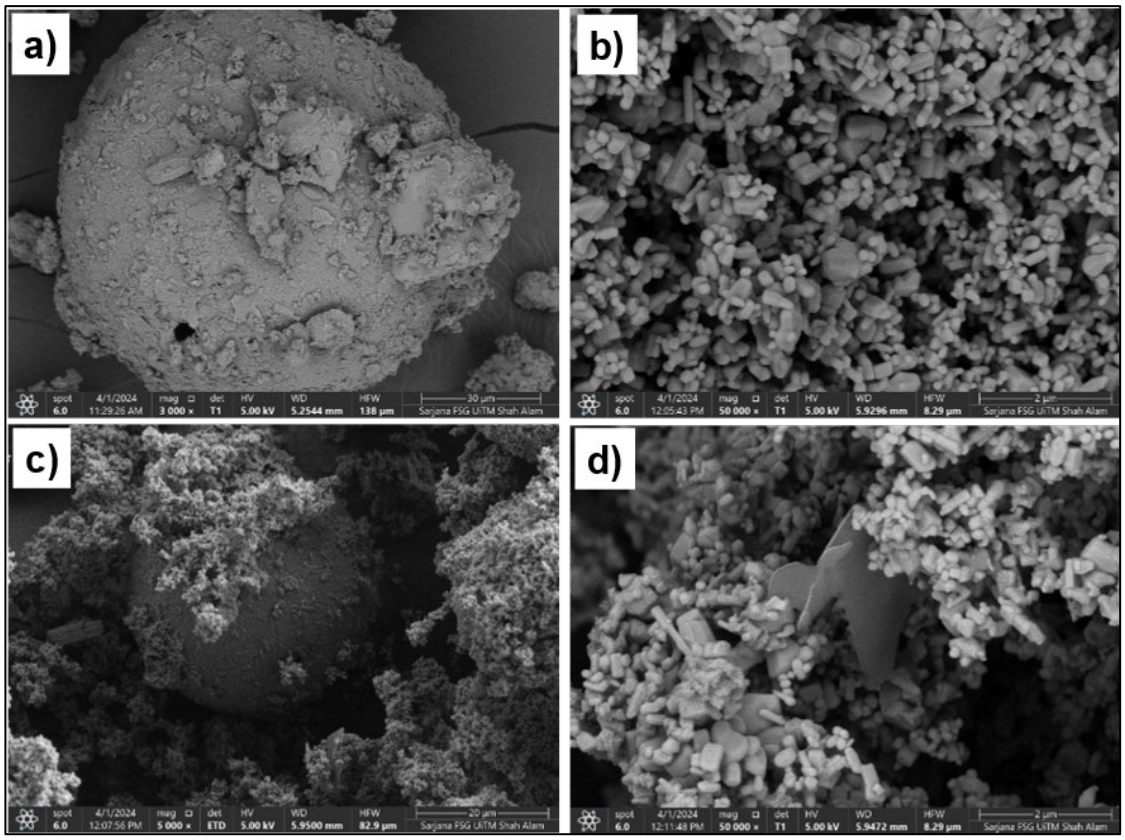


Figure 4.5 FESEM Analysis of a) EFBA at 3 k× Magnification, b) ZnO at 50 k× Magnification, c) Z11 at 5 k× Magnification and d) Z11 at 50 k× Magnification

In the Z11 composite (Figure 4.5c–d), ZnO nanoparticles are well dispersed within the porous EFBA framework. The ash matrix physically separates ZnO particles and introduces surface roughness. This increased roughness enhances light scattering and photon trapping within the composite while simultaneously providing nucleation and adsorption sites for reactant molecules (Tian et al., 2022). Such spatial separation promotes the formation of interfacial heterojunctions and supports directional charge transfer under irradiation. The improved interfacial contact between ZnO and ash-derived oxides to facilitate charge carrier separation and reduce recombination losses.

The EDX analysis (Table 4.6) shows that the Zn content in the composite decreases to 52.33%, compared with 82.50% in pure ZnO. Oxygen levels remain relatively high, and notable amounts of K, Si, Mg, Fe, and P are also detected. These elements may contribute to the formation of secondary oxide or silicate phases that can modify surface reactivity and influence the electronic properties of the catalyst (Singh & Ali, 2022).

Table 4.6
The Elemental Composition of the EFBA, ZnO and Z11 Composites

Catalyst	Elemental composition (%)										
	Zn	O	K	Si	C	Cl	Ca	P	Mg	S	Fe
EFBA	-	41.04	24.74	9.34	11.02	3.38	5.90	1.45	1.42	1.70	-
ZnO	82.50	17.50	-	-	-	-	-	-	-	-	-
Z11	52.33	27.77	7.08	6.18	3.35	0.19	-	0.84	1.39	-	0.89

Elemental mapping of the Z11 (Figure 4.6) confirms uniform distribution of Zn and O along with Si, Fe, Mg, K, and P. The homogeneous dispersion supports the formation of chemically interactive composite networks. These findings are consistent with XRD results indicating secondary phase formation, implying strong physicochemical interaction between ZnO and the EFBA matrix.

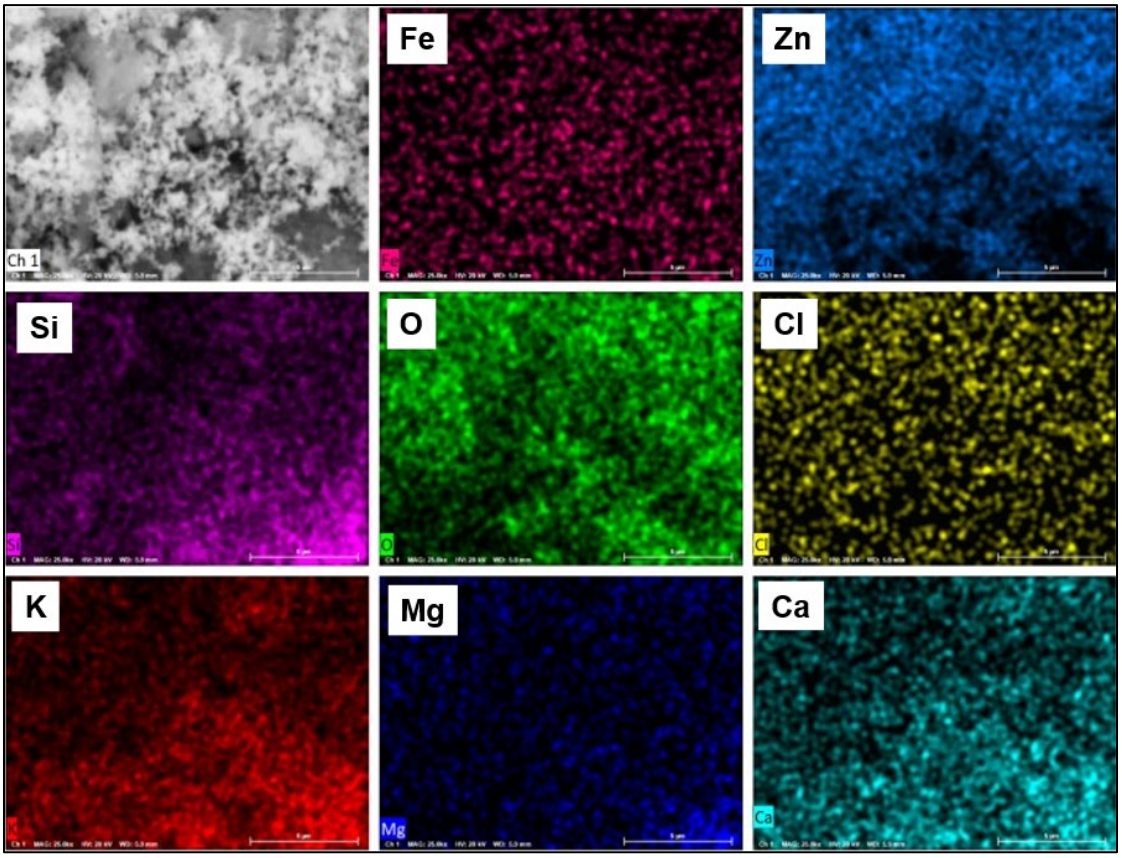


Figure 4.6 Elemental Mapping of Z11 Composites at 25 k× Magnification, 20 kV Accelerating Voltage, and a Scale of 5 µm

4.2.3 High-Resolution Transmission Electron Microscopy (HRTEM) and Selected Area Electron Diffraction (SAED) Analysis

4.2.3.1 EFBA and TiO_2-Based Composites Analysis

As shown in Figure 4.7a–c, EFBA exhibits a disordered and porous structure composed of loosely packed particles with substantial amorphous regions. At higher magnification, faint lattice fringes are observed in localized areas, indicating the presence of partially graphitized carbon domains. The presence of these graphitized regions suggests that EFBA may act as an electron reservoir, helping to suppress rapid electron–hole recombination. These sp^2-hybridized carbon structures, likely formed during biomass pyrolysis, may enhance surface conductivity and facilitate electron transport within the matrix (Alluqmani et al., 2021).

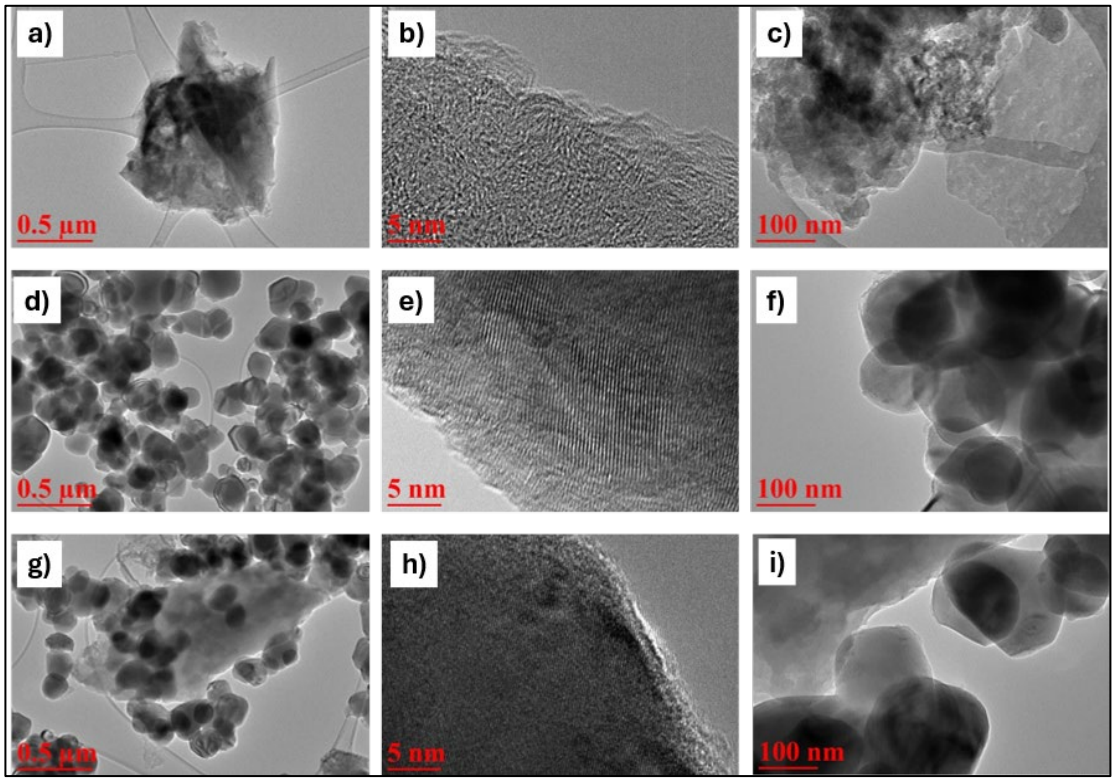


Figure 4.7 HRTEM Analysis of a-c) EFBA, d-f) TiO_2 and g-i) T11

Pure TiO_2, shown in Figure 4.7d–f, consists of well-defined spherical nanoparticles with clear lattice fringes. The measured lattice spacing of approximately

0.35 nm corresponds to the (101) plane of anatase, which agrees with the XRD results. The SAED pattern (Figure 4.8a) shows bright concentric rings characteristic of polycrystalline anatase. The sharp and uniform diffraction rings confirm high crystallinity and good structural order. This contributes to high charge carrier mobility (Payormhorm & Idem, 2020). However, the highly ordered and densely packed morphology may reduce interfacial interaction and limit surface accessibility, potentially restricting active sites for photocatalytic reactions.

In the T11 composite (Figure 4.7g–i), lattice distortion and slight bending are clearly observed at the interface through HRTEM imaging. Irregular lattice fringe periodicity and angular deviations are evident, indicating structural disruption at the interface. These distortions are likely caused by local strain and interfacial tension arising from the heterogeneous EFBA matrix. Such features are characteristic of lattice mismatch at heterointerfaces and suggest strong physicochemical interaction between EFBA and TiO_2. This interfacial disruption may facilitate enhanced charge carrier separation by disturbing electron–hole symmetry, thereby prolonging charge carrier lifetimes and improving photocatalytic performance under illumination (Tee et al., 2024).

The SAED pattern of T11 (Figure 4.8b) exhibits broadened and diffuse diffraction rings compared to pure TiO_2 (Figure 4.8a). This observation indicates reduced long-range crystallinity and suggests the presence of amorphous domains at the T11 interface. These features are consistent with the interfacial strain and lattice distortion observed in the HRTEM images, supporting the interpretation of partial structural disruption within the composite (Zhang et al., 2022). The observed interfacial restructuring suggests strong coupling between TiO_2 and EFBA. This interpretation is further supported by the XRD results, which show slight peak broadening and reduced diffraction intensity, confirming the presence of interfacial strain and chemical modification induced by EFBA incorporation.

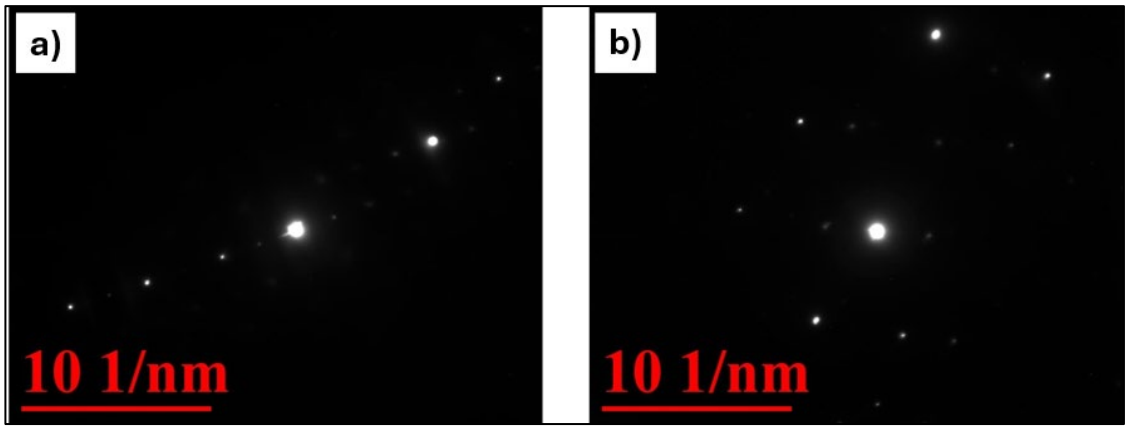


Figure 4.8 a) SAED of TiO_2 and b) SAED of T11

4.2.3.2 ZnO and ZnO/EFBA Composite Analysis

As shown in Figure 4.9d–f, pure ZnO exhibits well-defined nanocrystalline grains with distinct lattice fringes. The measured interplanar spacing of approximately 0.281 nm corresponds to the (101) plane of the hexagonal wurtzite structure, confirming the phase identity of ZnO. The corresponding SAED pattern (Figure 4.10a) features bright and evenly spaced diffraction rings, indicating a highly crystalline polycrystalline structure (Raha & Ahmaruzzaman, 2022). This suggests that pure ZnO contains minimal structural defects which limit intrinsic charge separation efficiency, potentially leading to faster electron–hole recombination.

HRTEM image of Z11 composite (Figure 4.9g–i) show that the ZnO lattice fringes remain well-defined, although slight distortions are observed. These include minor fringe displacement, subtle curvature of lattice planes, and localized contrast variations, where certain regions appear darker or brighter than the surrounding areas. Such distortions are primarily observed at the Z11 interfaces, indicating strong interfacial interactions and good dispersion of ZnO crystallites within the textured EFBA matrix. The interfacial strain may influence charge distribution at the interface, which is beneficial for photocatalytic activity. This facilitates charge separation by creating preferential pathways for electron migration and suppressing electron–hole recombination. Consequently, more photogenerated charge carriers are retained under illumination, thereby enhancing photocatalytic efficiency (Bora et al., 2023).

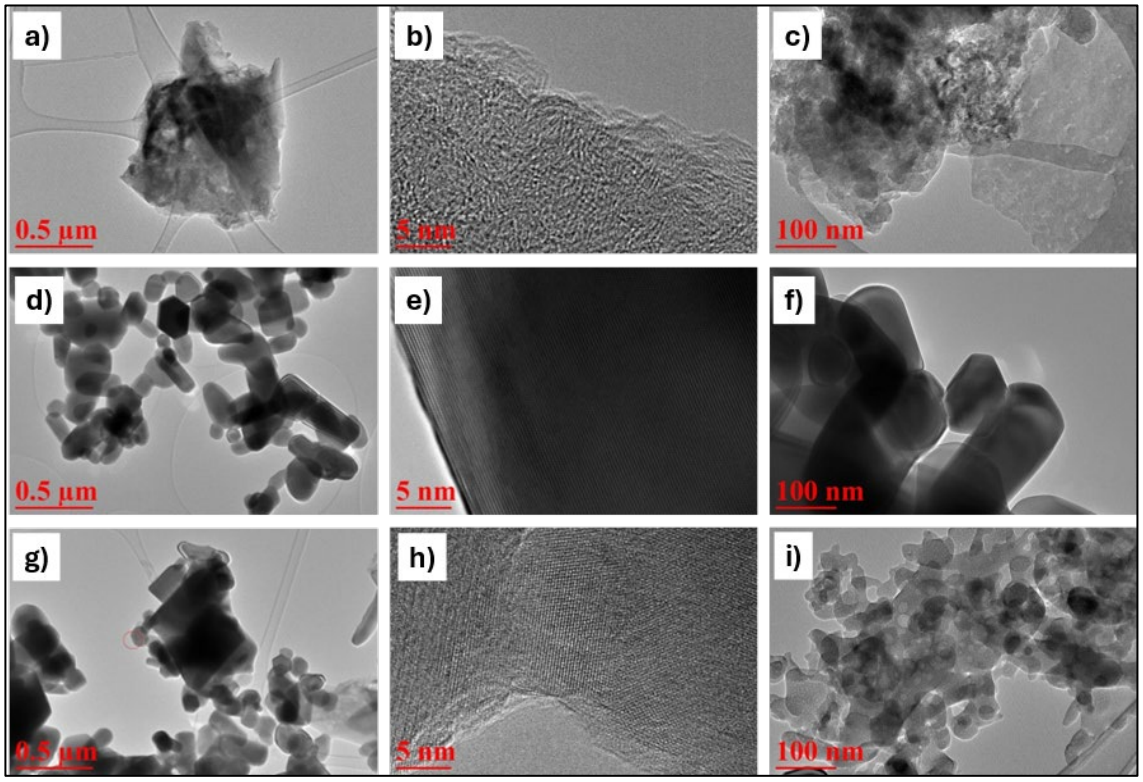


Figure 4.9 HRTEM Images of a-c) EFBA, d-f) ZnO and g-i) Z11 at Different Magnification

The SAED pattern of Z11 (Figure 4.10b) exhibits sharp diffraction rings corresponding to crystalline ZnO, overlaid with diffuse halos attributed to amorphous EFBA, confirming the semi-crystalline nature of the composite. The presence of distinct ZnO rings indicates that the crystallinity of ZnO is preserved after composite formation, while the diffuse background suggests the disordered structure of the EFBA matrix. The partial embedding of ZnO nanoparticles within the amorphous EFBA phase implies the formation of heterogeneous interfaces between the two components.

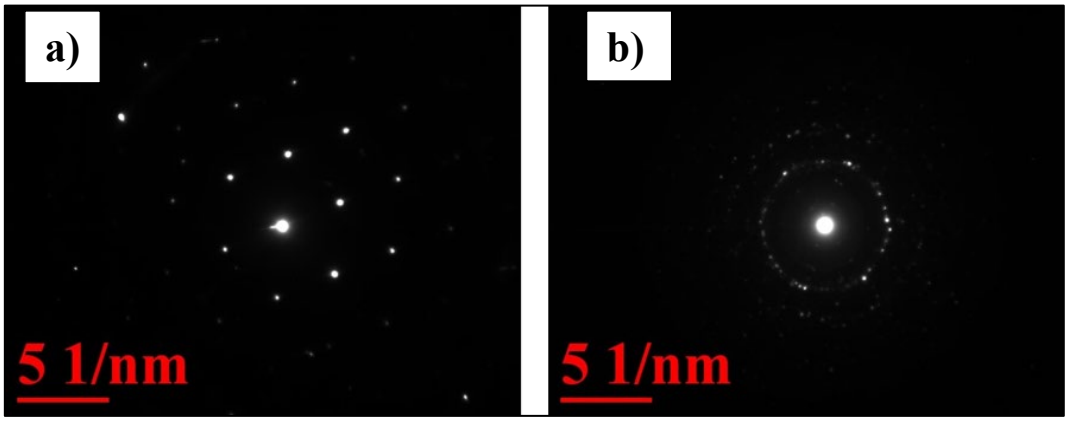


Figure 4.10 SAED Patterns of (a) ZnO and (b) Z11

4.2.4 Ultraviolet–Visible Diffuse Reflectance Spectroscopy (UV–Vis–DRS) and Photoluminescence (PL) Analysis

4.2.4.1 TiO_2 and TiO_2-Based Composites Analysis

As shown in Figure 4.11a, pure TiO_2 exhibits a sharp absorption edge at approximately 387 nm, corresponding to a bandgap energy of 3.20 eV, which is characteristic of anatase-phase TiO_2 (Fotiou et al., 2024). Upon incorporation of EFBA, the absorption edge shifts toward longer wavelengths (420–430 nm), accompanied by a decrease in reflectance intensity. This red shift suggests bandgap narrowing and enhanced visible-light absorption. The surface modification with EFBA alters the optical properties of TiO_2, likely due to the introduction of oxygen vacancies (Simanjuntak et al., 2025). This interpretation is consistent with the XRD results, which show preserved crystallinity, and the HRTEM analysis, which indicates strong interfacial integration between TiO_2 and EFBA. The improved light absorption is expected to enhance photon utilization during the photo-esterification reaction, thereby contributing to the increased ester yield. Similar bandgap reduction in TiO_2/carbon composites has been reported by Guan et al. (2023), where defect-induced mid-gap states were responsible for the extended visible-light response.

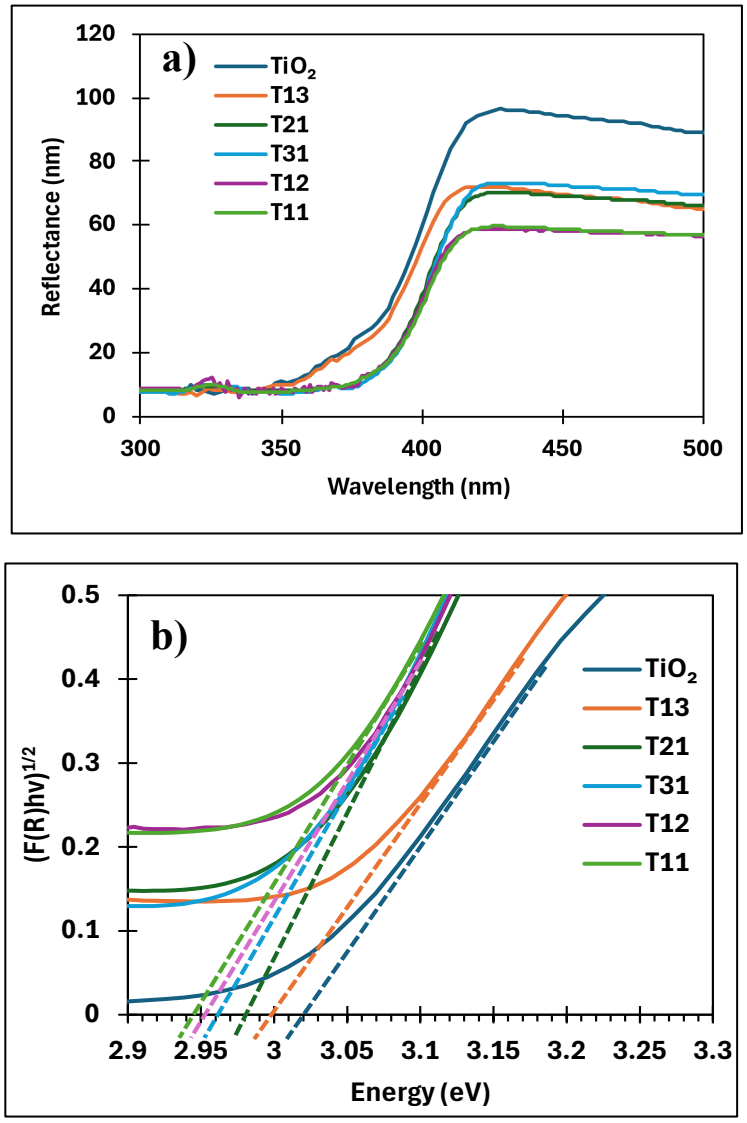


Figure 4.11 Reflectance of TiO_2 and TiO_2/EFBA Composites (a) and Tauc Plot Derived from Kubelka–Munk Function of TiO_2 and TiO_2/EFBA Composites (b)

Table 4.7
Bandgap Energy of TiO_2 and TiO_2/EFBA Composites Using Tauc Plot Method

Catalyst	TiO_2	T13	T21	T11	T31	T12
Bandgap (eV)	3.2	3.0	2.98	2.94	2.96	2.95

The Tauc plot analysis (Figure 4.11b) quantitatively confirms the bandgap narrowing with increasing EFBA content, decreasing from 3.20 eV for pristine TiO_2 to 2.94 eV for the T11 composite (Table 4.7). Although a red shift is observed, the overall

reduction is relatively modest (~0.26 eV), suggesting that the incorporation of EFBA does not significantly modify the intrinsic electronic structure of TiO_2. Instead, the slight narrowing likely reflects surface effect interaction. This moderate change indicates that the improved photo-esterification performance may involve enhanced interfacial charge transfer and surface adsorption effects.

The Tauc relation used to estimate the band gap energy using this following equation:

$$(F(R)hv)^n = A(hv) - E_g \tag{4.2}$$

where *F(R)* is the reflectance-transformed Kubelka–Munk function, *hv* is the photon energy, *A* is a constant, E_g is the optical band gap, and n depends on the nature of the electronic transition. For indirect semiconductors like TiO_2, n = ½.

PL spectra further highlight the effect of EFBA incorporation on charge recombination behavior. Pure TiO_2, under 275 nm excitation, exhibits strong emission in the 390–500 nm range, indicating a high rate of electron–hole recombination (Figure 4.12a). The excitation wavelength of 275 nm corresponds to a photon energy of approximately 4.51 eV, which exceeds the bandgap energy of TiO_2 (3.20 eV). This allows direct band-to-band excitation, generating intense near-band-edge (NBE) emission. The intense NBE contributes to fast recombination of photogenerated charge carriers. The strong PL intensity suggests that electrons excited from the valence band to the conduction band recombine directly without significant involvement of trapping states or interfacial charge separation.

However, Figure 4.12b shows that T11 still exhibits strong PL emission at 275 nm, although the intensity is lower than that of pristine TiO_2. This indicates that, even after EFBA incorporation, fast electron–hole recombination occurs. The high-energy electrons generated by 275 nm excitation are excited far above the conduction band edge, producing carriers that tend to recombine very rapidly. This is because the photon energy (~4.51 eV) is much higher than the TiO_2 bandgap (~3.2 eV). As a result, EFBA can partially trap electrons, but it cannot fully prevent ultrafast recombination at such high excitation energies.

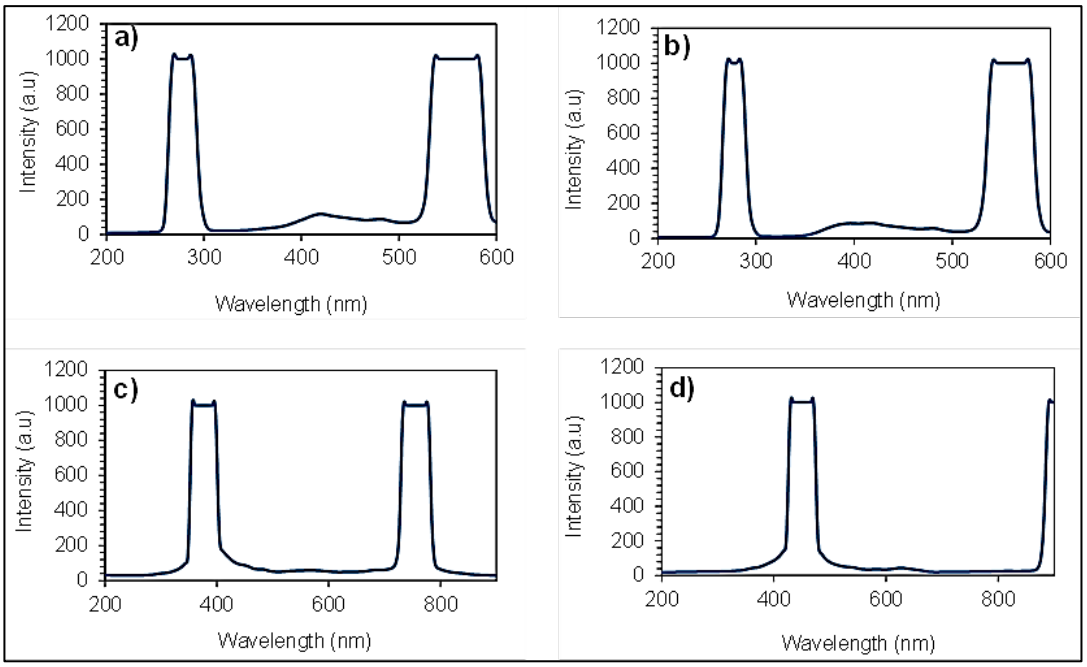


Figure 4.12 PL Analysis of a) TiO_2 at 275 nm Excitation, b) T11 at 275 nm Excitation, c) T11 at 375 nm Excitation and d) T11 at 450 nm Excitation

Furthermore, excitation at 375 nm (~3.31 eV) (Figure 4.12c) of TiO_2/EFBA shows a reduced PL intensity, indicating suppression of fast electron–hole recombination. This suggests that the photon energy is close to the bandgap of TiO_2 (~3.2 eV), allowing effective excitation without generating excessively high-energy carriers that recombine too rapidly. Moreover, the formation of defect states from EFBA within the composite further enhances charge carrier separation. This is supported by EDX analysis, which confirms the presence of these inorganic elements that contribute to the formation of oxygen vacancies and surface defect sites.

When excited at 450 nm (~2.76 eV) (Figure 4.12d), no significant PL emission is observed, indicating that the excitation energy is insufficient to promote electrons across the TiO_2 bandgap. This behavior occurs because the photon energy is lower than the bandgap energy of TiO_2 (~3.2 eV), preventing direct band-to-band excitation. As a result, electrons can only be excited into defect-related trap states within the bandgap, leading to very weak or negligible PL emission.

The deconvoluted PL spectra (Figure 4.13) reveal NBE emissions at 361 and 386 nm, indicating that T11 is effectively photoexcited at these wavelengths. These emissions correspond to band-to-band recombination processes within the TiO_2

structure. In contrast, emissions observed in the near-infrared region (~742 nm and 770 nm) are attributed to deep-level trap states associated with defects within the composite. The presence of multiple emission peaks suggests that T11 exhibits strong photoactivity in the UV region, particularly around 361–386 nm. This indicates that the composite is primarily activated under strong UV irradiation, with limited response in the visible-light region.

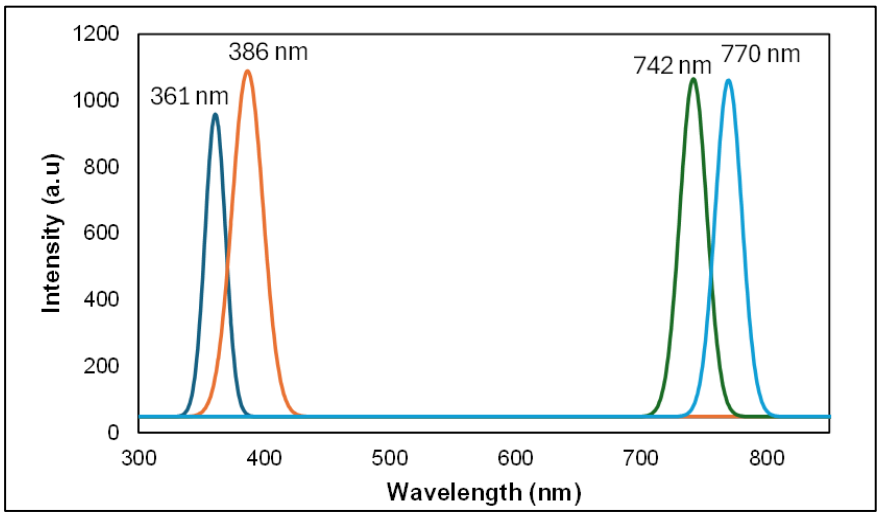


Figure 4.13 Deconvulated PL Spectra of T11 at 375 nm Excitation

4.2.4.2 ZnO and ZnO/EFBA Composite Analysis

The UV–Vis DRS of ZnO and Z11 composites are presented in Figure 4.14a. Pure ZnO exhibits an absorption edge around 387 nm, corresponding to a bandgap energy of 3.21 eV, which is consistent with the typical hexagonal wurtzite structure of ZnO. Upon EFBA incorporation, the absorption edge slightly red-shifts to approximately 395–400 nm, accompanied by a decrease in reflectance intensity. This suggests enhanced light absorption and improved interaction between incident photons and the catalyst surface.

Tauc plot analysis (Figure 4.14b) reveals only a negligible bandgap narrowing for Z11, from 3.21 eV to 3.19 eV. The small reduction of ~0.02 eV indicates that EFBA does not significantly modify the intrinsic band structure of ZnO. This may be attributed to the fact that EFBA mainly acts as a supporting matrix, thus preserving the fundamental electronic structure of ZnO. However, the surface oxygen vacancies still

influence charge carrier dynamics and enhance photocatalytic performance by facilitating charge trapping and reducing electron–hole recombination (Bouderbala et al., 2025).

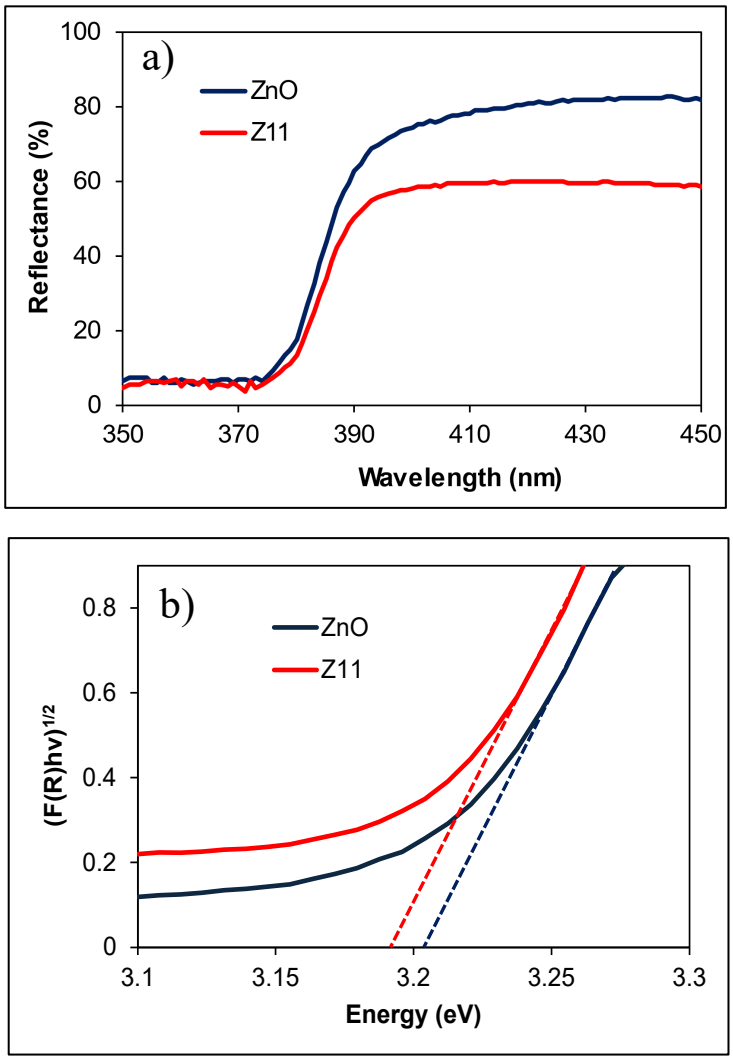


Figure 4.14 UV-Vis Diffuse Reflectance Spectra of ZnO and Z11 (a), and Tauc Plot Derived from Kubelka–Munk Function of ZnO and Z11 Composites (b)

Figure 4.15 shows the PL analysis of ZnO and Z11 composites under three excitation wavelengths: 275 nm, 375 nm, and 450 nm. Excitation of ZnO at 275 nm produced high PL intensity. This is attributed to the photon energy exceeding the bandgap of ZnO (3.21 eV), resulting in strong near-band-edge (NBE) emission due to the recombination of photogenerated electron–hole pairs. When excited at 375 nm, the PL intensity of ZnO decreased, indicating that the excitation energy is close to the

bandgap energy of ZnO (≈3.2 eV), which leads to reduced radiative recombination. This behavior may also be associated with lower kinetic energy of the excited charge carriers, resulting in shallow energy states due to oxygen vacancies and Zinc intestitial. This contributes to increase charge carrier mobility and potentially improve photocatalytic performance (Kumar et al., 2025).

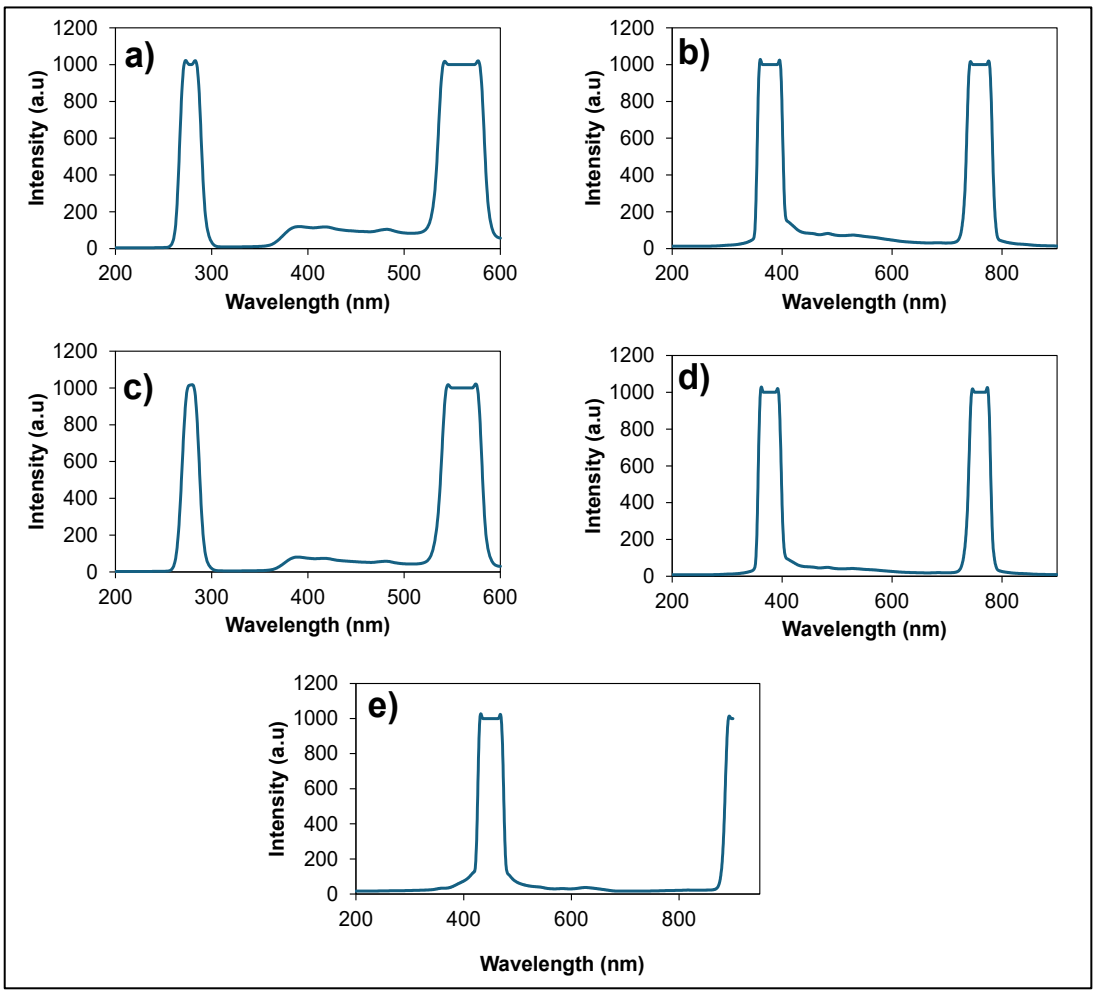


Figure 4.15 PL Analysis of a) ZnO at 275 nm Excitation, b) ZnO at 375 nm Excitation, c) Z11 at 275 nm Excitation, d) Z11 at 375 nm Excitation and e) Z11 at 450 nm

A similar trend was observed for Z11 at excitation wavelengths of 275 nm (Figure 4.15c) and 375 nm (Figure 4.15d), where the PL intensity was higher at 275 nm and decreased at 375 nm. This behavior explains the higher photocatalytic efficiency of both ZnO and Z11 under UV irradiation, where the photon energy is sufficient to excite electrons from the valence band to the conduction band.

However, the efficiency of pure ZnO after several reuse cycles was found to decrease based on the performance in the photoesterification reaction. This is mainly due to the aggregation of ZnO nanoparticles, which tend to clump together and become difficult to separate from the reaction product.

Moreover, for excitation at 450 nm (~2.76 eV) (Figure 4.15e), behavior similar to that observed in TiO_2 PL analysis was obtained, where the excitation energy falls below the bandgap of ZnO. The strong emission peak observed at ~450 nm indicates radiative recombination of electrons and holes. In addition, the strong PL peak at ~850 nm suggests the presence of deep-level trap states that act as recombination centers. These results indicate that Z11 exhibits stronger optical activity mainly in the UV region. Nevertheless, EFBA can still introduce defect states and improve charge carrier mobility due to the presence of trace metal elements such as Fe, Ca, and Mg in the ash matrix.

The deconvoluted PL spectra (Figure 4.16) at 375 nm exhibit NBE emissions at approximately 365 nm and 387 nm, while deep trap states are observed at around 750 nm and 771 nm. These trap states may prolong charge carrier lifetimes by suppressing rapid electron–hole recombination, thereby enhancing photocatalytic activity under UV-A irradiation, as reported by (Lage et al., 2023) The combined UV–Vis and PL results suggest that EFBA incorporation into ZnO introduces surface defect states and interfacial charge-transfer modifications under UV light.

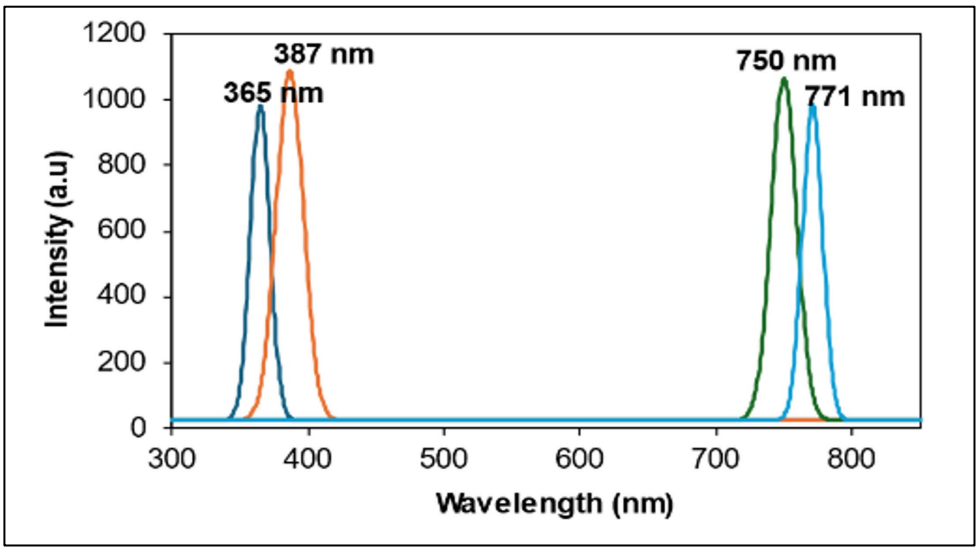


Figure 4.16 Deconvulated PL Spectra of Z11 at 375 nm Excitation

4.2.5 Fourier-Transform Infrared Spectroscopy (FTIR) Analysis

FTIR spectroscopy was conducted to analyze the surface functional groups of EFBA-based photocatalysts.

4.2.5.1 EFBA and TiO_2-Based Composites Analysis

As shown in Figure 4.17, the FTIR spectrum of EFBA reveals several characteristic bands. A broad region around 3490 cm^{-1} is typically associated with O–H stretching vibrations originating from adsorbed moisture and surface hydroxyl groups from H_2O. Distinct peaks at 1640 cm^{-1} and 1232 cm^{-1} are assigned to C=O and C–O stretching vibrations, respectively, which originate from residual organic matter such as lignin or charred carbon species. A strong band at 1026 cm^{-1} corresponds to Si–O–Si asymmetric stretching, confirming the presence of silicate frameworks. Low-wavenumber bands at 487 cm^{-1} and 630 cm^{-1} indicate metal–oxygen (M–O) vibrations from mineral oxides such as SiO_2, Al_2O_3, and CaO (Hussein et al., 2024; Rahmat et al., 2021).

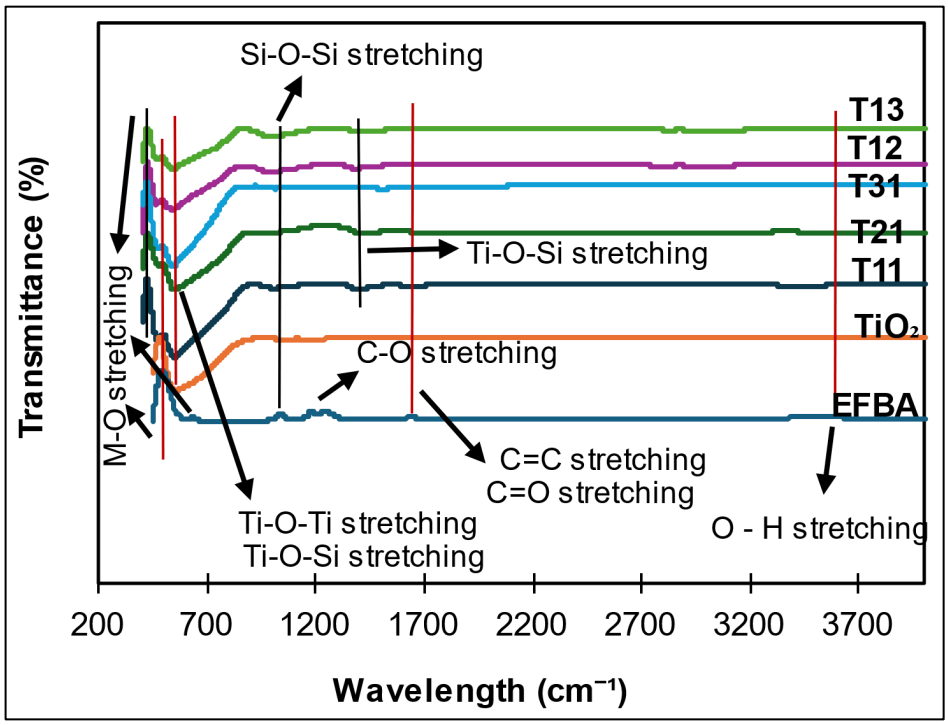


Figure 4.17 FTIR Analysis of EFBA, TiO_2 and TiO_2/EFBA Composites

Pure TiO_2 displays distinct bands at approximately 416 cm^{-1} and 548 cm^{-1}, which are attributed to Ti–O–Ti lattice vibrations corresponding to both anatase and rutile phases. This observation is consistent with the structural characteristics of Degussa P25 TiO_2, which is known to contain a mixed anatase–rutile crystalline composition (Aghababaei et al., 2025).

In all TiO_2/EFBA composites, similar functional groups are observed. This indicates that the fundamental chemical structures of both EFBA and TiO_2 remain largely preserved after composite formation. However, several spectral changes suggest interactions between TiO_2 and the EFBA matrix. The broadening of the absorption region between 1200–1750 cm^{-1} can be attributed to overlapping vibrational modes of C=O, C–O, and Ti–O–C groups, which may arise from carbonate species formed when CaO present in the ash reacts with TiO_2 or atmospheric CO_2.

At around 416–548 cm^{-1}, the Ti–O–Ti lattice vibrations remain clearly identifiable, confirming that the core crystalline structure of TiO_2 is preserved within the composite material. Meanwhile, the diminished intensity of the M–O band at 487 cm^{-1}, together with a noticeable shift of the Si–O–Si stretching band toward higher wavenumbers (approximately 1080–1100 cm^{-1}), suggests the formation of Ti–O–Si interfacial bonds between TiO_2 and the silicate framework of EFBA. This new linkage indicates strong incorporation of TiO_2 onto the EFBA matrix.

Furthermore, previous studies have reported that surface hydroxyl groups on TiO_2 can undergo condensation reactions with silanol (Si–OH) groups present in silicate-based supports, forming Ti–O–Si bonds through a dehydration process (Tinoco Navarro & Jaroslav, 2023). These interfacial bonds enhance the dispersion of TiO_2 particles and facilitate electron transfer between TiO_2 and the EFBA support. Improved interfacial interaction can promote charge carrier separation and reduce electron–hole recombination.

This effect is also reflected in the PL quenching observed under 375 nm excitation, where TiO_2/EFBA composites exhibit lower emission intensity compared to pure TiO_2. Overall, the FTIR features confirm the successful chemical integration and interfacial interaction between TiO_2 and the EFBA matrix.

4.2.5.2 ZnO and ZnO/EFBA Composite Analysis

Figure 4.18 shows the FTIR spectra of ZnO and Z11. Pristine ZnO exhibits dominant Zn–O stretching vibrations in the 400–600 cm^{-1} region, which are characteristic of the wurtzite crystal phase (Figure 4.18a). The absence of significant high-wavenumber absorption bands indicates the high crystallinity of ZnO with minimal organic or inorganic contamination (Ansari et al., 2025).

In the Z11 composite (Figure 4.18b), several additional absorption features appear, reflecting the incorporation of ash-derived functional groups. A broad band in the 3410–3490 cm^{-1} region corresponds to O–H stretching vibrations, indicating increased surface hydroxylation and moisture adsorption resulting from EFBA integration. A distinct absorption band at approximately 1640 cm^{-1} is attributed to C=O stretching and possibly C=C vibrations, which originate from residual carbonaceous species present within the ash matrix.

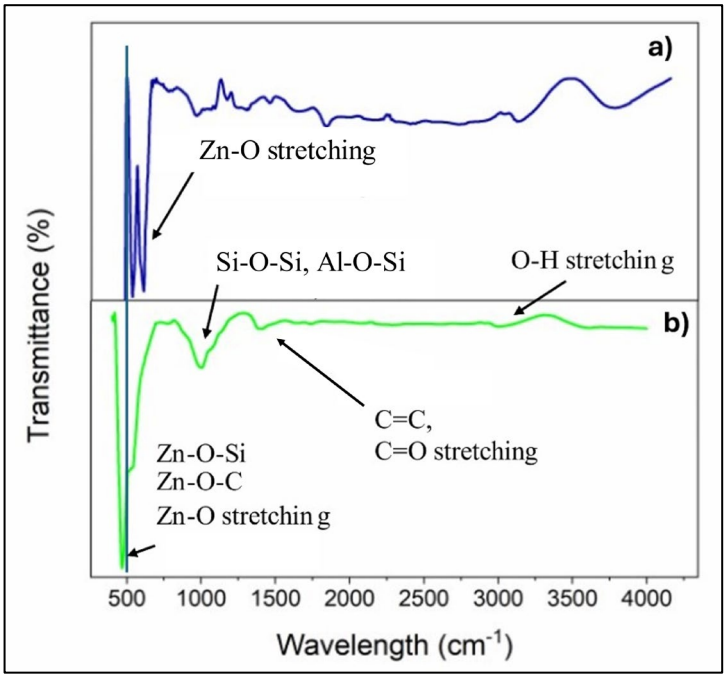


Figure 4.18 FTIR Analysis of a) ZnO and b) Z11

In the 950–1100 cm^{-1} region, the emergence of new peaks is associated with Si–O–Si and Al–O–Si stretching vibrations, confirming the presence of aluminosilicate components derived from EFBA (Kokab et al., 2025). These features suggest the

formation of an interactive interface between ZnO and the mineral-rich ash support, which may influence the surface chemistry of the composite.

Notably, the Zn–O vibration band becomes slightly broadened and shifts toward lower wavenumbers (~435–490 cm^{-1}), indicating possible formation of Zn–O–Si or Zn–O–C interfacial bonds. These linkages suggest that partial surface modification and lattice distortion occur at the interface between ZnO and the EFBA matrix. Despite these modifications, the fundamental ZnO crystal structure remains well preserved, indicating that the interfacial interaction mainly occurs at the surface while maintaining the intrinsic properties of ZnO (Tiep et al., 2024).

4.2.6 Brunauer–Emmett–Teller (BET) Surface Area and Porosity Analysis

To further understand the structural behavior of EFBA-based photocatalysts, nitrogen adsorption–desorption measurements were carried out, and the results were analyzed using the Brunauer–Emmett–Teller (BET) method.

4.2.6.1 EFBA and TiO_2-Based Composites Analysis

As shown in Figure 4.19, all samples exhibit Type IV nitrogen adsorption–desorption isotherms with H3-type hysteresis loops. Its characteristic of mesoporous materials with slit-like pores typically associated with layered or aggregated structures. Such textural features are beneficial for catalytic systems as they enhance reactant diffusion, reduce mass transfer limitations, and improve accessibility to photocatalytic active sites.

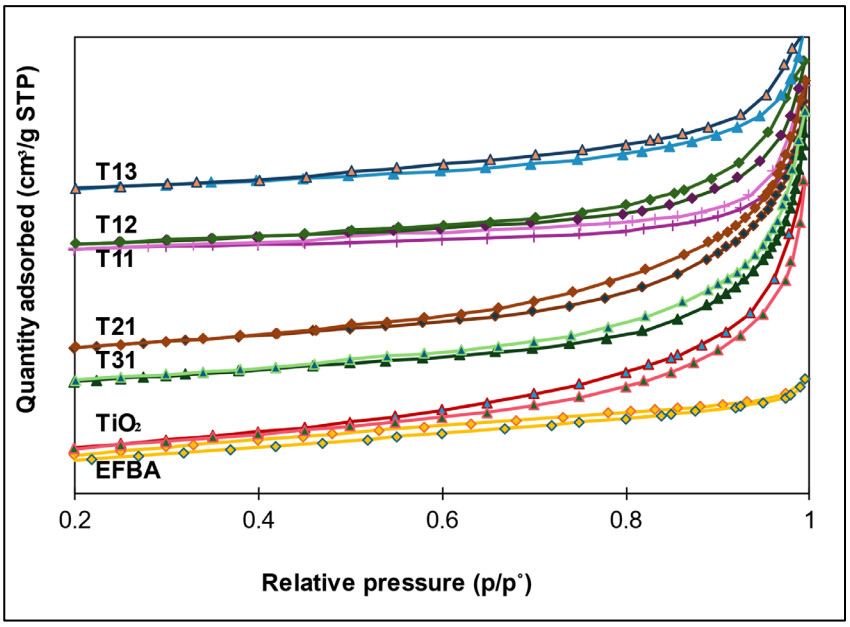


Figure 4.19 Nitrogen Adsorption-Desorption Isotherms of EFBA, TiO_2, and TiO_2/EFBA Composites Catalysts

As summarized in Table 4.8, EFBA exhibited a relatively low surface area of 9.76 m^2/g and the smallest pore volume (0.0116 cm^3/g), reflecting its heterogeneous mineral–carbonaceous composition and irregular surface morphology. Nevertheless, its porous structure, as observed from FESEM analysis, suggests that EFBA can function as a suitable support material for dispersing semiconductor nanoparticles.

Table 4.8
BET Surface Area, Total Pore Volume, and BJH Desorption Average Pore Width of EFBA, TiO_2, and TiO_2/EFBA Composites

Catalyst	BET surface area (m^2/g)	Total pore volume (cm^3/g)	BJH desorption average pore width (nm)
EFBA	9.76	0.0116	5.52
TiO_2	15.12	0.0441	9.81
T31	14.32	0.0253	12.93
T21	14.59	0.0269	12.14
T11	8.41	0.0181	14.27
T12	7.26	0.0261	13.55
T13	8.46	0.0162	11.13

Pristine TiO_2 shows the highest nitrogen uptake and pore volume, corresponding to a relatively higher surface area of 15.12 m^2/g (Table 4.8). This indicates a larger number of available adsorption sites for catalytic reactions. However, as discussed previously, TiO_2 nanoparticles tend to agglomerate during catalytic reactions, which

may reduce the number of accessible active sites. This behavior can be related to the relatively narrow average pore diameter of 9.81 nm, suggesting closely packed particles that are prone to clustering and aggregation.

Upon incorporation with the EFBA ash matrix, the TiO_2/EFBA composites exhibit noticeable changes in their textural properties depending on the TiO_2-to-EFBA ratio. In general, the surface area of the composites decreases compared to pure TiO_2, suggesting that immobilization of TiO_2 on the ash support may lead to partial pore blocking or coverage of surface pores. Among the composites, the T11 sample (1:1 ratio) shows a surface area of 8.41 m^2/g with the widest average pore diameter (14.27 nm). The wider pores may arise from interparticle voids formed during the dispersion of TiO_2 particles on the ash matrix (Awoke et al., 2020). These larger pores can provide more accessible pathways for reactant molecules, thereby facilitating adsorption and photocatalytic reactions.

Composites with higher TiO_2 loading, such as T21 and T31, demonstrate a more balanced combination of surface area (14.59 and 14.32 m^2/g, respectively) and mesopore width (12.14 and 12.93 nm), suggesting improved TiO_2 anchoring while maintaining the mesoporous structure. In contrast, composites with higher EFBA content, such as T12 and T13, exhibit lower surface areas (7.26 and 8.46 m^2/g) with pore widths of 13.55 and 11.13 nm, respectively. Overall, the pore volume of all composites decreases after incorporation of EFBA, indicating that the ash matrix partially fills or restructures the pore network. Meanwhile, the increase in pore width suggests the formation of slit-like mesopores associated with aggregated or layered morphologies. Such pore structures are advantageous for the adsorption of relatively larger molecules, such as oil-based reactants, thereby reducing mass transfer limitations during the photocatalytic process.

The FTIR analyses further support the role of EFBA as a structural scaffold that modifies and stabilizes the porous architecture of the composite. This structural modification enhances reactant accessibility to active sites while improving catalyst stability, which is beneficial for sustained photocatalytic performance during long-term applications.

4.2.6.2 ZnO and ZnO/EFBA Composite Analysis

Figure 4.20 presents the N_2 adsorption–desorption isotherms of EFBA, ZnO, and the Z11 composite. All samples exhibit Type IV isotherms with H3-type hysteresis loops, similar to those observed for the TiO_2 composites. This behavior is characteristic of mesoporous materials with slit-like pores, typically associated with layered or aggregated structures. Such mesoporosity indicates that the materials possess a considerable adsorption capacity.

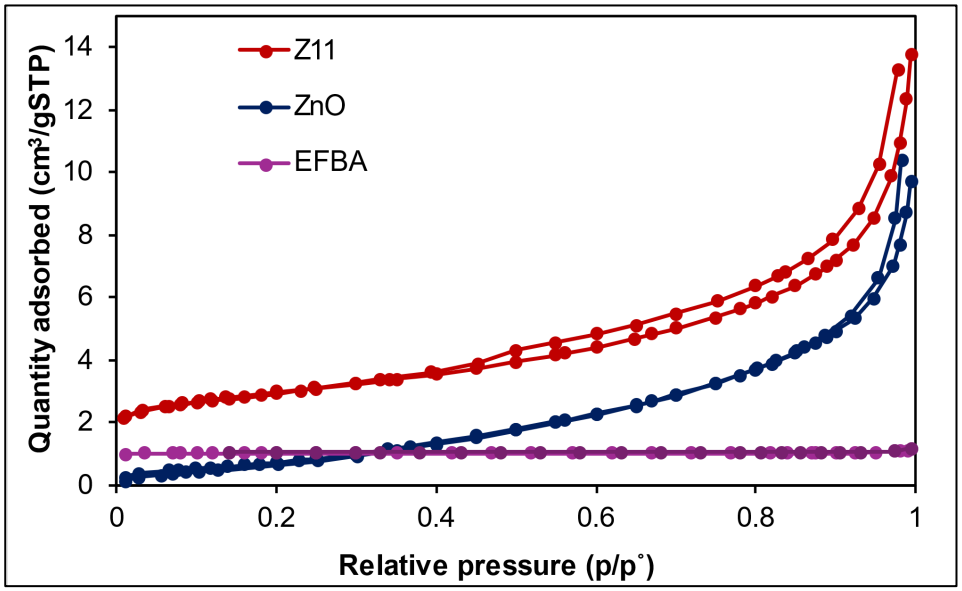


Figure 4.20 Nitrogen Adsorption-Desorption Isotherms of ZnO and Z11 Catalysts

Compared with ZnO and Z11, EFBA shows weaker N_2 adsorption–desorption behavior. This suggests that the pore structure of EFBA may be partially blocked or irregular, which restricts the accessibility of N_2 molecules during adsorption measurements. Nevertheless, as shown in Table 4.9, EFBA exhibits a relatively high surface area (9.76 $m^2\ g^{-1}$) and pore volume (0.0116 $cm^3\ g^{-1}$). These results indicate that EFBA contains a significant number of pores; however, their accessibility may be limited due to partial blockage or structural irregularities.

Table 4.9
BET Surface Area, Total Pore Volume, and BJH Desorption Average Pore Width of EFBA, ZnO, and ZnO/EFBA Catalysts

Catalyst	BET surface area (m^2/g)	Total pore volume (cm^3/g)	BJH desorption average pore width (nm)
EFBA	9.76	0.0116	5.52
ZnO	4.55	0.0085	5.21
Z11	6.95	0.0107	5.26

Meanwhile, pristine ZnO recorded the lowest surface area (4.55 $m^2\ g^{-1}$) and pore volume (0.0085 $cm^3\ g^{-1}$). This observation is consistent with its compact and aggregated morphology, which suggests limited surface exposure. The result also aligns with the XRD analysis, where ZnO exhibited the largest crystallite size (60.63 nm) compared with EFBA and Z11. The larger crystallite domains indicate that ZnO particles are more tightly packed, leading to reduced pore volume and limited surface adsorption.

After incorporation with EFBA, the surface area of the Z11 composite increased to 6.95 $m^2\ g^{-1}$, while the total pore volume increased to 0.0107 $cm^3\ g^{-1}$. This indicates that EFBA contributes to improved ZnO dispersion and helps prevent particle agglomeration, thereby increasing the accessible surface area. Such structural improvements may enhance reactant adsorption and potentially improve the efficiency of the photo-esterification reaction.

4.2.7 Carbon Dioxide Temperature–Programmed Desorption (CO_2-TPD) Analysis of Basic Surface Functionality

CO_2-TPD was conducted to evaluate the surface basicity of EFBA-based photocatalysts. The desorption temperatures correspond to the strength of CO_2-chemisorbed basic sites: weak (<300 °C), moderate (300–600 °C), and strong (>600 °C). The distribution and intensity of basic sites are crucial for catalytic performance in esterification systems, particularly those involving high FFA content, where both nucleophilic attack and intermediate stabilization are required.

4.2.7.1 EFBA and TiO_2-Based Composites Analysis

Figure 4.21 shows the CO_2-TPD profiles of EFBA, TiO_2, and the T11 composite. EFBA exhibits a broad desorption profile with peaks centered at

approximately 490 °C and 748 °C, corresponding to moderate and strong basic sites, respectively. These basic sites are attributed to the presence of alkaline and alkaline earth metal oxides, such as CaO, K_2O, and MgO, which originate from the biomass ash. The total CO_2 uptake of EFBA is 1134.02 µmol g^{-1}, which is the highest among the samples, demonstrating its strong intrinsic basicity (Table 4.10). Therefore, EFBA, when used as a support material, can enhance the overall basicity of semiconductor nanoparticles dispersed on its surface. This observation is further supported by the PL analysis, where the composite exhibited reduced emission intensity compared with the pristine semiconductor, indicating improved charge separation after EFBA incorporation.

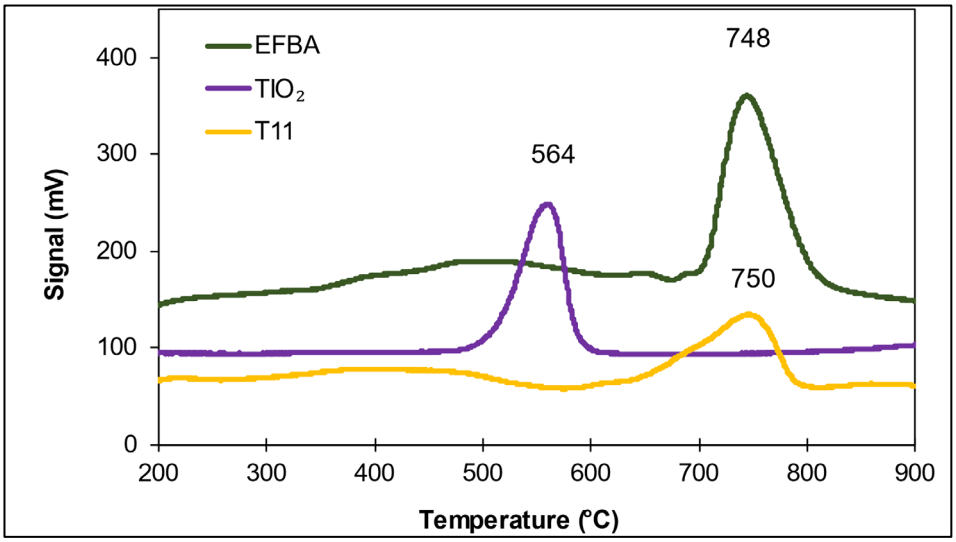


Figure 4.21 CO_2-TPD Profiles of EFBA, TiO_2, and T11

Table 4.10
CO_2 Adsorption Capacity of EFBA, TiO_2, and T11 at Different Desorption Temperatures

Catalyst	Temperature (°C)	Amount gas adsorbed (µmol/g)	Total amount gas adsorbed (µmol/g)
EFBA	350 − 650	339.10	1134.02
	748	794.92	
TiO_2	564	509.01	509.01
T11	300 − 550	157.82	508.69
	750	350.86	

Pristine TiO_2 exhibits a single desorption peak at approximately 564 °C, with a CO_2 uptake of 509.01 µmol g^{-1}, indicating the presence of medium-strength basic sites. These sites are typically attributed to Ti^{4+}–O^{2-} surface pairs and surface hydroxyl

groups, reflecting the amphoteric nature of TiO_2 and its potential role in facilitating interactions with FFA during esterification (Mino & Negri, 2020).

After incorporation with EFBA, the T11 composite displays a dual-peak desorption profile, consisting of moderate-strength basic sites at 300–550 °C (157.82 μmol g^{-1}) and strong basic sites at approximately 750 °C (350.86 μmol g^{-1}), with a total CO_2 uptake of 508.69 μmol g^{-1}. Although the total CO_2 uptake is comparable to that of pure TiO_2, the broader distribution of basic sites indicates a synergistic interaction between TiO_2 and EFBA. The moderate-strength sites may facilitate the adsorption and activation of FFA molecules, while the stronger basic sites can promote deprotonation and enhance the esterification process.

4.2.7.2 ZnO and ZnO/EFBA Composite Analysis

Figure 4.22 shows that pristine ZnO exhibits a desorption peak at approximately 263 °C, corresponding to a CO_2 uptake of only 79.55 μmol g^{-1} (Table 4.11). This indicates its inherently low surface basicity, which may limit its effectiveness in directly catalyzing FFA esterification. In contrast, the Z11 composite displays a substantial enhancement in surface basicity, with two prominent desorption peaks at 518 °C (518.70 μmol g^{-1}) and 767 °C (479.51 μmol g^{-1}), resulting in a total CO_2 uptake of 998.21 μmol g^{-1}. These peaks correspond to moderate- and strong-strength basic sites, respectively, similar to those observed in the T11 composite.

This result indicates the successful integration of ZnO within the EFBA matrix, which significantly enhances the basicity of the composite catalyst. The increased density of basic sites suggests that Z11 may exhibit improved performance in the photo-esterification reaction. Moreover, the high basicity of Z11, combined with the reactive oxygen species generated by ZnO under light irradiation, may enhance reactant adsorption and promote a dual-function catalytic mechanism for efficient and selective esterification of high-FFA feedstocks.

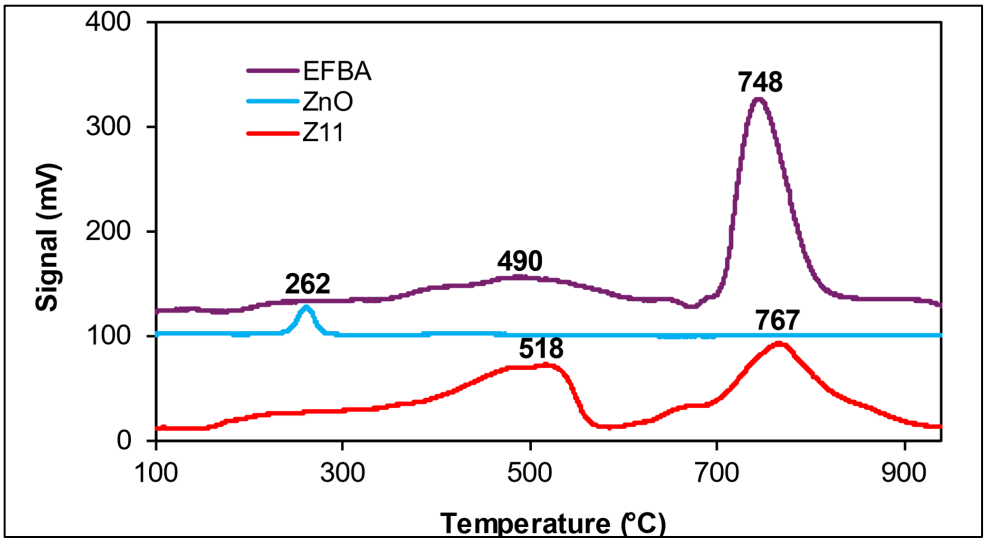


Figure 4.22 CO_2-TPD Profiles of EFBA, ZnO, and Z11

Table 4.11
CO_2 Adsorption Capacity of EFBA, ZnO, and Z11 at Different Desorption Temperatures

Catalyst	Temperature (°C)	Amount gas adsorbed (µmol/g)	Total amount gas adsorbed (µmol/g)
EFBA	490	339.10	1134.02
	748	794.92	
ZnO	262	79.55	79.55
Z11	518	518.70	998.21
	767	479.21	

4.2.8 Thermogravimetric Analysis (TGA)

Thermogravimetric analysis (TGA) was conducted to examine the thermal behavior, compositional transitions, and calcination tolerances of EFBA-based composites, particularly T11 and Z11 systems.

4.2.8.1 EFBA and TiO_2, and TiO_2/EFBA

Figure 4.23 presents the thermogravimetric analysis of EFBA, which undergoes a multi-stage decomposition process. The first weight loss begins at approximately 90.2 °C, with an initial mass reduction of 3.99% (Table 4.12). This loss is attributed to the removal of physically adsorbed moisture and light volatile molecules present on the EFBA surface. A second decomposition stage occurs between 299–413 °C, resulting in a 0.67% mass loss. This stage is likely associated with the release of weakly bound

carbonyl compounds and light hydrocarbons, suggesting that minor organic residues remain in the ash. These residues may originate from incomplete combustion during the biomass burning process, leaving small amounts of carbonaceous material embedded within the ash matrix (Shahdan et al., 2023).

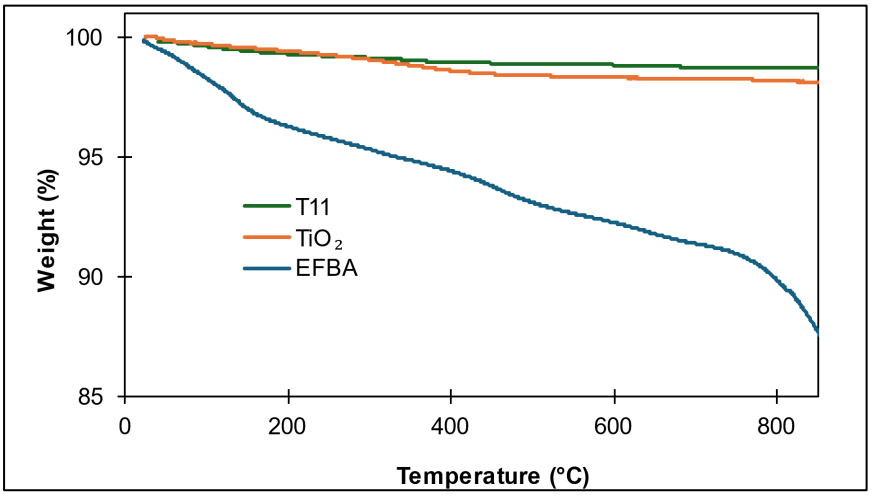


Figure 4.23 The TGA Analysis for EFBA, TiO_2 and T11

Table 4.12
TGA Analysis for EFBA, TiO_2 and T11

Catalyst	Onset temperature (°C)	Major weight loss range (°C)	Total weight loss (%)	Residue (%)
EFBA	90.2	90 - 299	3.99	78.30
	299.5	299 - 413	0.67	
	413.8	413 - 800	3.59	
	800.4	800 - 850	13.07	
TiO_2	106.6	106 - 847	1.57	98.43
T11	90.1	90 - 847	1.29	98.71

Between 413–800 °C, an additional 3.59% weight reduction is observed, which can be attributed to the gradual oxidation of residual carbonaceous species as well as possible mineral phase transitions. This behavior indicates that structural rearrangements may occur within the EFBA matrix at elevated temperatures. Such thermal effects may lead to partial pore collapse or a reduction in surface area, potentially affecting the structural integrity of the material. Consequently, excessive thermal exposure could weaken the interfacial interaction between EFBA and the semiconductor catalyst, which may negatively influence the catalytic performance during the photo-esterification process (Alessandro, 2023).

In addition, the most prominent weight loss occurs between 800–850 °C (13.07%), corresponding to the decomposition of carbonate species such as $CaCO_3$. The overall weight loss of 21.32%, with a final residue of 78.30%, confirms the presence of thermally stable mineral oxides such as CaO, SiO_2, and Al_2O_3, which are typical inorganic constituents of EFBA. Therefore, these results suggest that EFBA exhibits better performance at lower temperatures, where the inorganic mineral components of the ash remain stable and can effectively facilitate interaction with the semiconductor material during photocatalysis (Elanthikkal et al., 2023).

Pristine TiO_2 shows excellent thermal stability, with decomposition initiating at 106.6 °C and minimal total weight loss of 1.57% over the 106–995 °C range. This reflects the elimination of surface-bound hydroxyl groups and slight structural reordering. The high residue content (98.43%) confirms its resistance under high-temperature conditions. After incorporation with EFBA, T11 composite displays a thermal profile similar to that of TiO_2. Although decomposition begins at 90.1 °C, comparable to EFBA. The total weight loss is limited to 1.29%, with a residue of 98.71%. This suggests that TiO_2 effectively stabilizes the composite by immobilization on the EFBA matrix.

4.2.8.2 ZnO and ZnO/EFBA Composite Analysis

As shown in Figure 4.24, pure ZnO demonstrates minimal thermal degradation, with decomposition beginning at 166.1 °C and a total weight loss of just 0.31% across the 166–850 °C range (Table 4.13). The high residue value (99.69%) confirms the structural stability of ZnO under high thermal condition (Mustafa et al., 2024).

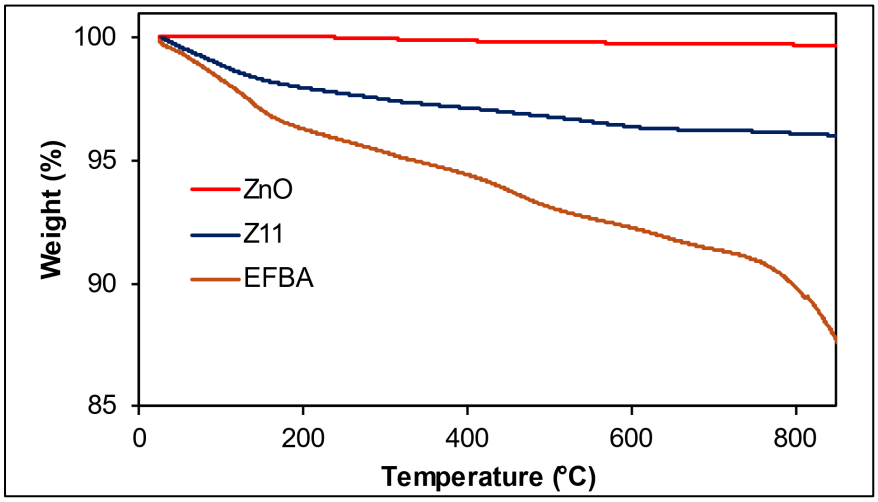


Figure 4.24 The TGA Analysis for EFBA, ZnO and Z11

Table 4.13
TGA Analysis for EFBA, ZnO and Z11

Catalyst	Onset temperature (°C)	Major weight loss range (°C)	Total weight loss (%)	Residue (%)
EFBA	90.2	90 - 299	3.99	78.30
	299.5	299 - 413	0.67	
	413.8	413 - 800	3.59	
	800.4	800 - 850	13.07	
ZnO	166.1	166.1 - 850	0.31	99.69
Z11	174	174 - 847	3.97	96.03

The Z11 composite displays a slightly broader degradation profile. Its decomposition begins at 174 °C, slightly higher than EFBA's onset, and reflects the onset of organic matter breakdown within the ash-based matrix. A total weight loss of 3.97% occurs over the 174–847 °C range, primarily attributed to organic decomposition and mineral phase transitions. This indicates the decomposition of EFBA, as the ZnO is thermally stable at high temperatures. Despite this loss, the composite retains a high residue of 96.03%, attributes to stability of ZnO at high temperature.

4.2.9 X-ray Fluorescence (XRF) Analysis

XRF spectroscopy was employed to evaluate the elemental stability and surface compositional changes of T11 and Z11 composites before and after five cycles of photocatalytic reaction.

4.2.9.1 XRF Analysis of TiO_2/EFBA Composites

As shown in Table 4.14, the T11 composite exhibited good elemental stability over five photocatalytic cycles. The TiO_2 content increased from 70.5% in the fresh sample to 73.9% after the fifth cycle, suggesting that some inorganic elements from EFBA may have migrated or partially dissolved. This indicates that TiO_2 became slightly more dominant in the composite after repeated use.

Table 4.14
XRF Analysis of the Optimized T11 Catalyst in its Fresh State and After the 5th Recycling Cycle

Component	T11	
	Fresh	Spent
TiO_2	70.5	73.9
ZnO	-	-
SiO_2	10.1	10.6
K_2O	9.61	6.06
CaO	2.72	2.93
Al_2O_3	2.68	2.35
Fe_2O_3	1.26	1.20
Cl	1.15	0.18
P_2O_5	0.98	0.98
MgO	0.37	0.78
SO_3	0.33	0.68
MnO	0.12	0.11
Other metal oxides	0.18	0.23

Moreover, the elemental composition of EFBA remained largely stable, with slight increases observed in several components. For instance, SiO_2 increased from 10.1% to 10.6%, CaO from 2.72% to 2.93%, MgO from 0.37% to 0.78%, and SO_3 from 0.33% to 0.68%. These increases may be attributed to re-adsorption or mineral transformations during the reaction cycles, indicating some structural evolution while maintaining overall composite stability (Rahmat et al., 2021)

In contrast, reductions were observed in K_2O (9.61% to 6.06%) and Cl (1.15% to 0.18%), suggesting leaching of soluble alkali and halide species during photocatalysis, likely due to methanol's solvent effect on these highly soluble elements. Minor changes in Al_2O_3, Fe_2O_3, and P_2O_5 indicate the stability of these elements, which helps preserve the composite framework. A slight increase in "other metal oxides" (0.18% → 0.23%) may reflect trace element accumulation (e.g., Ni, Cu, Zn, Sr), though these did not appear to affect catalytic performance.

Overall, the T11 composite retained its structural integrity throughout multiple cycles, as further supported by TGA analysis, which confirms the presence of a stable framework.

4.2.9.2 XRF analysis of ZnO and ZnO/EFBA Composite

XRF analysis has been done for ZnO and Z11 as the performance of ZnO and Z11 both high during the photo esterification. Table 4.15 presents the elemental composition of ZnO and Z11 in their fresh and spent states after five catalytic cycles. The pristine ZnO remained chemically stable, with only a minor reduction in ZnO content from 99.8% to 99.3% after five cycles, reflecting its inert nature and strong structural retention during the reaction process. However, ZnO alone tends to agglomerate with the oil sample, making the separation process difficult. This behavior is attributed to the nanoscale particle size of ZnO. The observation is supported by FESEM analysis, which revealed a cluster-like morphology that promotes particle aggregation.

Table 4.15
The XRF Analysis of ZnO and Z11 Catalyst in its Fresh State and After the 5th Recycling Cycle

Component	ZnO		Z11	
	Fresh	Spent	Fresh	Spent
ZnO	99.8	99.3	76.9	64.7
SiO_2	-	-	11.4	19.9
K_2O	-	-	4.74	5.82
CaO	-	-	3.22	4.84
Al_2O_3	-	-	0.30	0.59
Fe_2O_3	-	-	0.93	1.33
Cl	-	-	0.06	0.02
P_2O_5	-	-	0.99	1..47
MgO	-	-	1.22	1.03
SO_3	-	-	0.04	0.08
MnO	-	-	0.09	0.14
Other metal oxides	0.2	0.7	6.72	1.55

For the Z11 composite, the ZnO content decreased from 76.9% to 64.7%, suggesting partial surface depletion of ZnO after repeated photocatalytic cycles. This phenomenon may be associated with the amphoteric nature of ZnO and its susceptibility to photocorrosion, where Zn^{2+} ions can be released under UV irradiation. Therefore, the reduction in ZnO content in Z11 is likely attributed to surface restructuring and

photocorrosion rather than significant leaching of active species into the reaction medium. Furthermore, the presence of EFBA-derived oxides, methanol, and reactive species generated during photocatalysis could accelerate the surface depletion of ZnO. Similar observations have been reported in previous studies where ZnO-based photocatalysts experienced gradual Zn loss due to photocorrosion under prolonged UV exposure (Gegova-Dzhurkova et al., 2024).

Notably, the relative percentage of SiO_2 increased from 11.4% to 19.9%, along with increases in CaO (3.22% to 4.84%) and K_2O (4.74% to 5.82%). This apparent increment is consistent with the trend observed in T11 composites and likely reflects the relative enrichment of EFBA-derived inorganic oxides after partial ZnO depletion. As ZnO content decreases, the proportion of stable ash-derived oxides becomes more prominent in the overall composition. Additionally, the increase in oxides such as Fe_2O_3 (0.93% to 1.33%), Al_2O_3 (0.30% to 0.59%), and MnO (0.09% to 0.14%) suggests that these mineral phases remain structurally stable during the reaction, indicating low leaching potential and strong retention within the EFBA matrix.

This is further supported by the reusability test discussed in the following section, where the catalyst maintained high activity after several cycles. These findings suggest that the Z11 composite catalyst possesses good structural stability and is suitable for long-term photocatalytic applications.

4.3 Optimization on the Photocatalytic Esterification Reaction

These foundational tests were conducted using an initial 1:1 catalyst mass ratio (TiO_2:EFBA (T11) and ZnO:EFBA (Z11)), which served as the baseline formulation for photocatalytic performance screening. After that, post-OVAT refinements were introduced to examine the effect of varying mass ratios between semiconductor and EFBA and calcination temperatures.

4.3.1 Photocatalytic Performance of TiO_2 and TiO_2/EFBA

The initial FFA content of untreated WCO was 12.4 wt% and served as the baseline for evaluating photocatalytic esterification performance and calculating conversion efficiency.

4.3.1.1 Effect of Reaction Time

The effect of reaction time on the photocatalytic esterification of WCO was investigated using TiO_2 and T11 catalysts under UV-A irradiation (λ = 365 nm), with a fixed methanol-to-WCO molar ratio of 20:1 and catalyst loading of 4 wt%.

For pristine TiO_2, the FFA content decreased slightly from 12.4 wt% to 9.57 wt% after 1 h (Figure 4.25a), corresponding to a conversion of only 20% (Figure 4.25b). The limited reduction suggests that FFA molecules may not strongly interact with the TiO_2 surface. This behavior can be attributed to the hydrophilic nature of TiO_2, which tends to weakly interact with the carboxyl functional group of FFA while showing poor affinity toward the long hydrophobic hydrocarbon chain (Fadilah et al., 2023). Moreover, TiO_2 alone provides limited surface area and relatively low defect site density, which restricts the number of accessible active sites for FFA and methanol molecules. This indicates that pristine TiO_2 alone is insufficient for efficient FFA esterification.

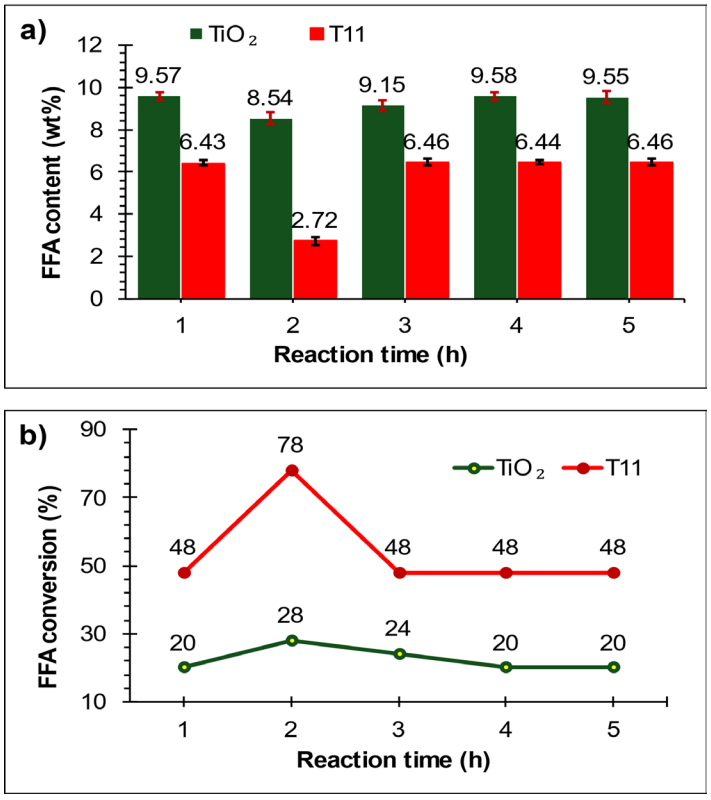


Figure 4.25 Effect of Reaction Time on a) FFA Content and b) Conversion for TiO_2 and TiO_2/EFBA 1:1 (T11) under UV-A Irradiation (λ = 365 nm) with 20:1 Methanol-to-WCO Molar Ratio and 4 wt% Catalyst Loading

At 2 h, the FFA content further decreased slightly to 8.54 wt%, corresponding to a conversion of approximately 28%. The improvement may be attributed to the longer reaction time, which allows more FFA molecules to adsorb onto the TiO_2 surface and participate in the esterification process. However, when the reaction time was extended from 3 h to 5 h, the conversion slightly decreased, with FFA content increasing again to 9.15 wt%, 9.58 wt%, and 9.55 wt%, corresponding to conversions of 24%, 20%, and 20%, respectively. This decline may be related to weak adsorption of long-chain FFA molecules on the TiO_2 surface and possible desorption during prolonged reaction time.

This observation is supported by the BET analysis, where the pore size of TiO_2 was found to be only 9.81 nm. Such relatively small pores may limit the diffusion and accommodation of bulky long-chain FFA molecules present in WCO, resulting in insufficient adsorption on the TiO_2 surface. Similar findings have been reported in previous studies, where pristine TiO_2 exhibited limited catalytic activity for esterification reactions due to its low affinity toward hydrophobic fatty acid molecules and restricted pore accessibility (Semenova et al., 2025).

In contrast, the T11 catalyst achieved a substantial reduction in FFA content, decreasing from 6.43 wt% at 1 h to 2.72 wt% at 2 h, corresponding to a conversion of 78%. This demonstrates that T11 exhibits significantly improved performance compared with pristine TiO_2, highlighting the effectiveness of EFBA as a support material in enhancing photocatalytic esterification performance. This improvement can be attributed to the immobilization of TiO_2 onto the EFBA matrix, which improves the dispersion of TiO_2 and increases the availability of catalytic active sites. In addition, the alkaline oxides present in EFBA, such as K_2O and CaO, enhance the surface basicity of the composite, thereby promoting stronger adsorption and activation of FFA molecules during the esterification process.

This observation is supported by CO_2-TPD analysis, where T11 exhibited both moderate and strong basicity, indicating the presence of active sites capable of strongly adsorbing FFA molecules onto the catalyst surface. Furthermore, BET analysis revealed that the pore size of T11 increased to 14.27 nm after modification, which facilitates improved diffusion and adsorption of bulky FFA molecules during the reaction.

In addition, PL analysis showed that T11 exhibited lower PL intensity under excitation at 375 nm, indicating reduced electron–hole recombination compared with pristine TiO_2. This suggests that the EFBA support enhances charge separation and

improves the photocatalytic efficiency of TiO_2 under UV-A irradiation. Overall, T11 emerges as a promising catalyst for efficient FFA reduction in WCO, making it a suitable candidate for scalable biodiesel pretreatment processes.

4.3.1.2 Effect of Methanol-to-WCO Molar Ratio

The influence of the methanol-to-WCO molar ratio on photocatalytic esterification was investigated for both TiO_2 and the T11 system under UV-A irradiation (λ = 365 nm), with a fixed reaction time of 2 h and catalyst loading of 4 wt%. Molar ratios ranging from 12:1 to 24:1 were evaluated to determine the optimal methanol dosage for maximizing FFA conversion.

For pristine TiO_2, the FFA content slightly decreased from 12.4 wt% to 9.19 wt% and 9.68 wt% across the tested range Figure 4.26a. This suggests that TiO_2 is relatively insensitive to variations in methanol concentration under the studied conditions.

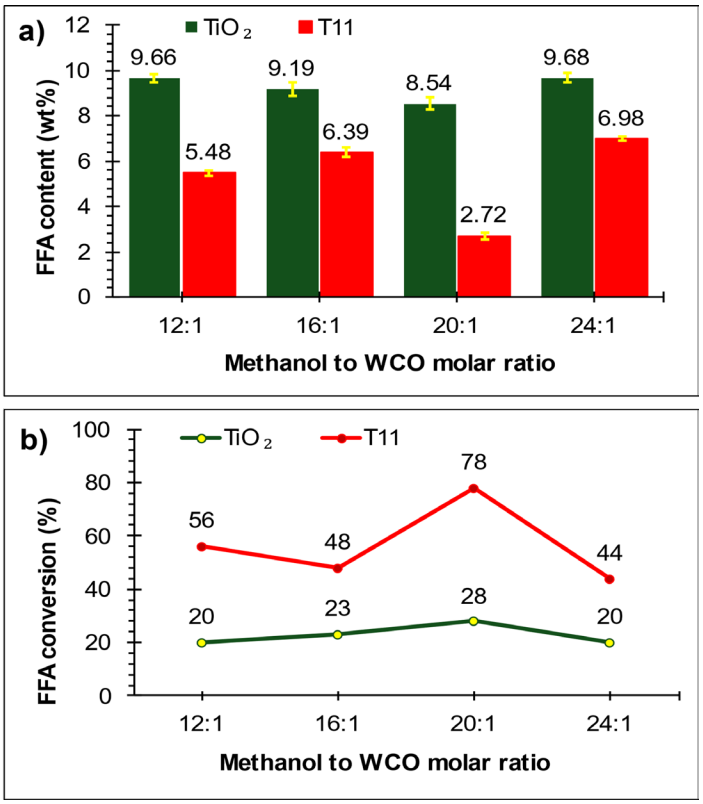


Figure 4.26 Effect of Methanol-to-WCO Molar Ratio on a) FFA Content and b) FFA Conversion for TiO_2 and T11 under UV-A Irradiation (λ = 365 nm), with 2 h Reaction Time and 4 wt% Catalyst Loading

The highest FFA conversion recorded was only 28% at a molar ratio of 20:1 (Figure 4.26b). This minor improvement can be explained by Le Chatelier's principle, where an excess of methanol shifts the esterification equilibrium toward ester formation (Fazil & Ahmad, 2023). However, when the molar ratio was increased to 24:1, the conversion decreased to 20%. This decline may be attributed to excessive methanol diluting the reaction mixture, which reduces the effective interaction between FFA molecules and the TiO_2 surface. In addition, excess methanol may hinder photon penetration and reduce photocatalytic efficiency by interfering with light absorption at the catalyst surface (Khan et al., 2021).

In contrast, the T11 composite exhibited significantly higher activity, achieving up to 78% conversion with a reduction of FFA content to 2.72 wt% at a 20:1 molar ratio. This substantial enhancement can be attributed to the synergistic interaction between TiO_2 and the EFBA support. The alkaline oxides present in EFBA enhance the surface basicity of the catalyst and improve methanol adsorption, thereby facilitating the esterification reaction (Gao et al., 2023). Moreover, the irregular pore structure of EFBA observed from FESEM analysis may improve light scattering and photon utilization, which further enhances photocatalytic activity during the reaction process.

However, when the molar ratio was increased to 24:1, the conversion decreased to 44%. This reduction indicates that excessive methanol may negatively affect the reaction system. Since esterification is a reversible reaction, an excessive amount of methanol may disrupt the optimal interaction between reactants and catalyst surfaces. Furthermore, excess methanol can introduce mass transfer limitations and optical dilution effects, where the high methanol concentration reduces effective light absorption by the catalyst. These results suggest that a methanol-to-WCO molar ratio of 20:1 is optimal for achieving high FFA conversion under the studied photocatalytic conditions.

4.3.1.3 Effect of Catalyst Loading

The effect of catalyst loading on photocatalytic esterification was investigated while maintaining constant reaction conditions of 2 h reaction time and a 20:1 methanol-to-oil molar ratio. Catalyst loading ranging from 1 to 5 wt% was evaluated using both pristine TiO_2 and the T11 composite.

Across all tested dosages, pristine TiO_2 displayed consistently low photocatalytic performance. The FFA content remained relatively high (8.54–9.26 wt%), while the conversion increased only slightly from 24% at 1 wt% loading to 28% at 4 wt%, before decreasing marginally to 27% at 5 wt% (Figure 4.27b). As discussed previously, the limited catalytic improvement of TiO_2 may be attributed to its relatively small pore size and highly crystalline structure, which restrict the adsorption and activation of bulky FFA molecules and methanol on the catalyst surface. Consequently, the number of accessible active sites remains limited, resulting in low photocatalytic esterification efficiency.

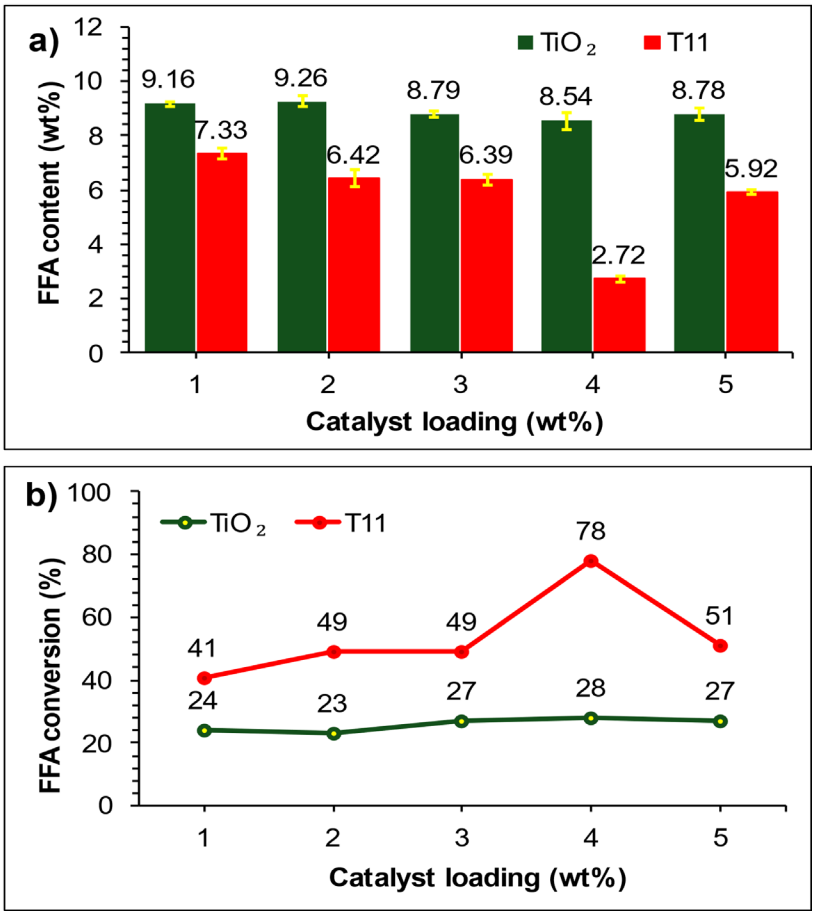


Figure 4.27 Effect of Catalyst Loading on a) FFA Content Reduction and b) FFA Conversion, Catalyzed by TiO_2 and TiO_2/EFBA 1:1 (T11) under 20:1 Methanol-to-Oil Molar Ratio and 2 h Reaction Time

Furthermore, increasing TiO_2 loading beyond 4 wt% did not significantly enhance the reaction activity. This behavior may be associated with particle

agglomeration at higher catalyst concentrations, which can hinder light penetration and reduce effective photon absorption on the catalyst surface.

In contrast, the T11 composite demonstrated significantly enhanced photocatalytic performance across the investigated dosage range compared with pristine TiO_2. As the catalyst loading increased from 1 wt% to 4 wt%, the conversion improved substantially from 41% to 49%, 49%, and reached the highest conversion of 78% at 4 wt%, with the FFA content decreasing to 2.72 wt%. This improvement suggests that higher catalyst loading increases the number of available surface-active sites, while the synergistic interaction between TiO_2 and EFBA promotes more effective adsorption and activation of FFA molecules.

In addition, PL analysis showed that the T11 composite exhibited lower emission intensity compared with pristine TiO_2, indicating reduced electron–hole recombination. This suggests that the EFBA matrix may act as an electron sink, facilitating charge separation and prolonging the lifetime of photogenerated charge carriers. The presence of mineral oxides from EFBA, as indicated by FTIR analysis, may further assist in temporarily trapping electrons, thereby suppressing rapid recombination and enhancing photocatalytic activity. These combined effects contribute to improved photo-esterification efficiency and higher adsorption capacity of the catalyst.

However, when the catalyst loading was further increased to 5 wt%, the FFA conversion decreased to 51%, with the FFA content increasing to 5.92 wt%. This reduction in performance indicates that excessive catalyst loading may negatively affect the reaction system. At high catalyst concentrations, the reaction mixture becomes more turbid, which can block light penetration and reduce effective photon absorption by the catalyst surface (Ushasaraswathi, 2023). In addition, excessive catalyst particles may lead to aggregation and increased mass transfer limitations, hindering the diffusion of reactant molecules to the active sites (Sharma & Prakash, 22025). Therefore, a catalyst loading of 4 wt% was identified as the optimal dosage for achieving the highest FFA conversion under the studied photocatalytic conditions.

4.3.1.4 Effect of Light Sources on TiO_2/EFBA Performance

The influence of light sources on photocatalytic esterification was investigated using the T11, based on its superior performance compared with pristine TiO_2 in the previous optimization studies. The reaction was conducted under the optimized conditions of 2 h reaction time, a 20:1 methanol-to-WCO molar ratio, and 4 wt% catalyst loading.

Prior to evaluating different light sources, a control experiment was conducted to determine whether the catalyst could perform in the absence of light irradiation. As shown in Figure 4.28, the reaction without light resulted in only 9.45% conversion, indicating minimal catalytic activity. This suggests that T11 requires light irradiation to activate the photocatalytic process. Under irradiation, photogenerated electron–hole pairs are produced on the catalyst surface, which subsequently generate reactive oxygen species that facilitate the conversion of FFA into FAME. This observation confirms that photocatalytic activation is essential for initiating the oxidation–reduction reactions that drive the esterification process.

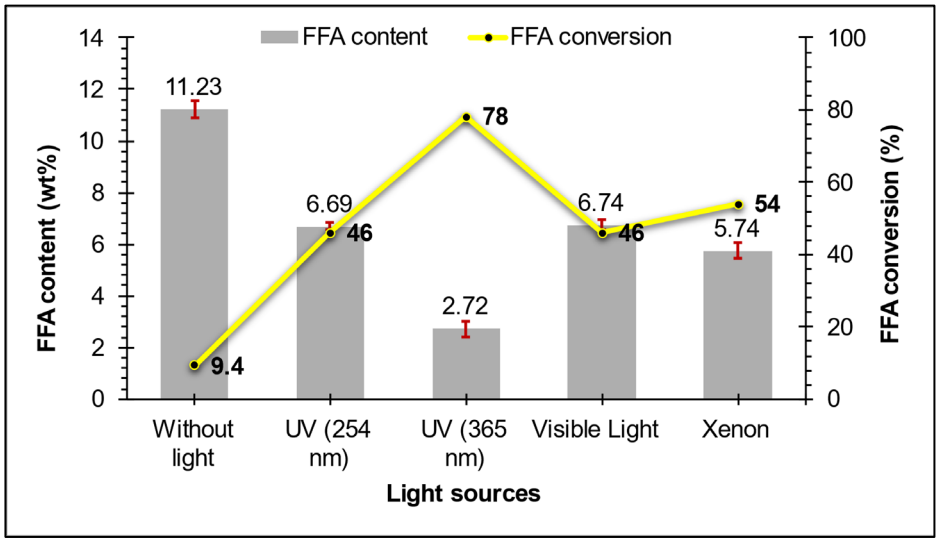


Figure 4.28 Effect of Different Light Sources on FFA Content Reduction and Conversion During Photo-Esterification Catalyzed by TiO_2/EFBA 1:1 (T11) under Optimized Conditions: 2 h Reaction Time, 20:1 Methanol-to-WCO Molar Ratio, and 4 wt% Catalyst

Ultraviolet (UV) radiation typically ranges from 100 nm to 400 nm and can be categorized into three regions: UV-A (320–400 nm), UV-B (280–320 nm), and UV-C

(100–280 nm). In this study, the photocatalytic performance was evaluated under UV-A and UV-C irradiation. UV-C irradiation resulted in a conversion of 46%, which is lower than the 78% conversion achieved under UV-A irradiation. This indicates that the T11 catalyst performs more efficiently under longer wavelength UV-A light. The improved performance is likely related to the bandgap energy of T11, which was estimated to be 2.94 eV. This bandgap corresponds well to the energy of UV-A photons, enabling efficient electron excitation and photocatalytic activation under UV-A irradiation (Mohamadpour & Amani, 2024).

In comparison, irradiation under visible light resulted in a lower conversion of 46%, which can be attributed to the lower photon energy of visible light that limits the excitation of electrons across the catalyst bandgap. As a result, the photocatalyst cannot effectively utilize the broader visible light spectrum for catalytic activation. A similar trend was observed when a xenon lamp was used as the light source. Although the xenon lamp emits a broad-spectrum covering UV, visible, and near-infrared regions, the conversion achieved was only 54%. This suggests that the catalyst primarily absorbs photons within the UV region, particularly UV-A, while the visible and infrared components contribute minimally to the photocatalytic process. Overall, these findings confirm that UV-A irradiation at 365 nm is the most suitable light source for activating the T11 catalyst, providing sufficient photon energy to initiate electron excitation and enhance photocatalytic esterification performance.

4.3.1.5 Effect of TiO_2/EFBA mass ratio

The mass ratio between TiO_2 and EFBA plays a pivotal role in modulating the composite's photocatalytic performance in the esterification of WCO. This section evaluates TiO_2/EFBA mass ratios ranging from 3:1 to 1:3 under optimized conditions of 2 h reaction time, a 20:1 methanol-to-WCO molar ratio, and 4 wt% catalyst loading under UV-A irradiation (λ = 365 nm).

Figure 4.29 presents the catalytic performance of different TiO_2/EFBA composites, namely T31 (3 g TiO_2 : 1 g EFBA), T21 (2 g TiO_2 : 1 g EFBA), T11 (1 g TiO_2 : 1 g EFBA), T12 (1 g TiO_2 : 2 g EFBA), and T13 (1 g TiO_2 : 3 g EFBA). Among these composites, T11 achieved the highest FFA conversion of 78% compared with other TiO_2/EFBA mass ratios. This result suggests that, at the 1:1 ratio, the TiO_2

nanoparticles are more uniformly dispersed within the porous EFBA matrix. The balanced proportion between TiO_2 and EFBA allows sufficient photocatalytic active sites while maintaining good dispersion of TiO_2 particles. In addition, the EFBA matrix can reduce particle agglomeration and provide surface defects that facilitate electron transfer during the photocatalytic redox reaction.

In contrast, composites with higher TiO_2 content such as T31 and T21 achieved lower FFA conversions of 44% and 30%, respectively. This behavior indicates that excessive TiO_2 loading may lead to particle agglomeration, which reduces the effective surface area and causes light shielding effects. As a result, fewer catalyst surfaces are exposed to light irradiation, thereby limiting photon absorption and reducing photocatalytic activity.

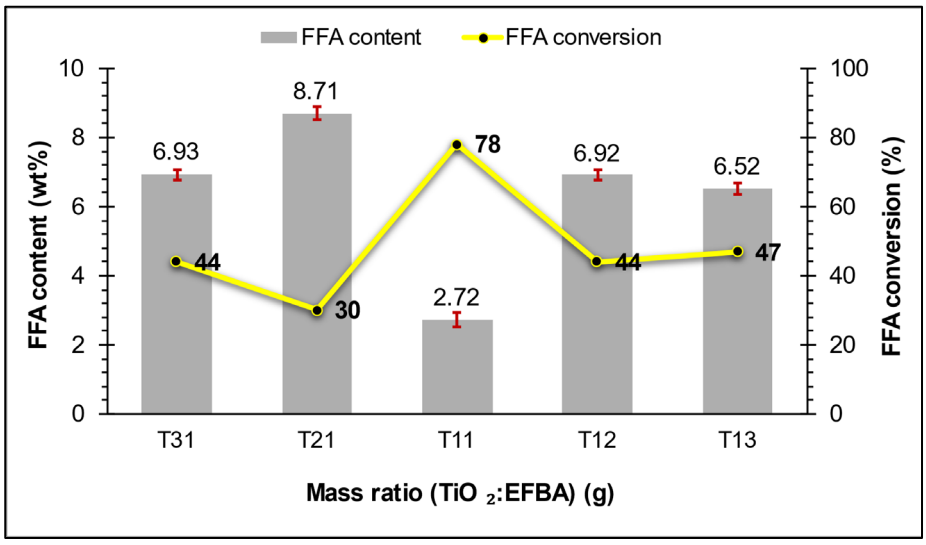


Figure 4.29 Effect of TiO_2/EFBA Mass Ratio on FFA Content Reduction and Conversion Under 2 h Reaction Time, 20:1 Methanol-to-WCO Molar Ratio, and 4 wt% Catalyst Loading

On the other hand, T12 and T13, which contain higher EFBA loading, achieved FFA conversions of 44% and 47%, respectively. This suggests that excessive EFBA content may dilute the active photocatalytic sites of TiO_2 and decrease the number of available sites for the esterification reaction. Moreover, although EFBA can act as an electron trapping medium that facilitates charge separation, an excessive amount of EFBA may also introduce additional recombination centres that hinder efficient electron transfer during photocatalysis (Erfan et al., 2023).

Therefore, based on these observations, the 1:1 mass ratio of TiO_2 and EFBA (T11) represents the optimal composition, as it provides a balanced interaction between the photocatalytic activity of TiO_2 and the structural support of EFBA. This optimal ratio enhances light absorption, improves charge separation, and provides sufficient active sites for efficient photocatalytic esterification.

4.3.1.6 Effect of Thermal Treatment Temperature on TiO_2/EFBA Performance

Figure 4.30 shows the effect of thermal treatment on the photocatalytic performance of the T11 composite during photo-esterification. The calcination of T11 was conducted at 100 °C, 300 °C, and 500 °C. The reaction conditions were fixed at 2 h reaction time, a 20:1 methanol-to-WCO molar ratio, and 4 wt% catalyst loading.

T11 treated at 100 °C exhibited the best catalytic performance, achieving the highest FFA conversion of up to 78%. This high activity can be attributed to the preservation of surface functional groups such as hydroxyl groups, carbonate species, and alkali metal oxides derived from EFBA, as well as the retention of the porous structure of the composite. These surface functionalities play an important role in maintaining surface basicity and providing adsorption sites that facilitate the interaction between FFA and methanol molecules during the photocatalytic reaction (Arun et al., 2023)

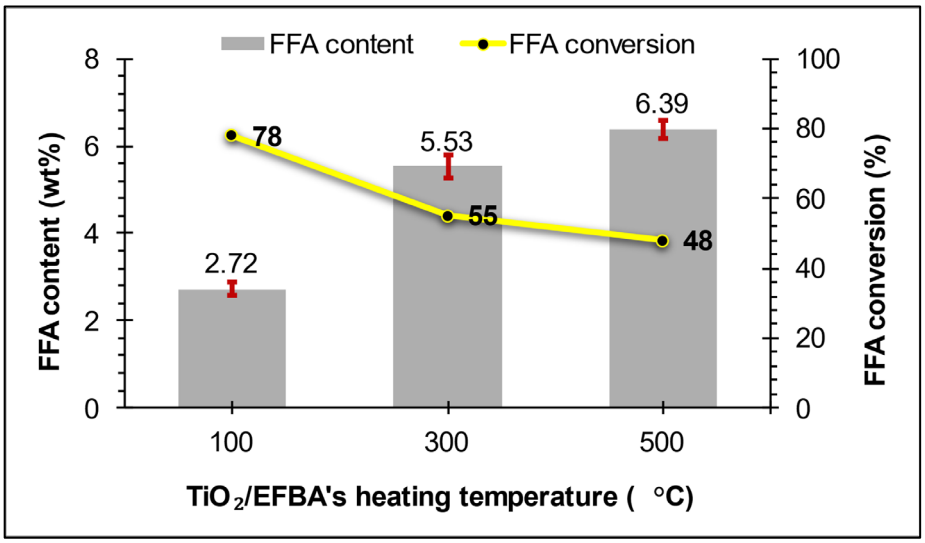


Figure 4.30 Effect of T11 Thermal Treatment Temperature on FFA Content Reduction and Conversion under 2 h Reaction Time, 20:1 Methanol-to-WCO Molar Ratio, and 4 wt% Catalyst Loading

This observation is supported by TGA analysis, which indicates that significant thermal decomposition of EFBA-derived inorganic components occurs between 100 °C and 300 °C. Therefore, at a calcination temperature of 100 °C, most of the beneficial inorganic constituents and surface functional groups remain intact, allowing the catalyst to maintain high photocatalytic activity. Similar observations have been reported in previous studies, where mild thermal treatment preserved surface-active species and enhanced the catalytic performance of ash-based photocatalysts (El-Sayed et al., 2024).

In contrast, calcination at higher temperatures of 300 °C and 500 °C resulted in lower FFA conversions of only 55% and 48%, respectively. The significant decrease in catalytic performance suggests the partial loss of surface-active species at elevated temperatures. High-temperature treatment may lead to the decomposition of surface functional groups and the removal of alkali components from EFBA, which reduces the surface basicity of the catalyst. In addition, excessive heating may induce pore collapse and promote agglomeration of TiO_2 particles, thereby reducing the accessible surface area and limiting reactant diffusion within the catalyst matrix. Therefore, calcination at 100 °C provides the optimal thermal treatment condition for preserving the structural integrity and photocatalytic functionality of the TiO_2/EFBA composite.

4.3.2 Photocatalytic Performance of ZnO and ZnO/EFBA

4.3.2.1 Effect of Reaction Time

Figure 4.31a and Figure 4.31b illustrates the reduction of FFA content and the corresponding FFA conversion for ZnO and the Z11 under different reaction times ranging from 1 h to 5 h. The reaction conditions were fixed at a 20:1 methanol-to-WCO molar ratio and 4 wt% catalyst loading.

For pristine ZnO, rapid catalytic activation was observed during the initial reaction stage. The FFA content decreased significantly from the initial value of 12.4 wt% in WCO to 4.20 wt% after 1 h. At 2 h, the FFA content slightly increased to 4.56 wt%, followed by a gradual decrease to 2.78 wt% after 5 h. Correspondingly, the FFA conversion increased from 66% at 1 h to 63% at 2 h and then progressively increased to a maximum of 78% at 5 h. This trend indicates that ZnO exhibits efficient catalytic

performance during the mid-to-late reaction stages (3–5 h), where longer reaction time allows more effective interaction between FFA molecules and the catalyst surface.

The relatively high catalytic activity of ZnO suggests that the catalyst can perform effectively even without a supporting matrix. This behavior may be attributed to the presence of surface oxygen species (O^{2-}) on the ZnO surface, which can facilitate strong interaction and adsorption of FFA molecules. In addition, ZnO possesses a relatively high exciton binding energy (~60 meV), which can stabilize photogenerated electron–hole pairs and enhance redox reaction efficiency under light irradiation. Previous studies have also reported that the stable wurtzite crystal structure of ZnO contributes to improved photocatalytic activity due to efficient charge transport and light absorption properties (Baig et al., 2025). Therefore, pristine ZnO demonstrates considerable potential as a photocatalyst for the photo-esterification process.

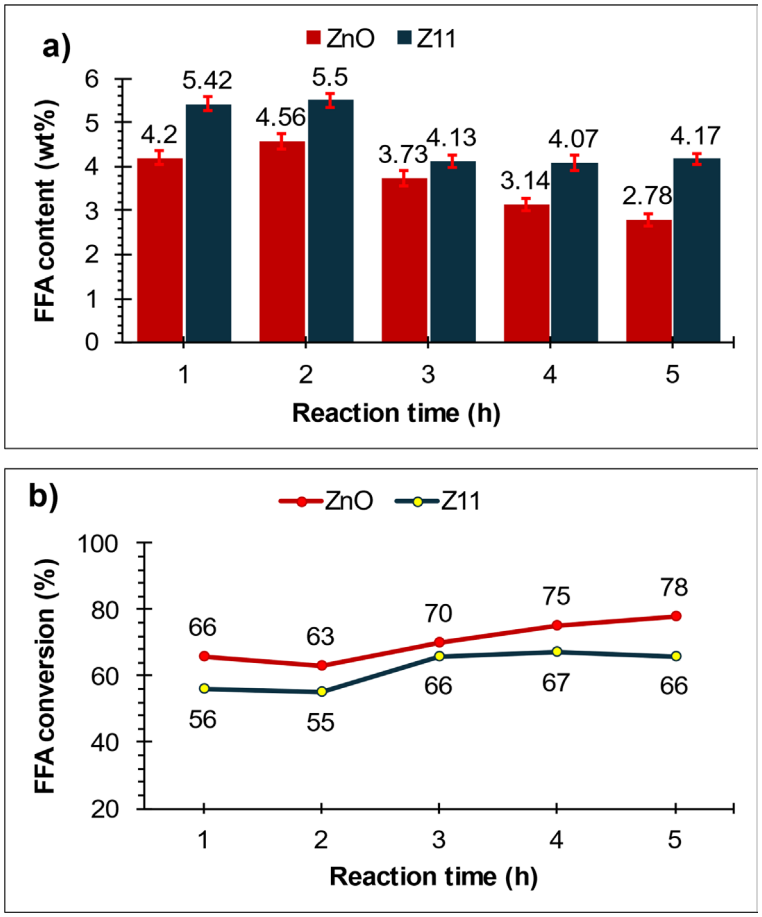


Figure 4.31 Effect of Reaction Time on a) FFA Content Reduction and b) FFA Conversion, Catalyzed by ZnO and ZnO/EFBA 1:1 (Z11), under Fixed Conditions: 20:1 Methanol-to-WCO Molar Ratio and 4 wt% Catalyst Loading

In contrast, the FFA conversion achieved using the Z11 composite increased from 56% at 1 h to a peak of 67% at 4 h before slightly decreasing to 66% at 5 h (Figure 4.31b). Compared with pristine ZnO, the Z11 catalyst shows a relatively slower kinetic response during the reaction process. This behavior may be attributed to the presence of the EFBA matrix, which can partially cover ZnO active sites and slow down the initial activation of the photocatalyst due to interfacial charge transfer resistance.

Nevertheless, the incorporation of EFBA improve the dispersion of ZnO particles within the composite matrix and help prevent particle agglomeration during the reaction process. Moreover, the porous ash structure facilitates easier catalyst recovery and separation from the reaction mixture compared with pristine ZnO nanoparticles. These structural benefits contribute to improved catalyst stability and recyclability, making Z11 a more practical catalyst for long-term photo-esterification applications.

4.3.2.2 Effect of Methanol-to-Oil Molar Ratio

Figure 4.32a and Figure 4.32b illustrates the effect of the methanol-to-WCO molar ratio, ranging from 12:1 to 24:1, on FFA content reduction and FFA conversion. The reaction conditions were fixed at 5 h reaction time and 4 wt% catalyst loading for ZnO, while for the Z11 the reaction time was fixed at 4 h and 4 wt% catalyst loading.

As shown in Figure Figure 4.32b, ZnO achieved an FFA conversion of 74% at a 12:1 molar ratio. The conversion slightly decreased to 70% at 16:1 before increasing again to 77% and 78% at 20:1 and 24:1, respectively. This trend suggests that ZnO requires a relatively higher methanol concentration to achieve maximum FFA conversion. The dependence on excess methanol may be attributed to the limited number of available active sites on the ZnO surface. Additional methanol helps to increase the probability of reactant adsorption and interaction with the catalyst surface, thereby promoting the esterification reaction (Salim et al., 2022).

This observation is supported by the BET surface area analysis, where ZnO exhibits a relatively low surface area of 4.55 $m^2 g^{-1}$, which is significantly lower than that of the Z11 composite. The clustered particle structure of ZnO may restrict the diffusion of methanol and FFA molecules toward the catalytic active sites, thus requiring a higher methanol concentration to drive the reaction forward. Although ZnO

maintained relatively stable catalytic performance across the investigated methanol ratios, the results indicate that an excess amount of methanol is necessary to achieve optimal conversion.

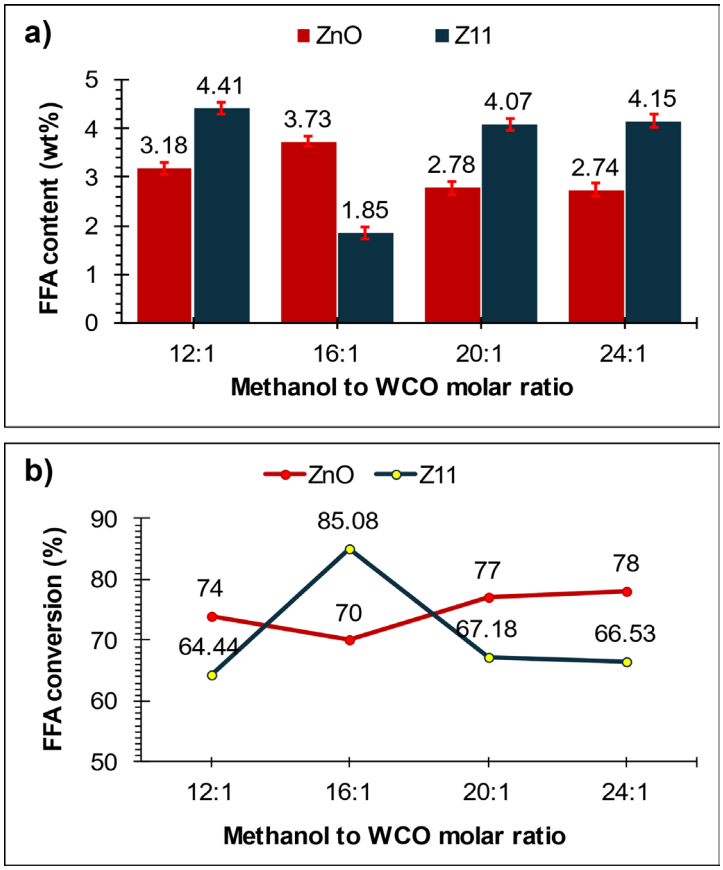


Figure 4.32 Effect of Methanol-to-WCO Molar Ratio on a) FFA Content Reduction and b) FFA Conversion, Catalyzed by ZnO (5 h Reaction Time, 4 wt% Catalyst Loading) and ZnO/EFBA 1:1 (Z11) (4 h Reaction Time, 4 wt% Catalyst Loading).

In contrast, the Z11 composite demonstrated a different trend. At a 12:1 methanol-to-oil ratio, Z11 achieved an FFA conversion of 64.4%, which increased significantly to 85.08% at a 16:1 ratio. However, further increases in the methanol ratio resulted in a decrease in conversion to 67.18% at 20:1 and 66.53% at 24:1. These results suggest that the optimal methanol ratio for Z11 is 16:1, where sufficient methanol is available to saturate the active sites and promote efficient interaction between methanol and FFA molecules.

The improved performance of Z11 can be attributed to the incorporation of the EFBA matrix, which introduces a more porous structure and increases the number of

accessible catalytic active sites compared to pristine ZnO. The porous EFBA structure facilitates better reactant diffusion and enhances charge carrier mobility during photocatalytic activation, thereby improving the overall esterification efficiency.

However, when the methanol ratio increases beyond the optimal level, a decline in Z11 conversion is observed. This reduction in activity may be attributed to several factors. Excess methanol can lead to light scattering and UV shielding effects, which reduce the penetration of irradiation into the reaction medium and consequently decrease photon absorption by the photocatalyst. In addition, excessive methanol may dilute the concentration of FFA molecules and competitively occupy active sites, thereby reducing the probability of effective esterification reactions. Excess methanol may also act as a hole scavenger, promoting recombination of photogenerated charge carriers and lowering photocatalytic efficiency (Wai & Li, 2023).

Overall, these results demonstrate that while ZnO requires higher methanol concentrations to achieve stable catalytic performance, the Z11 composite exhibits optimal performance at a moderate methanol ratio due to the enhanced porosity and active site availability provided by the EFBA matrix.

4.3.2.3 Effect of Catalyst Loading

Figure 4.33a and Figure 4.33b present the effect of catalyst loading ranging from 1–5 wt% on FFA reduction and FFA conversion during the photo-esterification process. The reaction conditions were fixed at 5 h reaction time and a 24:1 methanol-to-WCO molar ratio for ZnO, while for the Z11, the conditions were fixed at 4 h reaction time and a 16:1 methanol-to-WCO molar ratio.

For ZnO, the FFA conversion increased from 59% at 1 wt% catalyst loading to a maximum of 85% at 2 wt%. However, further increases in catalyst loading resulted in a decline in performance, with conversions of 74%, 78%, and 74% observed at 3 wt%, 4 wt%, and 5 wt%, respectively. These results suggest that ZnO requires only a relatively low catalyst dosage (2 wt%) to achieve optimal performance. Beyond this loading, the catalytic efficiency decreases, which may be attributed to particle aggregation and blocked active sites. This factor can result in mass transfer limitations and reduced photocatalytic activity at higher catalyst loadings (Pratiwi et al., 2026)

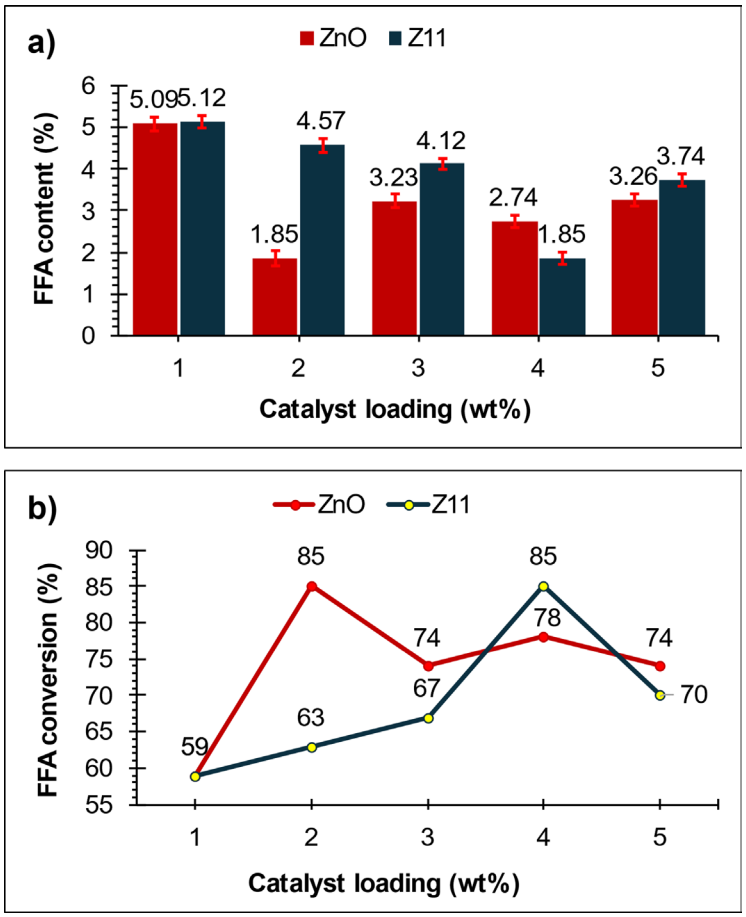


Figure 4.33 Effect of Catalyst Loading on a) FFA Content Reduction and b) FFA Conversion, Catalyzed by ZnO (5 h Reaction Time, 24:1 Methanol-to-WCO Molar Ratio) and ZnO/EFBA (Z11) (4 h Reaction Time, 16:1 Methanol-to-WCO Molar Ratio), under 4 wt% Catalyst Loading.

In contrast, the Z11 composite exhibited a gradual increase in catalytic activity with increasing catalyst loading. The FFA conversion increased from 59% at 1 wt% to 63% at 2 wt%, followed by 67% at 3 wt%, reaching the highest conversion of 85% at 4 wt%. However, when the catalyst loading was further increased to 5 wt%, the conversion decreased to 70%. These results indicate that 4 wt% represents the optimal catalyst loading for Z11, where sufficient active sites are available for effective interaction between methanol and FFA molecules while maintaining efficient photon absorption and mass transfer. At lower catalyst loadings (<4 wt%), the reduced conversion may be attributed to the limited number of accessible active sites within the porous EFBA matrix, which may not be sufficient to accommodate the adsorption of reactant molecules. But excessive loading more than 4 wt% lead to pore blockage and

reduced effective surface area, ultimately decreasing photocatalytic efficiency (Yaghi et al., 2025).

Overall, these results demonstrate that catalyst loading plays a critical role in balancing photon absorption, surface accessibility, and mass transfer efficiency. Under the investigated conditions, 2 wt% and 4 wt% were identified as the optimal catalyst loadings for ZnO and Z11, respectively, highlighting the influence of catalyst structure and support materials on photocatalytic performance.

4.3.2.4 Effect of Light Sources

Figure 4.34 presents the FFA content reduction and FFA conversion obtained under different light sources, including UV-A (365 nm), UV-C (254 nm), visible light, xenon lamp irradiation, and dark conditions. The photocatalytic performance of the Z11 was evaluated under optimized reaction conditions of 4 wt% catalyst loading, 4 h reaction time, and a 16:1 methanol-to-WCO molar ratio.

A control experiment conducted in the absence of light irradiation (dark condition) resulted in minimal FFA conversion of only 31.53%. This observation confirms the activation of the catalyst requires light irradiation to generate electron–hole pairs.

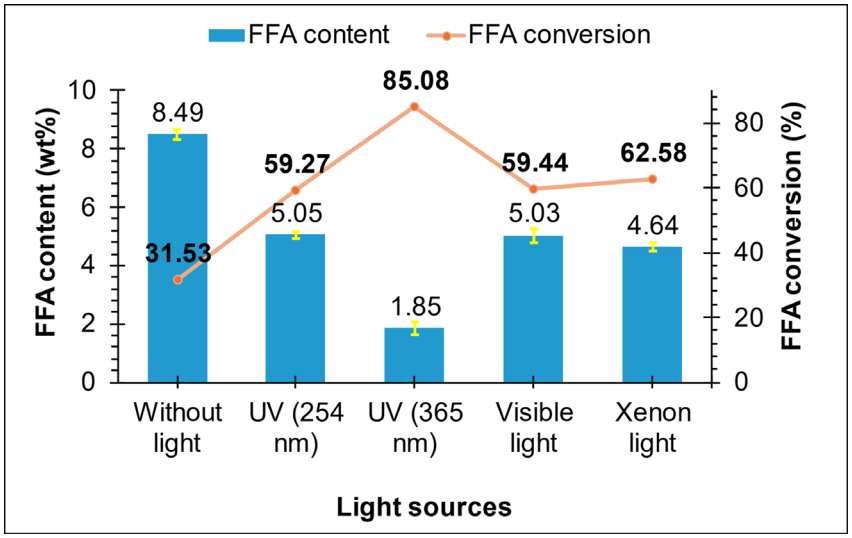


Figure 4.34 Effect of Various Light Sources on FFA Content Reduction and FFA Conversion During Photo-Esterification Catalyzed by Z11. Reactions were Conducted under 4 wt% Catalyst Loading, 4 h Reaction Time, and a 16:1 Methanol-to-WCO Molar Ratio

When exposed to high-energy UV-C light (254 nm), the FFA conversion reached 59.27%, which is significantly lower than that obtained under UV-A irradiation. Although UV-C photons possess higher energy, the excessive energy input may accelerate electron–hole recombination, thereby reducing the effective lifetime of charge carriers involved in the redox reaction (Tuama et al., 2024). As a result, the photocatalytic efficiency of the Z11 catalyst is reduced under UV-C irradiation.

In contrast, UV-A light (365 nm) produced the highest catalytic performance, achieving an FFA conversion of 85.08%. This indicates that the UV-A wavelength is well aligned with the band gap energy of the Z11 composite (~3.19 eV), enabling efficient excitation of photogenerated electrons from the valence band to the conduction band. In addition, the EFBA support provides a porous matrix with abundant surface functional groups that can act as electron trapping sites, thereby improving charge carrier separation and enhancing photon utilization during the photocatalytic reaction (Zhu & Wang, 2025).

Under visible light irradiation and xenon lamp exposure, moderate photocatalytic activity was observed, with FFA conversions of 59.44% and 62.58%, respectively. The lower activity under visible light can be attributed to its insufficient photon energy to effectively excite electrons across the band gap of ZnO. Meanwhile, the xenon lamp emits a broad-spectrum covering UV, visible, and near-infrared regions; however, only the UV fraction of the emitted light is effectively utilized by the ZnO-based catalyst (Zhu et al., 2021). Consequently, the overall photocatalytic efficiency under xenon irradiation remains lower than that achieved under targeted UV-A illumination. Overall, these findings confirm that UV-A irradiation provides the most suitable excitation energy for activating the Z11 photocatalyst, offering optimal spectral alignment with the catalyst band gap while promoting efficient charge carrier generation and utilization during the photo-esterification process.

4.3.2.5 Effect of Thermal Treatment Temperature on ZnO and ZnO/EFBA

The trends of FFA content reduction and FFA conversion under different thermal treatment temperatures are presented in Figure 4.35a and Figure 4.35b for ZnO and Z11, respectively. The optimized reaction conditions were 2 wt% catalyst loading, 5 h reaction time, and a 24:1 methanol-to-WCO molar ratio for ZnO, while for the Z11,

the conditions were fixed at 4 wt% catalyst loading, 4 h reaction time, and a 16:1 methanol-to-WCO molar ratio. Prior to the reaction, the catalysts were thermally treated at 100 °C, 300 °C, and 500 °C to evaluate the influence of thermal stability on photocatalytic performance. ZnO was also evaluated under these conditions since previous optimization results showed comparable catalytic performance to Z11.

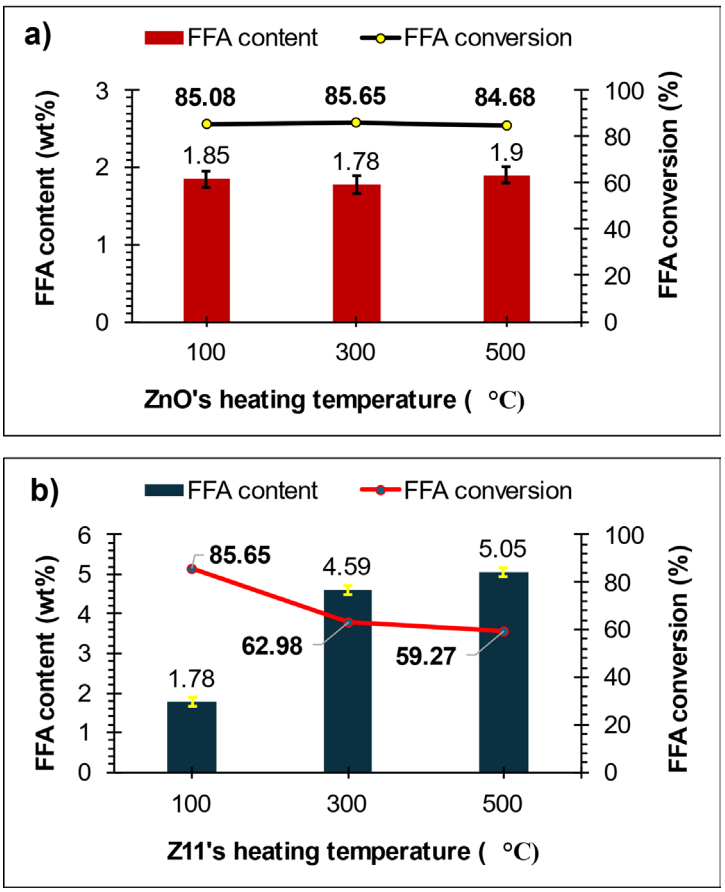


Figure 4.35 Influence of Thermal Treatment Temperature on (a) FFA Content Reduction and Conversion using ZnO at 2 wt% Catalyst Loading, 5 h Reaction Time, and 24:1 Methanol-to-WCO Molar Ratio, and (b) Z11 under 4 wt% Catalyst Loading, 4 h Reaction Time, and 16:1 Methanol-to-WCO Molar Ratio

As shown in Figure 4.35a, ZnO maintained consistently high FFA conversion across all tested temperatures, ranging from 84.7% to 85.7%. This indicates that ZnO exhibits excellent thermal stability, as the catalytic performance remains largely unchanged even after thermal treatment at elevated temperatures. This stability can be attributed to the wurtzite crystal structure and the wide band gap of ZnO, which enable it to withstand elevated temperatures without significant structural degradation (Zhu et

al., 2021). This observation is supported by TGA analysis, which shows that ZnO experiences only minimal weight loss of approximately 0.31% between 166 °C and 850 °C. Such insignificant mass loss indicates strong structural stability, which can be attributed to the robust metal–oxygen bonding within the ZnO lattice. The strong Zn–O bonds allow the material to withstand high temperatures without significant structural degradation.

In contrast, the Z11 composite exhibited significant sensitivity to thermal treatment temperature. The sample treated at 100 °C demonstrated the best photocatalytic performance, achieving the highest FFA conversion of 85.7%. However, the catalytic activity decreased substantially when the treatment temperature increased to 300 °C and 500 °C, where the FFA conversion dropped to 62.98% and 59.3%, respectively. This decline in performance indicates that the EFBA matrix plays a crucial role in determining the catalytic stability of the composite. At moderate temperatures (100 °C), the porous structure and surface functional groups of EFBA remain intact, allowing efficient dispersion of ZnO nanoparticles and maintaining effective interaction between reactant molecules and active sites. However, at higher temperatures, partial decomposition of EFBA components and structural changes in the ash matrix may occur.

Thermogravimetric analysis of EFBA indicates gradual weight loss beginning near 100 °C and continuing up to approximately 800 °C, which suggests the removal of surface functional groups and possible collapse of the porous structure at elevated temperatures. Such structural degradation can reduce the surface area and disrupt the interaction between ZnO and the EFBA matrix. Consequently, this may lead to agglomeration of ZnO particles and partial detachment of active species, resulting in reduced photocatalytic efficiency (Chehhat et al., 2025).

Overall, these results demonstrate that pristine ZnO remains thermally stable across the investigated temperature range, while the ZnO/EFBA composite performs optimally at lower thermal treatment temperatures. The superior performance of Z11 at 100 °C highlights the importance of preserving the porous structure and surface functionalities of biomass-derived materials. Maintaining these structural features is essential for maximizing catalytic activity and supports the development of sustainable photocatalysts for efficient biodiesel production.

4.3.2.6 Effect of ZnO-to-EFBA Mass Ratio

The effect of varying the ZnO-to-EFBA mass ratio on photocatalytic esterification was investigated under optimized conditions of 4 wt% catalyst loading, 4 h reaction time, and a 16:1 methanol-to-WCO molar ratio. As illustrated in Figure 4.36, several catalyst compositions were evaluated, including Z31 (3 g ZnO:1 g EFBA), Z21 (2 g ZnO:1 g EFBA), Z11 (1 g ZnO:1 g EFBA), Z12 (1 g ZnO:2 g EFBA), and Z13 (1 g ZnO:3 g EFBA).

Among the investigated ratios, the Z11 composite exhibited the highest catalytic efficiency, achieving an FFA conversion of 85.08% (Figure 4.36). This result indicates that a balanced 1:1 ratio between ZnO and EFBA provides the most effective synergistic interaction compared with the other compositions. The enhanced activity can be attributed to improved dispersion of ZnO nanoparticles on the EFBA matrix, which increases the accessibility of catalytic active sites and facilitates efficient light absorption. In this configuration, the EFBA support provides sufficient surface area and porous structure to anchor ZnO particles, preventing nanoparticle agglomeration.

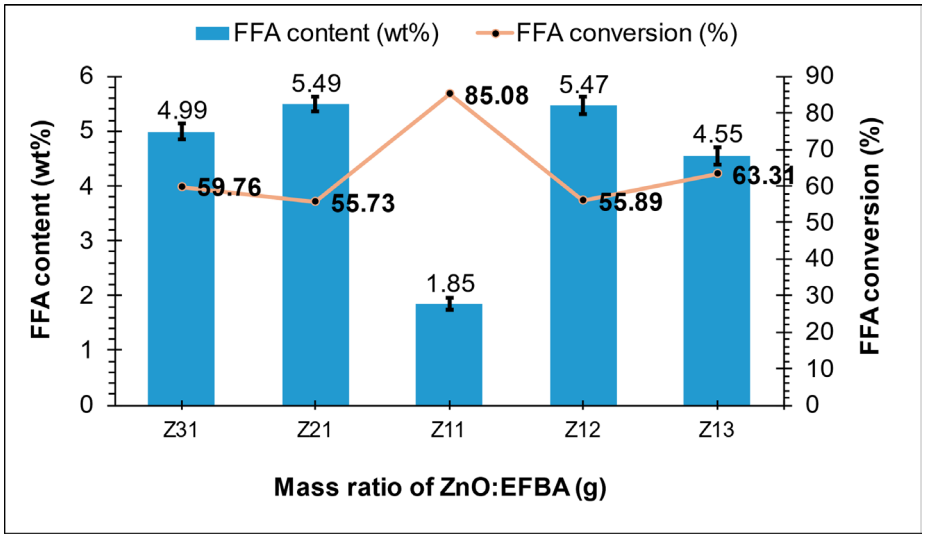


Figure 4.36 Effect of ZnO to EFBA Mass Ratio on FFA Content Reduction and FFA Conversion Efficiency under Photo-Esterification Conditions. Reactions Were Carried Out at 4 wt% Catalyst Loading, 4 h Reaction Time, and a 16:1 Methanol-to-WCO Molar Ratio

In contrast, higher ZnO loadings in the Z31 and Z21 formulations resulted in lower FFA conversions of 59.76% and 55.73%, respectively. This decline suggests that

excessive ZnO loading on the EFBA surface may lead to particle agglomeration, which reduces the effective surface area and limits the number of accessible catalytic active sites. Furthermore, densely packed ZnO particles may create a light shielding effect that restricts photon penetration into the catalyst layer, thereby reducing the generation of photogenerated charge carriers.

Conversely, increasing the EFBA content in the Z12 and Z13 formulations also led to reduced catalytic performance, with FFA conversions of 55.89% and 63.31%, respectively. This behavior suggests that excessive EFBA content may dilute the active ZnO component, resulting in fewer photoactive sites available for the esterification reaction. In addition, the EFBA matrix may introduce deep trapping sites that hinder the effective generation and migration of photogenerated electrons and holes, thereby suppressing the formation of reactive radical species (Navidpour et al., 2026).

Overall, the 1:1 ZnO-to-EFBA ratio maximizes catalytic performance while minimizing ZnO usage. These findings highlight the importance of compositional optimization in ash-derived photocatalyst systems for efficient biodiesel production.

4.3.2.7 Visual Comparison of Esterified WCO Using ZnO and ZnO/EFBA Catalysts

Figure 4.37 illustrates the physical appearance of the esterified WCO obtained after the photo-esterification process using (a) ZnO and (b) Z11 catalysts. The esterified WCO produced using ZnO (Figure 4.37a) appears turbid and emulsified, with visible suspended particles and poor phase separation between the catalyst and liquid product. This observation indicates limited catalyst–product separation after the reaction. The turbidity is likely associated with the clustered particle structure of ZnO nanoparticles, which tend to agglomerate due to strong interparticle interactions such as van der Waals forces (Wang et al., 2021). As a result, the agglomerated particles remain dispersed within the reaction mixture, making separation difficult. Although ZnO demonstrated catalytic performance comparable to Z11 during the reaction, its poor separation behavior may increase downstream processing complexity and operational costs in practical biodiesel production (Huang et al., 2022).

In contrast, the esterified WCO obtained using the Z11 composite (Figure 4.37b) appears visibly clearer, with minimal emulsion formation and no noticeable solid residues. This improved clarity indicates better phase separation and enhanced product

quality. The presence of the EFBA support plays an important role in stabilizing the ZnO particles within the composite structure. The supported structure reduces the formation of emulsions and facilitates easier separation of the catalyst from the reaction mixture. This demonstrates that incorporating EFBA as a support material can enhance physicochemical performance of ZnO-based photocatalysts.

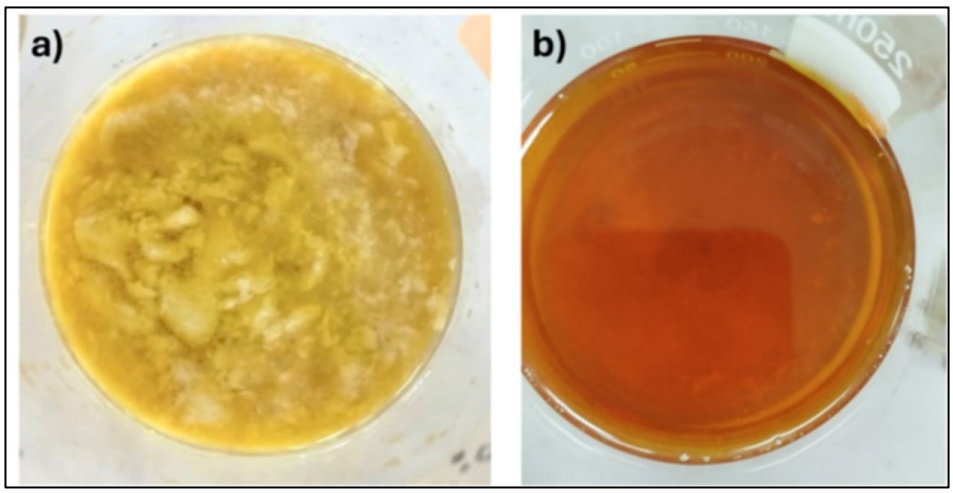


Figure 4.37 Visual Comparison of Esterified Waste Cooking Oil (WCO) Following Photo-Esterification using (a) ZnO and (b) Z11 Catalysts

4.3.3 Effect of Reactive Species Scavenger on Photocatalytic Activity

4.3.3.1 Effect of Scavenger Agent on TiO_2/EFBA

Scavenger analysis was conducted to identify the dominant reactive species involved in the photo-esterification process. In this study, different scavenger agents were introduced to selectively quench specific reactive species generated during photocatalysis. Ethylenediaminetetraacetic acid (EDTA), silver nitrite ($AgNO_3$), p-benzoquinone (p-BQ), and isopropanol (IPA) were used to trap valence band holes (h^+), conduction band electrons (e^-), superoxide radicals ($\bullet O_2^-$), and hydroxyl radicals ($\bullet OH$), respectively. The results are presented in Figure 4.38 (Schneider et al., 2020).

The addition of $AgNO_3$ significantly suppressed the photocatalytic activity, reducing FFA conversion from 78% to 33%. This strong inhibition indicates that photogenerated electrons play a crucial role in the reaction mechanism. Electrons in the conduction band can participate in reduction reactions that promote the formation of

reactive species such as $\bullet O_2^-$, which contribute to the activation of fatty acid molecules during the esterification process. Therefore, trapping electrons with $AgNO_3$ reduces the generation of these reactive intermediates and significantly decreases FFA conversion. Similarly, IPA also suppress the conversion up to 31%. This suggests trapping of hole pair can prevent the formation of fatty acid, hydroxyl and methoxy radical. These two scavengers demonstrated that e^- and •OH radicals play dominant and cooperative roles in the overall esterification pathway (Ahmed & Haider, 2021). These results indicate that both photogenerated electrons and hydroxyl radicals play dominant and cooperative roles in the overall photocatalytic esterification pathway.

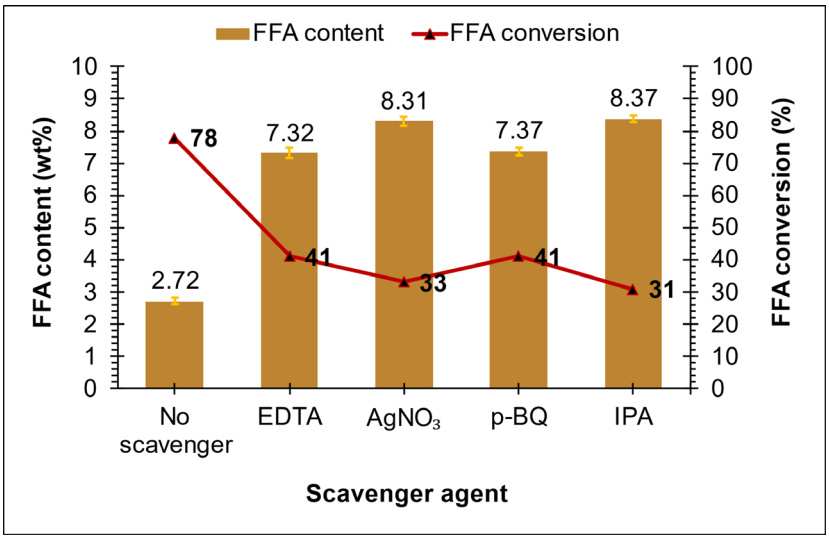


Figure 4.38 FFA Content Reduction and Conversion over Scavenger Agent Catalyze by T11 with Optimized Reaction Condition of 2 h Reaction Time and 20:1 Methanol to WCO Molar Ratio and 4 wt% Catalyst Loading

The addition of EDTA and p-benzoquinone, which selectively quench valence band holes (h^+) and superoxide radicals ($\bullet O_2^-$), respectively, also resulted in a noticeable reduction in catalytic activity, with both systems showing FFA conversion of approximately 41%. This observation suggests that valence band holes and superoxide radicals also participate in the photocatalytic reaction mechanism. The photogenerated holes can promote the formation of methoxy radicals from methanol, while superoxide radicals may assist in activating fatty acid molecules during the reaction process. Overall, the scavenger experiments demonstrate that multiple reactive species contribute to the photocatalytic esterification mechanism. The cooperative participation

of photogenerated e^-, h^+, •OH, and $•O_2^-$ plays an important role in facilitating the conversion of FFA into FAME.

4.3.3.2 Effect of Scavenger Agent on ZnO/EFBA

Figure 4.39 presents the results of the scavenger analysis conducted during the photo-esterification process using the Z11 catalyst. Similar to the T11 system, the results indicate that multiple reactive species participate in the reaction mechanism. In the absence of scavengers, the Z11 catalyst achieved an FFA conversion of 85%. However, the introduction of different scavenger agents significantly reduced the catalytic activity. The presence of EDTA, $AgNO_3$, p-BQ, and IPA decreased the FFA conversion to 42%, 51%, 40%, and 43%, respectively. These results indicate that the corresponding reactive species play important roles in the photocatalytic reaction. The involvement of these species suggests that the activation of FFA molecules and methanol leads to the formation of intermediate radical species such as acyl radicals (R–COO•) and methoxy radicals ($•OCH_3$). These intermediates can subsequently undergo radical–radical coupling or surface-mediated reactions to produce FAME.

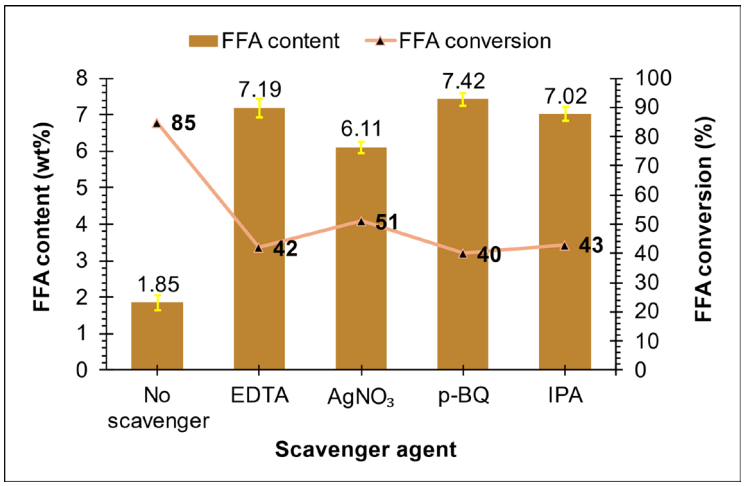


Figure 4.39 FFA Content Reduction and Conversion over Scavenger Agent Catalyze by Z11 with Optimized Reaction Condition of 4 h Reaction Time and 16:1 Methanol to WCO Molar Ratio and 4 wt% Catalyst Loading

4.3.4 Reusability Test

4.3.4.1 Reusability Performance of TiO_2/EFBA

Figure 4.40 presents the photocatalytic reusability performance of the T11 catalyst over five consecutive cycles, conducted under optimized reaction conditions. After each reaction cycle, the biodiesel product was separated by centrifugation at 4500 rpm for 15 minutes. The recovered catalyst was then washed to remove residual reactants and products. Approximately 10 mL of hexane was added to the spent catalyst, followed by brief shaking and centrifugation at 3000 rpm for 5 minutes. This washing procedure was repeated several times with fresh hexane until the supernatant appeared clear, indicating effective removal of residual oil and organic impurities. The cleaned catalyst was subsequently dried at 70°C for 15 minutes before being reused in the next cycle.

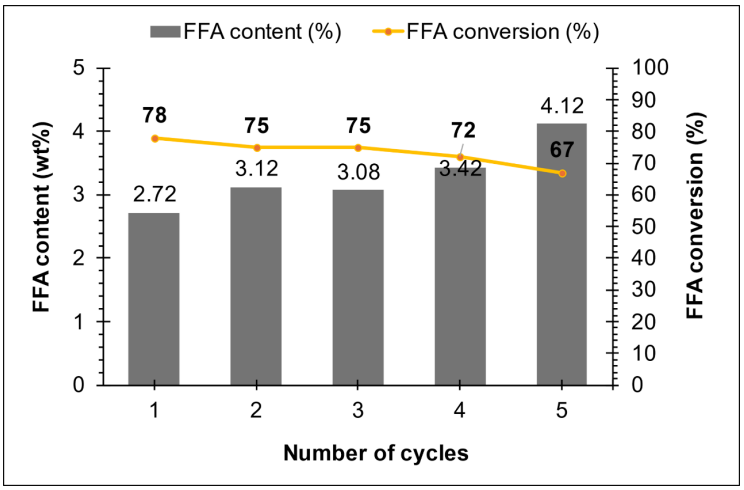


Figure 4.40 FFA Content Reduction and Conversion Over Reusability Test Catalyze by T11 with Optimized Reaction Condition of 4 h Reaction Time and 20:1 Methanol to WCO Molar Ratio and 4 wt% Catalyst Loading

In the first cycle, the T11 catalyst exhibited strong photocatalytic activity, achieving an FFA conversion of 78%. However, a gradual decline in performance was observed in subsequent cycles, with the conversion decreasing to 67% by the fifth cycle. This 11% reduction in catalytic efficiency suggests moderate catalyst deactivation during repeated use. The decline in performance is likely attributed to catalyst fouling, where residual organic compounds or reaction intermediates accumulate on the catalyst

surface and block active sites. This surface coverage can reduce photon penetration and limit the generation of ROS, thereby lowering photocatalytic activity (Guliani et al., 2022).

Despite the observed decrease in conversion, the T11 catalyst maintained a relatively high level of activity throughout the five reuse cycles. This result indicates that the EFBA support provides structural stability and effective anchoring of the photocatalyst, which helps prolong the durability and reusability of the TiO_2-based system. Overall, the findings demonstrate that the TiO_2/EFBA catalyst exhibits acceptable stability and can be reused multiple times with only moderate loss in catalytic performance.

4.3.4.2 Reusability Performance of ZnO and ZnO/EFBA

Figure 4.41a presents the reusability performance of ZnO over five consecutive esterification cycles under optimized reaction conditions. The initial FFA conversion reached 86% in the first cycle. However, by the second cycle, conversion dropped sharply to 67%, and by the fifth cycle it further declined to 60%. This significant reduction in activity is likely due to the tendency of ZnO nanoparticles to agglomerate and their difficulty in separating from the product. This behavior is supported by the visual appearance of esterified WCO catalyzed by ZnO, which shows visible suspended particles. Such agglomeration and masking of active sites by the product can hinder photon penetration and reduce ROS generation, leading to decreased catalytic performance (Güell et al., 2023).

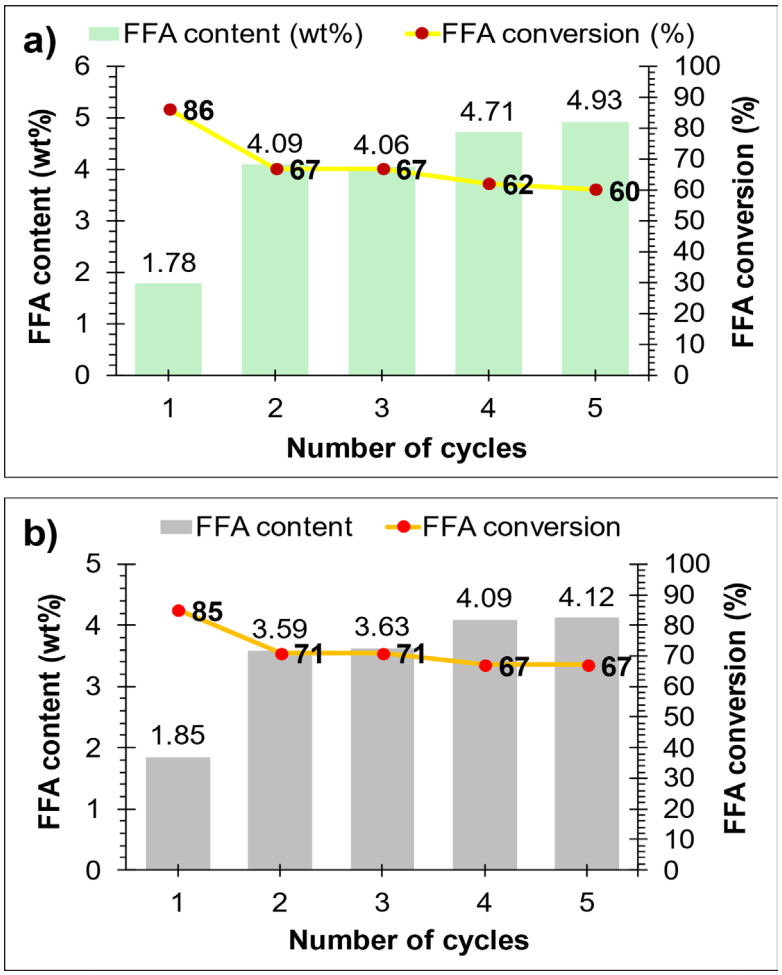


Figure 4.41 Reusability Test on (a) FFA Content Reduction and Conversion Using ZnO at 2 wt% Catalyst Loading, 5 h Reaction Time, and 24:1 Methanol-to-WCO Molar Ratio, and (b) Z11 under 4 wt% Catalyst Loading, 4 h Reaction Time, and 16:1 Methanol-to-WCO Molar Ratio

In contrast, the Z11 composite exhibited an initial FFA conversion of 85% in the first cycle (Figure 4.41b). Conversion declined to 71% in the second cycle but remained relatively stable through the fifth cycle, finishing at 67%. This trend indicates only moderate deactivation compared to pristine ZnO. The decline is likely due to surface fouling from residual organic species adhering to the catalyst surface, partially blocking pores and reducing light absorption at active sites (Yadav et al., 2025). Nevertheless, the Z11 catalyst maintained good photocatalytic activity over multiple cycles, demonstrating improved long-term stability.

These results underscore the benefits of incorporating EFBA as a support material. Its porous structure and mineral composition help prevent nanoparticle

agglomeration and mitigate photo corrosion, thereby sustaining catalytic efficiency over repeated cycles (Baig et al., 2025).

4.3.5 Proposed Photocatalytic Reaction Mechanism

Figure 4.42 illustrates the mechanistic study using the Z11 composite. The overall FFA conversion follows a dual-pathway mechanism that integrates both radical–radical coupling and classical nucleophilic substitution (Zhu & Wang, 2025). The scavenger study confirmed that the key reactive species involved are electrons (e^-), holes (h^+), hydroxyl radicals (•OH), and superoxide radicals ($•O_2^-$).

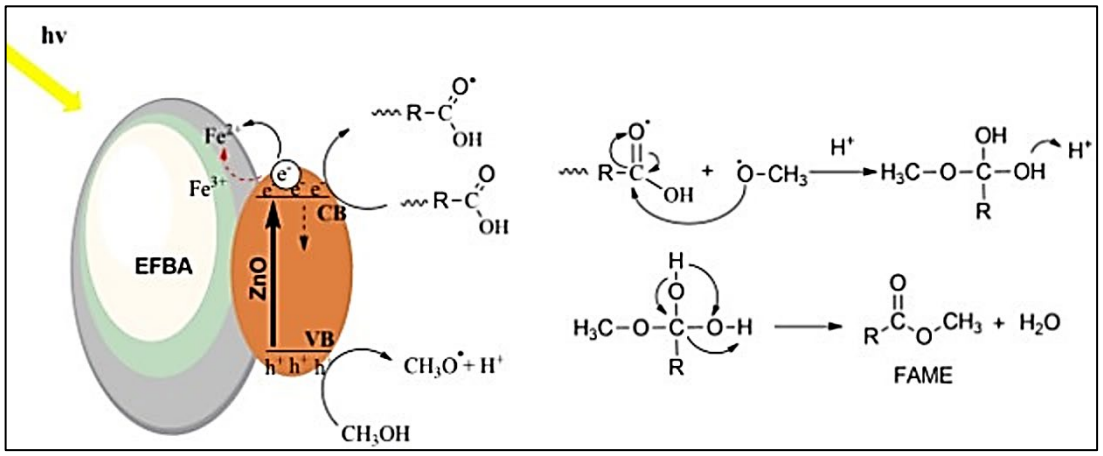


Figure 4.42 Schematic Illustration of the Photocatalytic Esterification Mechanism over Z11 under UV-A Irradiation

Stepwise Photocatalytic Mechanism:

Photoexcitation and Charge Carrier Generation:

- Upon UV-A illumination ($\lambda \approx 365$ nm), ZnO or TiO_2 absorbs photons and promotes electrons from the valence band (VB) to the conduction band (CB), generating electron–hole pairs:

$$TiO_2 \text{ or } ZnO + hv \rightarrow e^-_{CB} + h^+_{VB} \quad (4.3)$$

Formation of Reactive Oxygen Species (ROS):

- Conduction band electrons reduce surface-adsorbed oxygen, generating

superoxide radicals ($\bullet O_2^-$):

$$e^- + O_2 \rightarrow \bullet O_2^- \quad (4.4)$$

- Simultaneously, holes oxidize water or surface hydroxide to form hydroxyl radicals (•OH):

$$h^+ + H_2O/OH^- \rightarrow \bullet OH \quad (4.5)$$

Methanol Oxidation:

- Methanol molecules (CH_3OH) adsorbed on the catalyst surface, are oxidized by h+ to yield $\bullet OCH_3$ and proton (H^+):

$$CH_3OH + h^+ \rightarrow \bullet OCH_3 + H^+ \quad (4.6)$$

FFA Activation via ROS and Direct Electron Reduction:

- $\bullet O_2^-$ and •OH abstract hydrogen atoms from FFAs (R–COOH), yielding fatty acyloxy or FFAs radicals (R - COO•):

$$\bullet O_2^- \text{ and } \bullet OH + R\text{-}COOH \rightarrow R - COO\bullet \quad (4.7)$$

- Alternatively, direct reduction by electrons contributes to radical formation:

$$R\text{-}COOH + e^- \rightarrow R - COO\bullet + H^+ \quad (4.8)$$

Radical Coupling and Tetrahedral Intermediate Formation:

- The R–COO• radical combines with the $\bullet OCH_3$, forming a high-energy tetrahedral intermediate:

$$R - COO\bullet + \bullet OCH_3 \rightarrow [R\text{-}COOCH_3] \rightarrow FAME + H_2O \quad (4.9)$$

Rearrangement, Dehydration, and Desorption:

- The tetrahedral intermediate undergoes proton rearrangement and elimination of water yield the final FAME product. FAME molecules then desorb from the catalyst surface and diffuse into the liquid phase. Vigorous stirring enhances this mass transfer, facilitating reactant–product exchange and sustaining surface turnover.

This mechanistic framework highlights the synergistic action of ZnO as a semiconductor, EFBA as a support material, and reactive oxygen species in promoting high-conversion esterification under mild conditions. The oxide species in EFBA help stabilize radicals and facilitate electron shuttling, functioning as both a structural support and a functional co-catalyst. Overall, the Z11 system illustrates efficient charge generation, radical formation, intermediate stabilization, and product desorption within a synergistic photocatalytic environment.

4.4 Fatty Acid Methyl Ester (FAME) Composition and Yield Analysis

The FAME composition of the biodiesel product derived from esterified WCO was analyzed using gas chromatography–mass spectrometry (GC–MS), and the results are presented in Table 4.16. The FFA content of the esterified WCO used for analysis was 1.85 wt%, obtained after photo-esterification using the Z11 catalyst.

The FAME yield was calculated according to the European biodiesel standard EN 14103, which resulted in a total FAME content of 89.2%. This result confirms the successful conversion of WCO into biodiesel after the photo-esterification process. As shown in Table 4.16, the dominant FAME species identified in the WCO-derived biodiesel include methyl laurate (1.48%), methyl myristate (3.65%), methyl palmitate (30.25%), methyl heptadecanoate (18.25%), methyl oleate (32.82%), and methyl linoleate (10.55%). Among these, methyl palmitate and methyl oleate represent the major components, which are commonly found in biodiesel derived from vegetable oil-based feedstocks.

The presence of saturated methyl esters such as methyl laurate, methyl myristate, and methyl palmitate contributes positively to the oxidative stability of biodiesel. Saturated fatty acid chains are generally more resistant to oxidative degradation, thereby improving fuel storage stability. In contrast, unsaturated methyl esters such as methyl oleate and methyl linoleate contribute to improved cold-flow properties and lubricity, which are beneficial for engine performance.

Overall, the balanced composition of saturated and unsaturated FAME components indicates that the biodiesel produced from WCO possesses favorable fuel characteristics. Therefore, WCO can be considered a promising and sustainable feedstock for biodiesel production, particularly when combined with efficient photocatalytic pretreatment to reduce its high FFA content.

Table 4.16
Composition of FAME in WCO-Derived Biodiesel Based on GC-MS Analysis

Retention time (min)	FAME compound (Methyl ester)	Composition (% by weight)
25.753	Methyl laurate (C12:0)	1.48
29.215	Methyl myristate (C14:0)	3.65
33.278	Methyl palmitate (C16:0)	30.25
35.029	Methyl heptadecanoate (C17:0)	18.25
37.518	Methyl oleate (C18:1)	32.82
38.216	Methyl linoleate (C18:2)	10.55

4.5 Evaluation of Fuel Properties

This section evaluates the fuel properties of biodiesel derived from esterified WCO and compares them with conventional diesel, as well as the specifications outlined in ASTM D6751. The analysis follows standard testing procedures.

As shown in Table 4.17, it exhibited a density of 871.7 kg/m³ at 30 °C, aligning well with the EN 14214 range (860–900 kg/m³) and close to diesel's typical density (840–850 kg/m³), suggesting good volumetric efficiency and lubricity. The kinematic viscosity of 4.383 mm²/s falls comfortably within the ASTM D6751 specification (1.9–6.0 mm²/s), supporting efficient fuel injection and smooth combustion. Although its calorific value (40.075 MJ/kg) is lower than diesel's (~45 MJ/kg), it still offers sufficient energy for engine operation with only a minor increase in fuel consumption

expected. The biodiesel produced from WCO demonstrated fuel properties that meet key standards outlined in ASTM D6751 and EN 14214, confirming its viability for diesel engine use.

Table 4.17
Comparison of WCO-Biodiesel Properties from This Study with Conventional Diesel and Relevant Fuel Standards (ASTM D6751, EN 14214)

Parameters	Method	Unit	WCO-biodiesel	Diesel	ASTM D6751 Standard
Density at 15 °C	ASTM D4052-11	kg/m³	~871.7 @30°C	~840-850	860-900 (EN 14214)
Heat of combustion	ASTM D240	Mj/kg	40.075	~45	-
Kinematic viscosity at 50 °C	ASTM D445	mm²/s	4.383	1.9-4.1	1.9-6.0
Cloud point	ASTM D2500	°C	12	-5	-
Sulfur by ICP-OES	ASTM D5185	mg/kg	<1	2-6	≤15 ppm (ASTM D5453)
Flash Point by PMCC Tester	ASTM D93	°C	174.5	>52	≥93
Pour point	ASTM D97	°C	6	-15	-

Cold flow properties, including a cloud point of 12 °C and a pour point of 6 °C, are notably higher than those of diesel (–5 °C and –15 °C, respectively), due to the presence of saturated fatty acid esters such as methyl palmitate, methyl laurate and methyl myristate which contribute to oxidative stability but may limit cold-weather performance. However, blending with diesel or using cold-flow additives can address this issue.

The sulfur content was found to be <1 mg/kg which is far below the ASTM D6751 limit of 15 ppm and much lower than diesel (2–6 mg/kg). It is offering environmental benefits like reduced SO_x emissions and better compatibility with emission control technologies. Additionally, the flash point of 174.5 °C exceeds both the ASTM requirement (≥93 °C) and diesel's average (~52 °C), indicating high purity and safer handling. Overall, these findings support the use of esterified-WCO as a sustainable, low-emission, and cost-effective biodiesel feedstock, particularly suitable for use in tropical and temperate regions.

CHAPTER 5
CONCLUSIONS AND RECOMMENDATIONS

5.1 Conclusions

This study highlights the pivotal role of EFBA in enhancing the structural, surface, and photocatalytic properties of TiO_2 and ZnO. The characterization results showed that EFBA successfully functions as both a support material and a co-catalyst. The incorporation of EFBA introduces active mineral species and acts as a mediator for photogenerated electrons and holes, thereby facilitating charge carrier separation and improving photocatalytic efficiency.

The T11 composite exhibited a multiphase structure consisting of anatase and rutile TiO_2 together with EFBA-derived inorganic phases, confirming the synergistic interaction between the semiconductor and the support material. T11 demonstrated extended light absorption in the 420–430 nm region, which was further supported by PL analysis showing significant quenching, indicating improved electron–hole separation. In addition, BET analysis revealed a mesoporous structure with an average pore width of 14.27 nm and a surface area of 8.41 $m^2 g^{-1}$, which facilitates the adsorption of FFA molecules and methanol during the reaction. Under UV-A irradiation, the T11 catalyst achieved 78% FFA conversion within 2 h, outperforming pristine TiO_2.

Similarly, the Z11 composite retained the wurtzite crystal structure of ZnO, indicating structural stability after EFBA incorporation. The presence of EFBA improved UV absorption in the 395–400 nm range and enhanced the physicochemical properties of the catalyst, which helped suppress electron–hole recombination. BET analysis showed an increase in surface area to 6.95 $m^2 g^{-1}$, while FTIR analysis confirmed the formation of new metal–oxygen bonds between ZnO and EFBA.

Scavenger studies further revealed that photogenerated electrons (e^-), holes (h^+), hydroxyl radicals (•OH), and superoxide radicals ($\bullet O_2^-$) were the key reactive species involved in the photocatalytic esterification mechanism. These reactive oxygen species facilitate the activation of free fatty acids and methanol, promoting the formation of FAME through radical-mediated pathways.

Overall, the findings demonstrate that EFBA is an effective and sustainable support material for semiconductor photocatalysts. The synergistic interaction between the semiconductor and EFBA enhances charge separation, improves catalytic stability, and promotes efficient FFA conversion under mild UV-A irradiation conditions. This work highlights the potential of EFBA-supported photocatalysts as a cost-effective and environmentally sustainable approach for upgrading high-FFA waste cooking oil into biodiesel feedstock.

5.2 Recommendations

To build upon the promising outcomes of this study and support future efforts in sustainable biodiesel production, the following recommendations are proposed:

1. Enhancing Solar Responsiveness

As both TiO_2/EFBA and ZnO/EFBA catalysts exhibited strong UV dependence, future studies should explore co-doping with non-metallic elements such as nitrogen, sulfur, or carbon to extend their light absorption into the visible region.

2. Reactor and Light Delivery Optimization

The development of solar concentrator systems or illuminated panel reactors is recommended to improve light intensity, mass transfer, and catalyst exposure.

3. Mechanistic Clarification via Computational and Spectroscopic Tools

Incorporating computational modeling techniques such as Density Functional Theory (DFT) or Time-Dependent DFT (TD-DFT) would offer valuable insights into band alignment, charge localization, and FFA adsorption behavior.

4. Feedstock Versatility and Performance Benchmarking

A comparative study using different types of waste oils (e.g., palm fatty acid distillate, animal fats, or grease trap waste) is recommended to assess variations in FAME yield, product selectivity, and oxidative stability.

5. Expanding Biomass Valorization Pathways

Inspired by the success of EFBA, future work should investigate other palm industry residues, such as boiler ash, mesocarp fibre ash, or press cake ash, as alternative catalyst supports.

REFERENCES

Abbasi, Z., & Ahmadi, M. (2023). Process Optimization Photo-Esterification of Free Fatty Acids in Waste Cooking Oils under UV Irradiation via the RSM Method. *Chemical Methodologies*, *7*, 799–824.

Abdelrahman, A. A., & Abo El-Khair, M. A. (2025). Advanced Biodiesel Production: Feedstocks, Technologies, Catalysts, Challenges, and Environmental Impacts. *Journal of Environmental Chemical Engineering*, 13(1), 114966.

Aghababaei, E., Alizadeh, M., & Bahrami, A. (2025). Synthesis and characterization of Ce-doped TiO_2/Cu-doped Fe_3O_4 heterogeneous photocatalyst for antibacterial applications and visible-light photocatalytic degradation of methylene blue. *Ceramics International*, 1–19.

Ahmad, S. M., Ismail, A., Wahab, N. A., Salleh, K. M., Kamil, N. N., & Abdullah, N. (2024). Comparative analysis of current biomass utilisation by palm oil mills in peninsular Malaysia. *Journal of Sustainability Science and Management*, *19*(7), 167–177.

Ahmed, S. N., & Haider, W. (2021). Enhanced photocatalytic activity of ZnO-graphene oxide nanocomposite by electron scavenging. *Catalysts*, 11(2), 1–8.

Alessandro, B. (2023). Thermal Behavior of Biomass Ashes with the Influence of Additives: A Critical Review. *Journal of Alternate Energy Sources and Technologies*, *14*.

Aljaafari, A., Fattah, I. M. R., Jahirul, M. I., Gu, Y., Mahlia, T. M. I., Islam, M. A., & Islam, M. S. (2022). Biodiesel Emissions: A State-of-the-Art Review on Health and Environmental Impacts. *Energies*, *15*(18), 6854.

Alluqmani, S. M., Loulou, M., Ouerfelli, J., Alshahrie, A., & Salah, N. (2021). Elaboration of TiO_2/carbon of oil fly ash nanocomposite as an eco-friendly photocatalytic thin-film material. *Ceramics International*, *47*(10), 13544–13551.

Amakali, T., Daniel, L. S., Uahengo, V., Dzade, N. Y., & de Leeuw, N. H. (2020). Structural and optical properties of ZnO thin films prepared by molecular precursor and sol–gel methods. *Crystals*, *10*(2), 1–11.

Andrade, P. H. M., Palhares, H., Volkringer, C., Loiseau, T., Hureau, M., Nunes, E., & Moissette, A. (2023). State of the art in visible-light photocatalysis of aqueous

pollutants using metal-organic frameworks. *Journal of Photochemistry & Photobiology, C: Photochemistry Reviews*, *57*, 100635.

Ansari, A. T. A., Mukherji, S., & Mukherji, S. (2025). Enhanced visible-light photocatalysis of a senary mixture of antibiotics using a low-dose of TiO_2–ZnO nanocomposite. *Environmental Research*, *282*, 122083.

AOCS-CD-3d-63. (2009). *AOCS-CD-3d-63 Acid Value Titration*.

Arun, J., Nachiappan, S., Rangarajan, G., Alagappan, R. P., Gopinath, K. P., & Lichtfouse, E. (2023). Synthesis and application of titanium dioxide photocatalysis for energy, decontamination and viral disinfection: a review. *Environmental Chemistry Letters*, *21*(1), 339–362.

Asfaw, B. T., Gari, M. T., & Jayakumar, M. (2025). Transesterification of biodiesel from non-edible oils using heterogeneous base catalysts: A comprehensive review of potential renewable biomass feedstocks. *Chemical Engineering Journal*, *511*, 162028.

Ash, B. E., Nelson, E. S., Iyuke, S., & Daramola, M. O. (2023). Extraction and Characterization of Silica from Empty Palm Fruit. *Processes*, *11*, 1684.

Awogbemi, O., Inambao, F., & Onuh, E. I. (2020). Optimization of FAME composition for improved engine performance and emissions reduction. *International Journal of Low-Carbon Technologies*, *15*(4), 583–593.

Awoke, Y., Chebude, Y., & Díaz, I. (2020). Controlling Particle Morphology and Pore Size in the Synthesis of Ordered Mesoporous Materials. *Molecules (Basel, Switzerland)*, *25*(21), 1–12.

Baig, A., Siddique, M., & Panchal, S. (2025). A Review of Visible-Light-Active Zinc Oxide Photocatalysts for Environmental Application. *Catalysts*, *15*(2), 100.

Balakrishnan, A., Mathew, F. P., Tom Joseph, M., Varghese, M. M., Aryamol, K. S., Chinthala, M., Rajamohan, N., & Weng, B. (2025). Engineered cellulose-supported photocatalysts for clean energy and environmental remediation: progress and prospects. *Journal of Materials Chemistry A*, 14, 5473

Barange, S. H., Subodh, Raut, U., Bhansali, K. J., Kamlesh, Balinge, R., Dipesh, Patle, S., Pundlik, & Bhagat, R. (2023). Biodiesel production via esterification of oleic acid catalyzed by Brønsted acid-functionalized porphyrin grafted with benzimidazolium-based ionic liquid as an efficient photocatalyst. *Biomass Conversion and Biorefinery, 13*, 1873–1888.

Bekhradinassab, E., Haghighi, M., & Shabani, M. (2025). A review on acidic metal oxide-based materials towards heterogeneous catalytic biodiesel production via esterification process. *Fuel*, *379*, 132986.

Bhansali, K. J., Balinge, K. R., Raut, S. U., Deshmukh, S. A., Senthil, M., Kumar, C. R., Bhagat, P. R., Senthil Kumar, M., Ramesh Kumar, C., & Bhagat, P. R. (2021). Visible light assisted sulfonic acid-functionalized porphyrin comprising benzimidazolium moiety for photocatalytic transesterification of castor oil. *Fuel*, *304*, 121490.

Bian, R., An, S., Wang, X., Xue, Y., Tian, J., Liang, Z., & Song, Z. (2024). Ca^{2+} doped TiO_2 nano-sized polygon plates with oxygen vacancies for photocatalytic hydrogen evolution. *International Journal of Hydrogen Energy*, *51*, 787–795.

Boehm, S., & Schumer, C. (2023). *Intergovernmental Panel on Climate Change's (IPCC) Sixth Assessment Report (AR6)*.

Boichenko, S., Yakovlieva, A., Zubenko, S., & Shkilniuk, I. (2025). Physical, Chemical, and Performance Properties of Biodiesel Fuels: A Comparative Study of Lipid-Based Feedstocks. *Energies*, *18*(16), 4274.

Bora, L. V., Thakkar, S. P., Vadaliya, K. S., & Bora, N. V. (2023). Waste fly ash–ZnO as a novel sunlight-responsive photocatalyst for dye discoloration. *Water Science and Engineering*, *16*(1), 76–82.

Bouderbala, I. Y., Guessoum, A., Rabhi, S., Herbadji, A., & Bouras, I. E. (2025). Layer-dependent photocatalytic efficiency of ZnO Thin films: kinetic analysis, structural insights and optical bandgap characterization using absorption spectrum fitting, Tauc's plot, and Cody models. *Journal of Materials Science: Materials in Electronics*, *36*(27).

Chandroday, B., Shivaji, V., Radheshyam, P., Ganesh, R., Devidas, V., Baburao, V., Rudreshwar, K., Shikchand, D., & Rambhau, P. (2024). Novel porphyrin photocatalyst intertwined with ionic liquid and sulfonic acid groups for facile photo-transesterification of used frying oil. *Fuel*, *373*, 132295.

Cho, Y., Yanagiyama, K., Mukherjee, P., Phulkerd, P., Sathiyan, K., Sawade, E., Wada, T., & Taniike, T. (2025). Identifying rate-limiting steps in photocatalysis: a temperature-and light intensity-dependent diagnostic of charge supply vs. charge transfer. *Journal of Materials Chemistry A*, *13*(21), 16204–16211.

Chukwu, J. J. K., Egbuna, S. O., Ekpe, C. J., Edeh, C., & Agu, U. A. (2025). Examining the effects of process paramaters on the production of glycerol from castor seed oil. *Global Scientific Journal*, *13*(10), 531–538.

Crisóstomo, C. A. B., Damaceno, F. B., de Mesquita, J. P., Torres, J. A., Ribeiro, C., Ribeiro, R. A., Lopes, O. F., Avansi, W., Almeida, J. S., & Mourão, H. A. de J. L. (2025). Esterification of free fat acids from waste cooking oil using $BiVO_4$ photocatalysts under visible irradiation. *Reaction Kinetics, Mechanisms and Catalysis*, *138*(3), 1453–1467.

Cui, J., Zhang, F., Li, H., Cui, J., Ren, Y., & Yu, X. (2020). Recent progress in biochar-based photocatalysts for wastewater treatment: Synthesis, mechanisms, and applications. In *Applied Sciences (Switzerland)*, 10(3)

da Cunha, T., Maulu, A., Guillot, J., Fleming, Y., Duez, B., Lenoble, D., & Arl, D. (2021). Design of silica nanoparticles-supported metal catalyst by wet impregnation with catalytic performance for tuning carbon nanotubes growth. *Catalysts*, *11*(8), 986.

Dellisanti, A., Chessa, E., Porcheddu, A., Carraro, M., Pisano, L., De Luca, L., & Gaspa, S. (2024). Visible Light-Promoted Oxidative Cross-Coupling of Alcohols to Esters. *Molecules*, *29*(3), 570.

Deng, Y., Yang, T., Wang, H., Yang, C., Cheng, L., Yin, S. F., Kambe, N., & Qiu, R. (2021). Recent Progress on Photocatalytic Synthesis of Ester Derivatives and Reaction Mechanisms. *Topics in Current Chemistry*, 379(6).

Dharanya, C., & Dharmalingam, G. (2022). Oxygen vacancies in nanostructured hetero-interfacial oxides: a review. *Journal of Nanoparticle Research*, 24(3)

Dimitropoulos, M., Aggelopoulos, C. A., Sygellou, L., Tsantis, S. T., Koutsoukos, P. G., & Yannopoulos, S. N. (2024). Unveiling the photocorrosion mechanism of zinc oxide photocatalyst: Interplay between surface corrosion and regeneration. *Journal of Environmental Chemical Engineering*, *12*(2), 112102.

Dogar, S., Nayab, S., Farooq, M. Q., Said, A., Kamran, R., Duran, H., & Yameen, B. (2020). Utilization of biomass fly ash for improving quality of organic dye-contaminated water. *ACS Omega*, *5*(26), 15850–15864.

dos Santos, H. C. L., Gonçalves, M. A., da Rocha Filho, G. N., & da Conceição, L. R. V. (2025). Environmentally sustainable production of biodiesel from waste edible

oil using Mn–Fe supported magnetic acid heterogeneous catalyst: Optimization via Taguchi L9 technique. *Sustainable Chemistry and Pharmacy*, *45*, 102030.

Easwaran, G., Packialakshmi, J. S., Syed, A., Elgorban, A. M., Vijayan, M., Sivakumar, K., Bhuvaneswari, K., Palanisamy, G., & Lee, J. (2022). Silica nanoparticles derived from Arundo donax L. ash composite with Titanium dioxide nanoparticles as an efficient nanocomposite for photocatalytic degradation dye. *Chemosphere*, *307*, 135951.

Ebitei, S. N., Sunny, I., Michael, O. D., & Akindele, O. (2026). *Extraction and Characterization of Silica from Empty Palm Fruit Bunch (EPFB) Ash*.

Eddy, D. R., Permana, M. D., Sakti, L. K., Sheha, G. A. N., Solihudin, G. A. N., Hidayat, S., Takei, T., Kumada, N., & Rahayu, I. (2023). Heterophase Polymorph of TiO_2 (Anatase, Rutile, Brookite, TiO_2 (B)) for Efficient Photocatalyst: Fabrication and Activity. In *Nanomaterials*, 13(4)704.

Elanthikkal, S., Mohamed, H. H., & Alomair, N. A. (2023). Extraction of biosilica from date palm biomass ash and its application in photocatalysis. *Arabian Journal of Chemistry*, *16*(3), 104522.

El-Sayed, S. A., Khass, T. M., & Mostafa, M. E. (2024). Thermal degradation behaviour and chemical kinetic characteristics of biomass pyrolysis using TG/DTG/DTA techniques. *Biomass Conversion and Biorefinery*, *14*(15), 17779–17803.

Energy Agency, I. (2024). *World Energy Outlook 2024*. www.iea.org/terms

Erfan, N. A., Mahmoud, M. S., Kim, H. Y., & Barakat, N. A. M. (2023). Synergistic doping with Ag, CdO, and ZnO to overcome electron-hole recombination in TiO_2 photocatalysis for effective water photo splitting reaction. *Frontiers in Chemistry*, *11*, 1301172.

European Biodiesel Board. (2023). *EBB statistical report 2023: Global biodiesel production and market trends*.

Fadilah, C., Kurniawan, C., Ridwan, M., Al Muttaqii, M., Agustian, E., Andreani, A. S., Dwiatmoko, A. A., & Yati, I. (2023). Synthesis of superacid sulfated TiO_2 nanowires for esterification of waste cooking oil. *Reaction Kinetics, Mechanisms and Catalysis*, *136*(3), 1529–1544.

Farouk, S. M., Tayeb, A. M., Abdel-Hamid, S. M. S., & Osman, R. M. (2024). Recent advances in transesterification for sustainable biodiesel production, challenges,

and prospects: a comprehensive review. *Environmental Science and Pollution Research*, *31*(9), 12722–12747.

Fattah, I. M. R., Ong, H. C., Mahlia, T. M. I., Mofijur, M., Silitonga, A. S., Rahman, S. M. A., & Ahmad, A. (2020). State of the Art of Catalysts for Biodiesel Production. *Frontiers in Energy Research*, *8*, 1–17.

Fazil, M., & Ahmad, T. (2023). Pristine TiO_2 and Sr-Doped TiO_2 Nanostructures for Enhanced Photocatalytic and Electrocatalytic Water Splitting Applications. *Catalysts*, *13*(1), 93.

Ferrusca, M. C., Romero, R., Martínez, S. L., Ramírez-Serrano, A., & Natividad, R. (2023). Biodiesel Production from Waste Cooking Oil: A Perspective on Catalytic Processes. *Processes*, *11*(7), 1952.

Gadore, V., & Mishra, S. R. (2025). SnS_2/ZIF-67 nanocomposite: A novel bifunctional, highly efficient, and reusable photocatalyst for enhanced visible-light-assisted biodiesel production and degradation of tinidazole. *Materials Research Bulletin*, *183,* 113177.

Gadore, V., Ranjan Mishra, S., & Ahmaruzzaman, M. (2025). Visible light-driven photocatalytic biodiesel production using novel SnS_2/Fly ash photocatalyst. *Fuel*, *382*, 133615.

Gakuru, S. W., Kiprotich, S., & Waithaka, P. (2024). Structural and Optical Properties of Fe Doped TiO_2 Nanoparticles: Investigation of Effects of Different Doping Concentration. *Advances in Materials*, *13*(2), 20–30.

Gao, X., Cai, P., Wang, Z., Lv, X., & Kawi, S. (2023). Surface Acidity/Basicity and Oxygen Defects of Metal Oxide: Impacts on Catalytic Performances of CO_2 Reforming and Hydrogenation Reactions. *Topics in Catalysis*, *66*(5–8), 299–325.

Gartner, M., Szekeres, A., Stroescu, H., Mitrea, D., & Covei, M. (2024). Advanced Nanostructured Coatings Based on Doped TiO2 for Various Applications. *Separate and Joint Continuity*, *28*, 7828.

Gautam, S., Agrawal, H., Thakur, M., Akbari, A., Sharda, H., Kaur, R., & Amini, M. (2020). Journal of Environmental Chemical Engineering Metal oxides and metal organic frameworks for the photocatalytic degradation: A review. *Journal of Environmental Chemical Engineering*, *8*(3), 103726.

Gegova-Dzhurkova, R., Nesheva, D., Stambolova, I., Zaharieva, K., Dzhurkov, V., & Miloushev, I. (2024). Enhanced Photocatalytic Performance under Ultraviolet and

Visible Light Illumination of ZnO Thin Films Prepared by Modified Sol-Gel Method. *Molecules*, *29*(17), 4005.

Guan, S., Cheng, Y., Hao, L., Yoshida, H., Tarashima, C., Zhan, T., Itoi, T., Qiu, T., & Lu, Y. (2023). Oxygen vacancies induced band gap narrowing for efficient visible-light response in carbon-doped TiO_2. *Scientific Reports*, *13*(1), 1–9.

Güell, F., Galdámez-Martínez, A., Martínez-Alanis, P. R., Catto, A. C., da Silva, L. F., Mastelaro, V. R., Santana, G., & Dutt, A. (2023). ZnO-based nanomaterials approach for photocatalytic and sensing applications: recent progress and trends. *Materials Advances*, *4*(17), 3685–3707

Guliani, D., Sobti, A., & Toor, A. P. (2022). Titania impregnated mesoporous MCM-48 as a solid photo-catalyst for the synthesis of methyl palmitate: Reaction mechanism and kinetics. *Renewable Energy*, *191*, 405–417.

Guo, M., Jiang, W., Chen, C., Qu, S., Lu, J., Yi, W., & Ding, J. (2021). Process optimization of biodiesel production from waste cooking oil by esterification of free fatty acids using La^{3+}/ZnO-TiO_2 photocatalyst. *Energy Conversion and Management*, *229*, 113745.

Hamed, H. H., Mohammed, A. E., Habeeb, O. A., Ali, O. M., Aljaf, O. H. S., & Abdulqader, M. A. (2021). Biodiesel production from waste cooking oil using homogeneous catalyst. *Egyptian Journal of Chemistry*, *64*(6), 2827–2832.

Hanafiah, M. K., Abd Mutalib, A. H., Miard, P., Goh, C. S., Mohd Sah, S. A., & Ruppert, N. (2022). Impact of Malaysian palm oil on sustainable development goals: co-benefits and trade-offs across mitigation strategies. *Sustainability Science*, *17*(4), 1639–1661.

Hayyan, A., Hizaddin, H. F., Abed, K. M., Mjalli, F. S., Hashim, M. A., Abo-Hamad, A., Saleh, J., Aljohani, A. S. M., Alharbi, Y. M., Alhumaydhi, F. A., Ahmad, A. A., Yeow, A. T. H., Aldeehani, A. K., Alajmi, F. D. H., & Al Nashef, I. (2022). Encapsulated deep eutectic solvent for esterification of free fatty acid. *Biomass Conversion and Biorefinery*, *12*(9), 3725–3735.

Hisham, N. S., & Jamil, Z. (2020). Utilisation of oil palm empty fruit bunch ash as potential natural coagulant for palm oil mill effluent treatment. *GADING Journal of Science and Technology*, *3*(2), 178–186.

Hmoudah, M., Paparo, R., Chianese, C., El-qanni, A., Salmi, T., Tesser, R., Russo, V., & Di, M. (2025). Ibuprofen photodegradation promoted by ZnO and TiO_2-P25

nanoparticles: A comprehensive kinetic, reaction mechanisms, and thermodynamic investigation. *Journal of Water Process Engineering*, *69*, 2–11.

Hsiao, M.-C., Liao, P.-H., Lan, N. V., & Hou, S.-S. (2021). Enhancement of Biodiesel Production from High-Acid-Value Waste Cooking Oil via a Microwave Reactor Using a Homogeneous Alkaline Catalyst. *Energies*, *14*(2), 437.

Hu, Z., Shen, J., Tan, P., & Lou, D. (2025). Life cycle carbon footprint of biodiesel production from waste cooking oil based on survey data in Shanghai, China. *Energy*, *320*, 135318.

Huang, J., Jian, Y., Zhu, P., Abdelaziz, O., & Li, H. (2022). Research Progress on the Photo-Driven Catalytic Production of Biodiesel. *Frontiers in Chemistry*, *10*, 90421.

Hussein, M. A. T., Motawea, M. M., Elsenety, M. M., El-Bahy, S. M., & Gomaa, H. (2022). Mesoporous spongy Ni–Co oxides@wheat straw-derived SiO_2 for adsorption and photocatalytic degradation of methylene blue pollutants. *Applied Nanoscience (Switzerland)*, *12*(5), 1519–1536.

Hussein, O. N., AL-Jawad, S. M. H., & Imran, N. J. (2024). A Study on the Influence of Metal Fe, Ag, and Mn Doping and (Fe/Mn and Ag/Mn) Dual-Doping on the Structural, Morphological, Optical, and Antibacterial Activity of CuS Nanostructures. *Plasmonics*, *19*(3), 1101–1120.

Idris, M., Abdul Rasid, A. F., Mohd Zamberi, M., & Zhang, Y. (2024). Biodiesel Production from Waste Cooking Oil: A Review of Prospects and Challenges. *Journal of Advanced Research in Fluid Mechanics and Thermal Sciences*, *124*(1), 28–52.

Irshad, U., Aslam, Z., Sumbal, S., Hamza, A., & Zaka-ur-Rehman. (2024). CO_2 capture enhancement by metal oxides impregnated coal fly ash: a breakthrough adsorption study. *Environmental Science and Pollution Research*, *31*(52), 61592–61611.

Islam, A., Teo, S. H., Islam, M. T., Ahamed, E., Islam, M. S., Alsultan, A. G., Marwani, H. M., Rahman, M. M., Asiri, A. M., Taufiq-Yap, Y. H., & Awual, M. R. (2023). Boosting biodiesel production over silicon heterojunction with visible light irradiation. *Energy Conversion and Management*, *292*, 117435.

Jacob-Lopes, E., Zepka, L. Q., & Deprá, M. C. (2025). *The Essential Properties of Oils for Biodiesel Production. In Biodiesel Plants - Fueling the Sustainable Outlooks*. IntechOpen.

Jafarihaghighi, F., Ardjmand, M., Salar Hassani, M., Mirzajanzadeh, M., & Bahrami, H. (2020). Effect of Fatty Acid Profiles and Molecular Structures of Nine New Source of Biodiesel on Combustion and Emission. *ACS Omega*, *5*(26), 16053–16063.

Juera-Ong, P., Pongraktham, K., Oo, Y. M., & Somnuk, K. (2022). Reduction in Free Fatty Acid Concentration in Sludge Palm Oil Using Heterogeneous and Homogeneous Catalysis: Process Optimization, and Reusable Heterogeneous Catalysts. *Catalysts*, *12*(9).

Kadem, A. J., Tan, Z. M., Suntharam, N. M., Pung, S. Y., & Ramakrishnan, S. (2023). Synthesis of CuO, ZnO and SnO_2 Coupled TiO_2 Photocatalyst Particles for Enhanced Photodegradation of Rhodamine B Dye. *Bulletin of Chemical Reaction Engineering and Catalysis*, *18*(3), 506–520.

Kamat, P. V., & Sivula, K. (2022). Celebrating 50 Years of Photocatalytic Hydrogen Generation. *ACS Energy Letters*, *7*(9), 3149–3150.

Kanchanakul, I., Srinophakun, T. R., Kuboon, S., Kaneko, H., Kraithong, W., Miyauchi, M., & Yamaguchi, A. (2023). Development of Photothermal Catalyst from Biomass Ash (Bagasse) for Hydrogen Production via Dry Reforming of Methane (DRM): An Experimental Study. *Molecules*, *28*(12), 4578.

Katre, S., Baghmare, P., & Giri, A. S. (2024). Photocatalytic nanomaterials and their implications towards biomass conversion for renewable chemical and fuel production. *Nanoscale Advances*, *6*(21), 5258–5284.

Khalid, H., Umar, A., Nazir, M. S., Farid, M. A., Ali, Z., Mahmood, A., Al-Masry, W., Park, C. H., Akhter, T., & Hassan, S. U. (2024). Development and optimization of a sustainable polyoxometalate-kaolinite-based catalyst for efficient desulfurization of model and real fuel using Box-Behnken design. *RSC Advances*, *14*(44), 31979–31989.

Khalil, I. E., Das, P., Küçükkeçeci, H., Dippold, V., Rabeah, J., Tahir, W., Roeser, J., Schmidt, J., & Thomas, A. (2024). Hierarchical Porous Covalent Organic Frameworks: The Influence of Additional Macropores on Photocatalytic Hydrogen Evolution and Hydrogen Peroxide Production. *Chemistry of Materials*, *36*(17), 8330–8337.

Khan, H., & Shah, M. U. H. (2023). Modification strategies of TiO_2 based photocatalysts for enhanced visible light activity and energy storage ability: A review. *Journal of Environmental Chemical Engineering*, *11*(6), 111532.

Khan, Z., Javed, F., Shamair, Z., Hafeez, A., Fazal, T., Aslam, A., Zimmerman, W. B., & Rehman, F. (2021). Current developments in esterification reaction: A review on process and parameters. *Journal of Industrial and Engineering Chemistry*, *103*, 80–101.

Khlyustova, A., Sirotkin, N., Kusova, T., Kraev, A., Titov, V., & Agafonov, A. (2020). *Materials Advances Doped TiO_2: the effect of doping elements on photocatalytic activity*. *1*, 1193–1201.

Ko, H., Lee, M., Sen, R., Choi, J., & Oh, S. (2025). Pyrolysis Characteristics of Empty Fruit Bunches at Different Temperatures and Heating Rates. *Energies*, *18*(6), 1404.

Kokab, M., Bibi, I., Majid, F., Kamal, S., Taj, B., Fatima, G., Raza, Q., Lim, S., Alzahrani, F. M., Nazir, A., & Iqbal, M. (2025). Solar light-based photocatalysis for organic pollutant degradation: Mechanistic understanding of double Z-scheme dynamics in ZnO/Fe_2O_3-doped $NiCo_2O_4$. *Solar Energy*, *295*, 113519.

Kumar, A., Bhayana, S., Singh, P. K., Tripathi, A. D., Paul, V., Balodi, V., & Agarwal, A. (2025). Valorization of used cooking oil: challenges, current developments, life cycle assessment and future prospects. *Discover Sustainability*, *6*(1), 119.

Kumar, P., Banerjee, D., & Sharma, A. K. (2025). Photoluminescence Study of Sol–Gel Grown Zinc Oxide Rods under Varying Excitation Conditions. *Journal of The Institution of Engineers (India): Series D*.

Lage, V. M. A., Rodríguez-Fernández, C., Vieira, F. S., da Silva, R. T., Bernardi, M. I. B., Lima, M. M. de, Cantarero, A., & de Carvalho, H. B. (2023). On the vibrational properties of transition metal doped ZnO: Surface, defect, and bandgap engineering. *Acta Materialia*, *259*, 119258.

Lahur, M. V., Ajay, K., Aejaz, U. B., Upanshu, G., Pravin P. Ingole, & Satyawati, S. (2024). Phase controlled green synthesis of wurtzite (P63mc) ZnO nanoparticles: interplay of green ligands with precursor anions, anisotropy and photocatalysis. *Nanoscale Advances*, *6*, 155–169.

Li, R., Li, T., & Zhou, Q. (2020). Impact of titanium dioxide (TiO_2) modification on its application to pollution treatment-a review. *Catalysts*, *10*(7), 804.

Liu, Y., Yang, X., Adamu, A., & Zhu, Z. (2021). Economic evaluation and production process simulation of biodiesel production from waste cooking oil. *Current Research in Green and Sustainable Chemistry*, *4*, 100091.

Lojpur, V. (2025). Recent Advances in Photocatalysis for Environmental Applications. *Catalysts*, *15*(11).

Lokman Nolhakim, M. A. H., Shohaimi, N. A. M., Mokhtar, W. N. A. W., Ibrahim, M. L., & Abdullah, R. F. (2021). Immobilization of potassium-based heterogeneous catalyst over alumina beads and powder support in the transesterification of waste cooking oil. *Catalysts*, *11*(8), 976.

Ma, C., Tang, J., Wang, Q., Meng, R., & Li, Q. (2025). Enhanced Photocatalytic Performances and Mechanistic Insights for Novel Ag-Bridged Dual Z-Scheme AgI/Ag_3PO_4/WO_3 Composites. *Inorganics*, *13*(7).

Mahayuddin, N. E. M. M., Mustaffa, S. N. A. S., Shukor, H., Tamayo, J. P., & Kasim, F. H. (2022). Biodiesel production in Malaysia: Current status and challenges. *AIP Conference Proceedings*, *2541*(1), 020005.

Mahesh, A., Kumar, G. P., Jawahar, I. N., & Biju, V. (2024). Temperature Dependent Photoluminescence Spectra of Nanocrystalline Zinc Oxide: Effect of processing condition on the excitonic and defect mediated emissions. *Chemical Physics Impact*, *8*, 100456.

Maj, I., Niesporek, K., Płaza, P., Maier, J., & Łój, P. (2025). Biomass Ash: A Review of Chemical Compositions and Management Trends. *Sustainability (Switzerland)*, *17*(11), 1–23.

Makota, O., Lisnichuk, M., Brian, J., Bednar, J., & Saf, P. J. (2025). Chemosphere Magnetically enhanced Fe3O4@ZnO and Fe_3O_4@ZnO@$Bi_2O_{2.7}$ composites for efficient UV and visible light photodegradation of methyl orange and ofloxacin. *Chemosphere*, *377*, 144365.

Maniam, G. P., Lim, H. S., & Mat Hussin, N. (2023). Effect of Free Fatty Acid on Transesterification of Waste Cooking Oil. *Current Science and Technology*, *3*(1), 57–63.

Markushyna, Y., & Savateev, A. (2022). Light as a Tool in Organic Photocatalysis: Multi-Photon Excitation and Chromoselective Reactions. *European Journal of Organic Chemistry*, e202200026.

Masango, S. B., Ngema, P. T., & Olagunju, O. A. (2024). The effect of reaction temperature, catalyst concentration and alcohol ratio in the production of biodiesel from raw and purified castor oil. *Advances in Chemical Engineering and Science*, *14*, 137–154.

Mathew, G. M., Raina, D., Narisetty, V., Kumar, V., Saran, S., Pugazhendi, A., Sindhu, R., Pandey, A., & ParameswaranBinod. (2021). Recent advances in biodiesel production: Challenges and solutions. *Science of the Total Environment Journal*, *794*, 148751.

Medeiros Vicentini-Polette, C., Rodolfo Ramos, P., Bernardo Gonçalves, C., & Lopes De Oliveira, A. (2021). Determination of free fatty acids in crude vegetable oil samples obtained by high-pressure processes. *Food Chemistry: 12*, 100166.

Medjahed, L., Bousbaa, H., Benramdane, M., Naima, K., Ameur, H., Ozsahin, D. U., & Ahmad, H. (2025). Integrated valorization of waste cooking oil into biodiesel: optimizing upstream processes and blend performance for sustainable energy. *Modeling Earth Systems and Environment*, *11*(6), 389.

Meirelles, M. R., Giroto, A. S., Furukawa, K., & Gonçalves, M. (2025). Valorization of Lignocellulosic Biomass for Photocatalytic Applications: Development of Activated Carbon-TiO²Composites. *ACS Sustainable Resource Management*, *2*(3), 524–535.

MIDA. (2025). *Food Technology - Palm Biomass - Malaysian Investment Development Authority (MIDA)*.

Ministry of Economy, M. (2023). *National Energy Transition Roadmap*.

Mino, L., & Negri, C. (2020). Morphology, Surface Structure and Water Adsorption. *Molecules*, *25*, 4605.

Moafi, Z., Abbasi, Z., & Ahmadi. (2023). Biodiesel Production Using a Photocatalytic Process: A Review. *Journal of Medicinal and Nanomaterials Chemistry*, *5*(1), 1–15.

Mohamadpour, F., & Amani, A. M. (2024). Photocatalytic systems: reactions, mechanism, and applications. *RSC Advances*, *14*(29), 20609–20645.

Mohamed, K. M., Benitto, J. J., & Vijaya, J. J. (2023). Recent Advances in ZnO - Based Nanostructures for the Photocatalytic Degradation of Hazardous, Non-Biodegradable Medicines. *Crystals*, 13, 329.

Mu, M., Liu, H., Chen, J., Li, L., Liu, D., Yang, Y., Shang, L., & Zhao, B. (2025). Light-dependent electron transfer mechanism on a Z-scheme MIL-100 (Fe)/AgCl/Ag heterostructure for photocatalytic degradation. *Journal of Colloid and Interface Science*, *680*, 623–631.

Mustafa, M. G., Singh, B., & Dey, R. K. (2024). Biogenic (Lantana camara L) synthesis of ZnO as a catalyst for the production of biodiesel from nonedible waste cooking oil: Materials characterization; studies of kinetics and thermodynamics of biodiesel production and optimization using RSM. *Journal of the Indian Chemical Society*, *101*(6).

Nagakawa, H., Ochiai, T., Ma, H., Wang, C., Zhang, X., Shen, Y., Takashima, M., Ohtani, B., & Nagata, M. (2020). Elucidation of the electron energy structure of TiO_2(B) and anatase photocatalysts through analysis of electron trap density. *RSC Advances*, *10*(31), 18496–18501.

Naveed, A. B., Javaid, A., Zia, A., Ishaq, M. T., Amin, M., Farooqi, Z. U. R., & Mahmood, A. (2023). TiO_2/g-C_3N_4 Binary Composite as an Efficient Photocatalyst for Biodiesel Production from Jatropha Oil and Dye Degradation. *ACS Omega*, *8*(2), 2173–2182.

Navidpour, A. H., Dashti, A., Dil, E. A., Asadi, P., Zhou, J. L., Moshfegh, A., & Altaee, A. (2026). Zinc oxide photocatalysis for pollutant degradation: a review of elemental doping, morphology, and microstructure, integrated with machine learning-based performance modelling. *Advanced Composites and Hybrid Materials*.

Nextgreen Global Bhd. (2024). *Nextgreen Global scales up operations, turning biomass into green products*. Malaysian Investment Development Authority (MIDA).

Ngobeh, J. M., Sannoh, M., & Thullah, J. (2023). A Comparative Analysis of the Sustainable Growth of Global Hydro, Solar, and Wind Power Systems (Renewable Energy Systems). *Open Journal of Energy Efficiency*, *12*(03), 49–61.

Ning, S., Wei, Z., Chen, Z., Wu, T., & Zhang, L. (2025). Curvature and defect formation synergistically promote the photocatalysis of ZnO slabs. *Chinese Chemical Letters*, *36*(7), 111057.

Niu, J., Zhou, Z., Song, S., Guo, B., Liu, H., Jin, Y., & Ran, J. (2025). The impact of oxide support on the reaction mechanism of copper-based catalysts for CO_2 activation. *International Journal of Hydrogen Energy*, *132*, 18–31.

Niyas, M. M., & Shaija, A. (2023). Effect of fatty acid profiles of waste cooking oil biodiesels on their thermal and physical properties. *Journal of Thermal Analysis and Calorimetry*, *148*(17), 9225–9235.

Oils & Fats International. (2024). Global biodiesel production rises to record level. *OFI Magazine*, 1–7.

Okechukwu, O. D., Joseph, E., Nonso, U. C., & Kenechi, N.-O. (2022). Improving heterogeneous catalysis for biodiesel production process. *Cleaner Chemical Engineering*, *3*, 100038.

Oladipo, B., Qasana, S., Zini, S. C., Menemene, N., & Ojumu, T. V. (2024). Microwave-assisted biodiesel synthesis from waste cooking oil: Exploring the potential of carob pod-derived solid base catalyst. *Fuel Processing Technology*, *266*, 108161.

Orudzhev, F., Muslimov, A., Selimov, D., Gulakhmedov, R. R., Lavrikov, A., Kanevsky, V., Gasimov, R., Krasnova, V., & Sobola, D. (2023). Oxygen Vacancies and Surface Wettability: Key Factors in Activating and Enhancing the Solar Photocatalytic Activity of ZnO Tetrapods. *International Journal of Molecular Sciences*, *24*(22), 16338.

Ou, X., Zhao, K., Chen, P., Xia, C., Wei, M., Zhang, M., & Wang, Y. (2024). Visible-light responsive Ag-doped ZnO/$InVO_4$ composite photocatalyst for efficient degradation of tetracycline and Inactivate E. coli. *Journal of Alloys and Compounds*, *1002*, 175230.

Outili, N., Kerras, H., & Meniai, A. H. (2023). Recent conventional and non-conventional WCO pretreatment methods: Implementation of green chemistry principles and metrics. *Current Opinion in Green and Sustainable Chemistry*, *41*, 100794.

Oyehan, T. A., Salami, B. A., Badmus, S. O., & Saleh, T. A. (2022). Technological trends in activation and modification of palm oil fuel ash for advanced water and wastewater treatment – A review. *Sustainable Chemistry and Pharmacy*, *29*, 100754.

Ozoani, E. O., George-okafor, U. O., & Ozoani, U. E. (2024). Evaluation of the phytochemical, mineral components and antimicrobial activity of empty palm fruit bunch ash and unripe plantain peel ash for use as alkaline bio activators of charcoal. *GCS Biological and Pharmaceutical Sciences,* 28(02)146-152.

Özyiğit, B., Sayilganlar, E., & Akbay, E. (2024). Photocatalytic esterification of acetic acid with methanol over metal-exchanged phosphotungstate. *Journal of Photochemistry and Photobiology A: Chemistry*, *447*, 115280.

Paiu, M., Lutic, D., Favier, L., & Gavrilescu, M. (2025). Heterogeneous Photocatalysis for Advanced Water Treatment: Materials, Mechanisms, Reactor Configurations, and Emerging Applications. *Applied Sciences (Switzerland)*, *15*(10), 5681.

Panda, S. S., Tripathy, H. P., Satapathy, L. M., Pattanaik, P., Kamilla, S. K., Mishra, D. K., & Mahapatra, P. K. (2024). Synthesis and characterization of zinc oxide reinforced fly ash piezoelectric floor tiles for automated sanitization system application. *Journal of Materials Science: Materials in Electronics*, *35*(15), 1–15.

Papagiannaki, D., Medana, C., Binetti, R., Calza, P., & Roslev, P. (2020). Effect of UV-A, UV-B and UV-C irradiation of glyphosate on photolysis and mitigation of aquatic toxicity. *Scientific Reports*, *10*, 20247.

Parvulescu, V., Ciobanu, M., & Petcu, G. (2020). Immobilization of semiconductor photocatalysts. In *Handbook of Smart Photocatalytic Materials: Fundamentals, Fabrications and Water Resources Applications* (pp. 103–140). Elsevier.

Pathak, A., Samanta, S., Bahadur, J., Kaur, M., & Singh, A. (2025). Applied Surface Science Tailoring ZnO-Au nanocomposites for enhanced NO_2 sensing: Synergistic effect of facet orientation and Au nano-particle surface functionalization. *Applied Surface Science*, *687*, 162199.

Patil, V. S., Mataghare, B. C., Maske, R. G., Yadav, P. R., Channe, V. D., Balinge, K. R., Khajone, V. B., Patle, D. S., & Bhagat, P. R. (2024). *Porphyrin derived from sulphonic acid functionalized pyridinium ionic liquid for sustainable photocatalytic conversion of frying oil to biodiesel compatible with diesel engine*.

Payormhorm, J., & Idem, R. (2020). Applied Catalysis A, General Synthesis of C-doped TiO_2 by sol-microwave method for photocatalytic conversion of glycerol to value-added chemicals under visible light. *Applied Catalysis A, General*, *590*, 117362.

Pinedo-Escobar, J. A., Junpeng Fan, Edgar Moctezuma, Gomez-Solís, C., Martinez, C. J. C., & Gracia-Espino, E. (2021). Nanoparticulate double-heterojunction photocatalysts comprising TiO_2(Anatase)/WO_3/TiO_2(Rutile) with enhanced photocatalytic activity toward the degradation of methyl orange under near-ultraviolet and visible light. *ACS Omega*, *6*(18), 11840–11848.

Podelinska, A., Neilande, E., Pankratova, V., Serga, V., Bandarenka, H., Burko, A., Piskunov, S., Pankratov, V. A., Sarakovskis, A., Popov, A. I., & Bocharov, D. V. (2025). Structural and Spectroscopic Characterization of TiO_2 Nanocrystalline Materials Synthesized by Different Methods. *Nanomaterials*, *15*(7), 1–21.

Pratiwi, S., Hauli, L., Marhadi, R., Mansur, D., & Budiman, A. (2026). Investigating the Catalytic Performance of ZnO/Sulfonated Biochar for the Simultaneous Production of Biodiesel from Waste Cooking Oil. *Catalysis Surveys from Asia*, *30*, 77–94.

Putra, H. P., Kuswa, F. M., Ghazidin, H., Darmawan, A., Prabowo, Hariana, Prida, H., Milkiy, F., Ghazidin, H., & Darmawan, A. (2023). Slagging-fouling evaluation of empty fruit bunch and palm oil frond mixture with bituminous ash coal as co-firing fuel. *Bioresource Technology Reports*, *22*, 101489.

Qi, K., Imparato, C., Almjasheva, O., Khataee, A., & Zheng, W. (2024). TiO_2-based photocatalysts from type-II to S-scheme heterojunction and their applications. *Journal of Colloid and Interface Science*, *675*, 150–191.

Qiu, Q., Zhu, P., Liu, Y., Liang, T., Xie, T., & Lin, Y. (2021). Highly efficient In2S3/WO3photocatalysts: Z-scheme photocatalytic mechanism for enhanced photocatalytic water pollutant degradation under visible light irradiation. *RSC Advances*, *11*(6), 3333–3341.

Raha, S., & Ahmaruzzaman, M. (2022). ZnO nanostructured materials and their potential applications: progress, challenges and perspectives. *Nanoscale Advances*, *4*(8), 1868–1925.

Rahmat, F., Fen, Y. W., Anuar, M. F., Oma, N. A. S., Zaid, M. H. M., Matori, K. A., & Khaidir, R. E. M. (2021). Synthesis and characterization of ZnO-SiO2 composite using oil palm empty fruit bunch as a potential silica source. *Molecules*, *26*(4), 1061.

Ramos-Justicia, J. F., Urbieta, A., & Fernández, P. (2026). Refined Langmuir–Hinshelwood Kinetics for Heterogeneous Photocatalytic Systems: Analytical Closed-Form Solution, Enhanced Approximations and Experimental Validation. *Physchem*, *6*(1), 5.

Randhawa, S., & Mukherjee, T. (2023). Effect of containers on the thermal degradation of vegetable oils. *Food Control*, *144*, 109344.

Razzak, S. A., Zakir Hossain, S. M., Ahmed, U., & Hossain, M. M. (2025). Cleaner biodiesel production from waste oils (cooking/vegetable/frying): Advances in catalytic strategies. *Fuel*, *393*, 134901.

Redjeki, A. S., Sukirno, S., & Slamet, S. (2021). Simultaneous photocatalytic esterification and addition reaction of fatty acids in kemiri sunan (reutealis

trisperma sp.) oil over CuO/TiO_2 catalyst - A novel approach. *Bulletin of Chemical Reaction Engineering & Catalysis*, *16*(4), 816–830.

Rizwanul Fattah, I. M., Ong, H. C., Mahlia, T. M. I., Mofijur, M., Silitonga, A. S., Ashrafur Rahman, S. M., & Ahmad, A. (2020). State of the Art of Catalysts for Biodiesel Production. *Frontiers in Energy Research*, *8*, 101.

Saanyol, I. I., Ekele, A. O., & Oluwamayokun, A. F. (2022). Effect of Vegetable Oil Viscosity on Biodiesel. *Industrial and Engineering Chemistry*, *3*(7), 2582–6832.

Salim, S. M., Izriq, R., Almaky, M. M., & Al-abbassi, A. A. (2022). Synthesis and characterization of ZnO nanoparticles for the production of biodiesel by transesterification: Kinetic and thermodynamic studies. *Fuel*, *321*, 124135.

Salim, S. M., Izriq, R., Almaky, M. M., & Al-Abbassi, A. A. (2022). Synthesis and characterization of ZnO nanoparticles for the production of biodiesel by transesterification: Kinetic and thermodynamic studies. *Fuel*, *321*.

Salu, D. E., James Lourd Raj, J. M., Ashok Balamurugan Ramya, K., Manivasagam, V. R., Eswaran, J., Kanthapazham, R., Vanaraj, R., & Daniel, S. (2026). Defect-engineered ZnO nanoparticles synthesized via green routes for enhanced solar photocatalytic activity. *Dalton Transactions*.

Santis, A., Arbeláez, O., Mendivelso, K., Riaño, M., Prieto, V., & Velásquez, P. (2025). Sustainable innovation: Removal of chromium (VI) from wastewater from plastic chromium plating industries using rice husk as photocatalyst. *Results in Engineering*, *26*, 104756.

Schneider, J. T., Firak, D. S., Ribeiro, R. R., & Peralta-Zamora, P. (2020). Use of scavenger agents in heterogeneous photocatalysis: truths, half-truths, and misinterpretations. *Physical Chemistry Chemical Physics*, *22*(27), 15723–15733.

Semenova, O., Dargie, Z. A., Yadgarov, L., Nakonechny, F., & Nisnevitch, M. (2025). Esterification of Free Fatty Acids Under Heterogeneous Catalysis Using Ultrasound. *Catalysts*, *15*(12), 1161.

Sen, P., Bhattacharya, P., Mukherjee, G., Ganguly, J., Marik, B., Thapliyal, D., Verma, S., Verros, G. D., Chauhan, M. S., & Arya, R. K. (2023). Advancements in Doping Strategies for Enhanced Photocatalysts and Adsorbents in Environmental Remediation. *Technologies*, *11*(5), 1–31.

Senusi, W., Ahmad, M. I., Binhweel, F., Shalfoh, E., Alsaedi, S., & Shakir, M. A. (2024). Biodiesel production and characteristics from waste frying oils: sources,

challenges, and circular economic perspective. *Environmental Science and Pollution Research*, *31*, 33239–33258.

Shah, R., Khan, D., Al-anazi, A., Ahmad, W., Ullah, I., Shah, N. S., & Ali, J. (2025). Non-metal doped ZnO and TiO_2 photocatalysts for visible light active degradation of pharmaceuticals and hydrogen production: A review. *Applied Catalysis O: Open*, *204*, 207043.

Shahdan, N. A., Balasundram, V., Ibrahim, N., & Isha, R. (2023). Thermogravimetric and kinetic studies on pyrolysis of empty fruit bunch over metal-impregnated rice husk ash catalysts. *Biomass Conversion and Biorefinery*, *13*(18), 16441–16451.

Sharma, R., Pal, B., & Barman, S. (2025). Synergistic effect of adsorption and photocatalytic activity of Cu deposited fly ash-TiO_2 composites for fuchsin blue removal under visible-solar light. *Solar Energy*, *287*.

Sharma, R., & Prakash, J. (2025). TiO_2 Nanomaterials: Synthesis, Properties, Modifications, and Applications. In *Engineering Materials*.

Shi, J., Huang, W., Zhu, H., Xiong, J., Bei, H., Wei, X., & Wang, S. (2020). Modified TiO_2 particles for heterogeneous photocatalysis under solar irradiation. *Materials Letters*, *279*, 128472.

Shohaimi, N. A. M., Adnan, N. K., & Ibrahim, S. F. (2024). Photoesterification of Waste Cooking Oil using ZnO Doped Empty Fruit Bunches Ash Heterogeneous Catalyst. *Recent Innovations in Chemical Engineering*, *17*(2), 119–133.

Siang Ng, D., Paul, S. C., Anggraini, V., Kong, S. Y., Qureshi, T. S., Rodriguez, C. R., Liu, Q. feng, & Šavija, B. (2020). Influence of SiO2, TiO2 and Fe2O3 nanoparticles on the properties of fly ash blended cement mortars. *Construction and Building Materials*, *258*, 119627.

Silva, T. H., Lara, L. F. S., Silva, G. J. B., Provis, J. L., & Bezerra, A. C. S. (2022). Alkali-activated materials produced using high-calcium, high-carbon biomass ash. *Cement and Concrete Composites*, *132*, 104646.

Sintipditsakul, P., Yang, C., Dai, Z., Kiatwisarnkij, N., Lolupiman, K., Woottapanit, P., Zhang, X., Wangyao, P., & Qin, J. (2025). Construction of Artificial Interface Layer in the Fly Ash Suspension for Durable Zn Anode. *ACS Applied Energy Materials*, *8*(3), 1766–1775.

Son, B. T., Long, N. V., & Nhat Hang, N. T. (2021). The development of biomass-derived carbon-based photocatalysts for the visible-light-driven photodegradation of pollutants: A comprehensive review. *RSC Advances*, *11*(49), 30574–30596.

Song, C., Xiao, L., Chen, Y., Yang, F., Meng, H., Zhang, W., Zhang, Y., & Wu, Y. (2024). TiO_2-Based Catalysts with Various Structures for Photocatalytic Application: A Review. *Catalysts*, *14*(6), 366.

Song, M., Lu, Z., & Li, D. (2020). Phase transformations among TiO_2 polymorphs. *Nanoscale*, *12*(45), 23183–23190.

Sordello, F., Calza, P., Minero, C., Malato, S., & Minella, M. (2022). More than One Century of History for Photocatalysis, from Past, Present and Future Perspectives. *Catalysts*, *12*(12), 1572.

Suzihaque, M. U. H., Alwi, H., Kalthum Ibrahim, U., Abdullah, S., & Haron, N. (2022). Biodiesel production from waste cooking oil: A brief review. *Materials Today: Proceedings*, *63*, S490–S495.

Tanaka, T., Ouchi, T., & Okabe, T. H. (2020). Lanthanothermic Reduction of TiO_2. *Metallurgical and Materials Transactions B: Process Metallurgy and Materials Processing Science*, *51*(4), 1485–1494.

Tang, X., Wen, L., Cui, C., Zhang, Z., Wang, Y., Cheng, Y., & Liu, B. (2025). In situ growth of Fe-doped TiO_2 on flexible Ti mesh for CO oxidation. *Research on Chemical Intermediates*, *0123456789*, 1–14.

Tang, Y., Shen, F., Huang, H., Shang, H., Mao, H., Ma, J., Liao, Y., & Zhao, S. (2020). Preparation of fluorine and carbon co-introduced TiO_2 at low temperature with enhanced visible-light degradation performance for 2,4,6-trichlorophenol. *Materials Research Express*, *7*(2), 0–12.

Tariq, I., Zubair, M., Iqbal, W., Badshah, A., Abbas, S. M., & Haider, A. (2025). Alkaline earth metal oxides supported on WO_3@MCM-41; bifunctional catalysts for biodiesel production from corn and waste cooking oil. *Hybrid Advances*, *10*, 100477.

Tashiro, A., Adachi, Y., & Uchino, T. (2023). Excitonic processes and lasing in ZnO thin films and micro/nanostructures. *Journal of Applied Physics*, *133*(22), 221101.

Tee, S. Y., Kong, J., Koh, J. J., Teng, C. P., Wang, X. Z., Wang, X., Teo, S. L., Thitsartarn, W., Han, M.-Y., & Seh, Z. W. (2024). Structurally and Surficially

Activated TiO_2 Nanomaterials for Photochemical Reactions. *Nanoscale*, *16*, 18165–18212.

Tian, D., Zhou, H., Zhang, H., Zhou, P., You, J., Yao, G., Pan, Z., Liu, Y., & Lai, B. (2022). Heterogeneous photocatalyst-driven persulfate activation process under visible light irradiation: From basic catalyst design principles to novel enhancement strategies. *Chemical Engineering Journal*, *428*.

Tiep, N. H., My, K. T. H., Lam, N. D., Nhat, H. N., Dang, N. T., Khan, D. T., Truong-Son, L. V., Yahya, B. N., & Phan, T. L. (2024). Structural, Phonon Vibrational, and Catalytic Properties of High-Energy Ground ZnO Nanoparticles. *Journal of Electronic Materials*, *53*(12), 7271–7281.

Tinoco Navarro, L. K., & Jaroslav, C. (2023). Enhancing Photocatalytic Properties of TiO_2 Photocatalyst and Heterojunctions: A Comprehensive Review of the Impact of Biphasic Systems in Aerogels and Xerogels Synthesis, Methods, and Mechanisms for Environmental Applications. *Gels*, *9*(12), 976.

Tratrat, C., Alomair, N. A., Kochkar, H., Jubran al Malih, R., Haroun, M., Abubshait, S., Younas, M., Berhault, G., Venugopala, K. N., Nagaraja, S., Emeka, P. M., Elsewedy, H. S., Nair, A. B., & Kamoun, M. (2023). Visible-light-driven selective esterification of benzaldehyde derivatives using strontium-modified 1D titanium dioxide nanotubes. *Journal of Photochemistry and Photobiology A: Chemistry*, *438*, 114508.

Tu, Y., Zhong, J., Ding, H., Zhang, H., Lv, G., Zhang, J., & Hou, X. (2022). Preparation of fly ash supporting nano-TiO2 composite photocatalyst by a wet mechanical grinding method. *Chemical Physics Letters*, *805*, 139978.

Tuama, A. N., Alzubaidi, L. H., Jameel, M. H., Abass, K. H., bin Mayzan, M. Z. H., & Salman, Z. N. (2024). Impact of electron–hole recombination mechanism on the photocatalytic performance of ZnO in water treatment: A review. *Journal of Sol-Gel Science and Technology*, *110*(3), 792–806.

U.S. Energy Information Administration (EIA). (2023). *EIA forecasts global oil supply to increase and per capita gasoline consumption to fall in 2024*.

USDA Foreign Agricultural Service. (2024). *Malaysia: Biofuels Annual*.

USDA/MPOB. (2026). *USDA raises Malaysia's palm oil production forecast for MY 2025/26*.

Ushasaraswathi, U. (2023). TiO_2 As an Effective Photocatalyst: A review. *International Journal of Research and Analytical Reviews (IJRAR), 10*(1), 920–931.

Varón, L. M., Narváez-Romo, B., Costa-Sobral, L., Barreto, G., & Simões-Moreira, J. R. (2023). Novel high-flux indoor solar simulator for high temperature thermal processes. *Applied Thermal Engineering*, *234*, 121188.

Verma, P., Kuwahara, Y., Mori, K., Raja, R., & Yamashita, H. (2020). Functionalized mesoporous SBA-15 silica: recent trends and catalytic applications. *Nanoscale*, *12*(21), 11333–11363.

Wai, H. S., & Li, C. (2023). Fabrication of Well-Aligned ZnO Nanorods with Different Reaction Times by Chemical Bath Deposition Method Applying for Photocatalysis Application. *Molecules*, *28*(1), 397.

Wang, A., Quan, W., Zhang, H., Li, H., & Yang, S. (2021). Heterogeneous ZnO-containing catalysts for efficient biodiesel production. *RSC Advances*, *11*(33), 20465–20478.

Wang, Q., Fang, X., Hao, P., Ren, H., Zhao, Y., Huang, F., Xie, J., Cui, G., & Tang, B. (2020). Controllable fabrication of TiO_2 anatase/rutile phase junctions by a designer solvent for promoted photocatalytic performance. *Chemical Communications*, *56*(79), 11827–11830.

Wang, Y., Chen, R., Zhu, F., Wang, H., Qiu, Y., Xue, B., Zhao, B., & Zhou, T. (2025). Optimization of transesterification of sewage sludge for biodiesel production using monosaccharide-, disaccharide-, and polysaccharide-based sulfonic acid solid catalysts. *Journal of Environmental Chemical Engineering*, *13*(3), 116826.

Wary, R. R., Narzary, M., Brahma, B. B., Brahma, D., Kalita, P., & Buzar Baruah, M. (2023). Nanostructural Design of ZnO Using an Agro-Waste Extract for a Sustainable Process and Its Photocatalytic Activity. *ACS Applied Biomaterials*, *6*(11), 4645–4661.

Weldeslase, M. G., Benti, N. E., Desta, M. A., & Mekonnen, Y. S. (2023). Maximizing biodiesel production from waste cooking oil with lime-based zinc-doped CaO using response surface methodology. *Scientific Reports*, *13*(1), 1–14.

Welter, R., Santana, H., de la Torre, L. G., Barnes, M. C., Taranto, O. P., & Oelgemöller, M. (2022). Biodiesel Production from Canola Oil by TiO_2-Photocatalysed Transesterification. *SSRN Electronic Journal*, 1–62.

Wu, C., Liu, Z., & Zhang, J. (2025). Development and enhancement of charge separation processes for the degradation of RhB using an innovative ZnO/$MgIn_2S_4$ S-scheme heterojunction photocatalyst. *Journal of Cleaner Production*, 124250.

Wulandari, A., Hartono, D. M., & Dahlan, A. V. (2023). Life cycle assessment analysis of empty oil palm fruit bunches waste from palm oil mill activities. *E3S Web of Conferences*, *422*, 01001.

Xu, H., Ou, L., Li, Y., Hawkins, T. R., & Wang, M. (2022). Life Cycle Greenhouse Gas Emissions of Biodiesel and Renewable Diesel Production in the United States. *Environmental Science and Technology*, *56*(12), 7512–7521.

Xu, S., Zhou, C., Fang, H., Zhu, W., Shi, J., & Liu, G. (2023). Synthesis of ordered mesoporous silica from biomass ash and its application in CO_2 adsorption. *Environmental Research*, *231*, 116070.

Yaakob, Y. D. S. I. S. (2021). *Twelfth Malaysia Plan (12MP)*.

Yadav, P., Aggarwal, S., Chaudhary, A., & Vaya, D. (2025). Zinc oxide-based nanomaterials as efficient photocatalysts and electrocatalysts. *Ionics*, *0123456789*, 1–27.

Yaghi, M., Chidiac, S., Awad, S., El Rayess, Y., & Zgheib, N. (2025). An Overview of Biodiesel Production via Heterogeneous Catalysts: Synthesis, Current Advances, and Challenges. *Clean Technologies*, *7*(3), 62.

Yanti, F. M., Arfiana, Murti, S. D. S., Valentino, N., Pertiwi, A., Heriyanti, S. I., Sevie, G. N., Destian, E. F., Zulianto, R. I., & Muhammad, I. S. A. B. (2023). Impregnation Effect of Iron (Fe) and Cobalt (Co) on ZSM-5 Zeolite Catalyst from Rice Husk Ash and Coal Fly Ash for Methanol Synthesis. *Evergreen*, *10*(3), 1889–1897.

Yusuf, B. O., Oladepo, S. A., & Ganiyu, S. A. (2024). Efficient and Sustainable Biodiesel Production via Transesterification: Catalysts and Operating Conditions. *Catalysts*, *14*(9).

Zailan, S. N., Bouaissi, A., Mahmed, N., & Abdullah, M. M. A. B. (2020). Influence of ZnO Nanoparticles on Mechanical Properties and Photocatalytic Activity of Self-cleaning ZnO-Based Geopolymer Paste. *Journal of Inorganic and Organometallic Polymers and Materials*, *30*(6), 2007–2016.

Zhang, F., Liu, J., Yue, H., Cheng, G., & Xue, X. (2023). Construction of g-C_3N_4 nanoparticles modified TiO_2 nanotube arrays with Z-scheme heterojunction for

enhanced photoelectrochemical properties. *Journal of Materials Science*, *58*(6), 2676–2688.

Zhang, G., Zhang, Q., Chen, G., Yan, B., Yao, J., Wang, H., Wang, R., & Zhang, Y. (2025). Application of S-type heterojunction $CaTiO_3$/ rGO-g-C_3N_4 photocatalyst in the conversion of waste cooking oil to biodiesel: Optimization via RSM and performance evaluation. *Separation and Purification Technology*, *362*(P3), 131922.

Zhang, J., & Li, J. (2022). The Oxygen Vacancy Defect of ZnO/NiO Nanomaterials Improves Photocatalytic Performance and Ammonia Sensing Performance. *Nanomaterials*, *12*(3), 433.

Zhang, P., Peng, C., Li, H., Huang, J., Wang, Y., Yu, Y., & Ding, S. (2022). Wavelength-dependent generation of reactive species in the photodegradation process over pure and C-doped Nb_2O_5. *Separation and Purification Technology*, *286*, 120406.

Zhang, W., Al Samarai, M., Zhao, H., Liu, D., Kiuchi, H., Ugalino, R., Li, S., Yao, F., Feng, Q., & Harada, Y. (2024). Facet-dependent photocatalytic performance and electronic structure of single-crystalline anatase TiO_2 particles revealed by X-ray photoelectron spectromicroscopy. *Journal of Materials Chemistry C*, *13*(1), 61–67.

Zhu, C., & Wang, X. (2025). Nanomaterial ZnO Synthesis and Its Photocatalytic Applications: A Review. *Nanomaterials*, *15*(9), 1–32.

Zhu, X., Wang, J., Yang, D., Liu, J., He, L., Tang, M., Feng, W., & Wu, X. (2021). Fabrication, characterization and high photocatalytic activity of Ag-ZnO heterojunctions under UV-visible light. *RSC Advances*, *11*(44), 27257–27266.

APPENDICES

APPENDIX 1

Calculation Acid Value by titration method

Method: AOCS; Cd 3d-63

Molarity isopropanol KOH = 0.1 M

Volume of titrant isopropanol KOH needed to neutralize WCO (0.2 $\pm$ 0.01 g) = 2.77 mL

Blank volume = 1.844 mL

$$AV = \frac{(V_S - V_B) \times C \times 56.11}{m_{WCO}}$$

= x mg KOH/g

V_S = volume of titrant needs to neutralize 1 g of oil

V_B = volume of titrant needs to neutralize blank solvent

C = concentration of titrant, isopropanol KOH

56.11 = molecular weight of KOH, g/mol

m_{WCO} = mass of WCO, g

$$AV = \frac{(2.77 - 1.84) \times 0.1 \times 56.11}{0.2095}$$

= 24.8 mg KOH/g

$$FFA = \frac{24.8}{2}$$

= 12.4 wt%

APPENDIX 2

Calculation Saponification Value by titration method

Method: ASTM D5558

Molarity HCl = 0.5 M

Molarity isopropanol KOH = 0.5 M

Volume of titrant HCl needed = 9.07 mL

Blank volume = 22.35 Ml

Mass WCO = 2 g $\pm$ 0.01 g

$$SV = \frac{(V_B - V_{HCl}) \times C \times 56.11}{m_{WCO}}$$

= x mg KOH/g

V_B = volume of titrant needs to neutralize blank solvent

V_S = volume of titrant

C = concentration of isopropanol KOH, 0.5 M

56.11 = molecular weight of KOH, g/mol

m_{WCO} = mass of WCO, g

$$SV = \frac{(22.35 - 1.84) \times 0.1 \times 56.11}{0.2095}$$

= 184 mg KOH/g

$$MW = \frac{56.11 \times 3 \times 1000}{SV}$$

56.11 = molecular weight of KOH, g/mol

3 = 3 moles of KOH for 1 mole triglycerides

1000 = converts g to mg (to match SV units)

SV = saponification value, mg KOH/g

$$MW = \frac{56.11 \times 3 \times 1000}{184}$$

= 915 g/mol

APPENDIX 3

Calculation Moisture content

Method: AOCS Aa 3-38

Mass WCO = 10 g $\pm$ 0.01 g

$$Moisture\ content = \frac{W_2 - W_3}{W_2 - W_1} \times 100$$

= x wt%

W_1 = weight of the empty beaker

W_2 = weight of the beaker with sample before drying

W_3 = weight of the beaker with sample after drying

$$Moisture\ content = \frac{54.374 - 54.223}{54.374 - 44.318} \times 100$$

= 1.49 wt%

APPENDIX 4

Calculation of Optical Band Gap Using the Tauc Plot

Step 1: Convert Wavelength (λ) to Photon Energy (hv)

$$hv = \frac{1240}{\lambda}$$

λ = wavelength in nm

hv = photon energy in eV

Step 2: Apply the Kubelka-Munk Function

$$F(R) = \frac{(1-R)^2}{2R}$$

R = reflectance (in decimal, not %) (R/100)

Step 3: Multiply by Photon Energy

$$F(R) \cdot hv$$

Step 4: Apply the Tauc Exponent

Choose n based on the material:

- n = ½ for direct allowed
- n = 2 for indirect allowed

Then compute: $[F(R) \cdot hv]^n$

Processed UV–Vis-DRS data showing the optical properties of the photocatalyst, prepared for Tauc plot construction and band gap energy estimation.

A	B	C	D	E	F	G	H	I
Wavelength	**Reflectance**	**Reflectance**	**Absorption coefficient**	**Scaterring coefficient**	**F(R)**	**Energy**	**(F(R)hv)^1/2**	**(F(R)hv)^2**
nm	%	R	m-1	m-1		eV	(eVcm-1)^1/2	(eVcm-1)^2
				s=2R	F(R)=k/s	E=hv	(F*G)^(1/2)	(F*G)^ 2
		B/100	(1-C)^2	2 * C	F=D/E	1240/A		
800	85.19	0.8519	0.02193361	1.7038	0.012873348	1.55	0.091133889	6.89794E-05
798	85.4	0.854	0.021316	1.708	0.012480094	1.553884712	0.089618883	6.45057E-05
796	85.48	0.8548	0.02108304	1.7096	0.012332148	1.557788945	0.088974397	6.26701E-05
794	85.29	0.8529	0.02163841	1.7058	0.012685198	1.561712846	0.09012557	6.59769E-05
792	85.41	0.8541	0.02128681	1.7082	0.012461544	1.565656566	0.089214959	6.33506E-05
790	84.84	0.8484	0.02298256	1.6968	0.013544649	1.569620253	0.092893767	7.4464E-05
788	85.32	0.8532	0.02155024	1.7064	0.012629067	1.573604061	0.089585537	6.44097E-05
786	85.22	0.8522	0.02184484	1.7044	0.012816733	1.577608142	0.090134095	6.60019E-05
784	85.37	0.8537	0.02140369	1.7074	0.012535838	1.581632653	0.089027438	6.28196E-05
782	85.52	0.8552	0.02096704	1.7104	0.012258559	1.585677749	0.087924975	5.97653E-05
780	85.38	0.8538	0.02137444	1.7076	0.012517241	1.58974359	0.088734143	6.19959E-05
778	85.13	0.8513	0.02211169	1.7026	0.012987014	1.593830334	0.090267956	6.63949E-05
776	85.33	0.8533	0.02152089	1.7066	0.012610389	1.597938144	0.088835032	6.22783E-05
774	84.97	0.8497	0.02259009	1.6994	0.01329298	1.602067183	0.091090023	6.88467E-05
772	85.3	0.853	0.021609	1.706	0.012666471	1.606217617	0.088802589	6.21874E-05
770	85.28	0.8528	0.02166784	1.7056	0.01270394	1.61038961	0.088818562	6.22322E-05
768	84.93	0.8493	0.02271049	1.6986	0.013370122	1.614583333	0.090999176	6.85725E-05
766	85.2	0.852	0.021904	1.704	0.01285446	1.618798956	0.089110825	6.30553E-05

APPENDIX 5

Calculation of ester content and FAME yield based on GC–MS peak

Note: The following dataset represents one of the experimental runs conducted during this study. The calculation procedure for ester content and FAME yield as per EN 14103 methodology.

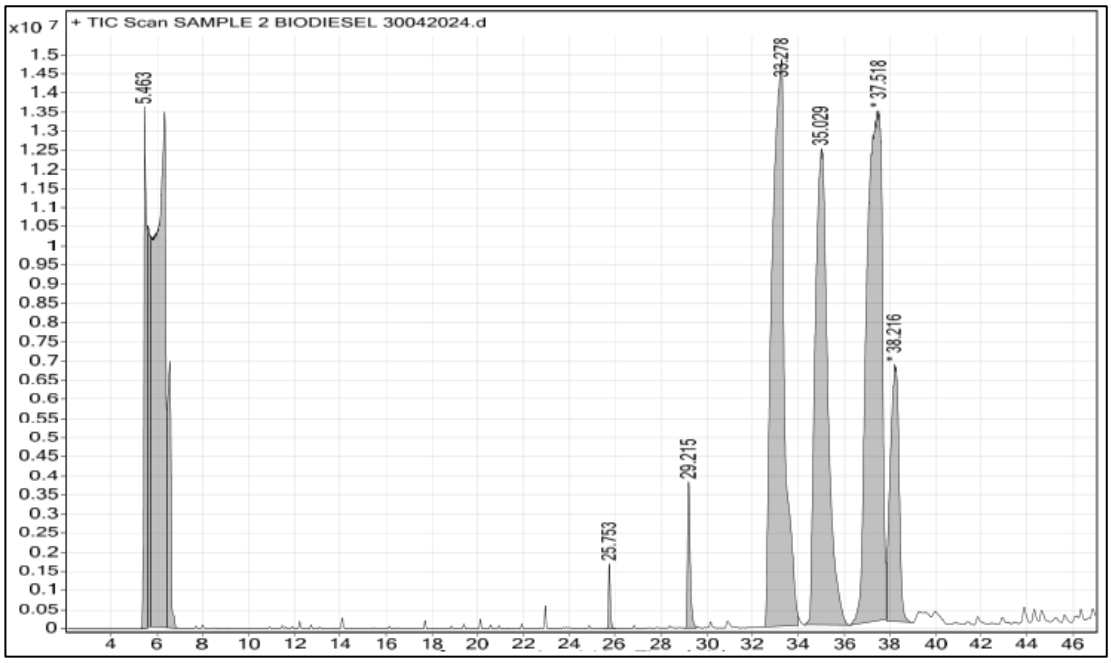


Figure A1 GCMS chromatogram of WCO Biodiesel produced by transesterification in the presence of 1 wt.% NaOH catalyst, 12:1 methanol, 65 ˚C at 1 h reaction time, (One of the esterified-WCO catalysed by TiO_2/EFBA)

Table A2
Composition of Fatty acid methyl ester in the WCO Biodiesel

Retention time (min)	FAME compound (Methyl ester)	Composition (% by weight)
25.753	Methyl laurate (C12:0)	1.48
29.215	Methyl myristate (C14:0)	3.65
33.278	Methyl palmitate (C16:0)	30.25
35.029	Methyl heptadecanoate (C17:0)	18.25
37.518	Methyl oleate (C18:1)	32.82
38.216	Methyl linoleate (C18:2)	10.55

Calculation FAME yield

Step 1: Ester content calculation

$$Ester\ content, c = \left(\frac{A_T - A_{IS}}{A_{IS}}\right) \times \left(\frac{C_{IS} - V_{IS}}{m}\right) \times\ 100$$

A_T = total peak area of FAMEs (C14 to C24:1)

A_{IS} = peak area of internal standard

C_{IS} = concentration of internal standard (10 mg/mL @ 1000 ppm)

V_{IS}= volume of internal standard added (2.5 mL)

m = mass of WCO-biodiesel sample (125 mg)

$$Ester\ content, c = \left(\frac{93\ -\ 18.25}{18.25}\right) \times \left(\frac{10 -\ 2.5}{125}\right) \times\ 100$$

= 106.3%

Step 2: Mass of Pure Biodiesel

$$Y = \left(\frac{c}{100}\right) \times d$$

Y = mass of pure biodiesel (g)

c = ester content (%)

d = total mas of biodiesel recovered after purification

$$Y = \left(\frac{106.3}{100}\right) \times 4.2$$

= 4.46 g

Step 3: FAME yield

$$FAME\ yield\ (\%) = \left(\frac{Y}{mass\ of\ feedstock\ oil}\right) \times 100$$

Y = mass of pure biodiesel, g

Feedstock oil = initial mass of esterified WCO, 5 g

$$FAME\ yield\ (\%) = \left(\frac{4.46}{5}\right) \times 100$$

= 89.2%

APPENDIX 6

Illustration of a Bench-Scale Photo-Reactor Setup for Laboratory Conditions



Figure A2 Illustration of a bench-scale photo-reactor setup under UV light using UV illumination



Figure A3 Illustration of a bench-scale photo-reactor setup under visible light using led illumination

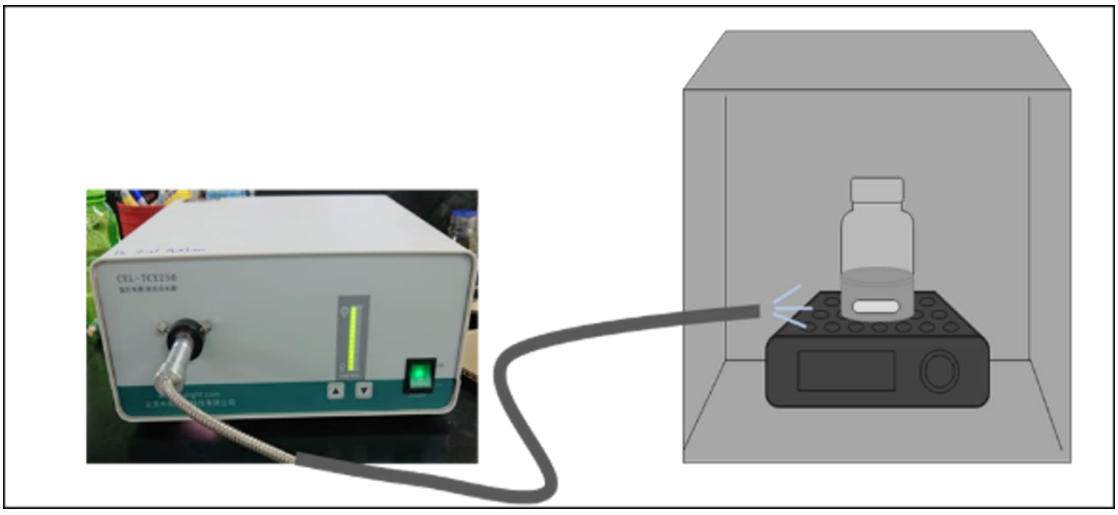


Figure A4 Illustration of a bench-scale photo-reactor setup under visible light using xenon illumination

AUTHOR'S PROFILE



Siti Fadhilah Ibrahim is a doctoral candidate in Chemistry at Universiti Teknologi MARA (UiTM), specializing in photocatalysis and biodiesel production. Her research focuses on the development of EFBA-supported TiO_2 and ZnO photocatalysts for the photocatalytic esterification of high-FFA waste cooking oil, contributing to sustainable fuel technologies. She holds a Master's degree in Catalysis from Universiti Putra Malaysia and a bachelor's degree in chemistry from Universiti Malaysia Terengganu. Her academic journey is marked by multiple research assistantships, peer-reviewed publications in high-impact journals, and awards for innovation and design. She has presented her work at national and international conferences and is actively involved in collaborative research on renewable energy and green chemistry. Upon completing her thesis, she aims to contribute to academia and industry through research, innovation, and sustainable development initiatives.

LIST OF PUBLICATIONS

Ibrahim, S. F., Mohd-Shohaimi, N. A., Mohd-Hir, Z. A., Mastuli, M. S., Taufiq-Yap, Y. H., & Ibrahim, M. L. (2024). Efficient Photocatalytic Esterification of Waste Cooking Oil Over Empty Fruit Bunches Ash- Supported TiO_2. *Iranian Journal of Catalysis, 14*(3). 142425 (1-16).

Ibrahim, S. F., Mohd-Shohaimi, N. A., Ibrahim, M. L., Mohd-Hir, Z. A., Mastuli M. S., & Wan-Mokhtar, W. N. A. (2023). Photo-esterification of Waste Cooking Oil Using a Novel Nanocatalyst TiO_2 Impregnated with Empty Fruit Bunches Ash Heterogeneous Catalyst. *Malaysian Journal of Analytical Sciences, 27*(3). 586 – 599.

Mohd-Shohaimi, N. A., Khairul-Adnan, N., & Ibrahim, S. F. (2024). Photo-Esterification of Waste Cooking Oil Using ZnO Doped Empty Fruit Bunches Ash Heterogeneous Catalyst. *Recent Innovations in Chemical Engineering, 17*(2).119-133.

Mat-Rosid, S., Mat-Rosid S. J., Mohd-Shohaimi, N. A., & Ibrahim, S. F. (2024). Unveiling the Antibacterial Potential of Biodiesel Derived from Waste Cooking Oil. *Gading Journal of Science and Technology*, *7*(2): 16-23.

Nizar, U. K., Gunawan, R., Taufiq-Yap, Y. H., Sundari, R., Mahmud, S., Ibrahim, S. F., Sazali, N., Sintia, A., Lazuardi, A., & Pernadi, N. L. (2023). Utilization of Avocado Seed Waste in the Synthesis of Sulfonated Carbon Catalysts Using Chlorosulfonic Acid for Biodiesel Production. *Rasayan Journal of Chemistry*, *16*(3). 1-9.

Rashid, U., Hazmi, B., Abdullah, R. F., Ibrahim, S. F., Alsalme. A., & Toshiki, T. (2023) Physicochemical Properties of Waste Palm-Based Catalysts Synthesized from Pyrolyzed and Hydrothermalized Chars for Biodiesel *Production. Topic in Catalysis,* 66. 723–739.